Influence of a Liquid Crystalline Block on the Microstructure and Optical Properties of Block Copolymers

by

John Tsen-Tao Chen

B.S., Physics
Massachusetts Institute of Technology, 1991

SUBMITTED TO THE DEPARTMENT OF MATERIALS SCIENCE AND ENGINEERING IN PARTIAL FULFILLMENT OF THE REQUIREMENTS FOR THE DEGREE OF

DOCTOR OF PHILOSOPHY IN MATERIALS SCIENCE AND ENGINEERING

AT THE
MASSACHUSETTS INSTITUTE OF TECHNOLOGY

JUNE 1997

Signature of Author .....
Department of Materials Science and Engineering
May 2, 1997

Certified by .....
Edwin L. Thomas
Morris Cohen Professor of Materials Science and Engineering
Thesis Supervisor

Accepted by .....
Linn W. Hobbs
John F. Elliott Professor of Materials
Chairman, Department Committee on Graduate Students

Influence of a Liquid Crystalline Block on the Microstructure and Optical Properties of Block Copolymers

by

John Tsen-Tao Chen

Submitted to the Department of Materials Science
and Engineering on May 2, 1997 in Partial
Fulfillment of the Requirements for the Degree of
Doctor of Philosophy in Materials Science and Engineering

ABSTRACT

The effect of a liquid crystalline block on the microstructure and optical properties of diblock copolymers was studied. In traditional flexible amorphous noncrystallizable AB (coil-coil) block copolymers, the tendency for the A and B blocks to phase separate due to their chemical incompatibility and the constraint imposed by the covalent bond between the two blocks results in the formation of spatially periodic microdomain morphologies. Each of the experimentally observed microdomain morphologies is characterized by well defined symmetry properties (i.e. point groups, space groups). In the long wavelength limit, in which the wavelength of light is much larger than the characteristic domain size of the block copolymer morphology ($\lambda >> D$), a microphase separated block copolymer behaves like a homogeneous dielectric medium which can be described by a single dielectric constant tensor, ε. In the most general case, the dielectric constant tensor is described by three independent principal dielectric constants, ε_1, ε_2, and ε_3, which are related to the principal refractive indices through the following relation, $n_i = \sqrt{\varepsilon_i}$. From symmetry arguments, all of the coil-coil block copolymer morphologies are found to exhibit either uniaxial ($n_1 = n_2 = n_o$, $n_3 = n_e$) or isotropic ($n_1 = n_2 = n_3 = n$) optical properties. Effective medium theory (EMT) is used to obtain well known expressions for the principal refractive indices of the various microdomain structures in terms of the isotropic refractive indices and volume fractions of each block.

The ability of coil-coil block copolymers to self-assemble into spatially periodic microstructures with well defined domain sizes makes them attractive as potential optical waveguide materials. An N-layer waveguide formalism was developed and used to theoretically predict the optical waveguiding properties of model lamellar-forming diblock copolymer films. In the long wavelength limit, lamellar films behave like optically uniaxial films with a well defined birefringence. When the domain size approaches the wavelength of light, the light is found to preferentially segregate into the

high index layers of a lamellar film. In addition, light can be concentrated in different regions of a block copolymer waveguide by choosing which mode is excited. Experimentally, a symmetric ultrahigh molecular weight poly(styrene-b-isoprene) diblock (MW = 1,000,000 g/mol) and its blends with a lower molecular weight diblock or low molecular weight polystyrene and polyisoprene homopolymers were used to fabricate optical waveguides. Despite high temperature annealing and a number of different sample processing procedures, long range order of the ultrahigh molecular weight diblock lamellae parallel to the substrate sufficient for optical waveguiding was not achieved. The highest degree of order was achieved for a diblock copolymer blend sample containing 13 wt% low molecular weight diblock.

While coil-coil diblock copolymers are nearly conformationally symmetric, liquid crystalline (LC) diblock copolymers which consist of a main-chain rodlike polymer covalently bonded to a flexible polymer (rod-coil) represent the extreme case in conformational asymmetry. The morphologies formed by a high molecular weight series of anionically synthesized poly(hexyl isocyanate-b-styrene), P(HIC-b-S), rod-coil block copolymers were studied using polarized optical microscopy (POM), transmission electron microscopy (TEM), and selected-area electron diffraction (SAED). Three new microphase separated morphologies (lenticular aggregate, zig-zag lamellar, and arrowhead) with domain sizes ranging from 60 nm to nearly a micron were observed as a function of volume fraction of rod (f_{PHIC} = 0.42 to 0.98). In each morphology, the rods exhibited orientational order characteristic of liquid crystalline polymers and tilt with respect to the intermaterial dividing surface (IMDS). The tilt angle is determined by the following factors: minimization of both the chain stretching experienced by the coil block and the interfacial area between the rod and coil domains, and axial registration of the chains within the crystallized PHIC domains. POM studies and TEM results obtained for ultrathin samples of the rod-coils suggest that the isotropic-nematic transition precedes the microphase separation transition during formation of the morphologies from solution.

A type of LC-coil block copolymer which has a LC block consisting of a flexible chain with pendent mesogens connected via flexible spacers (side-chain LC-coil) has a conformational asymmetry intermediate to that of coil-coil and rod-coil diblocks. The morphologies formed by a series of anionically synthesized poly(isoprene LC-b-styrene), P(ILC-b-S), diblocks with pendent azobenzene LC mesogens were studied with wide-angle X-ray diffraction (WAXD), TEM, and small-angle X-ray diffraction (SAXD). With the exception of a bicontinuous (possibly nonequilibrium) morphology at f_{PILC} = 0.29, classical cylinder and lamellar microdomain morphologies were observed for all the remaining six side-chain LC-coils (f_{PILC} = 0.20 to 0.82). Within the LC domains, the PILC block was observed to form a smectic A mesophase in which the azobenzene mesogens adopted a homogeneous anchoring condition with respect to the IMDS. The observation of only classical microdomain morphologies suggests that the microphase separation transition occurs first as solvent evaporates from the side-chain LC-coil solutions. With further solvent evaporation, an isotropic-smectic A transition occurs within the solvent-swelled PILC domains.

A framework based primarily on symmetry arguments was developed which can be used to predict what morphologies a particular LC-coil block copolymer is most likely to form and what its corresponding optical properties will be. The classical microdomain structures are good candidate structures for LC block copolymers because they both partition space efficiently and are periodic. An LC-coil block copolymer will tend to form morphologies in which the symmetry of the LC phase within the LC domains is such that overall translational symmetry of the microdomain structure is preserved subject to some important constraints. In particular, the LC phase must obey certain anchoring conditions (homogeneous or homeotropic) at the IMDS while maximizing the

overall point group symmetry of the microdomain structure. Energetically favorable structures also contain the fewest periodic defects (point and line) within the LC domains. Once the symmetry and orientation of the LC block within the LC domains is determined for a given structure, the appropriate EMT expressions can be used to determine actual values of the principal refractive indices.

Thesis Supervisor: Edwin L. Thomas

Title: Morris Cohen Professor of Materials Science and Engineering

Acknowledgments

This thesis is the culmination of nearly six years of research and hard work. For most people, however, a doctoral thesis is not the kind of thing one does alone. In fact, I was extremely fortunate to have people helping me each step of the way. In my opinion, the key ingredients to a successful thesis are the following: ideas, guidance, problem solving, determination, support, and luck. Every thesis begins with an idea. In my case, Professor Edwin (Ned) Thomas, my advisor, provided me with a thousand ideas everyday for which I am grateful. His enthusiasm and knowledge of science are limitless. An idea, however, is useless if you don't know what to do with it or how to make something out of it. Typically, a person is not born with the skills necessary to do a Ph.D. in his or her genes. If one is lucky, he or she is at least born with curiosity. This is why graduate students have a thesis committee and an advisor. I had the good fortune of having TWO advisors. My father, Sow-Hsin Chen, has been a role model for me since I was born and I am grateful to him for explaining the world of physics to me for as long as I can remember. If it wasn't for my father, I probably wouldn't have embarked on this *long* journey. The two people who really showed me how to perform experiments and conduct scientific research properly have been my father and Ned.

Besides my two advisors, I had a great (and large) committee: Professor Michael Rubner, Professor Anne Mayes, Professor Chris Ober at Cornell University, Professor John Rabolt at University of Delaware, and Dr. Carl Zimba. The committee members were extremely helpful during the past few years giving me valuable advice and guidance in my research endeavors. In addition, I had the opportunity to collaborate with many of them in the course of my stay at M.I.T. In particular, Professor Ober was instrumental in the rod-coil and side-chain LC-coil work which turned out to be a very fruitful area of research for both his and Ned's groups. Special thanks go out to his student Guoping

Mao who synthesized most of the LC block copolymers at Cornell and was an indispensable reference during these last few months. In addition, I'd like to thank John and Carl who introduced the world of waveguides to Ned and I and worked closely with us on the block copolymer waveguide project. I want to also thank Carl for developing the N-layer waveguide formalism from which he and I based the Mathematica program and all of our waveguide calculations. I won't forget our many discussions on Snell's Law, the WKB approximation, and OFI's.

In retrospect, I suppose one can always say, "It wasn't that bad." My memory, however, will probably never let me say this phrase. Everyday of a Ph.D. is a potential challenge where you face new problems no one ever encountered. Someone who I can't quite recall once asked me on a particular Friday afternoon to, "determine the crystal structure of PHIC from those electron diffraction patterns by Monday...it'll be easy." This *easy* task later turned into a problem which I didn't completely figure out for over half a year!!! Basically, the point is, a Ph.D. is one long exercise in problem solving. Therefore, I want to take some time now to thank those people in the group who especially helped me to *solve* some of the many problems I had over my many years at M.I.T. Early on, Dwight Schwark helped "show me the ropes" on the TEM, microtome, sample preparation, and also gave me a lot of neat things like tweezers. Stephanie Simmons was always someone I could count on to be a knowledgeable, objective, and calm person to talk to. We also became quite proficient on the Maelstrom apparatus as well. In my last two years, I enjoyed discussing more humorous issues with Len Radzilowski who has great patience. I have probably asked Len tons of dumb questions which he has always given an answer to. One thing nice about the Thomas Group is the influx of foreign visitors. I greatly enjoyed meeting Susanne Brinkmann (Germany), Apostolos Avgeropolous (Greece), and Elisabeth Prasman (Belgium). Frisbee in Killian Court and lunches together were a fun distraction. I suppose I also learned a thing or two

from Susanne and Apostolos (chemists). Apostolos helped teach me and do glass blowing for me which was wonderful.

No matter how much help you have, in the end, you have to wake up every morning for five or six years, go to lab, and do research. This feat cannot be accomplished without enormous determination and support. I am deeply indebted to my fiancee and future wife Yi-Ling (Jennifer) Wang. Thanks for pushing me everyday, helping me to focus on the important things, and not slacking off (too much). I appreciate your patience in listening to my complaining too, Confucius would be proud. I also want to thank my mother, grandmother, sisters, Don, Eddie, and John Fiske for supporting me throughout these many years and telling me that a Ph.D. is worth getting. I have to also thank Yi-Ling's Golden Retriever Lucky (who will soon be my dog as well) for simply being Lucky. He helped remind me that there is more to life than getting block copolymer lamellae to lie flat or explaining why rod-coils form arrowheads.

Finally, I'd like to acknowledge Professor Ted Atkins for his help in interpreting *those* electron diffraction patterns, Professor Steve Senturia for use of his Metricon, George Fischer, Russell Gehr, and Professor Robert Boyd at the University of Rochester for extremely helpful discussions regarding effective medium theories. Oh yes, I also mentioned luck. Certainly, I have been lucky in my career as a graduate student. But if you think about it, with all the help and support I have received from all the people above, not to mention my own investment of hard work and sweat, you would have to say I was pretty lucky to not have to rely exclusively on luck.

Table of Contents

List of Figures

List of Tables

Chapter 1: Motivation and Organization

Liquid crystalline (LC) block copolymers are a unique form of self-assembling polymer which combines the physics of microphase separating block copolymers with the orientational order of liquid crystalline polymers. An entirely new area of research requiring a deep understanding of chemistry, physics, and materials science has emerged in recent years which is centered around the synthesis and characterization of these materials. In comparison to homopolymers and even traditional noncrystalline flexible block copolymer (coil-coil) materials, LC block copolymers offer unique opportunities for the design of periodic composite structures with characteristic length scales ranging from tens of nanometers (nanoscopic) to nearly a micron (microscopic). Control of the self-assembly of structures over such a wide range of size regimes has been previously unimaginable for traditional synthetic materials. In addition to their structural flexibility, LC block copolymers have highly tailorable optical properties. LC blocks can be chosen which have nonlinear optical, ferroelectric, electro-optic, or anisotropic optical properties. The novel structures formed by these kinds of LC block copolymers have potential uses as optical switches, optical waveguides, filters, dielectric mirrors, etc.

The morphologies formed by coil-coil block copolymers have been extensively studied experimentally and theoretically for decades and are well understood. Similarly, the thermodynamic principles which govern the microphase separation process are firmly established. In contrast, our current understanding of the morphologies formed by LC block copolymers containing one LC block and one noncrystallizable flexible coil block, hereafter called LC-coil diblocks, and the fundamental principles which govern the self-assembly of these materials is still in its infancy. Therefore, one goal of this thesis is to be able to understand the effect of an LC block on the morphology of block copolymers. We will find that the specific architecture of the block copolymer, whether coil-coil,

main-chain LC-coil (rod-coil), or side-chain LC-coil, plays an important role in determining the ultimate morphology.

Similarly, the optical properties of LC block copolymers and to a lesser degree traditional coil-coil block copolymers are not well understood. In comparison to the large body of research which has been devoted to studying the optical properties of homopolymers, very little research has been focused on the optical behavior of block copolymer systems, which are essentially composites. Unlike flexible polymers, LC polymers exhibit highly anisotropic optical properties. As a result, another goal of this thesis is to understand and characterize the optical properties of microphase separated LC block copolymers. Although not complete by any means, this thesis is an attempt to characterize and predict both the microstructures and the optical properties of LC block copolymers in a systematic way.

A brief description of how the thesis is organized will now be given. The main body of the thesis is contained in Chapters 2-5. Chapter 2 provides a detailed discussion of coil-coil block copolymer morphology and optical properties. This chapter serves as a platform from which to build our understanding in the following chapters. In addition, Chapter 2 includes a thorough discussion of the theoretical optical waveguiding properties of block copolymer thin films and the results of actual experiments on lamellar-forming poly(styrene-b-methyl methacrylate) and poly(styrene-b-isoprene) coil-coil diblock copolymers. The block copolymer waveguide section is based primarily on the 1995 Macromolecules paper (6) and APS talk (7) (see Biographical Note). Chapters 3 and 4 cover the two LC-coil block copolymer systems studied in this thesis: rod-coil and side-chain LC-coil, respectively. Each of these chapters is a self-contained unit having its own Introduction, Background and Previous Work, Synthesis and Characterization, Sample Preparation, Experimental Techniques, and Results and Discussion sections. In particular, Chapter 3 discusses the morphologies formed by a

novel series of poly(hexyl isocyanate-b-styrene) rod-coil diblock copolymers and is based on the 1996 Science (1) and 1995 Macromolecules (7) papers and the 1996 MRS talk (5). Chapter 4 discusses the morphologies formed by a novel series of poly(isoprene LC-b-styrene) side-chain LC-coil diblock copolymers and is based on the 1997 Macromolecules paper (2). In Chapter 5, a framework is developed which can be used to predict the most probable morphologies and optical properties of LC block copolymers from symmetry arguments. This work is based on the 1996 Macromolecular Symposia paper (3). Following Chapter 5, conclusions a discussion of possible future experiments is given. Related discussions which complement the main body of the thesis are included in the form of appendices. At the very end of the thesis, a bibliography and biographical note are given.

Chapter 2: Coil-Coil Block Copolymers

2.1 Introduction

Block copolymers are thermodynamically a one component system, which, from a microstructural point of view, behave as a composite material. As a result, a block copolymer medium exhibits optical properties which are directly dependent on both its microphase separated morphology and the optical properties of its individual constituents. The relative importance of each of these contributions depends on the specific nature of the block copolymer system: coil-coil, rod-coil, or side-chain LC-coil. LC polymers have conformations which are significantly different from those of noncrystalline flexible coil-like polymers. In addition, LC polymers have highly anisotropic optical properties. A priori, however, the effects of a LC component on the resulting microstructure and optical properties of a block copolymer are unknown and highly complex. Before we treat LC-containing block copolymers, the microphase separated morphologies and optical properties of traditional coil-coil block copolymers must first be understood. Coil-coil block copolymers thus serve as a natural point of reference and starting point from which to systematically introduce block copolymers with greater structural and optical complexity. As we shall see in this chapter, for coil-coil diblock copolymers, the morphology strongly influences the macroscopic optical behavior.

2.2 Coil-Coil Block Copolymer Morphology

2.2.1 General Description

Coil-coil block copolymers are noncrystallizable flexible long-chain molecules which are made up of two or more covalently bonded subchains or blocks which are themselves composed of identical monomeric repeat units. Linear AB diblock copolymers are the simplest type of block copolymer and consist of N_A linked monomer units of A covalently coupled to N_B linked monomer units of B. The total degree of polymerization for the diblock copolymer is $N = N_A+N_B$. In most cases, the A and B blocks are incompatible due to differences in the chemical structure of each kind of repeat unit. As a result, interactions between the A and B segments give rise to a positive heat of mixing which is characterized by the Flory-Huggins segment-segment interaction parameter, χ. As with polymer blends, χ is taken only to be a function of temperature with the form,

$$\chi(T) = \alpha + \frac{\beta}{T} \qquad (2.1)$$

where α and β are constants specific to a particular block copolymer system. For sufficiently high temperatures, a block copolymer melt is characterized by a single homogeneous disordered phase in which the A and B blocks are miscible. For temperatures lower than a critical temperature, called the order-disorder transition temperature T_{ODT}, the A and B blocks become immiscible and the thermodynamic one component system undergoes a disorder-order transition into spatially periodic A-rich and B-rich regions whose overall geometry is a function of composition, $f_A = N_A/N$. The transition is first order except at $f_A = 0.50$ where it is second order. As can be seen from

Equation 2.1, the driving force for phase separation increases with the amount of undercooling T_{ODT}-T. In contrast to polymer blends which macrophase separate for temperatures below the binodal with no inherent length scale to their final equilibrium phase separated morphology, diblock copolymers can only microphase separate locally on a length-scale comparable to the end-to-end distance of the block copolymer chain because of the constraint imposed by the covalent bond between the A and B blocks. The unique ability of block copolymers to microphase separate allows them to self-assemble into one, two, and three dimensionally periodic structures.

2.2.2 Previous Experimental Work

Experimental investigations of the morphologies formed by microphase separated diblock copolymers have been ongoing for more than three decades. Early on, studies of high molecular weight poly(styrene-b-isoprene) and poly(styrene-b-butadiene) diblock copolymers [1-4] showed the existence of lamellar, hexagonally packed cylindrical, and spherical morphologies (see Figure 2.1). Subsequent studies on sphere-forming diblock copolymers involving small-angle X-ray diffraction (SAXD) [5] and transmission electron microscopy (TEM) [6] showed that the spheres were actually arranged on a body-centered cubic lattice (see Figure 2.2). Another morphology possessing cubic symmetry called the ordered bicontinuous double diamond (OBDD) morphology was observed at compositions intermediate to those of lamellae and cylinders in styrene-isoprene star diblock copolymers [7] and linear diblock copolymers [8] for f_{PS} = 0.28 to 0.34 and 0.62 to 0.66 [9]. The OBDD morphology consists of two interpenetrating four-fold coordinated diamond lattices of the minority component embedded in a matrix of the majority component (see Figure 2.3). Anderson et al. [10] first showed that the intermaterial dividing surface (IMDS) separating the A and B domains could be closely

modeled as a constant-mean-curvature (CMC) surface based on the Schwarz D minimal (H = 0) surface (see Figure 2.4). Since then, some of the original OBDD-forming block copolymers were reexamined by Thomas and coworkers using TEM and SAXS and found not to be OBDD but to be a similar morphology called the double gyroid [11]. The double gyroid is also a bicontinuous morphology possessing cubic symmetry but consists instead of two interpenetrating three-fold coordinated lattices with opposite handedness composed of the minority component which are embedded in a matrix of the majority component. The double gyroid phase derives its name from the IMDS which is believed to be similar to a CMC surface based on the minimal surface discovered by Schoen called the Gyroid or G surface (see Figure 2.5).

In recent years, much experimental work has been focused on the phase behavior of block copolymers near the ODT which has proven to be an equally rich area of research. Several studies have been carried out on low molecular weight diblock copolymers of poly(ethylene-propylene-b-α-butylene), poly(ethylene-b-ethylene-propylene), poly(ethylene-propylene-b-ethylethylene), poly(ethylene-b-ethylethylene), and poly(styrene-b-isoprene) [12-21]. In addition to the lamellar, cylinder and BCC sphere morphologies, the double gyroid phase was first discovered near the ODT between the lamellar and cylinder morphologies by a number of researchers [17, 18]. At about the same time, the lamellar catenoid structure first proposed by Thomas et al. [22] was experimentally observed also between the lamellar and cylinder morphologies farther from the ODT than the double gyroid phase and given the name hexagonally perforated lamellae [14]. Both of these morphologies were later shown to exist on both sides of the morphology diagram in a number of block copolymer systems [19-21]. In addition, several studies [12, 13, 16] confirmed the existence of thermoreversible order-order transitions between morphologies, which were first predicted by theory (see next section).

2.2.3 Previous Theoretical Work

The phenomena of microphase separation in AB diblock copolymers has been extensively studied theoretically and is well understood. After the pioneering work of Meier [23], Helfand and coworkers were the first to use a self-consistent mean-field theory [24-27] of block copolymer microdomain structure to develop a thermodynamic morphology diagram which plotted segregation power vs. composition f_A. Segregation power can be expressed as the product χN and is inversely proportional to temperature. In this work, the free energy and composition profiles were calculated using modified diffusion equations which describe the statistics of the macromolecular conformations. In order to obtain analytical expressions for the free energy, the interface between block copolymer domains was assumed to be narrow relative to the domain size. As a result, the A and B domains are nearly pure and can be characterized approximately by square-wave composition profiles. The narrow interface approximation, however, is only valid in a regime known as the strong segregation limit (SSL) far from the ODT for $\chi N \geq 100$. In the SSL, the stability boundaries between the three classical microdomain morphologies (lamellar, hexagonally packed cylinders, and spheres) are vertical and independent of χN. In these early theories, a face-centered cubic (FCC) arrangement of spheres was always assumed. In a later work, Ohta and Kawasaki [28] showed that a body-centered cubic (BCC) packing of spheres is slightly more favorable than FCC packing which agrees with experimental results. SSL theories, however, have so far failed to predict the stability of bicontinuous cubic morphologies such as the OBDD or double gyroid.

In addition to the phase behavior of block copolymers, Helfand et al. also predicted that the block copolymer domain size D scales with $N^{0.636}$ in the SSL indicating that the block copolymer chains are stretched away from the IMDS. In the

work by Ohta and Kawasaki, a phenomenological SSL theory was developed which captures the basic physics of microphase separated block copolymers in an intuitive way and predicts that the domain size D scales as $N^{2/3}$. The $N^{2/3}$ scaling relationship arises from a competition between enthalpic and entropic driving forces between the homogeneous mixed disordered state and the demixed microphase separated ordered state. In the ordered state, creation of A/B interfaces increases interfacial energy. The interfacial energy per volume can be reduced by spreading the A/B interfaces farther apart. The larger the domain size, however, the greater the block copolymer chains are stretched relative to their unperturbed dimensions and the more the conformational entropy of the system is reduced, which again is energetically unfavorable. A minimization of the free energy increase between the ordered and disordered states gives the equilibrium domain size D and the $N^{2/3}$ scaling result. Phenomenological expressions for the free energy increase per chain and the equilibrium domain size for the case of the lamellar morphology are shown below,

$$\Delta F = \frac{2\sigma N}{\rho_o D} + \frac{3D^2}{8Na^2}, \tag{2.2}$$

$$D = D_e = 2\left(\frac{\sigma a^2}{3\rho_o}\right)^{1/3} N^{2/3}, \tag{2.3}$$

where σ, a, and ρ_o are the interfacial energy, the Kuhn statistical length, and the monomer number density, respectively. Equation 2.2 has been written with kT = 1. For the cylindrical and BCC spherical morphologies, similar expressions can be derived [28] which also predict a $N^{2/3}$ scaling relationship. In addition to the scaling relationship, Equation 2.3 can also be substituted into Equation 2.2 to obtain an expression for the minimum free energy of a lamellar block copolymer system. In a relatively

straightforward manner, this expression can be used to determine the relative partitioning of the free energy between enthalpy (or interfacial energy) and entropy (or chain stretching). For strongly segregated block copolymers, in the approximation that D scales as the end-to-end distance of the chain, interfacial energy and chain stretching are found to comprise 2/3 and 1/3 of the free energy, respectively. The exact numerical values of these fractions, however, will vary slightly depending on how the chain stretching term is treated.

After the SSL work by Helfand and coworkers, Leibler developed a microscopic statistical mean-field theory of phase equilibria [29] which was used to study the onset of microphase separation in block copolymers from the homogeneous melt. In his work, the free energy density of a block copolymer melt is expanded in terms of a local order parameter $\Psi(\mathbf{r})$, which measures the deviation of the local composition from the global spatial average. This Landau expansion is only applicable in the vicinity of the ODT for $\chi N \approx 10.5$ where the order parameter is small and composition profiles have a sinusoidal form. The regime which Leibler's theory describes has come to be known as the weak segregation limit (WSL). In contrast to the SSL, the phase behavior of block copolymers in the WSL is governed by both χN and f_A. Figure 2.6 shows the symmetric block copolymer morphology diagram predicted by Leibler. As expected, a disordered homogeneous melt exists for $T > T_{ODT}$ or $\chi N < \chi N_{spinodal}$. For $\chi N > \chi N_{spinodal}$, ordered lamellar, hexagonally packed cylindrical, and BCC spherical morphologies are predicted to be stable depending on the composition. In addition, first-order phase transitions separate each of the classical morphologies and a second-order critical point exists at $\chi N = 10.5$ and $f = 1/2$. The curved phase boundaries indicate that order-order transitions between morphologies are possible by changing temperature, as was later observed experimentally. In the WSL, the characteristic domain size, D, of each of the morphologies is comparable to the unperturbed end-to-end distance of the block

copolymer chain, which for a Gaussian coil scales as $\sim N^{1/2}$. In addition to the three classical microphase geometries, recent work by Matsen et al. [30] has shown that the double gyroid phase, first observed experimentally, is stable in the WSL and appears between the lamellar and cylindrical phases.

Leibler's WSL mean-field theory neglects second-order effects such as fluctuations and treats intrachain correlations using averaged quantities such as the volume fractions, the mean fields, and the polymer chain distribution functions. Fredrickson and Helfand [31] corrected Leibler's theory to include fluctuations that give rise to deviations in the averaged quantities which appear in the free energy. Unlike the large length scale coherent composition fluctuations which characterize the ordered phase, composition fluctuations present in the disordered phase are incoherent oscillations that average to zero. Fluctuations, however, are important near the ODT and stabilize the disordered region to higher χN values than those predicted by Leibler. In addition, the second order critical point at $f_A = 1/2$ becomes a first-order phase transition.

In recent years, a number of attempts have been made to develop a theory which can successfully be applied to all degrees of segregation [32-35]. Each of the these theories succeeded in predicting phase diagrams which have the expected limiting behavior at low and high χN. In the work by Matsen et al., a self-consistent field theory is used to study the intermediate segregation regime of the phase diagram between $\chi N \sim 15$ and $\chi N \sim 60$. In addition to the classical phases, a closed-packed spherical phase first predicted by Semenov [36] is found to be stable in a narrow region near the ODT for $\chi N \geq 17.67$. The double gyroid phase originally shown to be stable in the WSL is found to be stable in the range $11.14 \leq \chi N \approx 60$. The exact scaling relationship for the domain size in the intermediate segregation regime is still unclear, however. Some mean-field theoretical treatments of block copolymer melts [33, 37] suggest that the domain size exhibits a stronger N dependence in this regime than in either the WSL or the SSL.

2.3 Coil-Coil Block Copolymer Optical Properties

2.3.1 General Optical Properties

In order to characterize the optical properties of block copolymers one must understand how visible light or electromagnetic radiation with wavelengths between 400 nm and 700 nm propagates through a medium composed of a microphase separated block copolymer. The starting point for any discussion on the propagation of visible light in a medium is the classical theory of electromagnetism based on Maxwell's equations [38-40]. Maxwell's equations are shown below for Gaussian units.

$$\nabla \cdot \mathbf{D} = 4\pi\rho \tag{2.4}$$

$$\nabla \cdot \mathbf{B} = 0 \tag{2.5}$$

$$\nabla \times \mathbf{E} = -\frac{1}{c}\frac{\partial \mathbf{B}}{\partial t} \tag{2.6}$$

$$\nabla \times \mathbf{H} = \frac{1}{c}\frac{\partial \mathbf{D}}{\partial t} + \frac{4\pi}{c}\mathbf{J} \tag{2.7}$$

In Equations 2.4 to 2.7, **E** and **H** are the electric and magnetic fields, **D** and **B** are the electric displacement and the magnetic induction, ρ and **J** are the macroscopically averaged electric charge and current densities, and c is the speed of light in vacuum. The Maxwell equations uniquely determine the electric and magnetic fields in a medium composed of an arbitrary distribution of charges and currents provided the constitutive relations are known. In the most general case, the constitutive relations **D**(**E**, **B**), **H**(**E**, **B**), and **J**(**E**, **B**), which describe the behavior of a medium under the influence of the fields, are complicated functions of **E** and **B**. For polymers, however, a number of simplifications can be made. Unlike metals which have a large nonzero conductivity,

typical polymers are isotropic insulators and are a member of a class of materials known as dielectrics. As a result, $\rho = 0$ and $\mathbf{J} = 0$. In addition, polymers are also nonmagnetic materials and typically have a linear response to an applied electric field. Consequently, the constitutive relations can be written in the form:

$$\mathbf{D} = \varepsilon\mathbf{E}, \tag{2.8}$$

$$\mathbf{H} = \mathbf{B}, \tag{2.9}$$

where ε is called the dielectric constant or relative electric permittivity. Taking into account these simplifications, Maxwell's equations in an infinite homogeneous isotropic dielectric medium take the following symmetric form.

$$\nabla\cdot\mathbf{E} = 0 \tag{2.10}$$

$$\nabla\cdot\mathbf{B} = 0 \tag{2.11}$$

$$\nabla\times\mathbf{E} = -\frac{1}{c}\frac{\partial\mathbf{B}}{\partial t} \tag{2.12}$$

$$\nabla\times\mathbf{B} = \frac{\varepsilon}{c}\frac{\partial\mathbf{E}}{\partial t} \tag{2.13}$$

Equations 2.10 to 2.13 can be combined to yield the following differential wave equations,

$$\nabla^2\mathbf{E} - \frac{\varepsilon}{c^2}\frac{\partial^2\mathbf{E}}{\partial t^2} = 0 \tag{2.14}$$

$$\nabla^2 \mathbf{B} - \frac{\varepsilon}{c^2}\frac{\partial^2 \mathbf{B}}{\partial t^2} = 0 \qquad (2.15)$$

which the electric field and magnetic field have to satisfy, respectively. For monochromatic light, Equations 2.14 and 2.15 show that in a dielectric medium, the electric and magnetic fields behave like plane waves which propagate at a velocity $v = c/\sqrt{\varepsilon}$. The value of $\sqrt{\varepsilon}$, which is typically denoted by the letter *n*, is a material specific property which is equal to the ratio of the speed of light in vacuum to the speed of light in the dielectric medium and is called the index of refraction. Historically, the angles of incidence and refraction for light traveling from vacuum into a particular medium were used to determine n by using Snell's law of refraction, hence the name refractive index.

The refractive index is the single most important optical property of a homogenous isotropic dielectric medium. In addition to determining the velocity of light in a material, the refractive index can also be used to determine the magnitude of the wave vector and wavelength of light in the material according to the relations, $k = 2\pi n/\lambda_o = \omega/v$ and $\lambda = \lambda_o/n$ where λ_o is the wavelength of light in vacuum and ω the frequency. For all dielectric materials, $n > 1$ and the effect of a medium on light is to reduce the speed of propagation and to decrease the wavelength. The refractive index is equally important in describing how light reflects and refracts at the interface between two dielectric media. By knowing the refractive indices of the two media, Snell's laws of reflection and refraction can be used to determine the angular relationships between incident, reflected, and refracted light at the interface. In addition, by employing Fresnel's formulae, the intensities of the reflected and the refracted light can be determined.

For monochromatic light, the optical properties of a homogeneous isotropic dielectric are completely characterized by a single refractive index. However, in reality,

the refractive index is not a constant but depends on frequency, $n = n(\omega)$. Variation of the refractive index with frequency is known as dispersion and is a crucial effect to take into account especially for device applications where transmitted electromagnetic pulses or signals are not perfectly monochromatic but have a finite band width, $\Delta\omega$. A rigorous theory explaining the fundamental reasons for dispersion is beyond the scope of this thesis. However, an elementary treatment [39, 40] will be given below which explains the underlying interaction of matter with light that gives rise to the phenomenon of dispersion.

A dielectric material can be modeled, to a good approximation, as a collection of positively charged nuclei fixed in space which are surrounded by negatively charged electrons such that the net charge of the material is zero. In the presence of an external electric field **E**, spontaneous dipoles are formed which give rise to a net macroscopic polarization **P**. The fundamental problem of calculating the frequency dependence of n is equivalent to calculating the sum of all the displacements **r** of the electrons from their mean position. The most general equation of motion for a single electron in an oscillating electric field is shown below.

$$m\ddot{\mathbf{r}} + g\dot{\mathbf{r}} + k\mathbf{r} = e\mathbf{E} \qquad (2.16)$$

In Equation 2.16, m, g, k, and e are the electron mass (m), a constant characterizing the small damping force experienced by the oscillating electrons (g), a constant characterizing the linear restoring force which binds the electrons around their mean position (k), and the electron charge (e), respectively. Assuming the usual $e^{-i\omega t}$ time dependence for both the electric field and the electron displacement yields a stationary solution of the form,

$$r = \frac{eE}{m(\omega_o^2 - \omega^2) - i\omega g}, \qquad (2.17)$$

where $\omega_o = \sqrt{\frac{k}{m}}$ is the resonance or absorption frequency of a particular electron. Typically in a polymer, however, electrons can have many different resonant frequencies ω_e and thus different displacements r_e. As a result, the dipole moments from all the different electrons must be summed together to give the total polarization,

$$P = Ne\sum_e f_e r_e = Ne^2\sum_e \frac{f_e E}{m(\omega_e^2 - \omega^2) - i\omega g_e}, \qquad (2.18)$$

where N and f_e are the number of molecules per unit volume and the number of electrons per molecule with a given resonant frequency ω_e, respectively. Macroscopically, the polarization is defined as, $P = \chi(\omega)E = \frac{(\varepsilon(\omega) - 1)}{4\pi}E$, where $\chi(\omega)$ is defined as the dielectric susceptibility. Using this relation and Equation 2.18, the frequency dependent refractive index can be shown to satisfy the following relation.

$$n(\omega)^2 = 1 + 4\pi Ne^2\sum_e \frac{f_e}{m(\omega_e^2 - \omega^2) - i\omega g_e} \qquad (2.19)$$

Equation 2.19 shows that the refractive index, in addition to being a function of frequency, is also a complex quantity. The fundamental reason behind the complex refractive index is clear given the above discussion. As mentioned above, an oscillating electric field propagating through a dielectric material induces instantaneous dipole moments. The induced dipoles attempt to orient with and follow the electric field. The components of the polarization which are in-phase and out-of-phase with the electric field

are characterized by the real part and imaginary parts of the refractive index, respectively. The out-of-phase polarization leads to absorption of energy from the electric field through Joule heating. As can be seen from Equation 2.19, the small damping force experienced by the oscillating electrons is the ultimate reason for the out-of phase polarization and imaginary refractive index. The complex refractive index is commonly written in the following form,

$$\mathbf{n}(\omega) = n(\omega)(1 + i\kappa(\omega)), \qquad (2.20)$$

where $\kappa(\omega)$ is called the extinction coefficient or attenuation index. For an electromagnetic wave propagating through a medium with a complex frequency dependent dielectric constant, the extinction coefficient gives rise to the exponentially decaying term $e^{-\kappa \mathbf{k}\cdot\mathbf{r}}$ which results in attenuation of the light. The extinction coefficient (see Equation 2.19) becomes large relative to the real part of the refractive index only near resonant frequencies of the polymer. Most polymers, however, have few resonances in the visible region of the spectrum and are typically transparent. As a result, $\kappa(\omega) \approx 0$ and $n(\omega)$ can be taken to be real. For simplicity, in the remainder of this chapter, the complex nature of the indices will be dropped. The real part of the refractive index is found to slowly increase monotonically with frequency.

2.3.2 Long Wavelength Optical Properties

All of the optical properties of a homogeneous isotropic polymer can be predicted once the frequency dependent refractive index $n(\omega)$ is known. The situation is not nearly so simple for a microphase separated block copolymer. As discussed in Section 2.2, strongly segregated AB coil-coil diblock copolymers self-assemble into periodic

microphase separated morphologies consisting of discrete A and B domains. Within the A and B domains, the optical properties can be assumed (to a good approximation) to be isotropic and characterized by their bulk refractive indices $n_A(\omega)$ or $n_B(\omega)$, respectively. Although block copolymers are a one phase system from the large length scale point-of-view of thermodynamics, optically, these materials are heterogeneous two component composite materials. When the wavelength of light is much larger than the characteristic domain size of the morphology (i.e. $\lambda >> D$), which is the case for typical block copolymers ($D \sim 10^2$Å), the electromagnetic wave does not probe the discrete nature of the periodic morphology but sees a homogeneous dielectric medium which can be described by average optical properties. When $\lambda \lesssim D$, however, the heterogeneous nature of a microphase separated block copolymer cannot be ignored and the refractive index becomes a periodic function of position, $n(\mathbf{r}, \omega)$. We begin by discussing the long wavelength optical properties of noncrystalline flexible coil-coil diblocks when $\lambda >> D$.

In contrast to a homopolymer, a block copolymer can be optically anisotropic depending on the symmetries of the particular morphology. In other words, the refractive index depends on both the electric field's propagation direction and polarization direction. For an anisotropic dielectric medium [40], the polarization **P** does not necessarily point in the same direction as that of the electric field **E**. Similarly, **D** and **E** will, in general, have different directions because of the relation $\mathbf{D} = \varepsilon\mathbf{E} = \mathbf{E}+4\pi\mathbf{P}$. Thus, the dielectric constant is no longer a scalar quantity but a second rank tensor. All physical properties which are second rank tensors are also symmetric [41], (i.e. $\varepsilon_{ij} = \varepsilon_{ji}$). As a result, the dielectric tensor can always be written in the following diagonal form,

$$\varepsilon = \begin{bmatrix} \varepsilon_1 & 0 & 0 \\ 0 & \varepsilon_2 & 0 \\ 0 & 0 & \varepsilon_3 \end{bmatrix} \qquad (2.21)$$

where ε_1, ε_2, and ε_3 are known as the principal dielectric constants. To simplify notation, the frequency dependence of quantities will be implied. Using the principal dielectric constants we can define three principal refractive indices $n_1=\sqrt{\varepsilon_1}$, $n_2=\sqrt{\varepsilon_2}$, and $n_3=\sqrt{\varepsilon_3}$.

Given the dielectric constant tensor, one can show from generalized forms of Maxwell's equations how light propagates through an anisotropic medium. It is of more use to our present discussion concerning the optical properties of block copolymers, however, to summarize the essential results of such an analysis and refer the interested reader to several rigorous treatments given elsewhere [39, 40, 42]. Basically, light propagating in a given direction through an anisotropic medium can be resolved into two different components or waves. The two components travel at different phase velocities (thus experiencing different refractive indices) and have orthogonal polarizations. A relatively simple but highly illustrative geometrical construction is shown below which can be used to determine the velocities and polarizations of the two waves given the propagation direction relative to the geometry of the block copolymer.

The electric energy density of an electromagnetic wave in an anisotropic dielectric medium is equal to

$$w_e = \frac{1}{8\pi}\mathbf{E}\cdot\mathbf{D} = \frac{1}{8\pi}\left(\frac{D_x^2}{\varepsilon_x} + \frac{D_y^2}{\varepsilon_y} + \frac{D_z^2}{\varepsilon_z}\right), \qquad (2.22)$$

where the ε_i and D_i are the principal dielectric constants and the components of the electric displacement along the principal axes, respectively. Equation 2.22 can be easily recast into the form,

$$\frac{x^2}{\varepsilon_x} + \frac{y^2}{\varepsilon_y} + \frac{z^2}{\varepsilon_z} = 1, \qquad (2.23)$$

which describes an ellipsoid whose axes coincide with the principal axes of the dielectric constant tensor and whose semi-radii are equal to the principal refractive indices (see Figure 2.7). This ellipsoid is commonly referred to as the *ellipsoid of wave normals* or the *optical indicatrix*. To determine the velocities of propagation and polarization directions for the two waves, a line pointing in the direction of propagation, $\hat{\mathbf{k}}$, is drawn through the center of the ellipsoid (see Figure 2.8). Next, a plane orthogonal to the line is drawn which passes through the origin and whose intersection with the ellipsoid forms an ellipse. The directions in which the semimajor and semiminor axes of the ellipse are oriented correspond to the polarization directions of **D** in the two waves. The magnitudes of the corresponding radii along these directions yield the effective refractive indices of the two waves which are inversely proportional to their velocities of propagation.

According to their macroscopic optical behavior, all dielectric media can be classified as either isotropic, uniaxial, or biaxial. For isotropic materials, $n_1 = n_2 = n_3 = n$, and the ellipsoid of wave normals becomes a sphere of radius $n\omega/c$. For uniaxial materials, $n_1 = n_2 = n_o$ and $n_3 = n_e$, where n_o and n_e are known as the ordinary and extraordinary refractive indices. The corresponding index ellipsoid is a spheroid with major and minor radii of $n_e\omega/c$ and $n_o\omega/c$ or $n_o\omega/c$ and $n_e\omega/c$ depending on whether the material is uniaxially positive ($n_e > n_o$) or negative ($n_e < n_o$), respectively. A single propagation direction exists, which is called the optic axis, in which the ordinary and extraordinary waves have the same refractive index, n_o. In all other directions, the ordinary wave is characterized by the refractive index, n_o, and the extraordinary wave by the direction dependent index, $\left(\frac{\cos^2\theta}{n_o^2} + \frac{\sin^2\theta}{n_e^2}\right)^{-\frac{1}{2}}$, where θ is the angle between the wave vector and the optic axis. Finally, for biaxial materials, all three principal refractive indices are different and the index ellipsoid can be described as a general triaxial ellipsoid. As the name implies, biaxial materials have two optic axes.

One, two, and three dimensionally periodic crystals give rise to widely varying optical properties which are manifested in different dielectric tensors. Symmetry, however, can be used to greatly simplify the process of predicting the optical behavior of a given dielectric crystal. The point group symmetries, the space group, or the crystal system can all be used to determine whether a crystal behaves isotropically, uniaxially, or biaxially. For example, cubic crystals behave isotropically with a dielectric tensor characterized by a single refractive index. The principal axes of the dielectric tensor can have any orientation relative to the crystal axes. Trigonal, tetragonal, and hexagonal crystals all behave uniaxially and require two principal refractive indices, an ordinary and an extraordinary refractive index. One of the principal axes is found to be parallel to the highest symmetry axis of the crystal (3-fold, 4-fold, or 6-fold for trigonal, tetragonal, or hexagonal, respectively) while the remaining two are unrelated. In addition, the optic axis is oriented along the highest symmetry axis. Finally, orthorhombic, monoclinic, and triclinic crystals behave biaxially, are described by three principal refractive indices, and have two optic axes. For orthorhombic crystals, the principal axes coincide with the 2-fold axes of the crystal. For monoclinic crystals, one principal axis is parallel to the single 2-fold axis while the remaining two are unrelated. As one would expect, the principal axes can have any orientation for triclinic crystals because no special symmetry directions exist. Table 2.1 gives a summary of the above results including the point group symmetries (International notation) corresponding to each crystal system.

Table 2.1 Summary of the optical properties of the seven crystal systems and their associated point group symmetries.

Crystal Systems	Possible Crystallographic Point Groups	Optical Properties
Triclinic	$1, \bar{1}$	Biaxial ($n_1 \neq n_2 \neq n_3$)
Monoclinic	$2, \bar{m}, \frac{2}{m}$	
Orthorhombic	$222, mm2, \frac{2}{m}\frac{2}{m}\frac{2}{m}$	
Trigonal	$3, 32, \bar{3}, 3m, \bar{3}\frac{2}{m}$	Uniaxial ($n_1 = n_2 \neq n_3$)
Tetragonal	$4, 422, \bar{4}, \bar{4}2m, 4mm, \frac{4}{m}, \frac{4}{m}\frac{2}{m}\frac{2}{m}$	
Hexagonal	$6, 622, \bar{6}, \bar{6}m2, 6mm, \frac{6}{m}, \frac{6}{m}\frac{2}{m}\frac{2}{m}$	
Cubic	$23, 432, \frac{2}{m}\bar{3}, \bar{4}3m, \frac{4}{m}\bar{3}\frac{2}{m}$	Isotropic ($n_1 = n_2 = n_3$)

Given the above framework, we can classify the optical properties of the classical coil-coil block copolymer morphologies and the two bicontinuous cubic morphologies, double diamond and double gyroid. The lamellar morphology is the simplest microstructure and consists of alternating A and B layers which form a one dimensional crystal. In three-dimensional objects which are periodic in less than three dimensions, some symmetry elements will be distributed continuously rather than discretely. Thus, the allowed translation vectors are discrete and equal to the lamellar repeat distance, normal to the lamellae. In the plane of the lamellae, the allowed translations are continuous and located everywhere. A lamellar crystal has an ∞-fold rotation axis normal to the layers everywhere, an infinite set of mirror planes parallel to this axis, an infinite set of 2-fold rotation axes perpendicular to the axis located at the middle of each layer,

and mirror planes perpendicular to the axis which cut through the middle of each layer. Inversion centers are located at the intersection of the 2-fold axes and the mirror planes which are parallel to the lamellar normal. The resulting space group can be written as $P\frac{\infty}{m}m\,m$ (International notation). Although the point group, $\frac{\infty}{m}m\,m$, is not one of the 32 three dimensional crystallographic point groups, it can be grouped with those of the trigonal, hexagonal, and tetragonal crystal systems which have uniaxial optical properties. In agreement with this assignment, a lamellar block copolymer has only one optic axis which is perpendicular to the layers. The ordinary and extraordinary refractive indices, n_o and n_e, characterize light whose electric field is oriented perpendicular to and parallel to the lamellar normal, respectively.

The cylinder morphology is a two dimensional crystal which consists of infinitely long cylinders of the minority component arranged on a hexagonal lattice which are surrounded by a majority component matrix. The allowed translation vectors are continuous in the direction of the cylinders and located anywhere along the cylinder. Normal to the cylinders, the translation vectors are discrete. The highest point group symmetry in the cylinder morphology is $\frac{6}{m}\frac{2}{m}\frac{2}{m}$ with the 6-fold rotation axis parallel to and located in the center of the cylinders. Although it is not one of the 230 crystallographic space groups, the corresponding space group for cylinders which is denoted, $P\frac{6}{m}m\,m$, can clearly be grouped with the hexagonal crystal system. As a result, the cylinder morphology also exhibits uniaxial optical properties with its optic axis oriented along the cylinders. The refractive indices, n_o and n_e, characterize light whose electric field is oriented perpendicular to and parallel to the cylinder axis, respectively.

The remaining three morphologies of body-centered cubic spheres, (ordered bicontinuous) double diamond, and double gyroid, which all have three dimensional translational symmetry, are based on the same point group symmetry, $\frac{4}{m}\bar{3}\frac{2}{m}$, and are members of the cubic crystal system. The crystallographic space groups of BCC spheres

[5], double diamond [7], and double gyroid [17, 18] are $Im\bar{3}m$, $Pn\bar{3}m$, and $Ia\bar{3}d$, respectively. As cubic dielectric crystals, these morphologies behave optically as isotropic dielectrics described by a single refractive index. Assigning the bicontinuous cubic morphologies isotropic optical properties is by no means obvious given their complicated interconnected composite-like nature. However, knowledge of the symmetry of the bicontinuous cubics constrains the dielectric constant tensor to only have one independent component. The block copolymer symmetries and optical behavior are summarized in Table 2.2. Symmetry will be used again as a powerful tool in predicting the effects of a LC block on the microstructure and optical properties of LC block copolymers in Chapter 5.

Table 2.2 Summary of the space groups, highest point group symmetries, and optical properties which characterize the classical block copolymer morphologies and the two bicontinuous cubic morphologies.

Morphology	Space Group	Highest Point Group	Optical Properties
Lamellae	$P\frac{\infty}{m}mm$	$\frac{\infty}{m}mm$	Uniaxial
Cylinders	$P\frac{6}{m}mm$	$\frac{6}{m}\frac{2}{m}\frac{2}{m}$	
Spheres	$Im\bar{3}m$	$\frac{4}{m}\bar{3}\frac{2}{m}$	Isotropic
Double Diamond	$Pn\bar{3}m$	$\frac{4}{m}\bar{3}\frac{2}{m}$	
Double Gyroid	$Ia\bar{3}d$	$\frac{4}{m}\bar{3}\frac{2}{m}$	

While symmetry is helpful in determining the macroscopic optical behavior of a microphase separated block copolymer, it can not be used to calculate the specific values of the principal refractive indices. For this problem, effective medium theories (EMT) must be used to calculate the principal refractive indices in terms of the constituent

properties, n_A, n_B, f_A, and f_B, where f_A and f_B are volume fractions of the A and B block, respectively. As mentioned earlier, effective medium theories are valid in the long wavelength limit because the domain size of the block copolymer is much smaller than the wavelength of light and individual domains can be characterized by their bulk properties. The optical properties of composite systems have been studied for over a century and numerous effective medium theories have been developed. The earliest work was done by Lord Rayleigh in 1892 who derived expressions for the principal values of the conductivity tensor of composite media for the specific cases of A cylinders arranged on a square lattice surrounded by a B matrix and A spheres arranged on a simple cubic lattice embedded in a B matrix [43]. Rayleigh's results are equally applicable to the optical properties of these structures because both conductivity and dielectric constant are second rank tensor properties. Some years later, Maxwell Garnett studied the optical properties of metal-doped glasses, in which the metal grains were modeled as spherical particles randomly arranged in the glass matrix [44, 45]. Shortly after, Wiener treated the composite dielectric properties of two component layered structures and also assemblies of cylinders in which the cylinders were randomly arranged [46]. In addition, he derived the well-known Wiener limits or bounds for layered structures (originally written in terms of dielectric constants) which describe the limiting cases in composite media for no screening of the polarization (electric field polarized in the direction of the layers) and maximum screening of the polarization (electric field polarized perpendicular to the layers). More recently, Bruggeman developed a theory [47] which could be used for two component composite media in which grains of the two materials are randomly interspersed and have similar volume fractions. These effective medium theories will be used to obtain expressions for the principal refractive indices of the various block copolymer morphologies.

For the lamellar morphology, the Wiener limits provide expressions for the ordinary and extraordinary refractive indices in terms of the refractive indices, n_i, and volume fractions, f_i, of each block (see Table 2.3). These expressions were first used to calculate the birefringence of lamellar-forming poly(styrene-butadiene-styrene) triblock copolymers by Folkes and Keller [48]. Block copolymers with any other morphology will have principal refractive indices which fall between these limits. The resulting birefringence, defined as $\Delta n = n_e - n_o$, is known as form birefringence and arises purely from the structural arrangement of the A and B domains (which are themselves optically isotropic) in the morphology giving rise to different optical properties for light polarized along different directions. Because $\Delta n < 0$ always, the lamellar morphology has uniaxially negative optical properties.

In the hexagonally-packed cylinder morphology, the expressions derived by Lord Rayleigh or Wiener can be used to calculate the principal dielectric constants n_o and n_e (see Table 2.3). Folkes and Keller were also the first to use the Wiener expressions for randomly arranged cylinders to calculate the form birefringence of cylinder-forming poly(styrene-butadiene-styrene) triblock copolymers [49]. The n_e expressions listed in Table 2.3 correspond to the case of no screening and are exact. The n_o expressions, however, are approximate. For typical block copolymers, the numerical difference between the n_o expressions for square-packed and randomly arranged cylinders is insignificant. In fact, when the f_A^4 term, which arises from the higher order cooperative effects present in the square-packed lattice, is set to zero, Rayleigh's expression simplifies to the Wiener expression. Consequently, the differences in the principal refractive indices between a square lattice and hexagonal lattice of cylinders are expected to be negligible. In the long wavelength limit, the specific local packing arrangement of the cylinders is not probed at all by the light. The form birefringence for the cylinder

morphology is found to be, $\Delta n > 0$. As a result, the cylinder morphology is a uniaxially positive material.

For the BCC sphere morphology, the single principal refractive index can be calculated using either Rayleigh's expression for the effective refractive index of a simple cubic lattice of spheres or Maxwell Garnett's expression for randomly arranged spheres (see Table 2.3). As was the case for the cylinder morphology, although these expressions are only approximate, they are expected to differ insignificantly from the true isotropic refractive index. One can easily show that the only difference between simple cubic and randomly arranged spheres is the higher order $f_A^{10/3}$ term, which is small for most block copolymers. Consequently, the difference in the principal refractive index between a simple cubic and BCC packing of spheres is again negligible.

The situation is somewhat more complicated for the bicontinuous cubic morphologies, double diamond and double gyroid. No one has previously calculated the effective index of a triply periodic bicontinuous composite material before. Bruggeman's EMT, however, comes the closest to modeling composite structures which resemble the bicontinuous cubics. In Bruggeman's theory for a two component composite, domains of A and B are randomly interspersed. At compositions between the percolation thresholds of either component, both the A and B domains form continuous interconnected channels in all directions much like the bicontinuous cubic morphologies. Again, as we saw in the cylinder and sphere morphologies, the error caused by neglecting the three dimensional periodicity of the A and B domains in the double diamond and double gyroid morphologies is expected to be a higher order effect. In addition, Bruggeman's theory treats composites with nearly symmetric compositions which is also the case for the experimentally observed volume fractions of the bicontinuous cubics (f = 0.34 to 0.37 and 0.63 to 0.66 [9]). As a result, Bruggeman's expression is a good approximation for the effective refractive index of both bicontinuous cubic morphologies (see Table 2.3).

Table 2.3 Effective medium theory expressions for the principal refractive indices of the classical block copolymer morphologies and the two bicontinuous cubic morphologies.

Morphology	Principal Refractive Indices
Lamellae	$n_o = \sqrt{f_A n_A^2 + f_B n_B^2},\ n_e = \sqrt{\dfrac{n_A^2 n_B^2}{f_A n_B^2 + f_B n_A^2}}$
Square-packed Cylinders ($P\frac{4}{m}mm$)	$n_o = n_B\left[1 - \dfrac{2f_A}{\left(\dfrac{n_B^2 + n_A^2}{n_B^2 - n_A^2}\right) + f_A - \dfrac{9.453}{\pi^4}\left(\dfrac{n_B^2 - n_A^2}{n_B^2 + n_A^2}\right) f_A^4}\right]^{\frac{1}{2}},\ n_e = \sqrt{f_A n_A^2 + f_B n_B^2}$
Random Cylinders	$n_o = n_B\left[\dfrac{(n_A^2 + n_B^2) + f_A(n_A^2 - n_B^2)}{(n_A^2 + n_B^2) - f_A(n_A^2 - n_B^2)}\right]^{\frac{1}{2}},\ n_e = \sqrt{f_A n_A^2 + f_B n_B^2}$
Simple Cubic Spheres ($P\frac{4}{m}\bar{3}\frac{2}{m}$)	$n = n_B\left[1 - \dfrac{3f_A}{\left(\dfrac{2n_B^2 + n_A^2}{n_B^2 - n_A^2}\right) + f_A - 61.901\left(\dfrac{3f_A}{4\pi}\right)^{10/3}\left(\dfrac{n_B^2 - n_A^2}{\frac{4}{3}n_B^2 + n_A^2}\right)}\right]^{\frac{1}{2}}$
Random Spheres	$n = n_B\left[\dfrac{(n_A^2 + 2n_B^2) + 2f_A(n_A^2 - n_B^2)}{(n_A^2 + 2n_B^2) - f_A(n_A^2 - n_B^2)}\right]^{\frac{1}{2}}$
Double Diamond Double Gyroid	$n = \frac{1}{4}\left[(3f_A - 1)n_A^2 + (3f_B - 1)n_B^2 + \sqrt{[(3f_A - 1)n_A^2 + (3f_B - 1)n_B^2]^2 + 8n_A^2 n_B^2}\right]$

2.3.3 Short Wavelength Optical Properties

In the previous section, we saw how microphase separated coil-coil block copolymers behave optically like homogeneous isotropic or anisotropic dielectric materials when the wavelength of light is much larger than the characteristic domain size. For ultrahigh molecular weights and shorter wavelengths of light (e.g. $\lambda \rightarrow \lambda_{UV}$), the wavelength of light can become comparable or less than the characteristic domain size (i.e. $\lambda \lesssim D$). In this limit, the optical properties of block copolymers are no longer adequately described by a single second rank dielectric tensor with average principal dielectric constants. In the short wavelength limit, the dielectric constant tensor becomes a function of position within the microstructure, $\varepsilon = \varepsilon(\mathbf{r})$. Inside the discrete A or B domains, light propagates as a normal plane wave characterized by either the refractive index n_A or n_B, respectively. However, now that the domain size of the block copolymer is comparable to the wavelength of light, scattering from the AB interfaces becomes a dominant effect. For a periodic dielectric crystal (or photonic crystal) destructive interference of the multiply-scattered waves within the material can cause certain frequencies to be forbidden [50]. For three dimensional periodic structures, bands of forbidden frequencies (or band gaps) can exist for all directions of the wave vector. Light incident on the dielectric crystal with a frequency within such a band gap can not propagate and will be totally reflected. Because of these unique optical properties, periodic dielectric materials such as block copolymers have the potential to be used in previously unimagined ways to control the propagation of light.

A complete discussion of photonic band theory in dielectric crystals is well beyond the scope of this thesis and is not in line with the principal goals of this work. To not mention photonic band theory at all, however, is shortsighted because of the valuable point-of-view it brings to our discussion on the optical properties of block copolymers

and the potentially new uses it suggests for block copolymers in optics. As a result, a brief summary of the principles underlying photonic band theory and some of the main results will be given below in the context of block copolymers. In addition, the insights gained in this section on how dielectric structures influence the propagation of light when $\lambda \lesssim D$ will allow us to better understand the results of the block copolymer waveguide predictions to be presented in the next section.

In the short wavelength limit, light propagating through a dielectric crystal must still obey Maxwell's equations. Following the treatment of Joannopoulos et al. [50], Maxwell's equations, however, must be modified to take into account the position dependent dielectric constant.

$$\nabla \cdot \varepsilon(\mathbf{r})\mathbf{E} = 0 \tag{2.26}$$

$$\nabla \cdot \mathbf{B} = 0 \tag{2.27}$$

$$\nabla \times \mathbf{E} = -\frac{1}{c}\frac{\partial \mathbf{B}}{\partial t} \tag{2.28}$$

$$\nabla \times \mathbf{B} = \frac{\varepsilon(\mathbf{r})}{c}\frac{\partial \mathbf{E}}{\partial t} \tag{2.29}$$

The dielectric constant is assumed to be independent of frequency in this treatment. While the fields in a dielectric crystal are no longer simple plane waves, they can still be separated into a space dependent component and a harmonic time component.

$$\mathbf{E}(\mathbf{r}, t) = \mathbf{E}(\mathbf{r})e^{i\omega t} \tag{2.30}$$

$$\mathbf{B}(\mathbf{r}, t) = \mathbf{B}(\mathbf{r})e^{i\omega t} \tag{2.31}$$

Using these field expressions, a generalized wave equation can be written for the space dependent component of the magnetic field.

$$\nabla\times\left(\frac{1}{\varepsilon(\mathbf{r})}\nabla\times\mathbf{B}(\mathbf{r})\right)=\frac{\omega^2}{c^2}\mathbf{B}(\mathbf{r}) \qquad (2.32)$$

Mathematically, the magnetic field is much simpler to deal with and can easily be used to determine the electric field using Equation 2.29. Those interested in a more detailed treatment of photonic band theory are referred to a work by Joannopolous et al. [50]. Equation 2.32 has the form of a typical eigenvalue equation whose eigenvectors and eigenvalues are $\mathbf{B}(\mathbf{r})$ and $(\omega/c)^2$, respectively. By considering the discrete translational symmetries present in a periodic dielectric crystal, $\mathbf{B}(\mathbf{r})$ can be shown to have the same general form as Bloch waves in periodic potentials,

$$\mathbf{B}_{\mathbf{k}}(\mathbf{r}) = e^{i\mathbf{k}\cdot\mathbf{r}}\mathbf{u}_{\mathbf{k}}(\mathbf{r}), \qquad (2.33)$$

where $\mathbf{u}_{\mathbf{k}}(\mathbf{r})$ is a periodic function possessing all the translational symmetries of the crystal such that $\mathbf{u}_{\mathbf{k}}(\mathbf{r}) = \mathbf{u}_{\mathbf{k}}(\mathbf{r}+\mathbf{R})$ for all lattice vectors $\mathbf{R}$. For a given dielectric crystal described by $\varepsilon(\mathbf{r})$, Equation 2.32 can then be used to solve for $\mathbf{u}_{\mathbf{k}}(\mathbf{r})$. For a given $\mathbf{k}$, an infinite spectrum of allowed frequencies exists which are labeled by the band index n (not to be confused with the refractive index). The frequencies within a given band vary continuously with $\mathbf{k}$. Together, the family of curves $\omega_n(\mathbf{k})$ represent what is known as the band structure and completely describe the optical properties of the dielectric crystal. Knowing the band structure, one can still define an effective refractive index according to the following relation.

$$n(\mathbf{k}) = \frac{ck}{\omega_n(\mathbf{k})} \qquad (2.33)$$

The refractive index, however, is now a complicated function which is strongly dependent on the wave vector, band index, and polarization direction. Band gaps in frequency will give rise to gaps in the refractive index as a function of wave vector. In addition, the symmetries of the underlying dielectric crystal will be directly manifested in n(**k**). For example, in a simple cubic photonic crystal, light propagating down any of the [100] family of directions (4-fold axes) experiences the same refractive index. Similarly, light propagating down any of the equivalent [110] directions (2-fold axes) experiences the same refractive index, which is different from the refractive index seen in the [100] direction. Optical behavior of this kind is completely different from the long wavelength limit behavior we saw earlier, which is a natural limiting case of photonic band theory when k -> 0. In the long wavelength limit, the dielectric constant tensor adequately describes all of the optical properties for a given crystal system. All 230 space groups can be classified as either having isotropic, uniaxial, or biaxial optical properties. In other words, although the effective refractive index can also be direction dependent, it possesses a much higher symmetry than the symmetry of the underlying dielectric crystal because the fine scale structure of the crystal is effectively averaged out. Taking the simple cubic photonic crystal again, in the long wavelength limit, a single refractive index governs light propagating in any direction of the crystal.

The band structures of the different block copolymer morphologies vary significantly. Since the lamellar morphology is a one dimensional periodic dielectric crystal, band gaps are only possible in the direction of periodicity or for propagation normal to the layers. Band gaps, however, will exist for any value of the dielectric contrast $\varepsilon_A/\varepsilon_B \neq 1$ and increase with increasing $\varepsilon_A/\varepsilon_B$. Given the two dimensional

periodicity of the cylinder morphology, band gaps are possible for propagation directions anywhere in the plane normal to the cylinders but are highly dependent on dielectric contrast and cylinder volume fraction. Achieving complete band gaps in three dimensional dielectric crystals is even more difficult. From previous experimental and theoretical work done on interconnected structures [51, 50], however, the bicontinuous cubic morphologies like the double diamond or double gyroid (not the BCC sphere morphology) appear to hold the most promise for achieving complete band gaps [52].

While the key asset of block copolymers is their ability to self assemble into periodic dielectric structures, their fundamental limitations as possible photonic band gap materials when compared to inorganic materials are their inherently small dielectric contrasts and their small characteristic domain sizes of $D \sim 10^2$Å. In addition, the equilibrium morphologies are determined by volume fraction and can have relatively narrow ranges of composition over which they exist. As a consequence, optimization of a given structure to maximize the band gap appears problematic. Without a doubt, significant challenges remain before block copolymers can feasibly be used as photonic band gap materials. The main point of the above discussion, however, was to give us an underlying framework by which to understand the optical behavior of block copolymers in all regimes of λ/D. In addition to being potential photonic band gap materials, however, block copolymers exhibit optical properties which make them ideal for uses in other areas of optics, as we shall see in the next section.

2.4 Block Copolymers as Optical Waveguides

2.4.1 Introduction

Since the development of integrated optics in the 1970's, homopolymers have played a major role in the optics industry as optical waveguide materials [53, 54]. An optical waveguide is basically a thin dielectric film or fiber which can be used to propagate light in a confined geometry. Homopolymers make excellent waveguide materials because they can be easily processed using existing microelectronics techniques into durable thin films which exhibit low transmission loss. In addition, homopolymers have a low specific gravity and span a wide range of refractive index. As a result, many integrated optical devices ranging from lenses and gratings to lasers, light couplers, and demultiplexers [55, 56] have been fabricated using homopolymer thin films. From a theoretical point of view, homopolymer waveguides have been extensively studied [56-59] and are well understood.

In contrast, block copolymers have not been previously considered as optical waveguide materials and relatively little work has been done to characterize their optical waveguiding properties. As we saw in the previous section, however, block copolymers possess unique properties which make them potentially useful as waveguide materials. In particular, block copolymers self-assemble into spatially periodic ordered dielectric structures on the length scale of tens of nanometers giving them an additional degree of freedom by which to control the propagation of light. In the SSL, these morphologies are characterized by narrow interfaces and well-defined domain sizes. As we have seen, the lamellar morphology, which can be formed by symmetric AB diblock and ABA triblock copolymers, has the simplest structure and will be the focus of this section. Russell and coworkers have shown that spin coated thin films of a symmetric P(S-b-MMA) diblock copolymer form lamellae which are oriented parallel to the substrate and air interfaces

when annealed [60-65]. Block copolymer films in which the lamellae are oriented parallel to the substrate and superstrate will behave as periodic multilayer structures and will exhibit optical properties different from homopolymer films. In terms of optical waveguiding, multilayer films have already been shown to be useful for studying nonlinear optical phenomena. In particular, multilayer Langmuir-Blodgett (LB) waveguide structures have been used to study the second harmonic generation (SHG) of certain NLO molecules. In particular, four- and five-layer structures were found to increase the efficiency of SHG through better phase matching of the fundamental and harmonic wave [66, 67]. Besides uses in nonlinear optics, Normandin et al. [68] showed that efficient coupling from an optical fiber was possible using a multilayer waveguide structure composed of 34 alternating $Al_{0.65}Ga_{0.35}As$ and $Al_{0.90}Ga_{0.10}As$ layers while still maintaining high nonlinear harmonic emission efficiencies. Although the LB and AlGaAs structures mentioned above were both composed of multiple layers, their discrete nature was not specifically exploited in any way.

Block copolymers, in addition to forming ordered structures, have greater flexibility in the tailoring of their optical properties in comparison to homopolymers. By changing the total molecular weight of a block copolymer, the lamellar domain size and also the individual block layer thicknesses can be varied from a few nanometers to hundreds of nanometers having a profound effect on the resulting optical waveguiding properties. By choosing the appropriate chemical composition of each block, the refractive index of each layer can be precisely controlled. In addition, the architecture of the block copolymer (i.e. diblock or triblock) can also be used to influence the resulting microphase separated morphology. Together, these properties can be used to tailor the refractive index profile of a waveguide greatly facilitating the design of novel waveguide structures.

In the following sections, we will first develop an N-layer waveguide formalism to model block copolymer waveguide structures and then use it to predict the optical waveguiding properties of model lamellar-forming diblock copolymers. After a short discussion about the ideal block copolymer characteristics desired for optical waveguiding, the experimental progress made toward actually making block copolymer waveguides will be presented.

2.4.2 N-layer Waveguide Formalism for Modeling Lamellar Block Copolymers

Homopolymer slab waveguides are accurately modeled as a simple three layer structure consisting of a homogeneous, isotropic, dielectric film located between a semi-infinite substrate (e.g. quartz) and superstrate (e.g. air) of smaller refractive index. A theoretical treatment of the homopolymer waveguide or asymmetric slab waveguide is presented in Appendix 1. An ideal lamellar-forming block copolymer film, however, is heterogeneous in nature and must be modeled as a multilayer waveguide structure. Shakir and Turner developed a method for calculating the waveguide modes of multilayer structures from the poles of the reflectance in the substrate or superstrate [69]. In a related approach, Chilwell and Hodgkinson [70] employed a 2*2 field-transfer matrix method which they used to calculate the waveguide modes and corresponding electric field profiles of various multilayer structures. In our present discussion, the optical field intensity distributions for the modes of a given block copolymer film are of particular interest because they show us directly how the light is concentrated in the various domains. As a result, a theoretical formalism based on the work of both Polky and Mitchell [71] and Marcuse [59] which treats the electric and magnetic fields in each layer explicitly and in a compact way is found to be more useful.

In order to predict the optical waveguiding properties of microphase separated lamellar block copolymer films in which the lamellae are parallel to the substrate, we must be able to solve for the waveguide modes of a multilayer dielectric structure. Figure 2.9 shows a schematic diagram depicting the structure of a multilayer waveguide consisting of N film layers, each characterized by a refractive index n_i and a thickness t_i along the $\hat{x}$ direction, which are sandwiched between a substrate and superstrate (air) of refractive indices n_0 and n_s, respectively. Typically, the refractive indices of the guiding layers must be greater than the substrate and superstrate indices to ensure confinement of the light. For planar waveguides, each layer is assumed to be infinite along the $\hat{y}$ and $\hat{z}$ directions. For light propagation along $\hat{z}$, the waveguide modes represent mathematical solutions to Maxwell's equations in which the light travels at the same velocity in the $\hat{z}$ direction in all the layers but is confined solely within the N film layers. For a given waveguide mode, the electric and magnetic fields in all the layers will have a common time and z dependence which can be expressed by the exponential factor $e^{i(\omega t - \beta z)}$, where ω is the angular frequency and β is the z component of the wave vector. In addition, because the direction of propagation is only in the xz plane, the electric and magnetic fields will not vary in the $\hat{y}$ direction. Dividing β by the free space wave vector, $k_0 = 2\pi/\lambda_0$, yields the propagation constant, n_{eff}, which is inversely proportional to the velocity of the mode. Waveguide modes can be classified into two groups, the transverse electric (TE) and transverse magnetic (TM) modes. TE modes are characterized by an electric field vector normal to the plane of incidence (see Figure A1.1) and have the field components (relative to the coordinate axes) $\mathbf{E} = (0, E_y, 0)$ and $\mathbf{B} = (B_x, 0, B_z)$. TM modes, on the other hand, are characterized by a magnetic field vector normal to the plane of incidence and have the field components $\mathbf{E} = (E_x, 0, E_z)$ and $\mathbf{B} = (0, B_y, 0)$. E_y and B_y, therefore, play analogous roles for TE and TM modes, respectively. For simplicity, only the solution of the TE modes will be presented. The following results,

however, can easily be generalized for TM modes. The full expression for the electric field in each layer can be written as,

$$\mathbf{E}(\mathbf{r},t) = E_y(x)e^{i(\omega t - \beta z)}\hat{y}. \qquad (2.34)$$

Using Equation 2.34, the problem of solving Maxwell's equations in each layer can be reduced to solving the one dimensional Helmholtz wave equation in each layer for $E_y(x)$,

$$\frac{\partial^2 E_y^i}{\partial x^2} + k_0^2\left(n_i^2 - n_{eff}^2\right)E_y^i = 0, \qquad (2.35)$$

where the index i = (0, 1, ..., N, s) labels each layer starting from the substrate, 0, and ending at the superstrate, s. In addition to being a solution of Equation 2.35 in each layer, E_y must also obey the boundary conditions at each interface. In particular, E_y and its derivative must be continuous across all interfaces. Because the waveguide modes are bound modes, Ey must also vanish at $x = \pm\infty$. Solutions of Equation 2.35 which simultaneously satisfy the boundary conditions can be written in the following general form,

$$E_y^s = A_0\left(\prod_1^N B_i\right)\exp\left[-k_s\left(x - \sum_1^N t_i\right)\right], \quad x \geq d_N$$

$$E_y^N = A_0\left(\prod_1^{N-1} B_i\right)\left\{\cos\left[k_N\left(x - \sum_1^{N-1} t_i\right)\right] + T_{N-1}\sin\left[k_N\left(x - \sum_1^{N-1} t_i\right)\right]\right\}, \quad d_{N-1} \leq x \leq d_N$$

$$\vdots$$

$$E_y^3 = A_0B_1B_2\{\cos[k_3(x - (t_1 + t_2))] + T_2\sin[k_3(x - (t_1 + t_2))]\}, \quad d_2 \le x \le d_3$$

$$E_y^2 = A_0B_1\{\cos[k_2(x - t_1)] + T_1\sin[k_2(x - t_1)]\}, \quad d_1 \le x \le d_2$$

$$E_y^1 = A_0[\cos(k_1x) + T_0\sin(k_1x)], \quad 0 \le x \le d_1$$

$$E_y^0 = A_0\exp[k_0x], \quad x \le 0 \qquad (2.36)$$

where $B_i = \cos(k_it_i) + T_{i-1}\sin(k_it_i)$, $S_i = T_{i-1}\cos(k_it_i) - \sin(k_it_i)$, $T_i = (S_i/B_i)(k_i/k_{i+1})$, and $T_0 = k_0/k_1$. The electric field amplitude coefficient, A_0, is a normalization constant defined such that the total power contained in a each mode is equal to 1 W/μm. The electric field expressions in Equation 2.36 were generalized from the three layer waveguide solutions obtained by Marcuse [59] (see Appendix 1). The k_i's in Equation 2.36 are equal to the x component of the wave vector in each layer and determine the electric field profile across the structure. In addition, the k_i's are a function of n_{eff} and can be written as follows,

$$\begin{aligned} k_s &= k_o\sqrt{n_{eff}^2 - n_s^2}, \\ k_N &= k_o\sqrt{n_N^2 - n_{eff}^2}, \\ &\vdots \\ k_1 &= k_o\sqrt{n_1^2 - n_{eff}^2}, \\ k_0 &= k_o\sqrt{n_{eff}^2 - n_0^2}, \end{aligned} \qquad (2.37)$$

where the definitions of k_s and k_0 ensure that the electric field decays in the substrate and superstrate.

Once the electric fields are obtained, the allowed n_{eff}'s must still be calculated. In the asymmetric slab waveguide, the solutions of Equation 2.35 have two unknown amplitude coefficients. Imposing the boundary conditions at the substrate-film and film-superstrate interfaces results in a homogeneous system of two equations whose determinant must vanish in order for a non trivial solution to exist. The determinant yields an eigenvalue equation whose discrete solutions are the allowed n_{eff}'s. For an N-layer waveguide, a similar derivation yields a 2N by 2N determinant which must vanish. Alternatively, a generalized eigenvalue equation for the multilayer waveguide can be obtained based on the work of Polky and Mitchell [71] thus avoiding the determinant approach entirely. This generalized eigenvalue equation can be written in the form,

$$k_N t_N - \tan^{-1}\left(\frac{k_{(N-1)p}}{k_N}\right) - \tan^{-1}\left(\frac{k_s}{k_N}\right) = m\pi, \qquad (2.38)$$

where the integer m = 0, 1, 2... labels each mode and

$$k_{(N-1)p} = k_{(N-1)}\left[\frac{\frac{k_{(N-2)p}}{k_{(N-1)}} - \tan\left(k_{(N-1)}t_{(N-1)}\right)}{1 + \frac{k_{(N-2)p}}{k_{(N-1)}}\tan\left(k_{(N-1)}t_{(N-1)}\right)}\right],$$

$$\vdots$$

$$k_{2p} = k_2 \left[\frac{\frac{k_{1p}}{k_2} - \tan(k_2 t_2)}{1 + \frac{k_{1p}}{k_2} \tan(k_2 t_2)} \right],$$

$$k_{1p} = k_1 \left[\frac{\frac{k_0}{k_1} - \tan(k_1 t_1)}{1 + \frac{k_0}{k_1} \tan(k_1 t_1)} \right]. \qquad (2.39)$$

For a given multilayer waveguide structure, Equation 2.38 must be numerically solved to obtain the allowed TE propagation constants. The resulting n_{eff}'s have values that range between n_0 and the largest n_i. In general, the low order waveguide modes (m small) have slowly varying electric field profiles in the $\hat{x}$ direction and large n_{eff}'s while the higher order modes have more frequent oscillations and small n_{eff}'s. For TM modes, the field expressions for B_y in each layer are analogous to Equation 2.36. In addition, the form of the generalized eigenvalue equation is identical to that of Equation 2.38 with one distinction. The k_i appearing in Equation 2.38 and 2.39 must be substituted with k_i / n_i^2.

The multilayer waveguide formalism shown above was originally developed by Dr. Carl Zimba and was used as the basis for a program written in collaboration with him using the software package Mathematica by Wolfram Research, Inc. Given the n_i and the t_i of an arbitrary N-layer waveguide and the wavelength of light, the program can calculate the allowed propagation constants using Equation 2.38. Given the recursive nature of Equation 2.38, the computation time increases significantly with the number of layers in the waveguide. As a result, for systems with more than 7 layers, Equation 2.38 can be solved more easily using graphical methods. Even so, the propagation constants can still be determined to any specified degree of precision. Using the calculated n_{eff}'s and Equations 2.36 and 2.37, the program can plot the corresponding optical field

distributions of each mode, which show directly how the light is concentrated in each of the N layers. The integrated intensity or power within each layer (normalized to the total power of a given mode) can also be calculated in a straightforward manner. In order to facilitate comparison with experiments, the angles for which light would excite a given waveguide mode using the technique of prism coupling (see Appendix 4) can be calculated with the program given the characteristic prism angle and refractive index. The accuracy and reliability of the N-layer waveguide formalism and program were confirmed by successfully reproducing the propagation constants and electric field profiles of three different model structures whose solutions have been previously published [57, 70, 72, 73]. The results showed that the multilayer formalism is not only useful for waveguides with step index profiles but can also be used successfully to model waveguides with slowly varying refractive index profiles.

2.4.3 Optical Waveguiding Properties of Model Block Copolymer Films

Having developed the computational means to accurately model multilayer waveguides, the optical waveguiding properties of block copolymer films can now be investigated. As a reminder, the following discussion will deal only with ideal lamellar forming microphase separated block copolymer films in which the lamellae are oriented parallel to the substrate and superstrate interfaces. Such an assumption, however, is reasonable for annealed strongly segregated films [60-65]. Considerable insight into the waveguiding properties of block copolymer films can be obtained by first understanding their bulk optical properties. Given our earlier discussion on the long wavelength optical properties of coil-coil block copolymers, a macroscopically oriented lamellar block copolymer film can be approximated as an optically anisotropic film composed of

individual optically isotropic A and B layers. In particular, a lamellar film will have negative uniaxial optical properties which arise from its form birefringence.

In an actual block copolymer film, however, chain stretching of the blocks away from the IMDS causes each of the A and B layers to have optically uniaxial properties which give rise to an intrinsic birefringence Δn_i. By analyzing the chain stretching experienced by a polymer brush, the following expression,

$$\Delta n_i = \frac{\pi^3}{90}(\alpha_{\parallel}-\alpha_{\perp})\frac{(n^2+2)^2}{n}\left(\frac{\rho N_{AV}}{M}\right)\frac{L^2}{\langle h^2\rangle_o}, \qquad (2.40)$$

was derived by Lodge and Fredrickson [74] for the intrinsic birefringence of a given block copolymer domain. In Equation 2.40, n, ρ, M, L, and $\langle h^2\rangle_o$ are the refractive index, density, molecular weight, half the layer thickness, and mean squared end-to-end distance of the block, respectively. The polarizability parallel and perpendicular to the monomer unit are given by $\alpha_{\parallel}$ and $\alpha_{\perp}$, respectively, while N_{AV} is Avogadro's number. For a given domain, $n_{\perp}$ and $n_{\parallel}$ will be the refractive indices which describe light polarized perpendicular and parallel to the optic axis (which is normal to the IMDS), respectively. When the chain stretching is small (i.e. $\langle h^2\rangle_o \ll Na$), the principal refractive indices for each domain can be simply related to the isotropic refractive index, n, and the intrinsic birefringence, Δn_i, according to the following relations,

$$n_{\perp} = n - \frac{1}{3}\Delta n_i, \qquad (2.41)$$

$$n_{\parallel} = n + \frac{2}{3}\Delta n_i, \qquad (2.42)$$

where $\Delta n_i << n$ is assumed. Because chain stretching is normal to the IMDS, the optic axes of the domains coincide with the optic axis of the lamellar structure. As a result, the symmetry of the lamellar morphology as a whole and thus our previous characterization of lamellar optical behavior remain unchanged. The expressions for the principal refractive indices in Table 2.3, however, must be modified to take into account the anisotropy of the A and B domains. The refractive indices used to calculate the ordinary refractive index will be those which result for light polarized perpendicular to the optic axis of a given domain, $n_{A\perp}$ and $n_{B\perp}$. Similarly, the refractive indices used to obtain the extraordinary refractive index will be those which result for light polarized parallel to the optic axis, $n_{A\parallel}$ and $n_{B\parallel}$. The importance of intrinsic birefringence depends greatly on the particular block copolymer system as well. For coil-coil diblock copolymers, intrinsic birefringence becomes important only for low molecular weights and typically has a small effect on the overall optical properties. This anisotropy can not be neglected for LC block copolymers, however, and has a profound effect on the optical properties as we shall see in Chapter 5.

For block copolymers in which intrinsic birefringence is significant, the equations derived for the N-layer waveguide need to be slightly modified. The anisotropic nature of the layers can be easily included in the formalism by modifying the expressions for the x component of the wave vector in each layer. For TE modes, the electric field in each layer is always polarized perpendicular to the optic axis which is oriented normal to the layer. As a result, the refractive index of a given layer appearing in Equation 2.37 is simply $n_{TE} = n_{\perp}$. For TM modes, however, the electric field in each layer has components both perpendicular and parallel to the optic axis (see Figure A1.1). Consequently, the effective refractive index of a given layer is now dependent on the direction of light propagation and can be shown to be [40, 42],

$$n_{TM} = \sqrt{\frac{n_{\perp}^2 n_{\parallel}^2}{n_{\parallel}^2 \cos^2\theta + n_{\perp}^2 \sin^2\theta}}, \qquad (2.43)$$

where θ is the angle between the wave vector and the optic axis. The form of the refractive index given in Equation 2.43 results in the following modified expressions [75] for the x component of the wave vector in each layer,

$$\begin{aligned} k_S &= k_0\sqrt{n_{eff}^2 - n_S^2}, \\ k_N &= k_0\left(\frac{n_{N\perp}}{n_{N\parallel}}\right)\sqrt{n_{N\parallel}^2 - n_{eff}^2}, \\ &\vdots \\ k_1 &= k_0\left(\frac{n_{1\perp}}{n_{1\parallel}}\right)\sqrt{n_{1\parallel}^2 - n_{eff}^2}, \\ k_0 &= k_0\sqrt{n_{eff}^2 - n_0^2}, \end{aligned} \qquad (2.44)$$

where the substrate and superstrate are still taken to be optically isotropic. Aside from the modified expressions in Equation 2.44, the k_i appearing in Equation 2.38 must be substituted with $k_i / n_{i\perp}^2$ for the TM modes.

The optical waveguiding properties of three model block copolymer waveguide structures will now be investigated. The first block copolymer waveguide consists of a 1.55 μm P(S-b-MMA) diblock copolymer film located between air and a quartz substrate. A lamellar domain spacing of 100 nm is chosen which corresponds roughly to a total molecular weight of 400,000 g/mol as estimated from an experimentally determined relationship between molecular weight and domain spacing [63]. In addition, previous work on this system has showed that PMMA and PS preferentially segregate to the

substrate and air interfaces, respectively in order to reduce interfacial energy. Consequently, the block copolymer film consists of 32 alternating layers of PMMA and PS where the first and last layers are half layers of 25 nm and all other layers are 50 nm. The isotropic refractive indices [76] of PMMA and PS at a wavelength of 488 nm are 1.4945 and 1.6008, respectively. Due to intrinsic birefringence, the PMMA and PS ordinary refractive indices used to calculate the TE modes are equal to 1.4945 and 1.6010. The values of the following parameters were needed to calculate the intrinsic birefringence: f_{PS} = 0.50, $(\alpha_{\parallel}-\alpha_{\perp})_{PS}$ = $-1.5*10^{-23}$ cm^3 [74], ρ_{PS} = 1.04 g/cm^3, $(L^2/\langle h^2\rangle_o)_{PS}$ = 2.53 [77], $(\alpha_{\parallel}-\alpha_{\perp})_{PMMA}$ = $1.6*10^{-24}$ cm^3 [74], ρ_{PMMA} = 1.19 g/cm^3, $(L^2/\langle h^2\rangle_o)_{PMMA}$ = 2.40 [77]. The resulting alternating step index profile for this waveguide is shown in Figure 2.10a. Using the Mathematica program, the waveguide was found to support three TE modes whose optical field intensity distributions (OFI's) are plotted in Figure 2.10b. The OFI's closely resemble those obtained for a homogeneous slab waveguide. Unlike the OFI's which result from a slab waveguide, however, the OFI's of the P(S-b-MMA) film exhibit a small oscillation commensurate with the periodic refractive index profile. In particular, the intensity of light is slightly augmented in the high index layers and slightly reduced in the low index layers.

The similarity in OFI's between the 32-layer P(S-b-MMA) waveguide and a homogeneous slab waveguide is not surprising. The domain spacing of 100 nm and incident wavelength of 488 nm places the block copolymer film approximately in the long wavelength limit ($\lambda/D \approx 5$). As a result, the 32-layer block copolymer waveguide can be modeled, to a good approximation, by an equivalent homogeneous optically uniaxial slab waveguide whose average ordinary and extraordinary refractive indices are given by the modified EMT expressions discussed earlier. The values of n_o and n_e calculated for the 32-layer P(S-b-MMA) waveguide using the EMT expressions modified for intrinsic birefringence are 1.54867 and 1.54473, respectively. The propagation

constants calculated for the 32-layer waveguide and the equivalent slab waveguide (assuming 488 nm light) are compared in Table 2.4.

Table 2.4 The propagation constants calculated for the 32 layer P(S-b-MMA) waveguide are compared with those obtained using the equivalent slab waveguide with the ordinary and extraordinary refractive indices 1.54867 and 1.54473, respectively.

Mode	n_{eff} (32 layer)	n_{eff} (Slab)
TE	1.54284	1.54253
TE	1.52448	1.52415
TE	1.49431	1.49399
TM	1.53854	1.53824
TM	1.51922	1.51890
TM	1.48790	1.48765

The two sets of propagation constants show close agreement with a mean squared error of only about .02%. These results confirm that an ideal block copolymer waveguide in the long wavelength limit behaves like a single optically anisotropic film with a well defined birefringence. In this regime, the periodic refractive index profile only causes a slight perturbation of the optical field intensity distribution of the waveguide modes. Block copolymers may therefore be an excellent material for fabricating thin film waveguides of controllable birefringence.

As λ/D decreases, the periodic nature of a block copolymer film plays an increasingly important role in determining where the optical field is located. In the next example, a 4.05 μm thick P(S-b-MMA) diblock copolymer waveguide consisting of 28

alternating PS and PMMA layers located between quartz and air is considered. All layers are 150 nm except for the 75 nm half layers at the substrate and air interfaces. The lamellar domain spacing of 300 nm corresponds roughly to a total molecular weight of 2,100,000 g/mol. At a wavelength of light of 488 nm, $\lambda/D \approx 2$ for this structure. The refractive indices of PMMA and PS are taken to be equal to their isotropic values because corrections due to intrinsic birefringence are negligible for such a high molecular weight diblock. The refractive index profile for this structure is shown in Figure 2.11a where the black and gray portions of the plot denote the high (PS) and low (PMMA) index layers, respectively. The 28 layer structure was found to support nine TE modes whose optical field intensity distributions are shown in Figure 2.11b. Similarly, the black and gray portions of each OFI plot denote the optical field located in the high and low index layers, respectively. The OFI's are significantly perturbed from the OFI's which would result from a homogeneous slab waveguide and reflect the periodicity of the lamellar lattice. The light tends to be peaked in the PS layers and reduced in the PMMA layers. When averaged over all nine modes, the amount of light found in a given PS layer is found to be 1.3 times larger than that found in a PMMA layer. As a result, on average, 56% of the total optical field intensity of a waveguide mode (guiding layers only) is preferentially distributed among the high index PS layers. Preferential segregation of the OFI increases for the higher order modes and reaches a maximum value of approximately 58% for the ninth mode.

Although light is preferentially located in the high index layers when averaged over the entire structure, the intensity of light found in a given high index layer is not uniform across the waveguide but varies strongly with mode. Inspection of the first three modes (see Figure 2.11b) shows how light can be concentrated in different regions of the multilayer waveguide (e.g. center vs. edges) by simply tuning which mode is excited. The OFI of the seventh mode is particularly interesting because the light is preferentially

segregated in every other high index PS layer. The average intensity of light found in the odd numbered PS layers is 2.5 times and 17.8 times greater than the light located in the PMMA layers and the even numbered PS layers, respectively. Thus, by selecting a given waveguide mode, an alternating multilayer waveguide structure can be used to direct light into specific high index layers. The flexibility that block copolymer waveguides possess in controlling where the light propagates could have widespread uses in integrated optics.

Both diblock copolymer waveguide structures considered above were characterized by refractive index profiles in which the block adjacent to the air-film interface had the higher refractive index. When the two structures above are inverted so that the low refractive index layer is at the air-film interface, the optical waveguiding behavior changes dramatically. Intuitively, given the inverted structure, light can no longer satisfy the constraint of total internal reflection at the superstrate/air interface for all modes. In other words, a cutoff condition is imposed which limits the range of allowed n_{eff}'s. For the 32-layer structure, the first two modes are no longer supported and only the third mode survives. For the 28-layer structure, all but the two highest order modes are eliminated. For these two modes, however, the preferential segregation of the optical field intensity into the high index layers is found to be the same as that observed for the original structure. Consequently, block copolymer structures in which the low index block segregates to the air interface exhibit an advantage from a device point of view. Only the high order modes, which generally have a greater degree of the optical field intensity segregated in the high index layers, can be excited which eliminates the possibility of scattering loss into low order modes.

The ability to separate and isolate light into designated layers of a multilayer waveguide is extremely valuable for integrated optics purposes. Diblock copolymer films, as shown above, may be one way to achieve controlled light confinement in a waveguide structure. The degree of confinement improves for lamellae with larger

domain spacings and a higher refractive index difference between the A and B blocks. In practice, the low polydispersities and high molecular weights needed for coil-coil diblocks are difficult to obtain synthetically. In addition, the attainment of well organized layers may be kinetically hindered by the slow dynamics of high molecular weight materials (see Results and Discussion). As an alternative to using pure AB diblock copolymers, previous studies [78, 79] have shown that the addition of A or B homopolymer can be used to preferentially swell the respective block resulting in an increase in the block domain spacing. By blending symmetric amounts of each homopolymer with the diblock copolymer, the lamellar domains can be swelled and the equilibrium domain spacing increased by almost a factor of two. Another possible way of achieving large domain size structures is through the use of rod-coil block copolymers. Because the characteristic length of a rod scales linearly with molecular weight, rather than to the 2/3 power as in coil-coil diblocks, for a given molecular weight, larger domain sizes are possible. An in-depth discussion of the very large (nearly a micron) and novel morphologies formed by model poly(hexyl isocyanate-b-styrene) rod-coil diblock copolymers is given in Chapter 3.

In addition to molecular weight and block composition, the degree of light confinement in a block copolymer waveguide can also be controlled through molecular architecture. Triblock copolymers represent an attractive alternative to diblock copolymers. Figure 2.12a shows the refractive index profile of a hypothetical 4.05 μm 55-layer ABC triblock copolymer film located between a quartz substrate and air. The refractive indices of the A, B, and C blocks at a wavelength of 4,880Å are 1.4945 (PMMA), 1.6008 (PS), and 1.6205 (P2VP), respectively and are representative values found for common homopolymers. The total molecular weight of this ABC triblock copolymer was chosen to be identical to that of the second AB diblock discussed above. For this structure, the A and C blocks are assumed to preferentially segregate to the

substrate and air interfaces forming half layers of 37.5 nm. All other layers are 75 nm thick. Figure 2.12a shows that the ABC triblock copolymer waveguide structure has an effective high index region 225 nm thick (black), which is composed of two B layers and a C layer. Although the total molecular weight of the block copolymer in the 28-layer and 55-layer waveguide structures is the same, the change in architecture from a diblock to a triblock copolymer enabled the design of a waveguide with high index regions significantly larger than their low index regions. The larger high index regions allow the light to be more easily confined. The 55-layer triblock copolymer film was found to support 10 TE modes whose optical field intensity distributions are shown in Figure 2.12b. The black and gray portions of each OFI denote the optical field located in the high index B and C layers and the low index A layers, respectively. The OFI's are qualitatively similar to those of the 28-layer diblock copolymer waveguide and exhibit oscillations with a periodicity equal to that of the lamellar refractive index profile. In contrast to the 28-layer waveguide where the average amount of light found in a high index layer was 1.3 times larger than in the low index layers, however, the average amount of light found in a high index (BCB) region is found to be 2.8 times larger than that found in the A layers. In addition, an average of 79% of the total optical field intensity of a waveguide mode is confined within the high index regions. Thus, a lamellar-forming triblock copolymer of equal molecular weight and comparable optical properties is able to achieve greater light confinement because the high index regions can be made effectively larger. As expected, segregation of the light increases for the higher order modes and reaches a maximum of 81% for the tenth waveguide mode. Calculations on triblock structures having layer thicknesses of 150 nm show preferential confinement of the light approaching 95% and an average of 6.6 times more light in a high index region than in a low index layer. Larger domain size does not always result in greater segregation, however. For lamellar block copolymers in the short wavelength limit,

interference at the block copolymer interfaces becomes important in determining the OFI's of the waveguide modes. Depending on the mode, the light can actually be preferentially segregated into low index layers.

2.4.4 Optimum Sample Characteristics for Waveguiding

Currently, a multitude of different polymers can be synthesized in block copolymer form using the synthetic techniques of anionic or cationic polymerization. Without a doubt, the list of polymers from which to choose will increase with time as new synthetic routes are developed. Not all block copolymer systems, however, make good optical waveguide materials for a number of reasons. To simplify the process of choosing candidate polymers, a brief discussion will now be given on what optimum sample characteristics a block copolymer should have to be a potentially viable waveguide material. Among the various characteristics, the most important are those which deal with morphological issues. To form a lamellar morphology, the volume fraction for typical coil-coil block copolymers must be nearly symmetric and in the approximate range $0.40 \leq f \leq 0.60$. For the lamellar domain sizes necessary to achieve preferential segregation of the light, molecular weights in excess of a million g/mol are required for typical coil-coil block copolymers. Currently, such high molecular weights push the limits of traditional synthetic approaches. As mentioned earlier, however, the molecular weight requirements may be somewhat reduced if block copolymer/homopolymer blend systems are used and dramatically reduced if other architectures such as rod-coil block copolymers are used. Indeed, the rod-coil block copolymer morphologies described in Chapter 3 have domain sizes approaching nearly a micron. Block copolymers must also be strongly segregated so that the interfacial width is small, the composition within the A and B domains is nearly pure, and the morphology

as a whole is well ordered. Flat parallel lamellae with narrow interfaces between domains give rise to low scattering losses and attenuation of the propagating light. Pure composition profiles translate into the step-function refractive index profiles needed to achieve a high confinement of the light.

In terms of optical properties, the polymers making up the individual blocks should have as little absorption as possible for the wavelength of light considered. In order to maximize the degree of OFI segregation, theoretical predictions show that block copolymers with large refractive index differences are desired. In fact, the larger the refractive index difference between the blocks, the more the molecular weight and domain size requirements can be relaxed. Choosing polymers with anisotropic optical properties can be useful for designing waveguide structures with tailorable birefringence. In highly birefringent multilayer waveguide structures, the TE and TM modes can exhibit very different waveguide behavior. Lamellar block copolymer waveguide structures have even greater flexibility when LC blocks are considered (see Figures 5.5 and 5.6). As will be discussed in Chapter 5, LC-containing block copolymers can exhibit biaxial optical properties in addition to the already discussed uniaxial optical properties. Also, in Chapter 4, the morphologies formed by a series of side-chain LC-coil block copolymers is presented. The particular azobenzene mesogen in those block copolymers can undergo a cis-trans conformational change upon irradiation with UV light. Photosensitive or electro-optic block copolymers like these open up another realm of possible ways for controlling light.

So far, we have discussed characteristics which can help produce the optimum lamellar morphology and desired waveguiding properties. Processing of these materials (using either temperature or solvent) to achieve a globally oriented lamellar structure suitable for waveguide purposes is equally if not more important, as will become evident in the experimental results obtained for real block copolymer systems. Obtaining well

ordered lamellar films in which the lamellae are oriented parallel to the substrate requires biased microphase separation. In a bulk block copolymer sample, microphase separated lamellar grains possess all orientations in space. For a thin film waveguide sample, a single orientation is required. Therefore, finding processing parameters and properties which can induce microphase separation with the lamellar normal orthogonal to the substrate is important. At the air interface, block copolymers, which have a surface tension difference between blocks, will preferentially segregate the lower surface tension component to the air surface. The preferential segregation of one block to the air interface induces a composition wave to propagate inward [33] which helps orient the lamellae. Similarly, block copolymers having a block which has an affinity for the substrate (e.g. PMMA on quartz) will preferentially segregate that block to the substrate interface, thereby creating another composition wave. In terms of processing, a block copolymer in which both blocks have similar glass transitions is helpful because it will behave homogeneously at all temperatures or concentrations (providing the solvent is nonpreferential). In addition to temperature and solvent processing, electric and magnetic fields can also be used to help bias microphase separation of a lamellar block copolymer. Thus, polymers with net electric or magnetic moments are desirable because of their strong coupling to externally applied fields which could be used to orient the global microstructure as well.

2.4.5 Synthesis and Characterization

Several anionically synthesized polymers were used in the experimental waveguide work. Homopolymers were used to fabricate multilayer waveguide samples and in blends to swell lamellar-forming diblock copolymers. All the diblock copolymers had symmetric compositions and were used to make waveguide samples either directly or

as part of diblock copolymer blends. Several other block copolymers including a poly(styrene-isoprene-methyl methacrylate) triblock copolymer were used in experiments. However, since waveguides based on these later samples did not yield meaningful results, the specific synthesis and characteristics of these polymers are not presented in the discussion. Only polymers for which actual data is presented or discussed are treated in this section. The molecular weight characterization data for the various homopolymers is listed in Table 2.5.

Table 2.5 Molecular weight characterization data for the homopolymers used in the waveguide experiments.

Homopolymer	Name	M_w (g/mol)	M_w/M_n
polystyrene	PS50	50,000	1.06
polystyrene	PS23	23,000	1.06
polymethylmethacrylate	PMMA49	48,600	1.05
polyisoprene	PI25	25,000	-----

Both PS homopolymers were molecular weight standards purchased from Pressure Chemical Company (Pittsburg, PA). The PMMA homopolymer was purchased from Polymer Laboratories, Inc. (Amherst, MA). The PI homopolymer, however, was synthesized by Dr. Lewis Fetters at Exxon Research and Development. All polymers were used as purchased with no further purification.

The molecular weight characterization data for the diblock copolymers used in the waveguide experiments is presented in Table 2.6. The volume fraction of PS is denoted as f_{PS}.

Table 2.6 Molecular weight characterization data for the lamellar-forming diblock copolymers used in the waveguide experiments.

Diblock Copolymer	Name	Total M_w (g/mol)	M_w/M_n	PS M_w (g/mol)	f_{PS}
P(dS-S-MMA)	SM50/50	100,000	-----	5,000 dPS / 45,000 PS	0.53
P(dS-b-I)	dSI20/20	40,000	-----	20,000	0.53
P(S-b-I)	SI20/20	40,000	1.03	20,000	0.54
P(S-b-I)	SI500/500	1,040,000	1.10	465,000	0.48

The diblock copolymer SM50/50, which was originally synthesized by Dr. Steve Smith at Procter and Gamble, was obtained from Dr. Tom Russell at IBM Almaden Research Center (now at the University of Massachusetts). The short deuterated PS segment had no noticeable effect on the microphase separated morphology and was used only for labeling studies. The diblock dSI20/20 was synthesized by Dr. Lewis Fetters several years earlier and previously used for other studies in the Thomas group. The remaining diblock copolymers, SI20/20 and SI500/500, were synthesized and characterized by members of Professor Nikos Hadjichristidis' group in the Department of Chemistry at the University of Athens. The anionic polymerizations were carried out under high vacuum in evacuated glass reactors which were washed in n-BuLi and rinsed with benzene. Additions of the reagents were made through glass membranes or break seals and removal of aliquots for characterization purposes through heat sealing of constrictions. The polymerizations were done in the solvent benzene using the initiator sec-BuLi which was prepared in vacuo from sec-butyl chloride and a lithium dispersion. For the ultrahigh molecular weight SI500/500 sample, extra purification procedures were needed due to the extremely low initiator concentrations needed (10^{-5} moles for 10 g of

copolymer). Fractionation of the SI500/500 was done in three cycles by adding methanol to the polymer solution (~0.1% w/v) in an 1:1 mixture of toluene and hexane. For those interested, detailed discussions of the anionic synthesis of these diblocks can be found elsewhere [80, 81].

The techniques of size exclusion chromatography (SEC), laser differential refractometry, low-angle laser light scattering (LALLS), and ^{1}H-NMR were used to obtain the molecular weight characteristics of the P(S-b-I) diblock copolymers listed in Table 2.6. The SEC setup, which measured the molecular weight distributions and composition, consisted of a Waters 501 solvent delivery pump, a Waters 401 differential refractometer, a Waters 486 UV detector, and four Phenomenex linear Styragel columns with porosities ranging from 50 to 10^5 nm. Solutions in THF at 30°C were pumped at a flow rate of 1 mL/min. The weight average molecular weights were determined by LALLS in THF at 25°C using a Chromatix KMX-6 apparatus operated at 633 nm. The refractive index increment and concentration were measured with a Chromatix KMX-16 instrument at 633 nm. The compositions were also determined with solution ^{1}H-NMR in $CDCl_3$ at 30°C using a Varian Unity Plus 300/54 apparatus.

2.4.6 Sample Preparation

Numerous samples were studied in the course of the block copolymer waveguide work of which only a small subset are discussed. Depending on the type of experiment, many widely varying sample preparation procedures were used to make the thin film structures. In general, however, the samples can be grouped roughly into the following three categories: multilayer homopolymer thin films, SM50/50 block copolymer thin films, and SI500/500 thin films. The basic steps used to make each type of sample will now be described.

Multilayer homopolymer films consisting of alternating layers of PS and PMMA were made as model waveguide structures. The experimentally determined waveguide modes of these structures were compared with theoretical predictions in order to confirm that the N-layer waveguide formalism was correct. In particular, two layer and four layer structures were fabricated by successive spin coating. A general discussion of the processes that take place during spin coating and the specific spinning conditions used for these experiments is provided in Appendix 2. Three different substrates were used as supporting materials for the homopolymer waveguides (see Figure 2.13). Thin polished fused quartz (0.75" x 0.75" x 0.02") substrates purchased from Dell Optics Company, Inc. (Fairview, NJ) and polished silicon wafers (1 inch diameter, 8-12 mils thick) purchased from Virginia Semiconductor, Inc. (Fredericksburg, VA) were used as substrates for prism coupling and ellipsometry experiments, respectively. For cross-sectional transmission electron microscopy (TEM) studies of the homopolymer films, SiO_2 coated epoxy disks (1.8 cm in diameter), which could be easily microtomed, were used as substrates. To make these substrates, a Sloan Multihearth 270° electron beam gun operated at -10 kV and equipped with a SiO_2 target was used to evaporate a thin layer (~100 nm) of SiO_2 onto fully cured (overnight at 80°C) epoxy disks which were held under a vacuum of less than $5*10^{-4}$ torr. The electron beam equipment was located in the Microelectronics Laboratory of the Center for Materials Science and Engineering at M.I.T. The Medcast™ Quik-mix (medium) brand embedding epoxy and silicone rubber epoxy molds were purchased from Ted Pella, Inc. (Redding, CA). To make the two layer waveguide structure, the bottom PMMA layer was first deposited by spin coating 200 μL of a 14 wt% solution in toluene (using a micropipet) onto one of the above substrates and then annealed in a vacuum oven at 80°C for an hour to remove any residual solvent. Similarly, the top PS layer was made by spin coating 200 μL of a 14 wt% solution in toluene onto a polished quartz substrate. After spin coating, the PS film was immediately

floated off on distilled water and carefully picked up using the substrate supported PMMA layer. Both PS and PMMA are hydrophobic polymers. Consequently, as the PS layer was picked up from one side, any water between the layers was naturally expelled when the PS and PMMA layers adhered to one another thereby reducing the presence of trapped water or air bubbles. The two layer structure was then annealed at 80°C for an hour to remove residual solvent and to improve adhesion between the PS and PMMA layers. The four layer homopolymer waveguide was made by extending the above process to include an additional PMMA and PS layer.

For ellipsometry and prism coupling experiments, no further processing of the samples was required. For cross-sectional TEM studies, however, the samples cast on the SiO_2 coated epoxy substrates required additional preparation. In order to protect the delicate multilayer films, the two and four layer waveguides were prestained for 15 minutes in RuO_4 vapors (which preferentially stains PS) and coated with a ~10 nm layer of carbon using a Ladd evaporator. Because of the high reactivity of RuO_4, a fresh 10 ml vial (0.5 wt% aqueous purchased from Electron Microscopy Sciences, Fort Washington, PA) was used each time. Small wedges of the coated and stained samples were cut and reembedded in new epoxy to provide the rigidity necessary for cross-sectional microtomy. Sections of the epoxy blocks were then microtomed at room temperature normal to the multilayer film using a Reichert-Jung FC4E Ultracut E microtome equipped with a 4 mm Diatome diamond knife (35° or 45°). Cutting speeds ranged from 0.5 to 2.0 mm/sec. Sections were floated on distilled water at room temperature and picked up on 600 mesh copper TEM grids purchased from Ted Pella, Inc. and stained again for 15 minutes in RuO_4 vapors to enhance the electron density contrast between the PS and PMMA layers. Prior to examination in the microscope, a thin carbon film was evaporated onto the sections to reduce beam damage of the samples. In addition, the

carbon film increases rigidity of the section and improves electrical and thermal conductivity.

Diblock copolymer thin films of SM50/50 served as a model system for studying the feasibility of forming a macroscopically oriented lamellar thin film multilayer waveguide through spin coating and annealing. The films were made by spin coating (see Appendix 2) 200 μL of a 6 wt% solution in toluene onto SiO_2 coated epoxy substrates. Samples were then annealed overnight in a VWR or Fischer Instruments vacuum oven (~0.03 torr) at either 170°C or 190°C to facilitate lamellar ordering. To protect the films from infiltration and swelling due to the epoxy monomer, the films were prestained and carbon coated the same way as the homopolymer thin films. Similarly, small wedges of the samples were cut, reembedded, and microtomed as described above. Sections were picked up on copper (600 mesh) grids, stained with RuO_4 vapors for 15 minutes, and lightly carbon coated prior to use. Extreme care was required during microtomy and section pickup due to the small thickness of the films (~300 nm). To reduce the likelihood of delamination of the diblock copolymer from the surrounding epoxy or SiO_2 layer, the films were microtomed so that the cutting direction was perpendicular to the film and the substrate was encountered first (see Figure 2.14).

The high molecular weight diblock SI500/500 and its blends with homopolymer or low molecular weight diblock were used as model materials for making block copolymer waveguide structures with expected domain sizes similar to those discussed in the theoretical block copolymer waveguide section. For the most part, the basic sample preparation steps used to make the SI500/500 films were identical to those described for the SI50/50 and multilayer homopolymer thin films. In contrast, however, a variety of processing conditions were explored (i.e. annealing temperatures, substrates, compositions, concentrations, and solvents). Rather than discuss all the specific steps required to make each of the many samples, only the processing procedures significantly

different from those previously described will be outlined. The specific characteristics of the samples are summarized in a Table 2.7. Data for the samples which are highlighted in bold will be presented in the results and discussion section.

Table 2.7 Listing of the characteristics for the SI500/500 thin film samples.

Polymers	Composition of Polymers (wt%)	Amount Solids (wt%)	Casting Method	Solvent	Substrate	Annealing Treatment	Ampule Sealing/ Irganox
SI500/500	**100**	**0.05**	**Thin**	**Toluene**	**Carbon/Mica**	**Unannealed**	**No/No**
SI500/500	100	0.05	Thin	Toluene	Carbon/Mica	1 day, 140°C	No/No
SI500/500	100	5.00	Spin	Toluene	SiO_2/Epoxy	Unannealed	Yes/Yes
SI500/500	100	5.00	Spin	Toluene	SiO_2/Epoxy	3 days toluene 2 days, 175°C	Yes/Yes
SI500/500	100	5.00	Spin	Toluene	SiO_2/Epoxy	5 days, 190°C	Yes/Yes
SI500/500	100	3.00	Spin	Toluene	SiO_2/Epoxy	Unannealed	Yes/Yes
SI500/500	100	3.00	Spin	Toluene	SiO_2/Epoxy	2 days, 160°C	Yes/Yes
SI500/500	**100**	**3.00**	**Spin**	**Toluene**	**SiO_2/Epoxy**	**2 days, 180°C**	**Yes/Yes**
SI500/500	**100**	**3.50**	**Spin**	**Toluene**	**SiO_2/Epoxy**	**Unannealed**	**Yes/Yes**
SI500/500	100	3.50	Spin	Toluene	SiO_2/Epoxy	2 days, 190°C	Yes/Yes
SI500/500	100	0.10	Simple	Toluene	SiO_2/Epoxy	3 days toluene Unannealed	Yes/Yes
SI500/500	100	0.10	Simple	Toluene	SiO_2/Epoxy	3 days toluene 2 days, 140°C	Yes/Yes
SI500/500	**100**	**1.00**	**Bulk**	**Toluene**	**-----**	**5 days, 120°C**	**No/Yes**
(SI500/500)/ PS23/PI25	49/27/24	0.10	Simple	Toluene	SiO_2/Epoxy	3 days toluene Unannealed	Yes/Yes
(SI500/500)/ PS23/PI25	49/27/24	0.10	Simple	Toluene	SiO_2/Epoxy	3 days toluene 2 days, 140°C	Yes/Yes
(SI500/500)/ PS23/PI25	86/7/7	0.15	Simple	Toluene	SiO_2/Epoxy	3 days toluene 2 days, 160°C	Yes/Yes
(SI500/500)/ PS23/PI25	95/3/2	0.20	Simple	Toluene	SiO_2/Epoxy	3 days toluene 2 days, 180°C	Yes/Yes
(SI500/500)/ dSI20/20	**87/13**	**0.10**	**Simple**	**Toluene**	**SiO_2/Epoxy**	**3 days toluene Unannealed**	**Yes/Yes**
(SI500/500)/ (dSI20/20)	**87/13**	**0.10**	**Simple**	**Toluene**	**SiO_2/Epoxy**	**3 days toluene 2 days, 140°C**	**Yes/Yes**
(SI500/500)/ (SI20/20)	98/2	0.15	Simple	Toluene	SiO_2/Epoxy	3 days toluene 2 days, 160°C	Yes/Yes
(SI500/500)/ (SI20/20)	99/1	0.20	Simple	Toluene	SiO_2/Epoxy	3 days toluene 2 days, 180°C	Yes/Yes
(SI500/500)/ (SI20/20)	98/2	5.00	Spin	Toluene	Free Standing	2 days, 160°C	No/Yes
(SI500/500)/ (SI20/20)	98/2	0.25	Simple	Cyclohexane	Free Standing	1 day cyclohexane, 2 days, 120°C	No/Yes

The extremely high molecular weight of the SI500/500 resulted in much slower kinetics for the microphase separation process as compared with block copolymers having molecular weights of 100,000 g/mol or less. As a result, annealing temperatures ranging from 120°C to 190°C were used to try to achieve macroscopically oriented near-equilibrium lamellar microstructures. P(S-b-I) diblock copolymers can typically be annealed in a vacuum oven (~0.03 torr) at 120°C (for times on the order of a week) with minimum crosslinking and degradation of the polyisoprene block (i.e. samples can be redissolved in THF and have characteristic SEC chromatograms which are indistinguishable from the original as-polymerized SEC chromatograms). However, for annealing temperatures much greater than 140°C, additional precautions were needed. Small amounts (0.1 wt%) of the antioxidant Irganox 10/76 were added to the solutions. Antioxidants prevent crosslinking by reacting with any trapped oxygen or radicals which are produced during annealing. In addition, when possible, samples were degassed in a vacuum oven for four hours at 80°C to remove any trapped oxygen and then immediately flame-sealed under high vacuum (~0.03 torr) in glass ampules prior to annealing.

Besides spin coating, a number of other casting techniques were employed to make samples of SI500/500 and its blends. Following the procedure of Henkee et al. [82], ultrathin (~50 nm) films, which can be easily examined in plan view without the need for microtoming, were made to carry out an initial screening of the SI500/500 morphology. Mica sheets purchased from Ted Pella, Inc. were cut into approximately 1 cm by 4 cm pieces using a razor blade or shears. The top few layers of the mica substrates were peeled off with tape to expose a fresh surface, dipped into a dilute surfactant solution (Victawet® purchased from Ladd Research Industries, Inc., Burlington, VT), and dried. A ~100 Å thick carbon support film was evaporated onto the mica using a Ladd Research Industries, Inc. thermal evaporator. Three equally spaced 30 μL drops of a 0.05 wt% solution in toluene were deposited using a micropipet onto the

carbon coated mica substrates and allowed to evaporate overnight in a covered petri dish with a (2 ml) toluene reservoir. Once the films were fully dried in a vacuum oven for an hour, they were floated off onto distilled water and picked up on copper (600 mesh) TEM grids. The surfactant layer facilitated removal of the carbon support film from the mica. The supported films could then be annealed and or stained and carbon coated for examination in the TEM as usual. Solution casting (called simple casting) was used to make both thicker films (~500 nm) and bulk samples (~1 mm).

In comparison to spin coating, simple casting is characterized by a much slower solvent evaporation rate which allows the block copolymer solution to pass through the order-disorder concentration more slowly thereby producing more near-equilibrium morphologies. For thin film samples of the SI500/500, (SI500/500)/homopolymer blends, and the diblock blends, 200 μL of the solution (0.10 to 0.25 wt% in toluene) was deposited directly onto the SiO_2 coated epoxy disks and allowed to evaporate for three days in a solvent saturated covered petri dish. Further processing was identical to that previously mentioned for the SM50/50 thin film samples. For bulk samples of SI500/500, 4 ml of a 1 wt% solution in toluene was cast into a small (7 ml) ceramic crucible and allowed to evaporate slowly for approximately two weeks. The resulting film was removed from the crucible by immersing the crucible in liquid nitrogen for several minutes. Thermal contraction of the film was typically sufficient to allow the film to be dislodged from the crucible. Part of the film was dried in a vacuum oven for one day and then annealed at 120°C for five days. Before microtomy, the sample was prestained in OsO_4 vapors (0.5 wt% aqueous purchased from Ted Pella, Inc.) for two hours and then embedded in epoxy. Prestaining was done to protect the sample from the epoxy monomer and also increase the samples rigidity during microtomy. Sections of the epoxy-embedded bulk sample were microtomed at room temperature, picked up on grids, stained for another two hours to increase the electron density contrast between the PS and

PI domains, and carbon coated prior to examination to reduce beam damage and sample distortion in the microscope. OsO_4 preferentially stains the PI block by reacting with the unsaturated double bonds.

In substrate-supported films, mobility of the block copolymer chains is always reduced at the polymer/substrate interface because of adsorption effects and the presence of an impenetrable substrate. As a result, free-standing films of the diblock copolymer blends were made to eliminate the effects of chain pinning by the substrate. In these samples, block copolymer chains on both the top and bottom surfaces were free to move without having their mobility constrained. Both simple casting and spin coating were used to make substrate-free thin films (~500 nm) on either fused quartz or NaCl substrates. The films were then scored, with a razor blade, floated off on distilled water, and picked up on copper grids for annealing. The annealed films were then prestained for two hours in OsO_4, and carbon coated on both sides. Epoxy molds which already contained half-filled precured epoxy plugs were filled with new epoxy monomer. The sample grids, which sink in epoxy monomer, were then carefully immersed in the epoxy monomer and placed on top of the precured plugs. In this way, all sides of the films were surrounded by epoxy. The cured samples were then microtomed in the same way used for the substrate-supported films. The effect of a preferential solvent on the morphology of the diblock blends was also studied. Cyclohexane, which is a poor solvent for PS, was used as the casting solvent to try to form swollen lamellar vesicles of the (SI500/500)/(SI20/20) blend prior to spin coating.

2.4.7 Experimental Techniques

Several techniques were used to characterize both the microstructure and the optical properties of the waveguide samples. The primary experimental technique used to

investigate the morphology of the thin film samples was cross-sectional TEM. Bright field TEM was performed on a JEOL 200CX microscope primarily operated at an accelerating voltage of 200 kV. For samples with inherently low electron density contrast between block copolymer domains or layers, the microscope was operated at 100 kV. Typically, condenser aperture #2 (300 μm), spot size #3, and objective aperture #4 (40 μm) were used during routine operation. For particularly delicate beam-sensitive films (SM50/50, PMMA easily beam damages), standard low-dose techniques were employed: C2 near cross-over, focusing on adjacent area of sample, condenser aperture #3 (200 μm), and a reduction of the gun bias and beam current. Beam damage and sample drift were minimized by the thin protective carbon layer evaporated prior to examination. The carbon layer increased the rigidity of the sample and improved electrical and thermal conductivity. Occasionally, a second carbon layer was evaporated on the bottom side of the grids to provide further mechanical stability.

Differential interference contrast (DIC) optical microscopy performed on a Carl-Zeiss Axioskop was used as a complimentary tool both for studying the surface morphology of the samples and for screening the best sections or most promising areas for cross-sectional TEM. In DIC mode, reflected light is used to generate an interference image of the sample in which color is correlated to film thickness. For lamellar-forming block copolymer films [62], the presence of discrete color changes across a film after annealing indicates the formation of terraces and can be used as a sign of lamellar ordering parallel to the substrate.

To measure the optical properties of the thin film samples, the techniques of ellipsometry and prism coupling were used. Ellipsometry is a non-destructive, non-contacting, and relatively simple technique for simultaneously determining the refractive index and thickness (≤ 6 μm) of thin polymer films located on semi-infinite substrates or the refractive index of bare substrates. Typical resolutions obtainable for the refractive

index and thickness are ±.005 and ±3 Å, respectively. A fully automated Gaertner L3W26C.488.830 multiple wavelength variable angle photometric ellipsometer located in the Analytical Shared Experimental Facility of the Center for Materials Science and Engineering at M.I.T. was used to study the homopolymer and block copolymer thin films. The three wavelengths of 633 nm, 488 nm, and 830 nm, which were generated by He-Ne, Ar-ion, and IR diode lasers, respectively, allowed the thickness of films to be determined uniquely. Dispersion information over most of the visible spectrum could be obtained using the three different wavelengths as well. In addition to the multiple wavelength capability, ellipsometric measurements could also be performed over a wide range of incident angles (30° to 80°) which allows a more accurate determination of the film thickness. For a discussion of the theory behind ellipsometry, its applications to anisotropic films, and how the refractive index and thickness are calculated see Appendix 3. For ellipsometry experiments, samples were deposited on both silicon wafers and fused quartz substrates frosted on the bottom side. Frosting of the fused quartz substrates was done to eliminate reflected light from the back surface which can lead to incorrect results. In order for ellipsometry to yield meaningful results, samples must also have a low surface roughness over the size of the beam (~1 mm), be free of large defects, and have few foreign dust particles.

Prism coupling, which uses integrated optical techniques, was used to measure the waveguide modes (both TE and TM n_{eff}'s), refractive index, and thickness of the multilayer homopolymer thin film samples. Measurements were performed on a fully automated Metricon Model 2010 prism coupler equipped with a 633 nm laser which was located in the laboratory of Professor Steve Senturia in the Department of Electrical Engineering and Computer Science at M.I.T. The high index (1.9650) prism used was made from a gallium-gadolinium-garnett crystal with cubic symmetry. Typical resolutions achievable for the refractive index and thickness are ±.0005 and ±15 Å,

respectively. In order for simultaneous determination of both refractive index and thickness, however, the polymer film must be thick enough to support at least two modes. As a result, films must be at least 480 nm thick. For a discussion of the principle behind prism coupling and how the refractive index and thickness are calculated see Appendix 4. As with ellipsometry experiments, thin films have to have highly uniform film thickness and surface roughness. In contrast, prism coupling experiments are much more sensitive to the presence of foreign dust particles which can prevent coupling of the light into the film. Depending on the quality of the polymer surfaces, coupling pressures ranging from 20 to 50 psi were employed.

2.4.8 Results and Discussion

The two and four layer alternating homopolymer waveguides were made not only to check the N-layer waveguide formalism but also to observe the preferential segregation of light predicted theoretically for multilayer waveguide structures with large layer sizes. Figure 2.15 shows a schematic diagram of the two layer Quartz/PMMA/PS waveguide. The thicknesses of the PMMA and PS layers and their corresponding optical constants for 633 nm light were determined from both ellipsometric and prism coupling measurements performed after spin coating of each layer. Spin coating was found to produce thickness variations of about ±5 nm over a given film. Despite the protective prestaining and carbon coating, cross-sectional TEM showed that epoxy monomer had swelled and dissolved most of the top PS layer after reembedding. Cracks in the carbon layer or large holes in the PS layer may have allowed the epoxy monomer to infiltrate the two layer structure and separate the PS layer from the Epoxy/SiO_2/PMMA substrate. Once separated, the epoxy could easily have dissolved the unprotected and unstained bottom surface of the PS layer. DIC of the two layer waveguide fabricated on the fused quartz

substrates, however, revealed large areas of the film free of defects which were suitable for waveguide experiments. As a result, no further TEM experiments were carried out on this structure. Prism coupling experiments showed that the structure supported two TE and two TM modes whose propagation constants are listed in Table 2.8.

Table 2.8 Comparison of the measured and theoretically predicted propagation constants for the two layer Quartz/PMMA/PS homopolymer waveguide.

Mode	Measured n_{eff}'s	Predicted n_{eff}'s
TE	1.5499	1.5495
TE	1.4757	1.4738
TM	1.5495	1.5483
TM	1.4731	1.4708

The refractive index at 633 nm of the fused quartz substrates was determined to be 1.4564 by ellipsometry. The experimentally determined optical constants for the two homopolymer layers and the substrate were input into the N-layer waveguide program and used to predict the TE and TM propagation constants shown in the third column of Table 2.8. The agreement between the measured and predicted propagation constants is excellent given the variation in thickness of the individual homopolymer layers.

Encouraged by the results of the two layer waveguide, the four layer alternating waveguide was then fabricated. Extreme care was required during the floating of each successive homopolymer layer. The presence of any trapped air pockets or folds can result in drastically different optical waveguiding properties. Figure 2.16 shows a representative cross-sectional bright-field TEM micrograph of the actual four layer waveguide structure, which was fabricated on a SiO_2 (~146 nm thick) coated epoxy

substrate, along with a schematic diagram. The PMMA (light) and PS (dark) layers are well adhered to one another and do not exhibit significant roughness or defects. In some places, the nearly perfect four layer structure extends for hundreds of microns. Other areas, however, did show significant swelling and delamination of the local homopolymer layers due to the reembedding process, which was only used for the TEM samples. What is also immediately apparent in the micrograph is the large discrepancy in layer thicknesses. The PMMA and PS layers differ by as much as 500 nm while the two PS layers which were spun under identical conditions differ by 300 nm. While some of the difference can be attributable to the shrinkage and depolymerization of the PMMA layers resulting from the electron beam, the film thickness differences between the two PS layers can only be a result of the spin coating process. No doubt, significantly more uniform films can be fabricated by spin coating. Even so, the consistently uniform domain sizes exhibited naturally by microphase separated block copolymers are extremely difficult to reproduce with successive spin coating of homopolymers. Once the correct structure was verified through TEM, the waveguiding properties of the four layer waveguide were studied using prism coupling. Five TE and five TM modes were observed for 633 nm light. As in the two layer waveguide, the theoretically predicted propagation constants were calculated using the optical constants and thicknesses of the individual homopolymer layers determined from TEM, ellipsometry, and prism coupling. Both sets of data are compared in Table 2.9.

Table 2.9 Comparison of the measured and theoretically predicted propagation constants for the four layer Quartz/PMMA/PS/PMMA/PS homopolymer waveguide.

Mode	Measured n_{eff}'s	Predicted n_{eff}'s
TE	1.5677	1.5653
TE	1.5476	1.5495
TE	1.4955	1.5199
TE	1.4716	1.4730
TE	1.4628	1.4590
TM	1.5685	1.5679
TM	1.5403	1.5483
TM	1.4943	1.5204
TM	1.4704	1.4720
TM	1.4612	1.4570

Again, the agreement is quite close between the experimentally measured and the theoretically predicted propagation constants which further supports the TEM results. In Figure 2.17, the OFI's corresponding to these five TE modes are plotted. The gray and black portions of each plot correspond to the optical field intensity which is located in the PMMA and PS layers, respectively. The OFI's show quite clearly that the large layer thicknesses of the four layer homopolymer waveguide give rise to preferential light confinement. In particular, for the first and second waveguide modes the light is almost totally segregated either in the first or the second PS layers, respectively. The success of the homopolymer waveguide experiments conclusively shows that the N-layer waveguide formalism which was developed earlier and its predictions are correct.

After completion of the multilayer homopolymer waveguide experiments, thin films of the SM50/50 copolymer were studied to see what processing conditions resulted in well-ordered lamellar microstructures in a modest molecular weight diblock copolymer. From the literature [60-65], annealing of P(S-b-MMA) spin coated films at 170°C was sufficient to induce parallel ordering of the lamellae when the film thickness was ~100 nm. Figure 2.18 shows a cross-sectional bright-field TEM micrograph of the ~210 nm thick SM50/50 spin coated film which was annealed for one day at 170°C. In the micrograph, the PMMA and PS (RuO_4 stained) domains are light and dark, respectively. The horizontal dark gray band is the ~120 nm thick SiO_2 layer. All other areas of the micrograph are epoxy. The Fresnel fringes which are visible at the polymer/carbon and carbon/epoxy interfaces are due to defocus of the objective lens. While the P(S-b-MMA) diblock copolymer is microphase separated, the morphology is a random bicontinuous structure and clearly lacks any long range lamellar order. The situation changes dramatically for the sample annealed one day at 190°C (see Figure 2.19). Orientation of the lamellae parallel to the substrate and long range order is now strikingly evident. In places, the degree of order shown in Figure 2.19 extends for distances approaching a hundred microns. Isolated edge dislocations and misaligned lamellae were also observed, however. These results clearly show the importance of annealing temperature and mobility for achieving well ordered lamellar morphologies. A difference of only 20°C was sufficient to allow the SM50/50 thin film to transform from a kinetically trapped bicontinuous structure to a macroscopically aligned lamellar morphology. The higher annealing temperature, which allowed sufficient mobility for large scale motion of the lamellar microdomains to take place, was needed because the SM50/50 films were almost twice as thick as the films studied by Russell and coworkers (for comparable molecular weights).

The primary reason for studying the SM50/50 thin films was to determine the necessary processing steps which influence the ordering of a lamellar-forming diblock copolymer thin film. As a result, the optical properties of the SM50/50 thin films were not measured directly. Kim et al., however, performed a prism coupling study of annealed P(S-b-MMA) thin films (~900 nm) [77] which is quite relevant to this chapter. They studied a symmetric (f_{PS} = 0.49) P(S-b-MMA) diblock copolymer with a molecular weight of 88,800 g/mol and domain spacing of 38 nm. Thus, their thin films are well within the long wavelength limit and can be described by an average ordinary and extraordinary refractive index. The average ordinary and extraordinary refractive indices for their annealed P(S-b-MMA) films were found from prism coupling to be 1.5343 and 1.5323, respectively. Assuming that the isotropic refractive indices of PS and PMMA are 1.5845 and 1.4856 for 633 nm light [76], respectively, and using the necessary parameters found earlier in this chapter for the intrinsic birefringence calculation of PS and PMMA, the predicted ordinary and extraordinary refractive indices are calculated to be 1.5349 and 1.5317, respectively. The close agreement between the calculated values and the experimentally determined values of Kim et al. is further confirmation of the long wavelength behavior of block copolymers discussed earlier in this chapter.

Having gained useful knowledge from the SM50/50 thin film experiments of the processing steps needed to achieve well ordered block copolymer films, we can now begin our discussion of the progress which has been made in actually making optical waveguide structures from the ultra high molecular weight SI500/500. Henkee films of the SI500/500 were studied first to check if the morphology was lamellar. Figure 2.20 shows a bright-field TEM micrograph of the ultrathin film morphology of SI500/500. In this micrograph, the PI domains appear dark due to OsO_4 staining and the PS domains appear light. In contrast to what would be expected for f_{PS} = 0.45, SI500/500 appears to be PS-rich. Because PI is the lower surface tension component, however, it forms a half

layer at both the air and substrate surfaces [9] which results in an effectively smaller PI volume fraction in the interior of the film. In addition, the presence of any PI surface layers are not visible in the plan projection since they only contribute a uniform background level to the image as a whole. The overall morphology of the SI500/500 ultrathin film, however, is similar to morphologies formed by other lamellar-forming diblocks. In addition, the volume fraction is well within the lamellar region of the morphology diagram for strongly segregated diblock copolymers. The approximate domain spacing of 240 nm is large enough for the SI500/500 thin film to exhibit some of the waveguiding properties predicted earlier in Chapter 2 provided the lamellae can be appropriately oriented.

Spin coated thin films of the pure SI500/500 were investigated first to see if high temperature annealing alone would be sufficient to orient the lamellar microdomains parallel to the substrate. Figures 2.21a and 2.21b show cross-sectional bright-field TEM micrographs of SI500/500 thin films spin coated on SiO_2/Epoxy (SiO_2 ~140 nm thick) substrates which have undergone no annealing (as-cast) and have been annealed at 180°C for two days, respectively. The unannealed film (~550 nm thick), which is PI-rich as expected, clearly shows that the shear forces experienced by the SI500/500 solution during the spin coating process have resulted in elongated block copolymer domains oriented in the direction of shear. In addition, the domains are significantly smaller than their equilibrium sizes. The highly nonequilibrium morphology was "frozen" and trapped in by the rapid solvent evaporation. The order-disorder concentration (ODC) for SI500/500 in toluene is known from light scattering studies to be 7.5 wt% [81]. Although the initial solution concentration was 3.5 wt%, the rapid solvent evaporation which takes place during spin coating undoubtedly caused the SI500/500 solution to pass above its ODC thereby inducing microphase separation and subsequent vitrification of the morphology. In fact, the iridescent optical properties of the solution prior to spin coating

suggest that the SI500/500 was already a swollen weakly segregated lamellar system. Upon annealing, the morphology of the SI500/500 film (~400 nm thick) changes dramatically as shown in Figure 2.21b. Relaxation of the block copolymer chains and large scale motion of the microdomains has led to a coarsening of the morphology, which is now characterized by domain sizes (~230 nm) approaching those measured for the Henkee film. The morphology, however, is still far from being globally oriented with respect to the substrate and superstrate. Except for the continuous PI layer at the top of the film, the air and substrate surfaces do not appear to be significantly influencing the microphase separation. The possibility exists that thermal degradation of the PI block could also be preventing the morphology from approaching equilibrium. Despite the use of antioxidants and ampule sealing, some samples definitely showed what appeared to be mass loss in the PI domains near the film surface.

Further attempts to get the pure SI500/500 diblock copolymer to form globally oriented lamellar films using high temperature annealing alone were not successful. As a result, several additional strategies were tried. Instead of the pure SI500/500, blends of the SI500/500 with either lower molecular weight PI (PI25) and PS (PS23) homopolymers or a lower molecular weight P(S-b-I) diblock (dSI20/20 or SI20/20) were tried. For the case of the homopolymer blend, the homopolymers were used to swell the SI500/500 lamellae and reduce the entanglements between the block copolymer chains. In the case of the diblock blend, the lower molecular weight component segregates to the IMDS and occupies some of the interfacial area which effectively increases the average lateral distance between the high molecular weight diblock chains [83]. The SI500/500 chains are thus less entangled and have greater mobility. A drawback, however, is that the effective lamellar domain size (which scales with the $M_n^{2/3}$) is reduced because the high molecular weight chains become less stretched at the IMDS. Besides the use of blends, spin coating was abandoned in favor of simple casting, which allowed the

solutions to pass through the ODC more slowly. In addition, simple casting gives the PI block chains more time to segregate to the air and substrate surfaces and induce coherent layered composition waves.

As a whole, the homopolymer blends exhibited poorly ordered thin film morphologies when compared with either the pure SI500/500 thin films or the diblock blend thin films. In addition, many of the homopolymer blend samples showed signs of micelle formation of the SI500/500 diblock within the homopolymer domains. Of all the samples listed in Table 2.7, only the diblock blend consisting of 13 wt% dSI20/20 was able to form well-ordered lamellae upon annealing. Figures 2.22a and 2.22b show cross-sectional bright-field TEM micrographs of the unannealed (as-cast) and annealed (2 days at 140°C) thin films of the (SI500/500)/(dSI20/20) diblock blend simple cast onto SiO_2/Epoxy (SiO_2 ~220 nm thick) substrates, respectively. The as-cast thin film (~500 nm thick) morphology alone is noticeably better ordered than either of the pure SI500/500 morphologies previously shown in Figure 2.21. The tendency for layers to form parallel to the air interface is clearly visible. The interior of the film, however, is still fairly disordered. An even greater improvement in order is apparent in the annealed film (~420 nm thick). Global orientation of the microphase separated lamellae parallel to the air interfaces can be seen to propagate nearly three layers into the film. Surprisingly, no preferential segregation of the PI block to the SiO_2 substrate is observed. Although well-ordered lamellae were achieved by blending SI500/500 with the lower molecular weight diblock, the domain size was significantly reduced to as expected. The domain size predicted from the weight averaged molecular weight of the diblock blend, using an experimentally determined domain spacing vs. molecular weight relationship for P(S-b-I) diblocks [2], is nearly identical with the observed domain size (~90 nm). In order for the SI500/500 waveguide structures to be able to exhibit any of the interesting optical

waveguiding properties discussed earlier, the domain size has to be greater than about 150 nm.

In an effort to increase the domain size while still maintaining the ability to form ordered structures, samples were made which had a smaller wt% (1 and 2 wt% SI20/20) of the low molecular weight diblock. Unfortunately, none of these samples yielded the desired morphology even for annealing temperatures of 180°C. At this point two additional strategies were tried. Since the air interface was clearly more important to the self-assembly of the SI500/500 than the substrate interface, free-standing thin films of the diblock blends were made. In addition to having two air/polymer surfaces to help organize and drive microphase separation, the free-standing films were free from substrate pinning effects on the block copolymer chains. Free-standing films were also simple cast from cyclohexane, which is a poor solvent for PS. Cyclohexane was used so that the SI500/500 would form swollen vesicles in solution thereby speeding up the self-assembly process. It was anticipated that after simple casting, the film of collapsed vesicles could be annealed to remove any remaining defects. Neither of these strategies, however, proved successful.

Why was the ultrahigh molecular weight SI500/500 diblock copolymer unable to form well-ordered globally oriented lamellae? From the cross-sectional TEM studies, the diblock was able to both microphase separate locally on the length scale of the radius of gyration of the block copolymer chain and undergo large scale center-of-mass motion (i.e. the thin film flowed upon annealing). In addition, the block copolymer was obviously strongly segregated with $\chi N = 900$ ($\chi(413K) = .070$ [84]). Several possible reasons exist which explain why SI500/500 did not form the expected morphology. Figures 2.23a and 2.23b show bright-field TEM micrographs of a bulk cast sample of SI500/500 far from the surface and near the surface of the film, respectively. Figure 2.23a shows that the preferred bulk morphology of SI500/500 is not lamellar at all but

more of a random bicontinuous structure. The tendency for SI500/500 to form a nonlamellar morphology in the bulk could also explain its inability to form a well ordered lamellar structure when cast as a thin film. Only near the surface, as shown in Figure 2.23b, are lamellae observed. The lower molecular weight species of a block copolymer are known [9] to migrate preferentially to the surface of bulk films. These results suggest that SI500/500 is actually a more polydisperse sample than previously thought whose actual f_{PS} is significantly less than 0.45. Besides the block copolymer itself, the ultrahigh molecular weight of SI500/500 undoubtedly poses severe kinetic barriers to the development of long range order. Large-scale diffusion of chains normal to the IMDS, which is required for reorientation of microphase separated lamellar grains to take place, is extremely difficult given the many entanglements per chain. In addition, since SI500/500 is strongly segregated, the interfacial width is expected to be extremely small. As a result, the AB junctions are highly localized at the IMDS which further hinders lateral diffusion of the chains. Finally, surface tension effects may also help to explain why SI500/500 does not, for most of the samples studied, form domains oriented parallel to the substrate and air interfaces. Interfacial tension is known [85] to obey the following relationship,

$$\gamma = \gamma_{\infty} - \frac{k_e}{M_n^{2/3}}, \qquad (2.45)$$

where γ_{∞} and k_e are the surface tension at infinite molecular weight and a characteristic constant of a given polymer, respectively. Because the molecular weights of each block are so large for SI500/500, the surface tension difference between PI and PS is essentially the difference between the γ_{∞} values of the two polymers. This difference is most likely

so small that the driving force for preferential segregation of the PI block to the air and substrate does not influence microphase separation significantly.

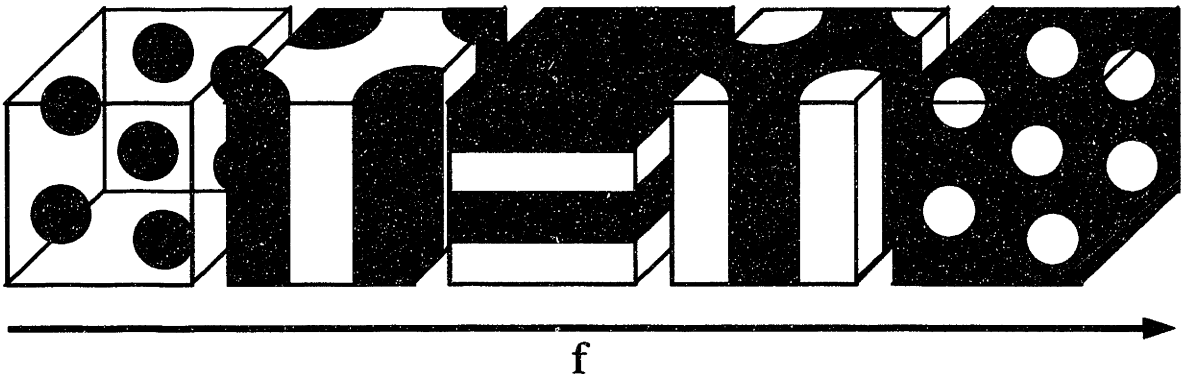

Figure 2.1 Schematic drawings of the coil-coil block copolymer morphologies observed in early experiments.

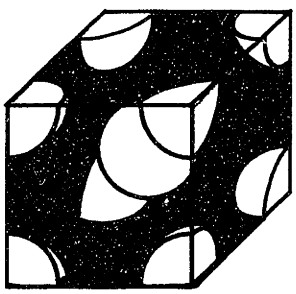

Figure 2.2 Schematic drawing of the body-centered cubic sphere morphology.

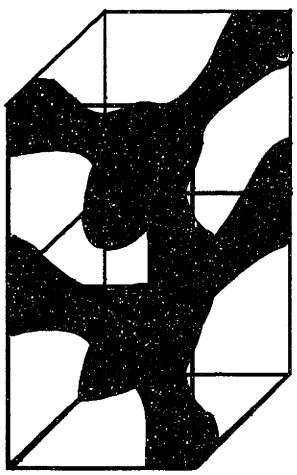

Figure 2.3 Schematic drawing of the OBDD morphology.

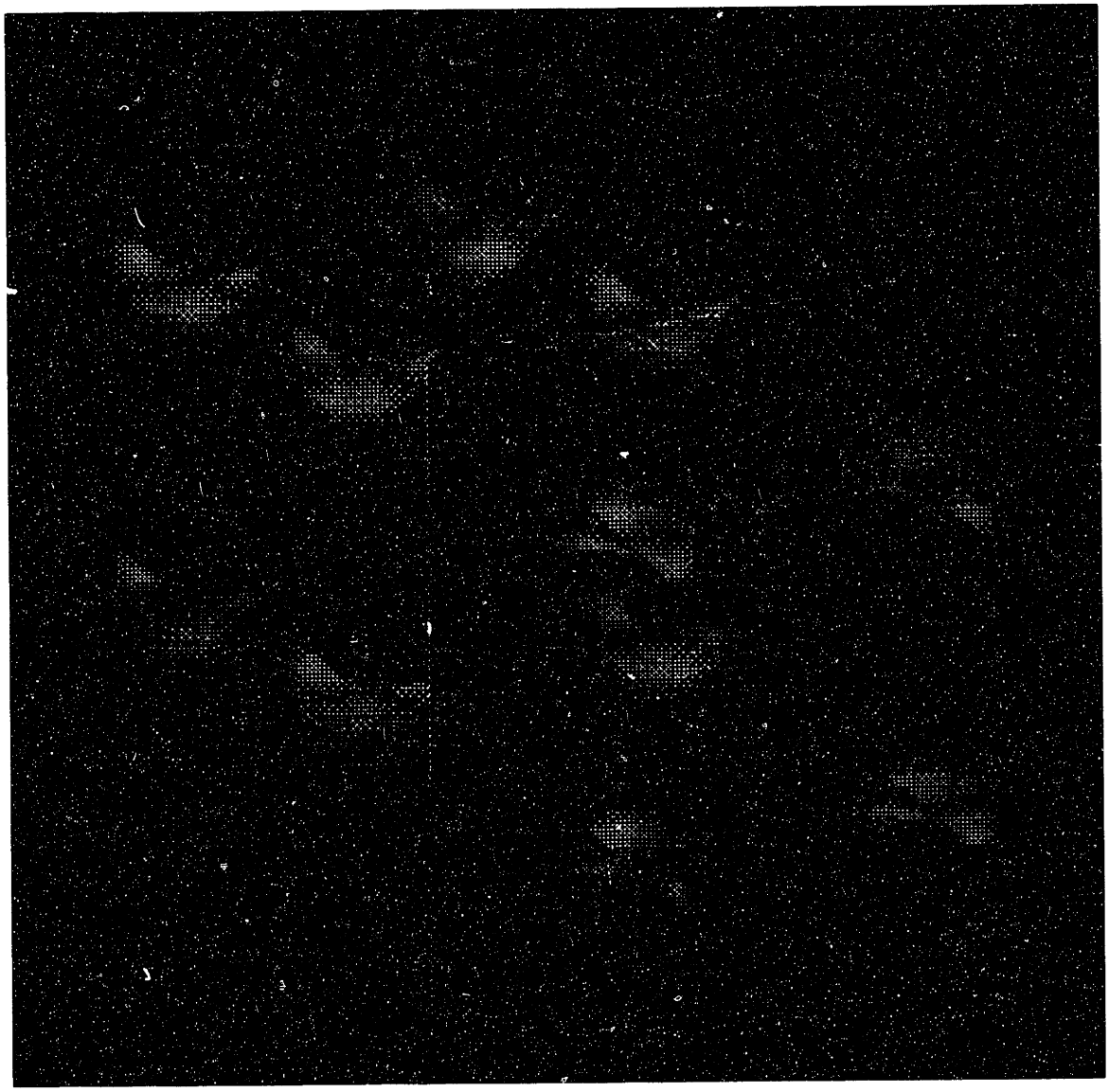

Figure 2.4 **A perspective view of the Schwarz D minimal surface generated using the program TEMsim written by Jim Hoffman.**

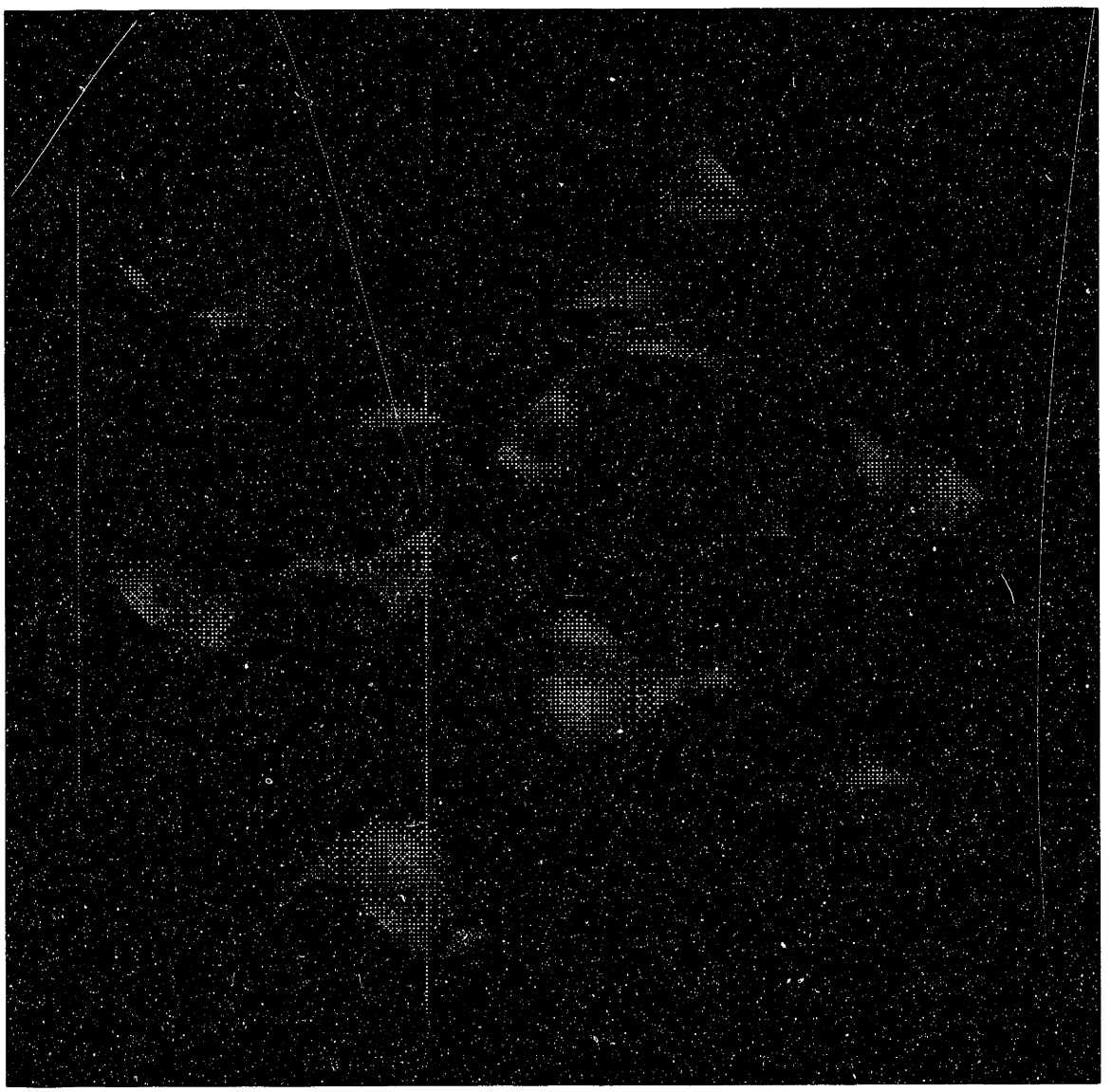

Figure 2.5 **A perspective view of the Schoen G minimal surface generated using the program TEMsim written by Jim Hoffman..**

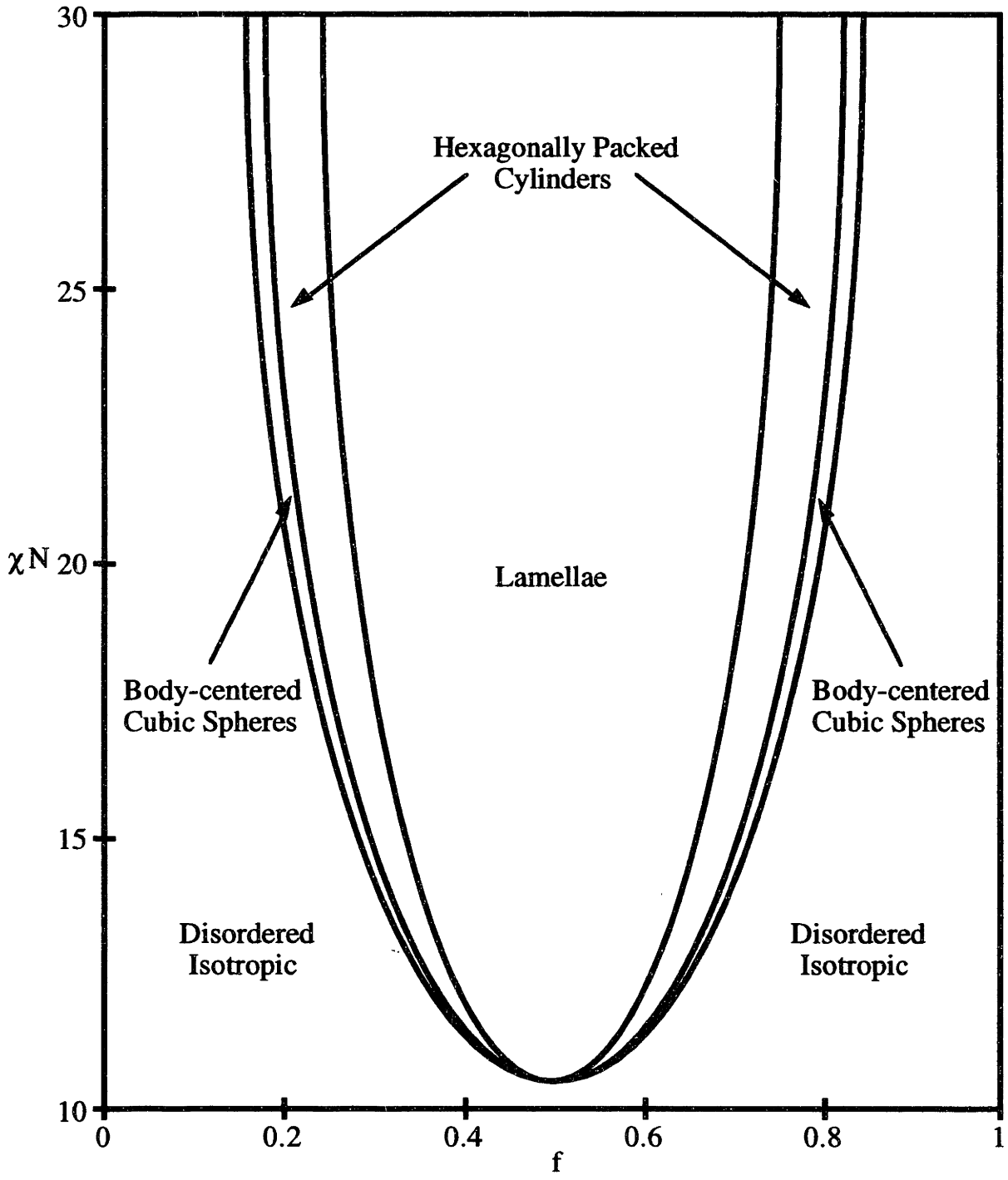

Figure 2.6 Leibler's classical morphology diagram for coil-coil diblock copolymers.

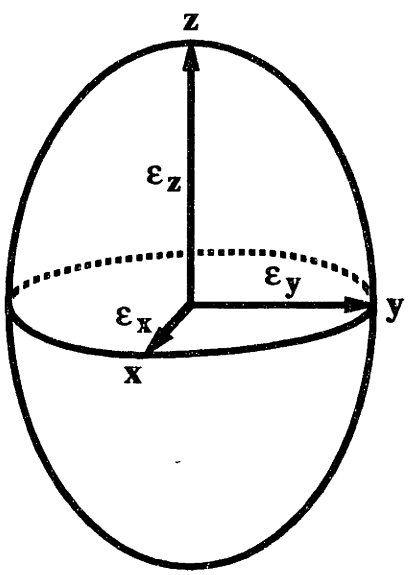

Figure 2.7 The ellipsoid of wave normals for an anisotropic medium.

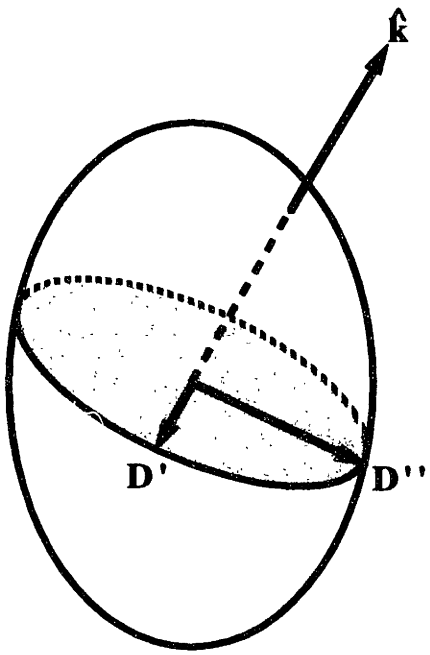

Figure 2.8 A schematic diagram showing how the two polarization directions **D'** and **D''** and their corresponding refractive indices can be determined in an anisotropic medium given the propagation direction.

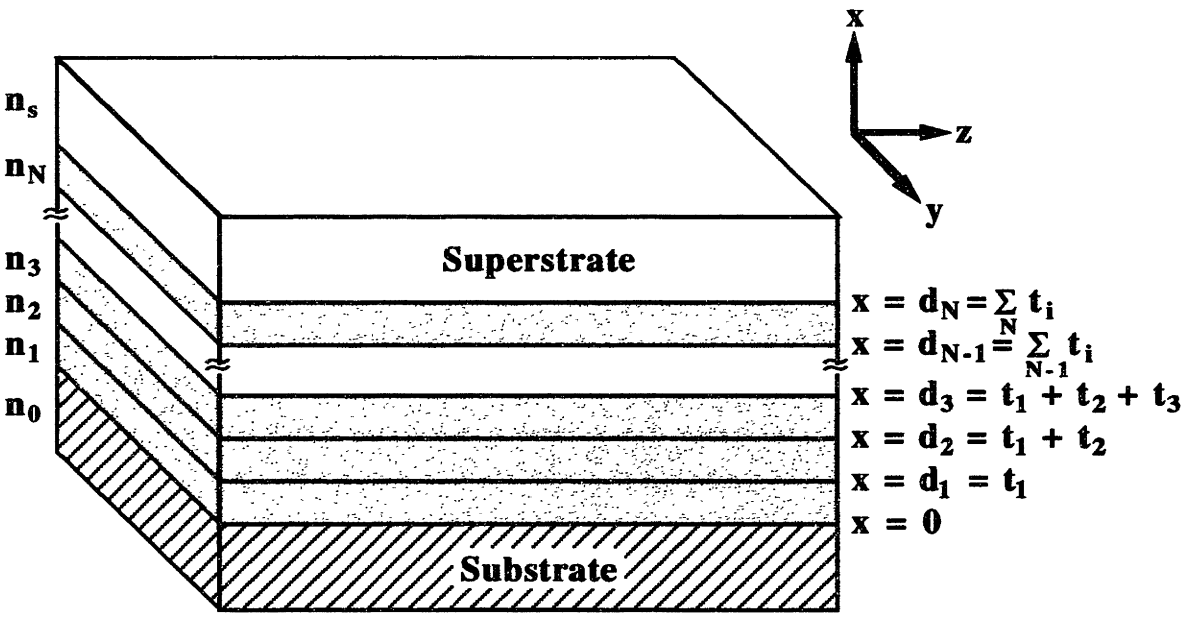

Figure 2.9 Schematic diagram of an ideal multilayer waveguide structure. The refractive indices and thicknesses of each layer are denoted by the n_i and the t_i, respectively. Light is assumed to propagate in the $\hat{z}$ direction.

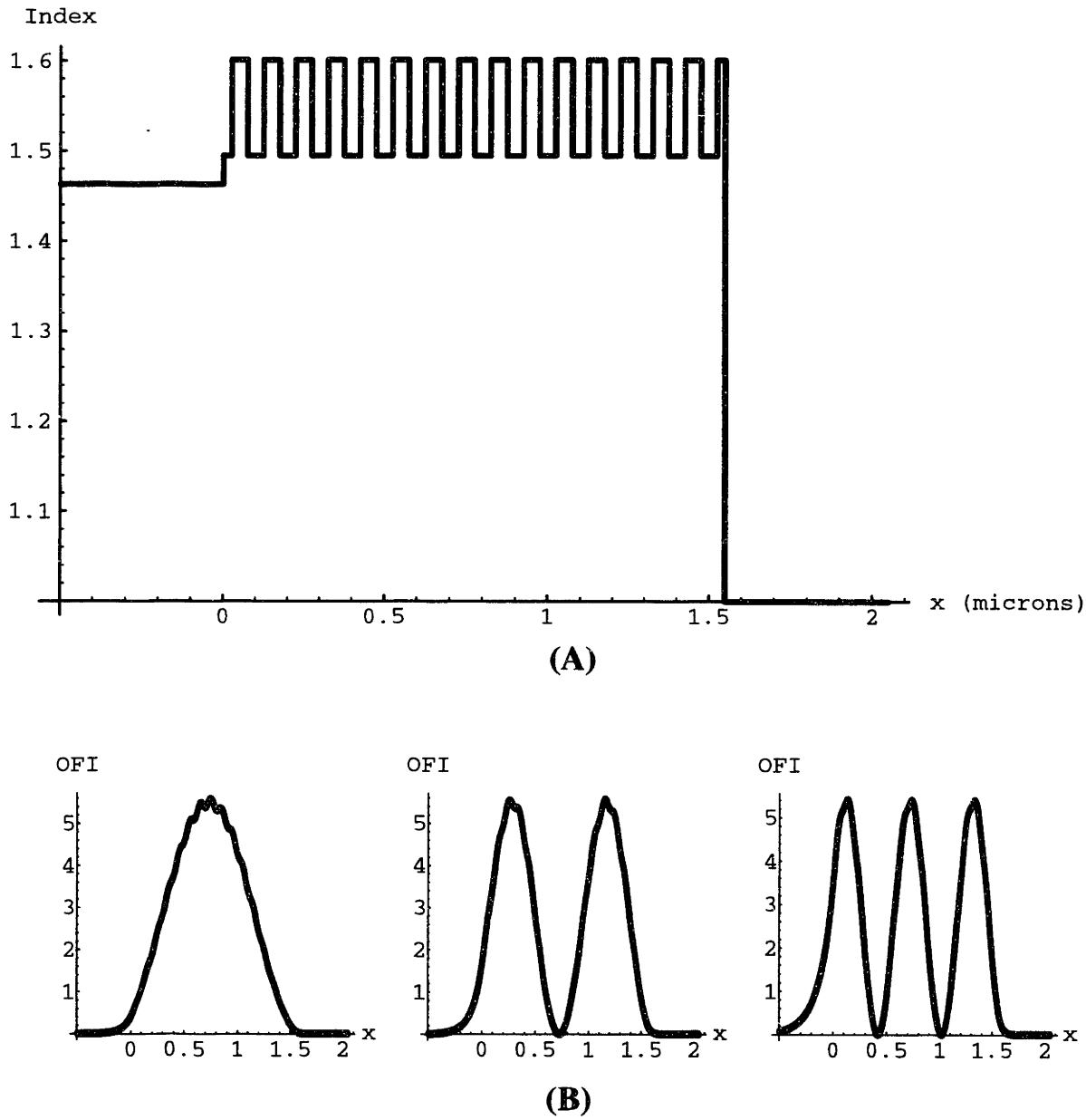

Figure 2.10 (A) Plot showing the refractive index profile for an ideal 32 layer P(S-b-MMA) diblock copolymer waveguide. (B) Optical field intensity distribution plots for the 3 TE modes of the 32 layer waveguide.

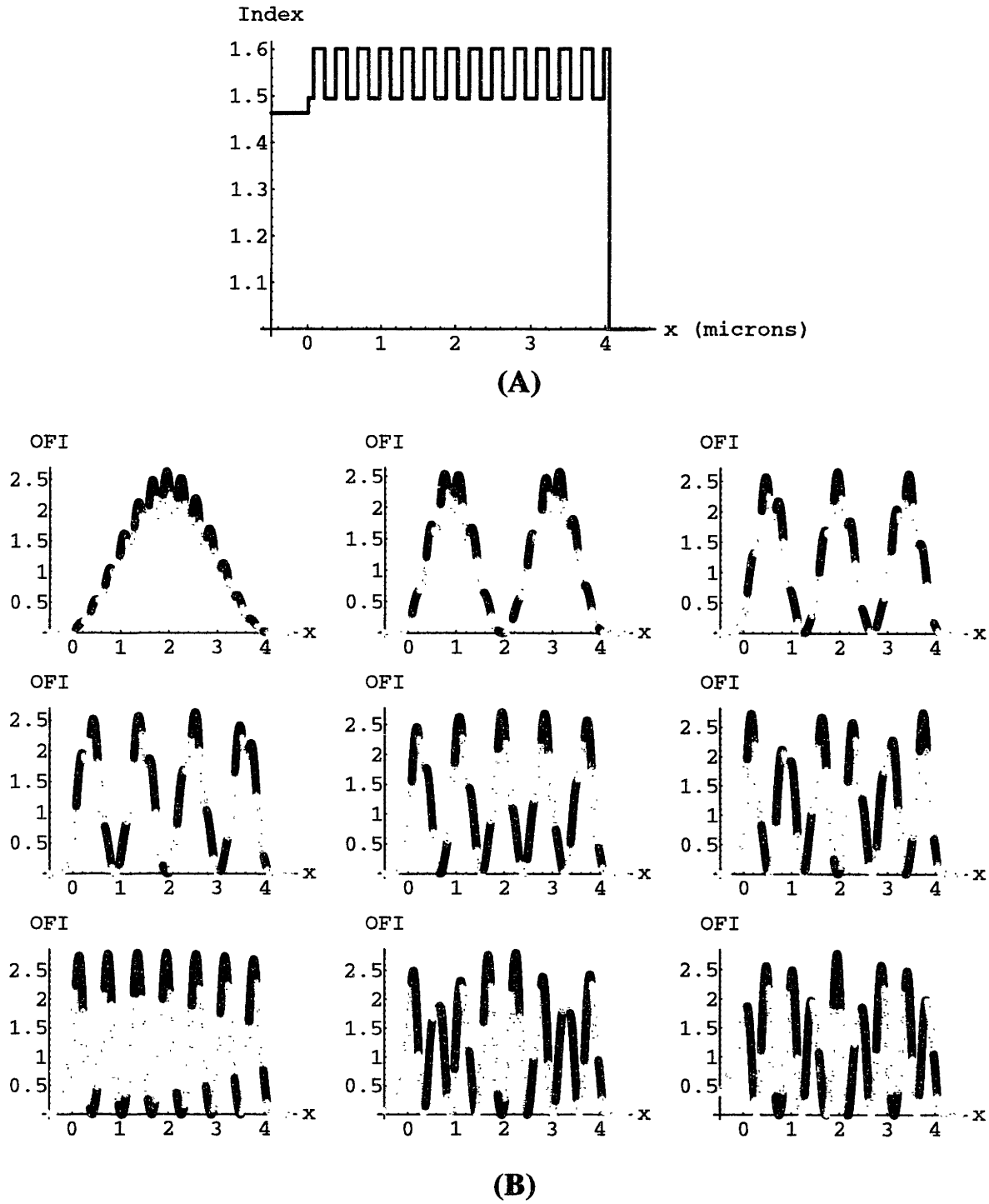

Figure 2.11 (A) Plot of the refractive index profile for an ideal 28 layer P(S-b-MMA) diblock copolymer waveguide. (B) Optical field intensity distribution (OFI) plots for the 9 TE modes. The black and gray portions of each plot correspond to the high and low index layers, respectively.

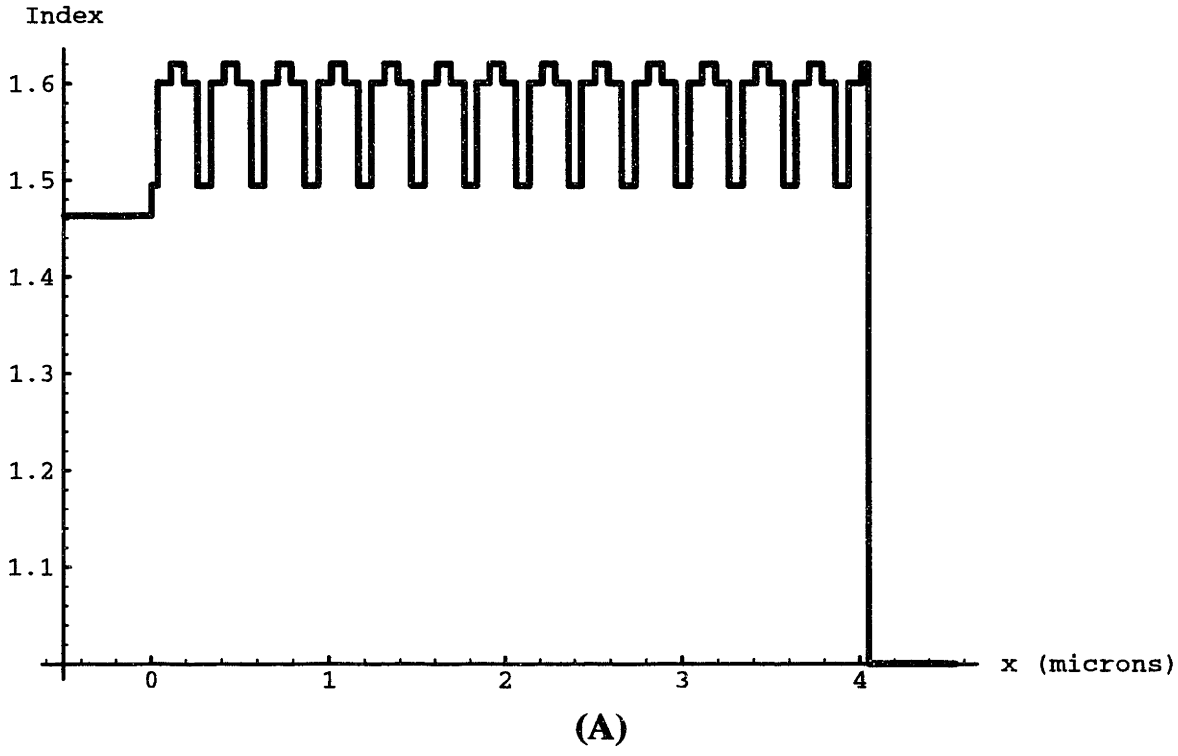

(A)

Figure 2.12 (A) Plot of the refractive index profile for an ideal 55 layer ABC triblock copolymer waveguide. The B block broadens the effective high index regions of the waveguide. The total molecular weight of the triblock was chosen to be the same as that of the diblock copolymer shown in Figure 2.11.

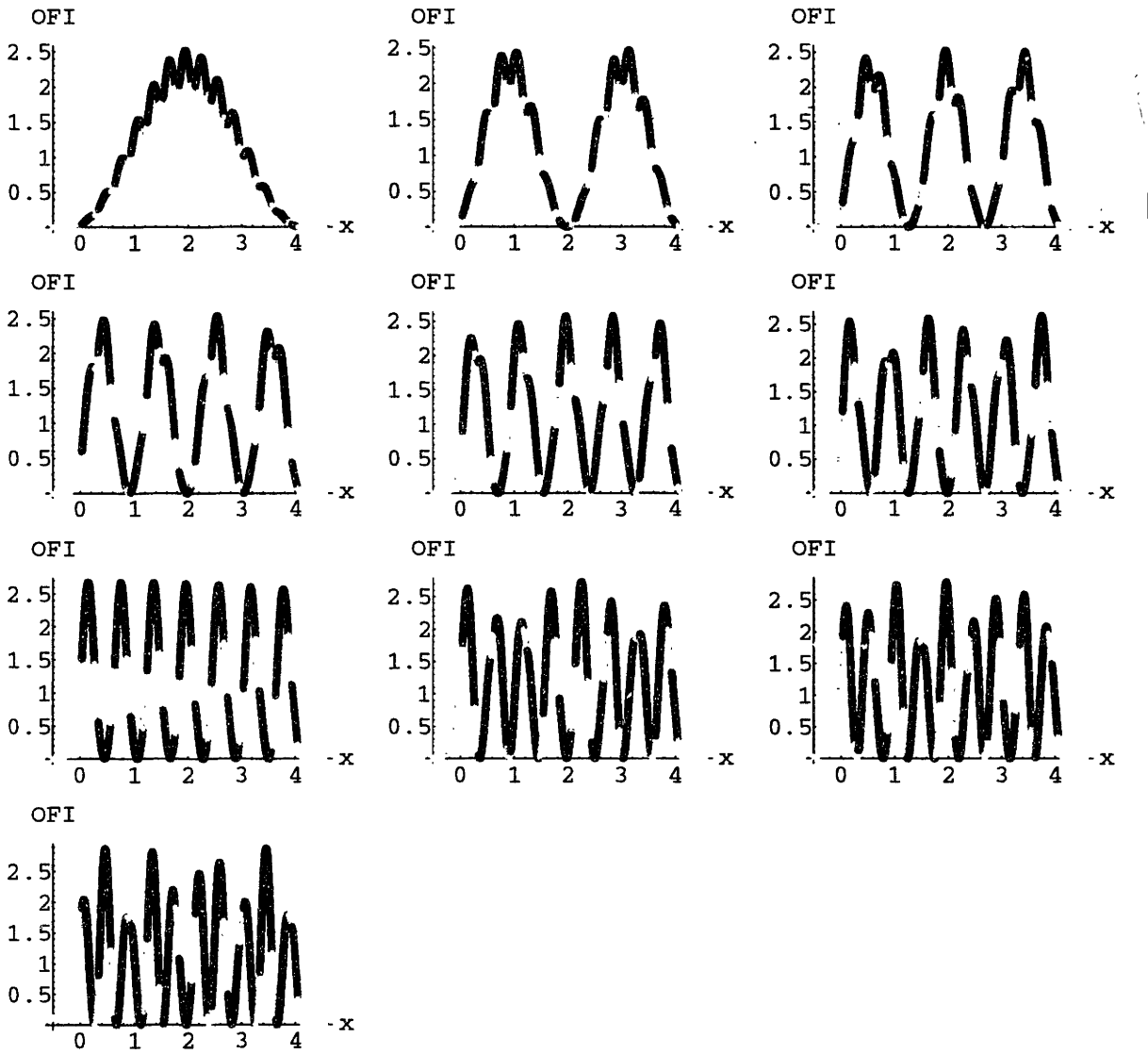

(B)

Figure 2.12 (B) Optical field intensity distribution plots for the 10 TE modes of the 55 layer ABC triblock copolymer waveguide. The black and gray portions of each OFI correspond to the high index B and C layers and the low index A layers, respectively.

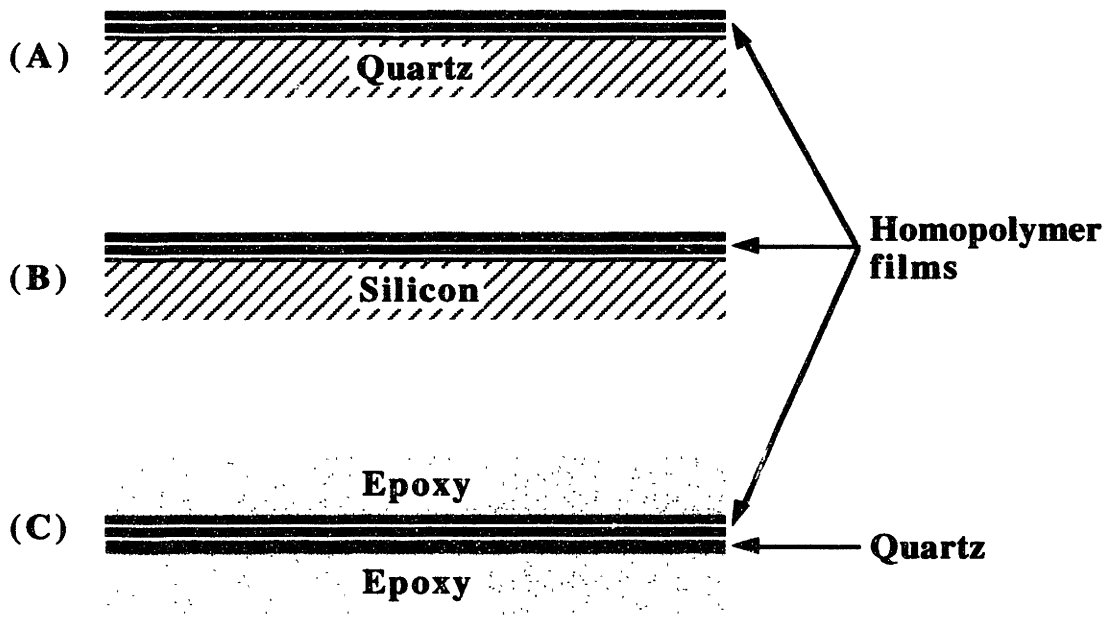

Figure 2.13 Schematic diagrams of the (A) prism coupling, (B) ellipsometry, and (C) cross-sectional TEM sample configurations used for the multilayer homopolymer waveguide samples.

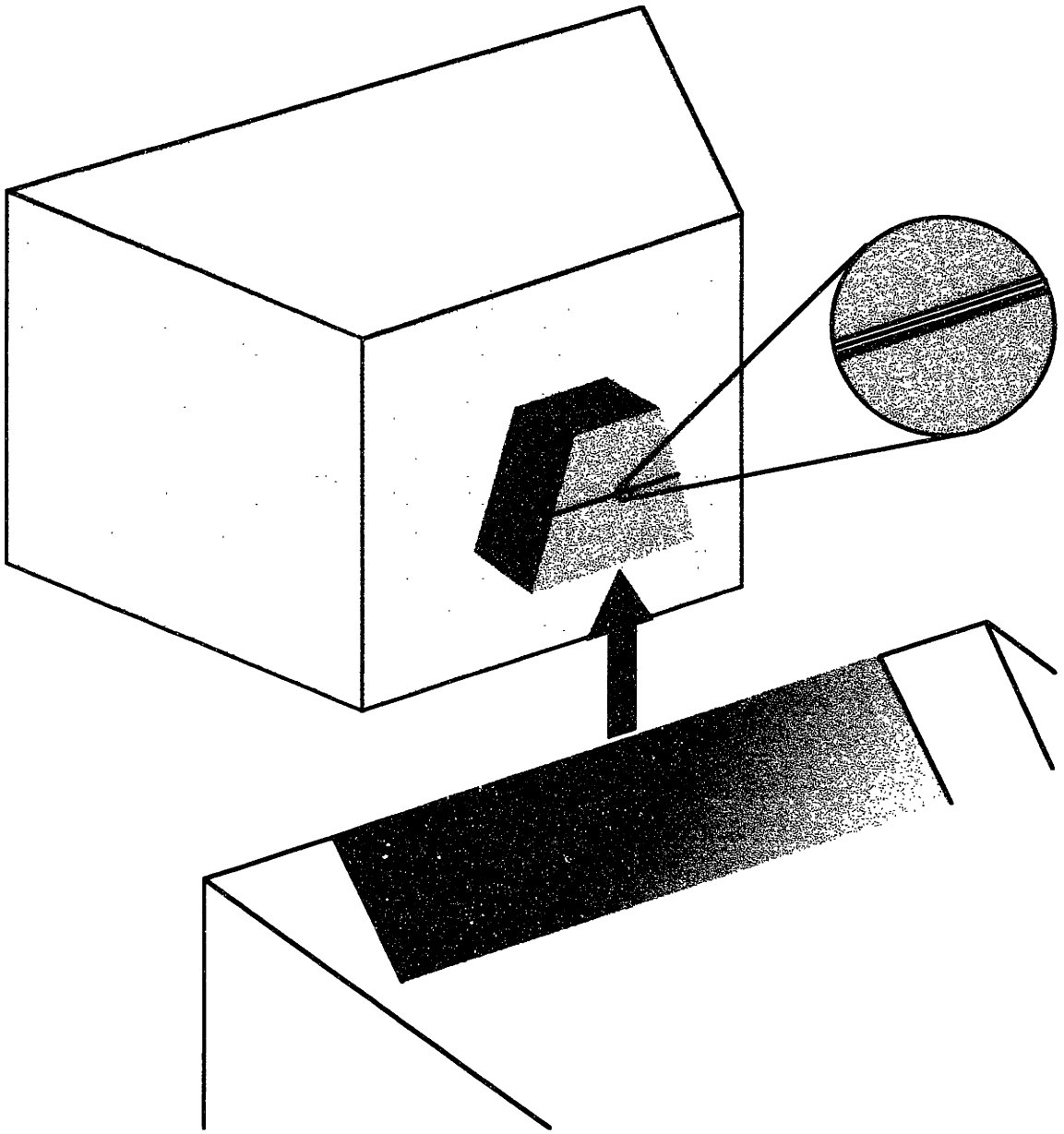

Figure 2.14 Schematic diagram of the microtoming geometry employed for the diblock copolymer thin films. The epoxy block is shown trimmed to the shape of a trapezoid. The diamond knife is shown below. The cutting motion is such that the bottom of the thin film is cut first.

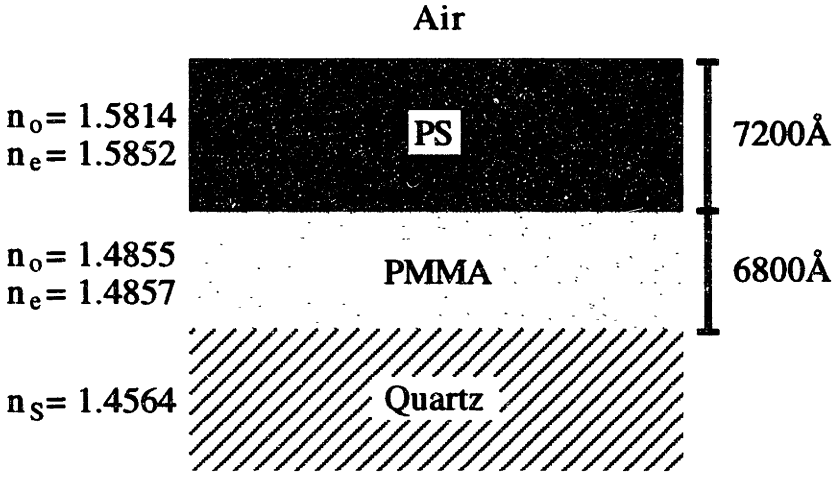

Figure 2.15 Schematic diagram of the two layer Quartz/PMMA/PS waveguide.

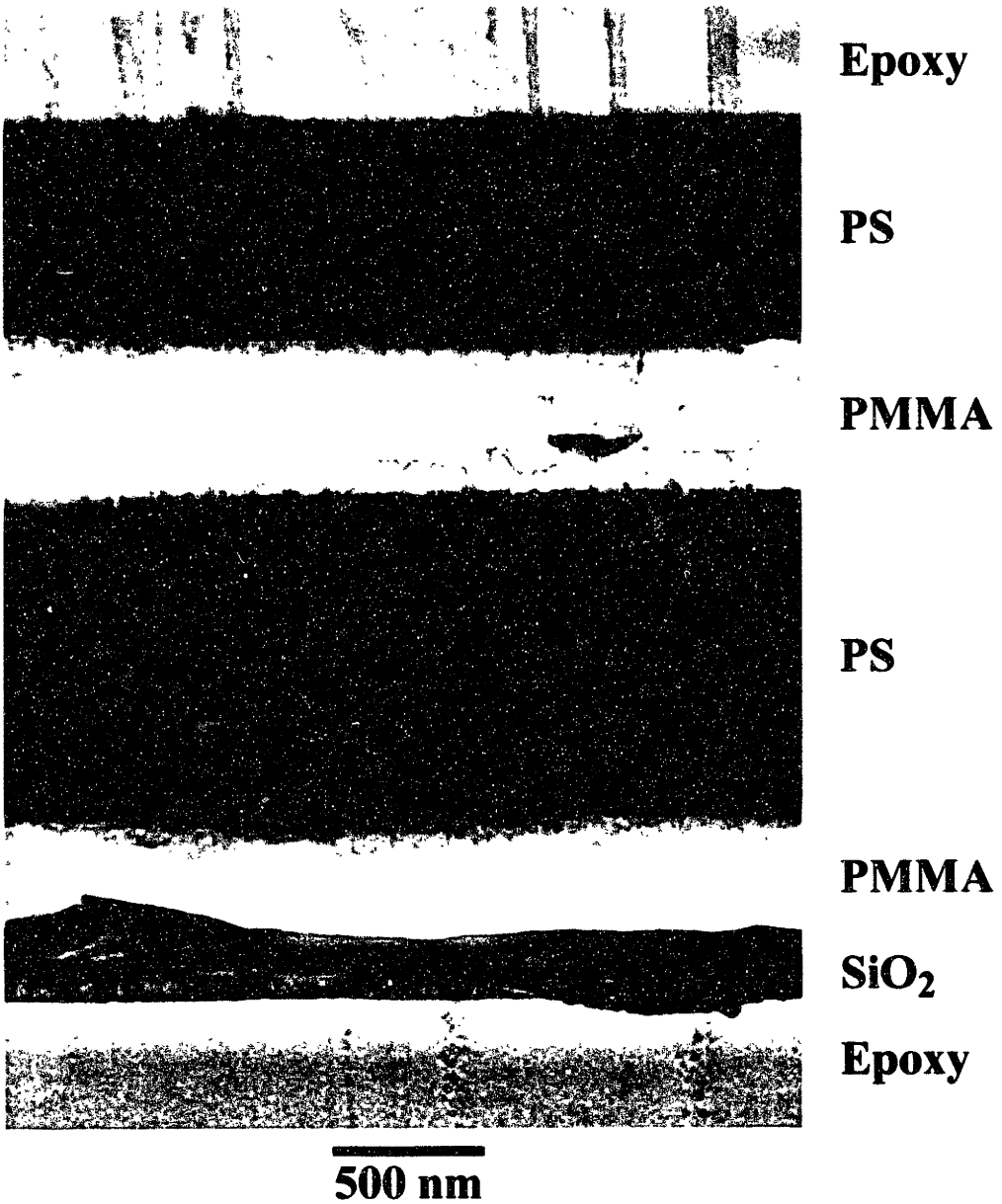

Figure 2.16 **Cross–sectional bright–field TEM micrograph of the alternating four layer homopolymer waveguide. The PS (dark) layers have been preferentially stained with RuO_4.**

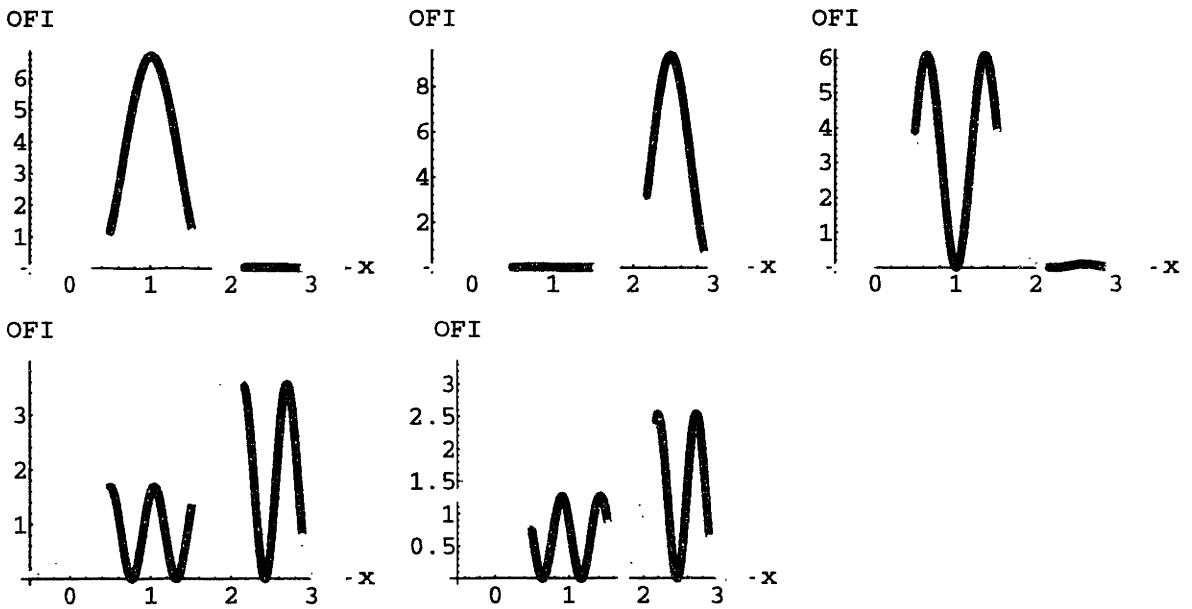

Figure 2.17 Optical field intensity distribution plots for the 5 TE modes of the four layer Quartz/PMMA/PS/PMMA/PS waveguide.

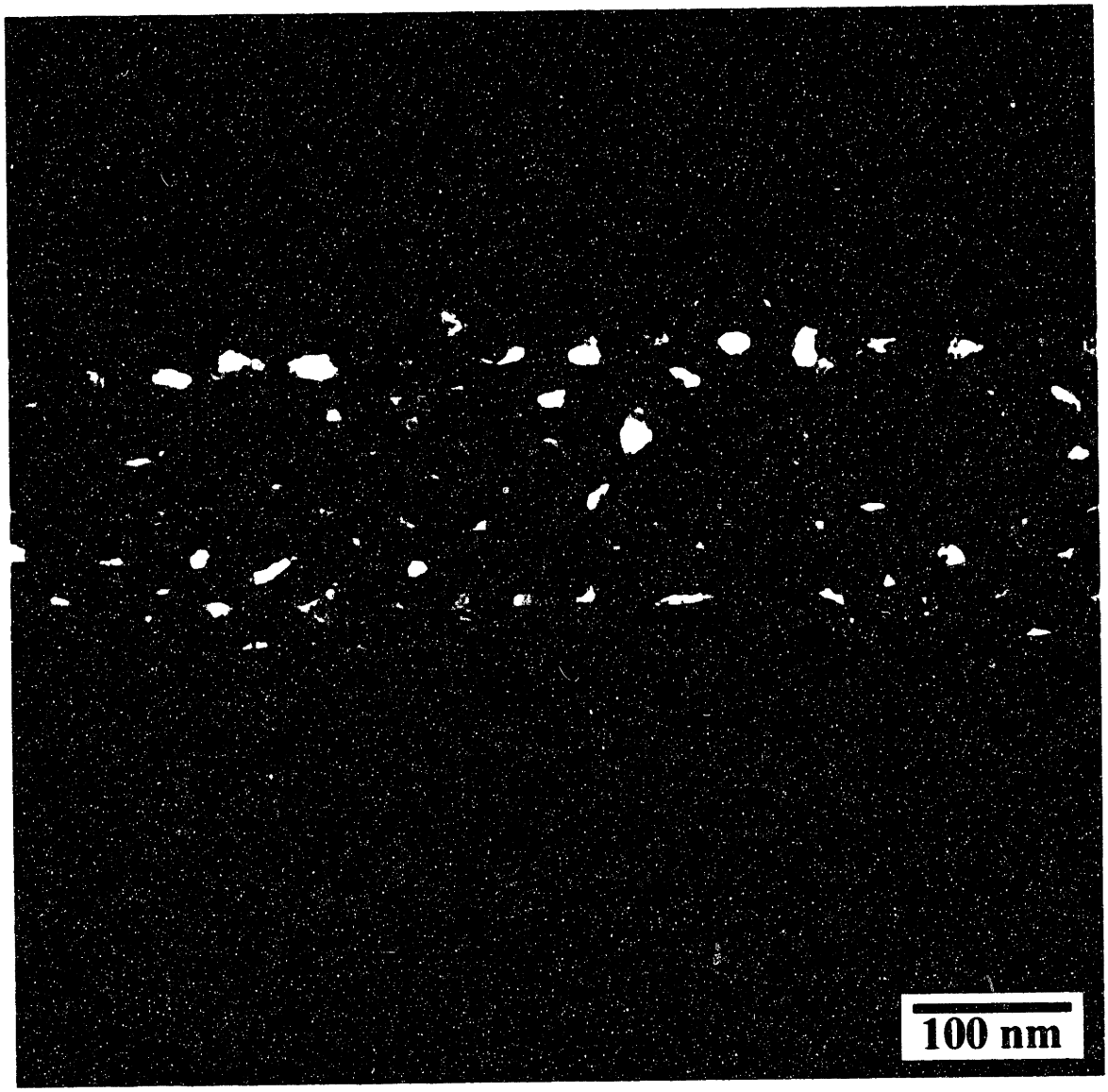

Figure 2.18 **Cross–sectional bright–field TEM micrograph of a SM50/50 spin coated thin film annealed for one day at 170°C. The PS (dark) domains have been preferentially stained with RuO_4.**

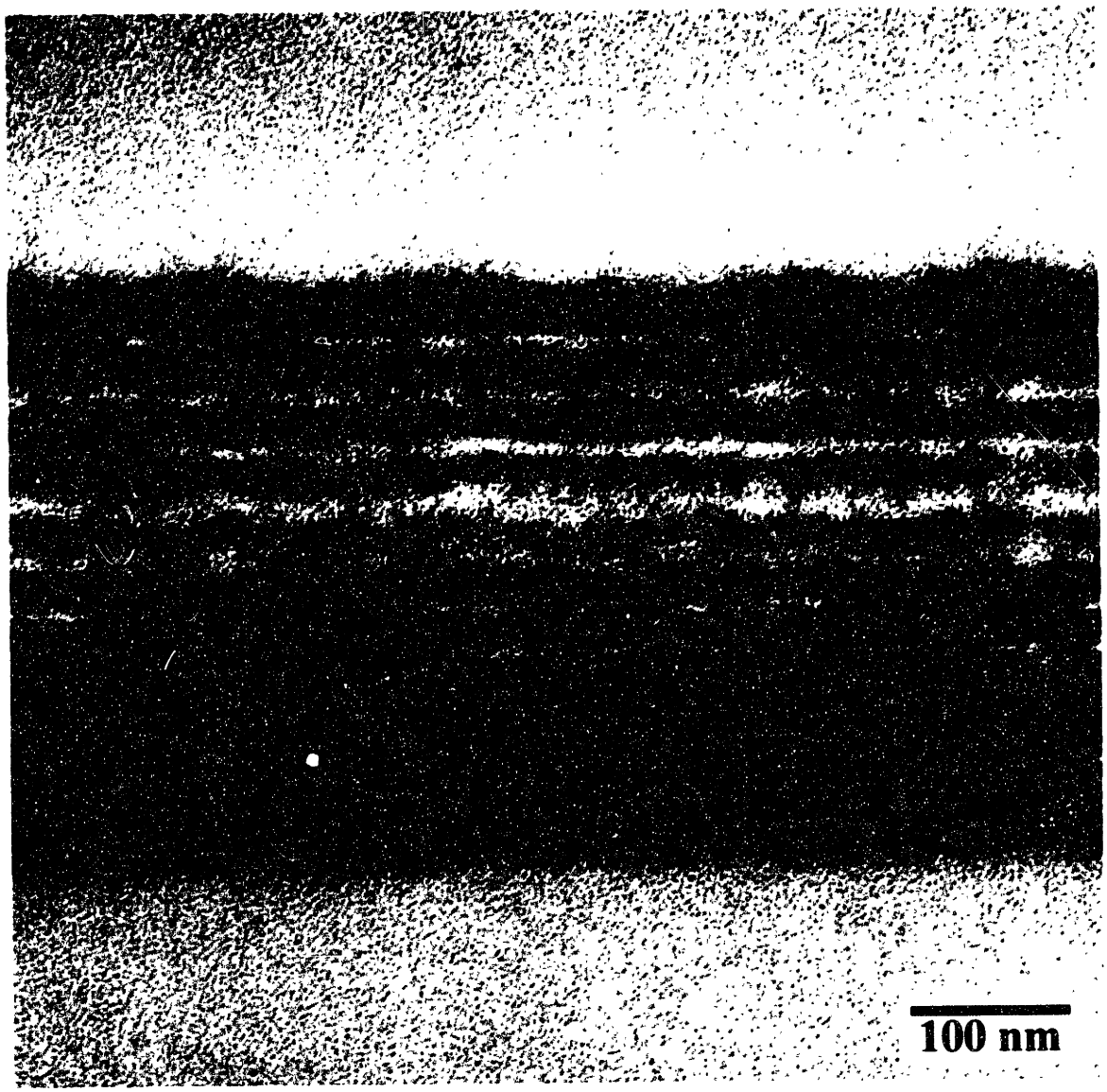

Figure 2.19 **Cross–sectional bright–field TEM micrograph of a SM50/50 spin coated thin film annealed for one day at 190°C. The PS (dark) layers have been preferentially stained with RuO_4.**

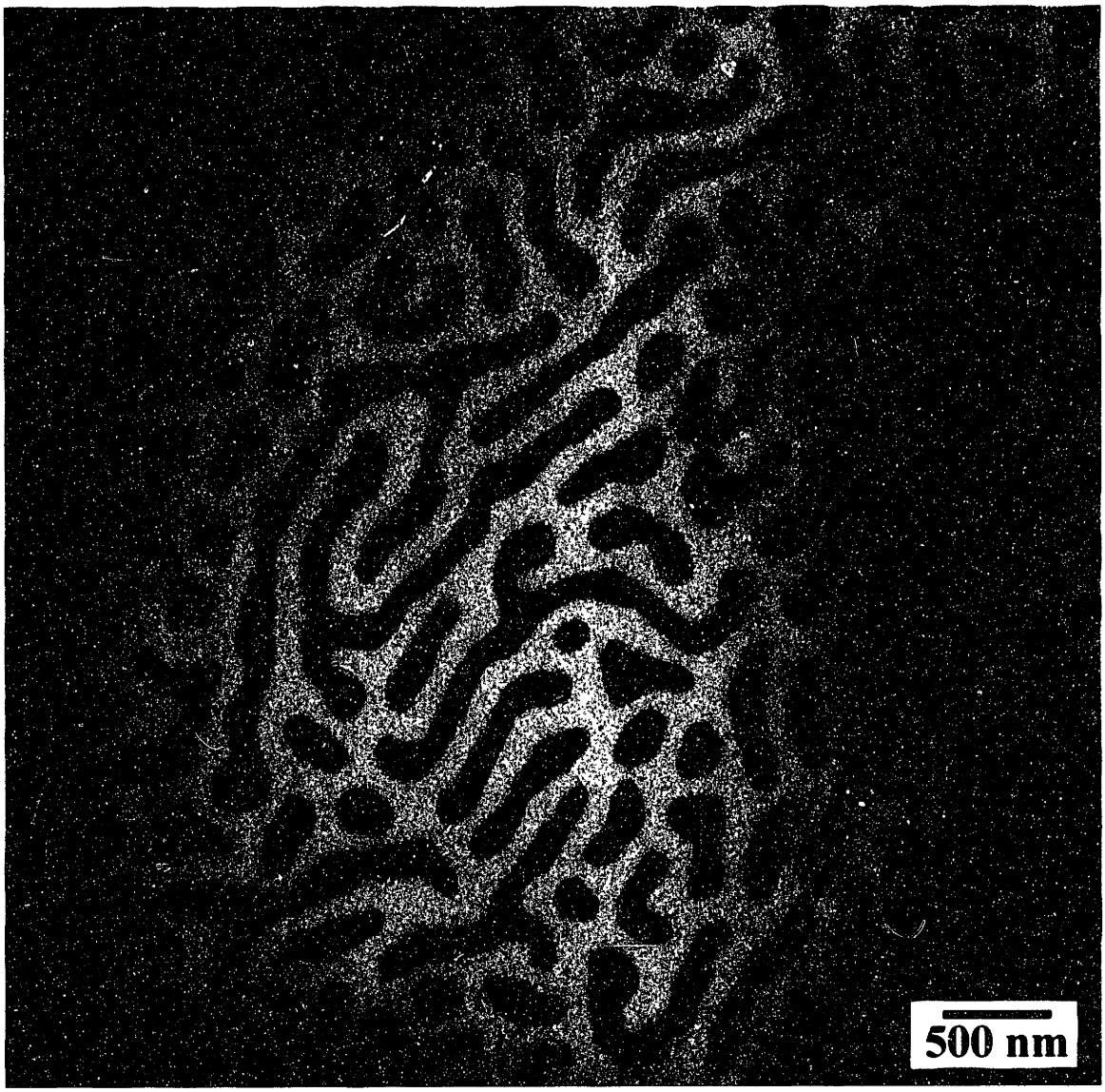

Figure 2.20 **Bright–field TEM micrograph of an ultrathin film of SI500/500. The PI (dark) domains have been preferentially stained with OsO_4.**

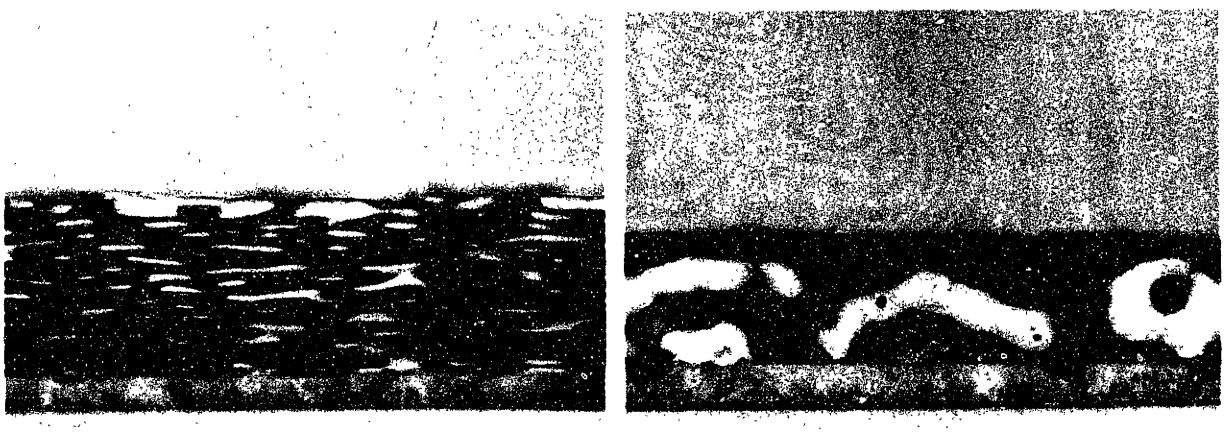

Figure 2.21 **Cross–sectional bright–field TEM micrographs of spin coated SI500/500 thin films which were examined (A) unannealed and (B) annealed for two days at 180°C in a vacuum sealed glass ampule. The PI (dark) domains have been preferentially stained with OsO_4.**

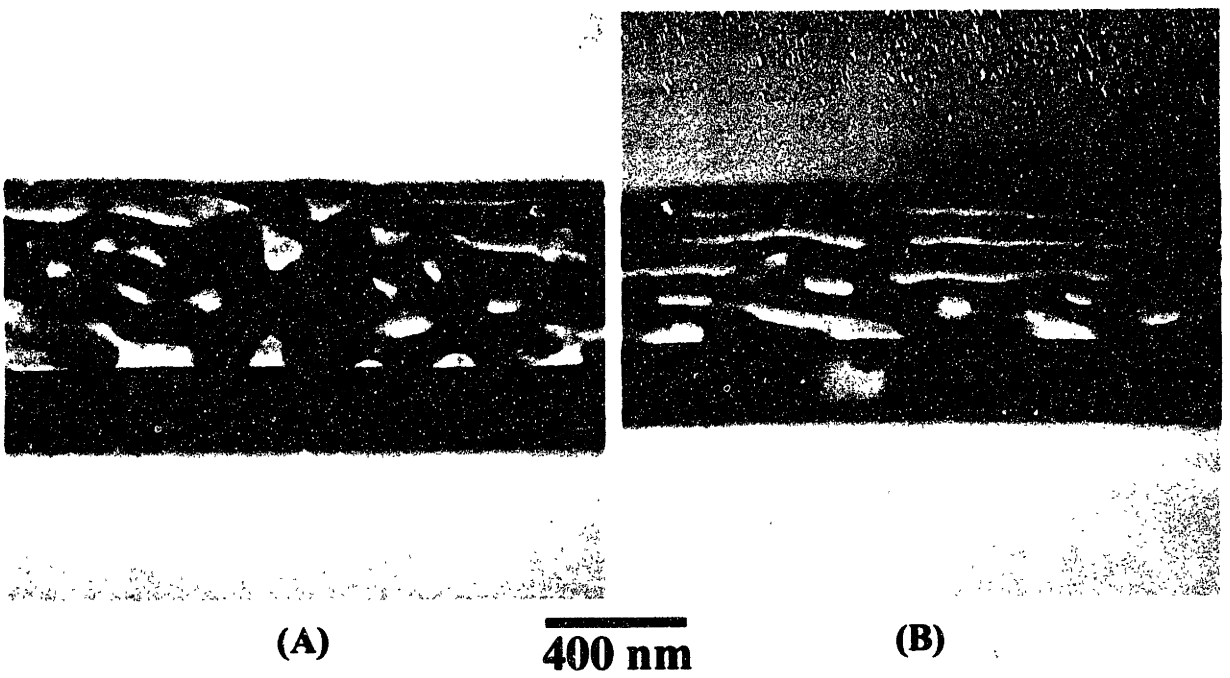

Figure 2.22 **Cross–sectional bright–field TEM micrographs of simple cast (SI500/500)/(dSI20/20) (13 wt% dSI20/20) thin films which were examined (A) unannealed and (B) annealed for two days at 140°C in a vacuum sealed glass ampule. The PI (dark) domains have been preferentially stained with OsO_4.**

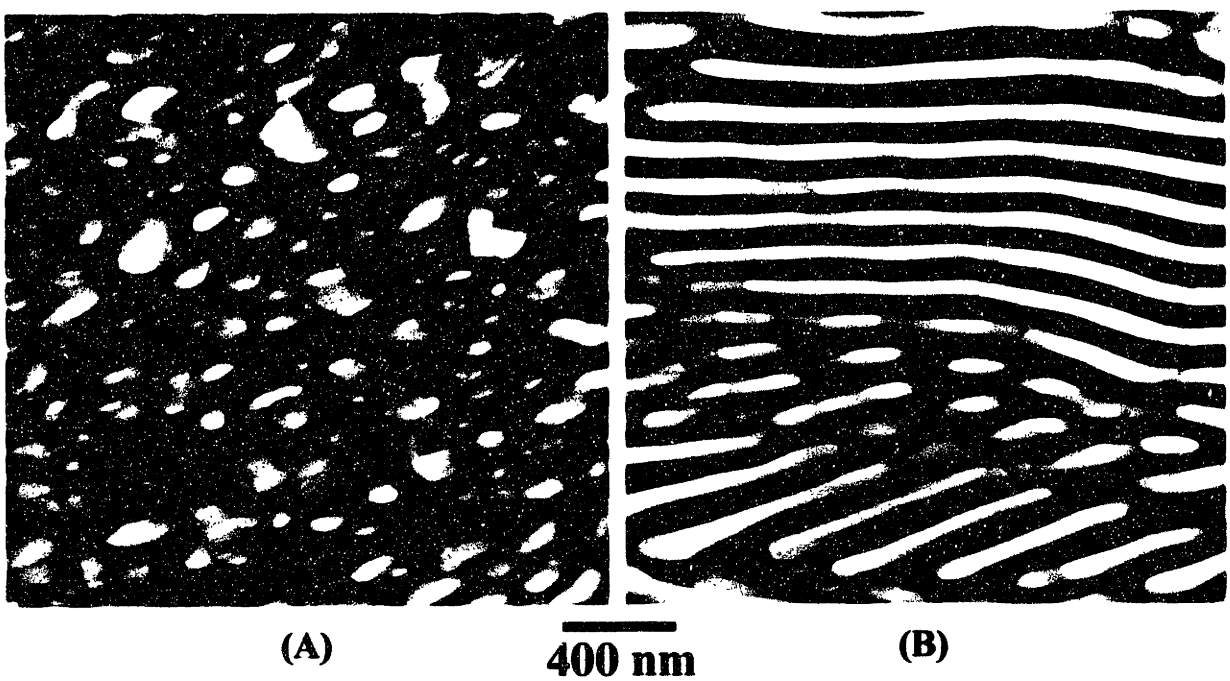

Figure 2.23 **Bright–field TEM micrographs of a bulk cast sample of SI500/500 (A) far from the surface and (B) near the surface of the film. The PI (dark) domains have been preferentially stained with OsO_4.**

Chapter 3: Rod-Coil Block Copolymers

3.1 Introduction

In Chapter 2, for coil-coil block copolymers, we saw how chemical incompatibility and molecular weight differences between the A and B blocks alone can result in a variety of one, two, and three dimensionally periodic microphase separated microstructures with very different optical properties. With our basic understanding of coil-coil block copolymers firmly established, we can now investigate how the incorporation of a liquid crystalline block into a block copolymer influences morphology. In a LC block copolymer, the two blocks are not only chemically incompatible but also conformationally different. One class of liquid crystal (LC) polymer is rodlike homopolymers. In contrast to flexible homopolymers, which obey Gaussian chain statistics and have persistence lengths of ~1 nm, rodlike polymers have nearly linear chain conformations and large persistence lengths ranging from 10 to 100 nm. The inherent chain stiffness of rodlike polymers causes them to form anisotropic LC phases in solution [86] in which the molecules are oriented locally along a preferred direction described by the director $\hat{\mathbf{n}}$. The phase behavior of rodlike polymers can be controlled by either temperature (thermotropic) or solvent concentration (lyotropic). AB diblock copolymers consisting of a rigid rod block and a flexible coil block, hereafter called rod-coil block copolymers, represent the extreme case in conformational asymmetry. The driving forces controlling the microphase separation behavior of rod-coil block copolymers are expected to be quite different from traditional flexible coil-coil block copolymers due to the mesogenic nature of the rod block. In these materials, the competition between the microphase separation of the coil and rod blocks into mesoscopically ordered periodic structures and the tendency of the rod block to form

anisotropic orientationally ordered structures can give rise to new morphologies. In this chapter, we describe the morphologies formed by a novel series of poly(hexyl isocyanate-b-styrene) rod-coil block copolymers. In addition, the process by which these morphologies form will be explored.

3.2 Background and Previous Work

3.2.1 Previous Experimental Work

In comparison to the numerous studies carried out on coil-coil diblock copolymers and rodlike homopolymers, only a few experimental studies have been performed on the microphase separation characteristics of rod-coil block copolymers in recent years. Historically, rod-coil-(rod) diblock and triblock copolymers with polypeptide rod blocks were the first type synthesized. The polypeptide-containing block copolymers were studied as model biological and biocompatible materials. X-ray diffraction and TEM studies showed that the rod-coils all formed lamellar morphologies [87-91]. In addition, one of the studies [91], which involved hydrophobic-hydrophilic polypeptide rod-coil block copolymers with coil volume fractions ranging between approximately 25-40%, showed that the rods were tilted between 15°-70° with respect to the lamellar normal and that the tilt angle increased with water content. The rod-like polypeptide chain had an α-helical conformation in all of these studies. Polypeptides, however, can also undergo various types of folding and are difficult to synthesize using traditional polymer synthesis techniques with narrow molecular weight distributions which makes them less attractive and somewhat problematic as model rod-coil materials. More recently, a low molecular weight ($N \sim 100$, $N_{rod} = 1$) monodisperse coil-rich rod-coil diblock copolymer series was anionically synthesized ($f_{rod} = 0.19$ to 0.36) [92, 93] and found by TEM to form new thin

film morphologies ranging from discrete aggregates to alternating strips with increasing rod content. The rod block, however, was not observed to have a pronounced effect on the global microstructure. None of the above studies involved rod blocks which were both rigid and polymeric (i.e. a high degree of polymerization, N_{rod}). As a result, more studies are needed on high molecular weight samples which span a wide range of rod volume fraction to be able to systematically map out the phase behavior of rod-coil diblocks.

3.2.2 Previous Theoretical Work

Significant theoretical work on rod-coil systems has lagged behind experimental studies for the most part. In the earliest theoretical work by Semenov and Vasilenko [94], a mean-field theoretical approach was used to study the stable phases and phase transitions which occur in rod-coil block copolymer melts. In addition to a nematic phase at low χN, monolayer and bilayer smectic A phases were predicted to exist for increasing degrees of segregation. The nematic-smectic A transition was found to be first-order and second-order in the cases of low and high rod volume fraction, respectively. The existence of a smectic C phase was speculated for $f_{rod} < 0.36$. Later work by Halperin on the aggregation behavior of rod-coil solutions in a solvent preferential for the coil block [95, 96] also predicted a smectic A-smectic C transition for high coil content. More recent work on the phase behavior of rod-coils has predicted not only the familiar lamellar phases but the stability of monolayer and bilayer "hockey puck" micelle phases for sufficiently low χ and rod volume fraction [97]. In these morphologies, the micelles consist of an inner core composed of either a monolayer or bilayer of rods which is surrounded by a corona of coils. Theoretical treatments of coil-rod-coil triblock copolymers [98, 99] have also predicted the possibility of "fence", and "needle"

morphologies. In a fence, m_1 (m_1 is an integer) rods are aggregated in a single row with a width equal to the width of a single rod. At the top and bottom of the fence, the coil blocks form tethered brushes. The rods can, in general, be tilted with respect to the rod/coil interface. In contrast, a needle is a (parallelepiped-shaped) aggregate of m_1m_2 rods with dimensions normal to the rod axis of m_1a and m_2a, where a is the width of a rod and m_1 and m_2 are integers, respectively. For the most part, the theories described above treat the aggregation of rod-coil block copolymers in a strictly geometrical fashion. Clearly, a rigorously valid theory that successfully treats the orientational ordering of the rod block and explains the underlying physics of rod-coil aggregation is still needed. A theory recently developed by Gurovich [100], however, which treats the microphase separation of LC diblock copolymer melts near the spinodal, makes significant progress toward a complete theory of rod-coil self-assembly. More details of this theory will be discussed later in the chapter.

3.3 Synthesis and Characterization

In this study, a series of high molecular weight rod-coil diblock copolymers having a PS coil block and a main-chain poly(hexyl isocyanate) (PHIC) rod block (see Figure 3.1) were synthesized anionically via sequential polymerization techniques. The synthesis of the rod-coil block copolymers was performed in the lab of Professor Chris Ober at Cornell University by Dr. Seung Hwang and Guoping Mao. Homopolymer PHIC is known from numerous studies [101-105] to be a lyotropic nematic LC and to behave as a stiff rod in a wide range of solvents with a persistence length of about 50-60 nm. The inherent chain stiffness of PHIC arises primarily from short-range interactions which restrict rotation along the backbone and is unaffected by long-range forces. In addition,

PHIC adopts a 12_5 helical conformation [106] and is three dimensionally crystalline in the solid state.

All the chemicals needed in the synthesis of the rod-coils were purchased from Aldrich Chemical Company, Inc. (Milwaukee, WI) except where noted. Prior to use, the solvents tetrahydrofuran (THF) and toluene were dried by distilling from Na/benzophenone (deep purple color). The styrene monomer was distilled over CaH_2 and stirred over di-butyl magnesium (bright greenish color) for 12 hours. The n-hexyl isocyanate (HIC) monomer, purchased from Eastman Chemical Company (Kingsport, TN), was distilled over CaH_2 after stirring overnight and then distilled from Et_3Al (bright orange yellow color). Depending on the desired composition of each rod-coil, a mixture of THF and toluene were used in the synthesis because PHIC is not completely soluble in THF. The use of the nonpolar solvent toluene, however, required that the PS polymerization take place at 25°C for some of the rod-coil syntheses to increase the polymerization kinetics. The exact conditions used for each rod-coil diblock copolymer synthesis and initial target compositions, f_{PHIC}^{Target}, are listed in Table 3.1. The poly(hexyl isocyanate-b-styrene), P(HIC-b-S), rod-coil block copolymers are designated HSx/y, where x and y are the M_w of the PHIC and PS blocks in units of 1 kg/mol, respectively.

Table 3.1 List of the conditions used for each rod-coil diblock copolymer polymerization. Data courtesy of Guoping Mao.

Sample	Toluene/THF (ml)	Initiator (ml)	S/HIC (ml)	T_{PS} /T_{PHIC} (°C)	t_{PS}/t_{PHIC} (hrs)	Yield after Fractionation (g)	f^{Target}_{PHIC}
HS73/104	200/50	0.06	8.10/2.00	-78/-78	16.0/36.0	0.02	0.1
HS36/14	90/54	0.20	2.75/5.50	-78/-78	4.0/2.5	2.00	0.6
HS58/7	250/150	0.20	3.00/27.00	-78/-78	24.0/2.0	6.00	0.7
HS245/9	300/0	0.20	3.00/7.00	25/-78	6.0/12.0	3.30	0.9
HS386/7	120/0	0.19	2.20/5.00	25/-78	9.0/48.0	3.57	0.9

In general, the following steps were used in each synthesis. Under nitrogen protection, the reaction flask was cooled down to the appropriate temperature and the initiator sec-ButylLi (1.3M in hexane) injected into the flask (greenish color appeared). To begin the polymerization, styrene monomer was added dropwise via a cannula (bright orange-red color appeared) to the reaction flask while stirring vigorously. Once the PS polymerization was completed, 1 ml of the solution was removed via a cannula for characterization of the PS block. At this point, HIC monomer was then added to the living PS solution using a cannula (the orange red color disappeared and a very light greenish color appeared). The polymerization was terminated by adding 1 ml of anhydrous methanol to the solution. Afterwards, the polymer solution was then precipitated in 500 ml of MeOH, filtered, and dried. Depending on the initial PS homopolymer content, the rod-coils were fractionated with ethyl acetate, THF and isopropanol to remove the PS homopolymer impurity.

Gel permeation chromatography (GPC) carried out by Dr. Lewis Fetters at Exxon Research and Development and nuclear magnetic resonance (NMR) carried out by

Guoping Mao at Cornell University were used to determine the molecular weight and composition of each rod-coil block copolymer, respectively. GPC was performed in THF using a Waters 150 GPC equipped with a Philips refractive index detector. A flow rate of 1 ml/min and six 30 cm linear Ultrastyragel columns with mixed pore sizes (10 to 10^5 nm) were used. Mondisperse PS standards were used for column calibration. ^{1}H NMR data was collected from a Varian 200 using $CDCl_3$ as the solvent. The resulting molecular weight characteristics and composition of each rod-coil sample (volume fraction of PHIC f_{PHIC}) are tabulated in Table 3.2.

Table 3.2 Molecular weight characterization data for the P(HIC-b-S) diblocks obtained from GPC and NMR. NMR data courtesy of Guoping Mao.

Sample	Total M_w (g/mol)	M_w/M_n	Molar Ratio PHIC:PS	M_{PHIC} (g/mol)	N_{PHIC}	f_{PHIC}	M_{PS} (g/mol)	N_{PS}	PS M_w/M_n
HS73/104	240,000	1.11	1:1.734	73,000	575	0.42	104,000	1000	1.05
HS36/14	68,000	1.40	1:0.477	36,000	283	0.73	14,000	135	1.04
HS58/7	222,000	1.86	1:0.138	58,000	457	0.90	6,600	63	1.08
HS245/9	1,819,000	2.52	1:0.046	245,000	1929	0.96	9,300	89	1.04
HS386/7	1,426,000	3.11	1:0.022	386,000	3039	0.98	7,100	68	1.04

Column 2 and 3 list the total M_w's and polydispersities of the rod-coil diblocks obtained from GPC which were determined relative to a PS (Gaussian coil) standard. For a discussion of how the GPC chromatographs were analyzed, see Appendix 5. The high polydispersities as compared to those typically obtained from anionic polymerization reflect the significant difficulties involved with the synthesis of the PHIC block. In particular, PHIC has the tendency to undergo a back biting reaction and is extremely

difficult to purify. As a result, the molecular weight of the PHIC block and the rod composition of the rod-coils was always much higher than expected.

Because the hydrodynamic volume has a stronger molecular weight dependence for a rodlike polymer than a coil-like polymer, the total rod-coil M_w's obtained from GPC significantly overestimate the true values. This effect is particularly noticeable for the samples HS245/9 and HS386/7 which have apparent total molecular weights in excess of one million g/mol. In addition, the uncertainty in the molecular weights for HS245/9 and HS386/7 is greater because their apparent M_w's (greater than 1,000,000 g/mol) are comparable to or greater than the highest molecular weights resolvable by the Ultrastyragel columns used during GPC. The tabulated polydispersities and total molecular weights are therefore useful only for comparison between the various rod-coils. More reliable absolute values of the PHIC block molecular weights (column 5) were determined, however, from NMR data and the PS block molecular weights obtained from GPC. Unfortunately, the extremely low PS:PHIC molar ratio for HS245/9 and HS386/7 limits the accuracy of the PHIC molecular weights and measured compositions for these samples to within ~10%.

To independently check the PHIC block molecular weights, light scattering and GPC were performed on two homopolymer PHIC samples to obtain an approximate calibration curve. The light scattering was done by Tom Mourey at Kodak. The molecular weight characteristics relative to a PS standard for each homopolymer were found to be M_w = 164,000 g/mol and M_w/M_n = 2.11 and M_w = 373,000 g/mol and M_w/M_n = 4.10, respectively. The lower molecular weight PHIC was anionically synthesized following the same steps outlined above for the rod-coil diblocks. The higher PHIC was commercially synthesized and purchased from Polysciences, Inc. (Warrington, PA). For the rod-coil samples with $f_{PHIC} > 0.90$, the PHIC block molecular weights determined from the calibration curve showed fair agreement with the tabulated

values. GPC was also used to determine the approximate PS homopolymer (premature termination) content in the rod-coil samples. After fractionation, the amount of homopolymer PS was less than 2 wt% in all of the rod-coil samples.

3.4 Sample Preparation

Concentrated rod-coil solutions were prepared in toluene (preferential for the PS block) to investigate the lyotropic behavior of the rod-coil diblocks as compared with that of pure PHIC homopolymer. The commercially synthesized PHIC homopolymer was used for comparison purposes. In previous studies of the lyotropic behavior of homopolymer PHIC [103-105], in a range of solvents, the critical concentration for the onset of liquid crystallinity (at room temperature) was found to vary between 15 and 25 wt% for molecular weights between 65,000 and 75,000 g/mol. The critical concentration also decreased with molecular weight. As a result, 5 wt% solutions of the PHIC homopolymer and the rod-coil samples HS73/104, HS36/14, and HS58/7 were prepared so that the transition from the isotropic to liquid crystalline phase could be observed easily. For the two remaining high molecular weight rod-coils, 0.05 wt% solutions were prepared.

Ultrathin samples (~50 nm thick) of the rod-coils, which were cast from dilute 0.05 wt% solutions in the solvents toluene, CCl_4 (nonpolar solvent preferential for PHIC), or $CHCl_3$ (nonpreferential polar solvent), were used in the investigation of the microphase separated morphologies formed in the solid-state. These films were studied using TEM, selected-area electron diffraction (SAED), and atomic force microscopy (AFM). The method used to make the thin films is essentially identical to that described in Chapter 2 for the SI500/500 thin film samples. Solvent annealing, however, was

employed exclusively for the rod-coil samples in place of high temperature annealing because PHIC is thermally sensitive and undergoes an unzipping reaction which results in significant mass loss for typical annealing temperatures of 120°C. In addition, to increase the mass-thickness contrast between the PS and PHIC domains in the TEM, the rod-coil samples were stained in RuO_4 vapors, which preferentially stains PS, for 15 to 20 minutes. AFM samples were imaged unstained.

In order to obtain more information about the three dimensional structure of the rod-coil morphologies, thick samples were prepared. In particular, thicker films of HS73/104 (~250 nm) and HS245/9 (~1000 nm) were cast from 0.05 wt% and 0.15 wt% solutions in toluene for cross-sectional TEM experiments, respectively. Using a micropipet, 20 μL drops of the rod-coil solutions were placed on 1 cm by 1 cm carbon coated mica substrates and allowed to evaporate slowly overnight in a solvent saturated petri dish. After drying in a vacuum oven for an hour, the films were floated off on distilled water, picked up on copper TEM grids, and stained in RuO_4 vapors for 15 to 20 minutes. For cross-sectional microtomy, the grids with the rod-coil films were then carbon coated for protection, embedded in Medcast™ Quik-mix (medium) brand epoxy monomer (purchased from Ted Pella, Inc., Redding, CA), and cured overnight in an oven at 80°C. Following the usual procedure (see sample preparation of SI500/500 thin films in Chapter 2), cross-sectional sections of the rod-coil films were obtained by microtoming, stained a second time, and lightly carbon coated prior to examination in the TEM. In addition to the these two rod-coil samples, a bulk film (~1 mm thick) of HS58/7 was also cast. A 5 wt% solution in toluene was cast in a Teflon dish and allowed to evaporate slowly for five days. After drying for three days in a vacuum oven, a piece of the film was cut off and embedded in epoxy. The cured epoxy block was then microtomed (see sample preparation of SI500/500 bulk film in Chapter 2) at room

temperature to obtain sections suitable for TEM. Sections were stained in RuO_4 vapors for 5 minutes prior to use.

In addition to the rod-coil samples used for the microscopy studies, samples of HS58/7 were made for wide-angle X-ray diffraction studies (WAXD). Films (~1 mm thick) identical to the bulk sample described above were slow cast from 5 wt% solutions in toluene. Fiber samples (~100 μm in diameter) were prepared by first heating a few drops of a 5 wt% solution in toluene to ~100°C on a hotplate. After most of the solvent had evaporated, tweezers were then used to pull small fibers from the melt.

3.5 Experimental Techniques

Several experimental techniques were used to study and characterize the P(HIC-b-S) rod-coil block copolymers. Polarized optical microscopy (POM) of the concentrated rod-coil and PHIC solutions was performed under crossed polarizers using a Carl-Zeiss Axioskop. Small drops of the solutions were placed on glass slides and viewed as is or after shearing with a razor blade. The maximum magnification achievable was obtained using a 100x objective. Under crossed polarizers, an isotropic sample does not allow any light to be transmitted and consequently appears dark. Conversely, optically anisotropic liquid crystalline domains appear light because they can allow a component of light to be transmitted which is polarized along the analyzer. For a highly oriented liquid crystal phase, maximum transmitted intensity occurs when the orientation direction is at 45° to both the polarizer and analyzer. POM was therefore used to see whether the rod-coil solutions could form anisotropic LC phases and to investigate the textures and defects present in the LC state.

Bright field transmission electron microscopy (TEM) was the primary experimental tool used to determine the microphase separated morphologies formed by the rod-coil diblock copolymers in the solid-state. Thin film, cross-section, and bulk samples were examined using a JEOL 200CX operated at either 100 kV or 200 kV depending on the contrast present in each sample. Early TEM experiments showed that the PHIC block was extremely beam sensitive. At an operating voltage of 200 kV, the electron beam lifetime of the PHIC crystals was about 1/3 that of a stretch-oriented polyethylene (PE) film. Using the known value for the maximum beam dosage of PE at 200 kV and 20°C, the maximum beam dosage for the PHIC is estimated to be ~$5*10^{-3}$ C/cm^2. As a result, standard low-dose techniques were employed (see the description given in Chapter 2) in the operation of the microscope. In addition to the real space investigations of the rod-coil morphologies using TEM, selected-area electron diffraction (SAED) was used to study both the orientation of the rods with respect to the microphase separated microstructures and the crystallinity of the rod block. Camera constants ranging from 55-137 cm were typically used to help resolve the high-Q or low-Q reflections, respectively. During SAED, the coherence of the electron beam was increased by underfocusing C2 and low-dose techniques were used as well. Additional information on the crystal structure of the PHIC block was provided by WAXD powder patterns of bulk films obtained on a Rigaku RU-300 rotating anode diffractometer and fiber patterns obtained on a sealed tube Enraf Nonius Diffractis 583 X-ray diffractometer (operated at 40 kV and 26 mA) both employing Ni-filtered 1.54 Å CuKα X-rays. X-ray patterns for the bulk films and fiber samples were recorded using a linear position sensitive detector and Statton camera equipped with Kodak film, respectively.

AFM was used to determine the surface structure of the rod-coil block copolymer films in order to better understand the internal microphase separated morphologies observed by TEM. In particular, a Digital Instruments, Inc. Multimode AFM with

Nanoscope III controller was operated in tapping mode [107]. Unstained rod-coil thin film samples were imaged under ambient conditions using either 125 μm or 226 μm long etched silicon cantilever substrates having spring constants ranging from 16.0 to 88.0 N/m and 1.7 to 4.3 N/m and resonant frequencies of ~300 kHz and ~70 kHz, respectively. Height images ranging in size from 1 μm by 1 μm to 2.5 μm by 2.5 μm in size were obtained at scan rates per line of 1-3 Hz. For those interested, a detailed discussion is given in Appendix 6 on the principles behind a variation of AFM called force modulation microscopy (FMM) and the use of FMM in the study of block copolymer surface morphology.

3.6 Results and Discussion

3.6.1 Polarized Optical Microscopy Studies

Using POM, optically birefringent textures were observed to develop in all of the P(HIC-b-S) rod-coil solutions as the solutions slowly evaporated, which is evidence of liquid crystalline ordering on the molecular scale. The similarity in the strength of the birefringence exhibited by the rod-coil and the PHIC homopolymer solutions suggests that the rod-coils undergo a isotropic-nematic transition with increasing concentration of polymer. If microphase separation of the rod-coils occurred directly from the isotropic state, the birefringence would be due entirely to form birefringence and would be much weaker. While HS73/104 formed a uniform birefringent texture (see Figure 3.2), the rod-coils HS36/14 and HS58/7 formed nonuniform textures containing numerous randomly oriented overlapping regions ~5 μm or less in size (see Figure 3.3). In contrast, solutions of the rod-coils HS245/9 and HS386/7 (M_{PHIC} > 200,000 g/mol) were found to form highly anisotropic birefringent textures consisting of long bands ~1 μm or less in width

and 10 μm or greater in length (see Figure 3.4). The characteristic sequence of transmitted light observed when the bands are rotated under crossed polarizers suggests that the orientation of the local director field undergoes a reorientation across the boundary between adjacent bands. The POM results clearly show that the P(HIC-b-S) rod-coils behave mesogenically despite the presence of the flexible PS coil block, which is particularly significant for HS73/104 (f_{PS} = 0.58). The orientational ordering of the PHIC block is thus a dominant factor in the self-assembly of these materials. In addition, high molecular weight (HS245/9 and HS386/7) rod-coils have the ability to spontaneously form macroscopically ordered structures on the micron length scale directly from solution.

3.6.2 Rod-coil Block Copolymer Morphologies

TEM was used to examine the solid-state morphologies of the rod-coils on the 10 nm to 100 nm length scale. The rod-coil HS73/104, which has a coil block significantly larger than its rod block (f_{PHIC} = 0.42), forms a microphase separated structure (in projection through the film) consisting of discontinuous lens-shaped PHIC (lighter) aggregates or domains ~60 nm in width which are surrounded by a continuous PS (darker because of RuO_4 staining) matrix (see Figure 3.5a). The rod-like nature of the PHIC block is reflected in the elongated shape and alignment of the PHIC domains. Cross-sectional TEM of thicker HS73/104 films provided more information about the three dimensional structure of the lenticular aggregate (LA) morphology (see Figure 3.5b). Figure 3.5b shows that the PS domains are indeed continuous and the PHIC domains discrete in nature. Given the PHIC M_{PHIC} of 73,000 g/mol and the monomer repeat distance of 1.95Å, the length of the rod block is predicted to be ~110 nm. Assuming

interdigitation, the PHIC rods are found on average to be tilted with respect to the IMDS normal by ~60°.

The lack of long range order in the LA morphology is most likely caused by reduced mobility of the rod-coils during microphase separation resulting from the entangled, high-viscosity 104,000 g/mol PS block. In order to test this hypothesis, ultrathin films of HS73/104 were cast and allowed to evaporate rapidly (few minutes). In principle, the rapid solvent evaporation causes the viscosity of the solution to increase rapidly which in turn leads to pinning of the rod-coil chains at the air and substrate surfaces effectively producing a kinetically trapped morphology. Indeed, TEM micrographs of the ultrathin films of HS73/104 show a dramatically different morphology (see Figure 3.6). The morphology consists of ellipsoidal-shaped PS domains which are elongated and oriented along the local PHIC director in a characteristically nematic-like texture. The departure from a spherical IMDS in the isolated PS domains is a clear manifestation of the influence of the orientational ordering of the rods on the flexible coil block. Although the nematic ellipsoid (NE) morphology is locally microphase separated, large scale self-assembly of the rod-coils into microdomains is prevented. As a result, the NE morphology provides further evidence that the rod-coil solutions pass through a isotropic-nematic liquid crystalline phase transition prior to microphase separation.

The two rod-coil diblocks, HS36/14 and HS58/7, have rod blocks significantly larger than their low molecular weight coil blocks (f_{PHIC} = 0.73 and 0.90, respectively) and both form a second type of rod-coil morphology. Figures 3.7a and 3.7b show the zig-zag (ZZ) lamellar morphology which consists of alternating PHIC and PS layers arranged in a unique zig-zag fashion. This morphology, which has not been observed previously in block copolymers, is also observed for bulk films as well (see Figure 3.8). In the ZZ morphology, the rods exhibit long-range orientational order (over several microns) which is manifested by the high degree of correlation observed between adjacent domains. In

addition, SAED patterns (see Figure 3.7b inset) show that the chain axis of the PHIC rods, $\hat{\mathbf{n}}$, is tilted with respect to the lamellar normals, $\hat{\mathbf{p}}$, by ~45° in both zig-zag morphologies and that the PHIC domains are three dimensionally crystalline. An in depth explanation of how the crystal structure and helical conformation of the PHIC block was determined using SAED and WAXD is given in Appendix 7. In addition, Appendix 7 shows how SAED and TEM were used to deduce the orientation of the PHIC block with respect to the zig-zag layers. The ZZ morphology is essentially a smectic C phase because it exhibits both rod tilt and a layered structure. In addition, the formation of the two distinct sets of lamellae with equal but opposite orientations with respect to the director is consistent with the nucleation of a smectic C phase in a thin film (assuming the director is in the plane of the film).

Within the PHIC domains, the rods are believed to adopt a bilayer rather than an interdigitated packing arrangement. Low dose serial images show that the lighter area located halfway across the PHIC domains (e.g. Figure 3.7a) results from preferential mass loss due to beam damage. Because depolymerization is facilitated at the chain ends, the location of the mass loss is consistent with a bilayer arrangement of the rods. Further evidence for a bilayer model is provided by atomic force microscopy images of the ZZ morphology (see Figure 3.9). In the height images, the PS domains (dark) correspond to the ~7 nm deep troughs located between the higher PHIC domains (light). Numerous packing defects (see arrows) can also be seen in the middle of the crystalline PHIC domains. In contrast to the PS domains, height profiles taken across these areas show that these defects are only shallow ~3 nm depressions in the surrounding rod domains. Based on a bilayer model, the predicted PHIC domain spacings parallel to the chain axis of 110 and 180 nm are found to be in good agreement with the average domain spacings measured from TEM of 120 and 190 nm, respectively.

The remaining rod-coils, HS245/9 and HS386/7, which both have a short PS coil block and a very long PHIC rod block (f_{PHIC} = 0.96 and 0.98, respectively), form a third alternating layer-type morphology. The microphase separated morphology (see Figures 3.10a and 3.10b) exhibits long-range order over tens of micrometers in comparison to most self-assembling polymers as was also observed in the POM results. In addition, the PS block forms unique arrowhead-shaped domains whose orientation flips by 180° between adjacent PS-rich layers. The apparent volume fractions of PS in the arrowhead (AH) morphologies are much larger than what would be expected from the composition data (see Table 3.2). As mentioned earlier, however, only approximate values of the composition could be obtained for the rod-coils HS245/9 and HS386/7 from NMR given the extremely small PS:PHIC monomer ratio. Cross-sectional TEM images (see Figure 3.11) show that, in three dimensions, the AH morphology is a lamellar structure which continues through the entire film (~1 μm). SAED patterns (see Figure 3.10a inset) of the AH morphology show a superposition of two distinct single crystal-like PHIC patterns rotated relative to each other by an angle $\alpha \approx 90°$, which indicates that the PHIC chain axis, $\hat{\mathbf{n}}$, alternates its orientation with respect to the layer normals, $\hat{\mathbf{p}}$, by about 45° and -45° in adjacent layers. This chevron-like arrangement of the rods causes the PS arrowheads to be concentrated in the relatively narrow (high energy) interfacial region separating adjacent PHIC domains where the local director abruptly changes its orientation. AFM images of the AH morphology (see Figure 3.12) confirm the presence of the PS ellipsoids, arrowheads (see arrows), and also the alternating orientation of the PHIC director.

A structure like the AH morphology has not been previously observed in block copolymers. However, smectic mesophases in which the director orientation flips from layer to layer have been observed in small molecule LC's for racemic mixtures of chiral molecules [108-112]. These mesophases were given the name smectic O. Orientational

phase transitions between the smectic O and the smectic C were also observed with increasing temperature or applied electric field strength. Currently, however, a theory still does not exist which explains why the smectic O structure forms in small molecule liquid crystals. As a result, it may also be some time before a suitable theory is developed to explain the fundamental reasons for the formation of the AH morphology.

In terms of rod packing within the PHIC domains, a bilayer model and an interdigitated model are found to be most consistent for HS245/9 and HS386/7, respectively. Given the M_{PHIC}'s listed in Table 1 for HS245/9 and HS386/7, the predicted PHIC domain spacings (parallel to the chain axis) of 750 and 590 nm agree quite well with the average values obtained from TEM of 740 and 550 nm, respectively. For HS245/9 and HS386/7, however, the large polydispersities did give rise to variations in the observed domain size in some areas of the sample (see Figure 3.13). In some areas of the samples, variations in domain size gave rise to unique edge dislocations (see upper right corner of Figure 3.13). An edge dislocation is always accompanied by the creation of two PS arrowhead layers which share the same orientation. Given the significant difficulties involved in the molecular weight determination of high molecular weight rodlike polymers, molecular weights based on TEM measurements may offer a more accurate and easy alternative. In addition to variations in domain size, polydispersity in the rod-coils HS245/9 and HS386/7 is evident by the numerous PS ellipsoids (similar to those observed in the NE morphology) within the PHIC domains which are oriented along the local director.

In addition to being orientationally ordered, the rods in all of the rod-coil morphologies were tilted with respect to the normal of the intermaterial dividing surface (IMDS) separating the rod and coil domains. Unlike coil-coil diblock copolymers, rod-coils have significant packing problems in the microphase-separated state. The area per chain of the PHIC block is approximately 1 nm^2 (estimated from crystal structure

information of PHIC, see Appendix 7) and is independent of the rod molecular weight. The area per chain of the PS coil, however, varies as $M_{PS}^{1/3}$ ($0.14M_{PS}^{1/3}$ nm^2 for strongly segregated lamellar polystyrene-polydiene diblocks) in the strong segregation limit. As a result, at the IMDS, the relatively smaller area per junction favored by the rod block results in significant chain stretching of the coil block which is energetically unfavorable. Two ways in which the rods can increase their area per junction while still maintaining constant density are to tilt at the IMDS and to interdigitate.

How can one determine the tilt angle adopted by a rod-coil block copolymer? According to work by Halperin [95], the free energy of a single rod-coil layer in a solvent preferential for the coil block is composed of two competing terms: an interfacial energy term and a deformation term caused by the chain stretching of the coil block away from the IMDS. Allowing the rods to tilt causes the interfacial area between the rod and coil domains to increase which is energetically unfavorable (see Figure 3.14). The larger area per chain, however, relieves chain stretching of the coil block causing a reduction in the free energy. The free energy as a function of the tilt angle, θ, can be written in the following general form which applies to both an interdigitated and a bilayer arrangement of rods.

$$F(\theta) \sim \gamma\sigma(1 + \tan\theta) + kTN_{coil}\left(\frac{a^2}{\sigma}\cos\theta\right)^{5/6} \qquad (3.1)$$

In Equation 3.1, γ, σ, a, and N_{coil} are the surface tension at the rod-coil interface, the area per chain for untilted rods, the characteristic size of the coil monomer, and the degree of polymerization of the coil block, respectively. The free energy equation can be rewritten in terms of a parameter δ which is simply the ratio of the interfacial to deformation free energy terms at zero tilt. When $\delta > \sim 1/3$, interfacial energy dominates and untilted rods are stable. Conversely, when $0 < \delta < \sim 1/4$, chain stretching becomes

dominant and a tilted rod phase becomes stable. In this regime, the equilibrium tilt angle increases for smaller δ and is determined by minimizing the free energy with respect to the θ.

While qualitatively correct in many ways, Halperin's theory does not successfully address all aspects of rod tilt observed in the P(HIC-b-S) rod-coils. Specifically, why is the tilt angle approximately the same for the zig-zag and the arrowhead morphologies if the PS molecular weights differ? An examination of Figure 3.14 shows that tilt of the rod blocks is equivalent to a successive translation along the rod chain axis between adjacent rods. As solvent evaporates, the PS coil block becomes less swollen and the average translation along the PHIC chain axis is expected to decrease continuously. Halperin's theory, however, eventually breaks down for the P(HIC-b-S) system. When the rod-coil solutions become highly concentrated, the PHIC crystallizes. As a result, in order to preserve translational symmetry and avoid a large lattice strain energy penalty within the rod domains, the translation of adjacent unit cells must be equal to nc where n is an integer and c is the c axis repeat distance of the unit cell (see Figure 3.15). Similarly, the allowed tilt angle θ also becomes quantized. Therefore, when crystallization of the PHIC block occurs, the rods adopt the crystallographically allowed tilt angle which is nearest to the minimum free energy tilt angle. Using the lattice constants of the PHIC unit cell (see Appendix 7), the allowed tilt angles for P(HIC-b-S) rod-coils can be shown to be θ = 50.0°, 67.2°, and 74.4° for n = 1, 2, and 3, respectively. The predicted tilt angle of 67.2° is similar to the tilt angle determined for the LA morphology of 60°, which is the largest tilt angle measured for all the rod-coil morphologies. Intuitively, one expects HS73/104 to have the largest tilt angle given its high molecular weight PS block. The predicted tilt angle, θ = 50.0°, which is the smallest allowed tilt angle, agrees well with the tilt angles measured for the two ZZ morphologies. The corresponding zig-zag angle of $\alpha = \pi - 2\theta$ = 80.0° is well within the range of experimentally observed values which from 67° to 105°.

Similarly, the tilt angles measured for the two AH morphologies also agree well with θ = 50.0°.

Using the TEM, SAED, and AFM results, schematic molecular models (see Figure 3.16) were constructed for the LA, ZZ, and AH rod-coil morphologies which illustrate how the P(HIC-b-S) chains pack together. Inspection of the schematic models reveal some characteristics which are common to all of the rod-coil morphologies. Namely, each morphology is a microphase separated structure consisting of PS and PHIC domains. The LA morphology has nematic order whereas the ZZ and AH morphologies have smectic order. Within the PHIC domains, the rods are orientationally ordered (i.e. liquid crystalline) and have a common director. In addition, rod tilt with respect to the IMDS is observed for all the morphologies. The similarities between the final solid-state morphologies are important because they provide valuable clues to the underlying process which controls the self-assembly of rod-coil block copolymers.

3.6.3 Formation of Rod-coil Morphologies

In addition to the rod-coil morphologies themselves, previous rod-coil theories suggest a pathway by which the microphase-separated P(HIC-b-S) morphologies form. In coil-coil block copolymers, solvent and temperature influence χ in similar ways. From the isotropic state, lowering temperature or increasing block copolymer concentration by solvent evaporation increases the incompatibility between blocks which results in microphase separation. For P(HIC-b-S), however, a competition exists between the onset of liquid crystallinity and microphase separation. Rod-coil theories have predicted that the isotropic solution will first form a homogeneously mixed nematic phase (with the rods orientationally ordered) prior to microphase separation. This sequence is also supported by the POM results. In the nematic state, the rods and coils are intimately

mixed. Eventually, the incompatibility of the rod and coil blocks drives the nematic P(HIC-b-S) solutions to microphase separate (forming a smectic phase) into the orientationally ordered morphologies (LA, ZZ, and AH). When the solvent is completely removed, the PHIC domains crystallize and lock in the microphase-separated structures.

Based on this discussion and the experimental results, a schematic morphology diagram in the variables χN and f_{PHIC} can be constructed for the P(HIC-b-S) rod-coil system (see Figure 3.17). The points indicate the locations of the five rod-coil diblock copolymers scaled relative to their total molecular weights. In the disordered state for low χN, the rod-coils form a homogeneously mixed nematic phase. Above the spinodal, in the ordered region of the morphology diagram, the rod-coils microphase separate into the three experimentally observed orientationally ordered phases, LA, ZZ, and AH, which depend on the rod volume fraction. The locations of the vertical orientational phase transitions separating the morphologies are approximate. The shaded region indicates the region of the morphology diagram which has not been experimentally investigated yet.

The experimental morphology diagram shown in Figure 3.17 is appropriate for the P(HIC-b-S) rod-coils cast from toluene. As is the case for lyotropic LC's, the sequence of phases formed by the rod-coils is determined to a large extent by the solvent quality. In rod-coils, solvent quality influences self-assembly in complex ways. The intermolecular interactions between the PHIC rods, which control the liquid crystalline ordering of the rod block, are screened to a different extent depending on the solvent. In other words, the order in which the PHIC LC transition and the microphase separation transition occur is solvent dependent. In addition, the relative importance of interfacial energy to coil deformation (Halperin's δ parameter) in the free energy is influenced by solvent through changes in the surface tension γ and the extent to which the solvent swells the PS block. Solvent-induced changes in the morphology of rod-coils were observed experimentally for the rod-coil HS58/7 by casting additional samples from CCl_4

(preferential for the PHIC) and $CHCl_3$ (nonpreferential). Figures 3.18a and 3.18b show the morphologies obtained for CCl_4 and $CHCl_3$, respectively. In contrast to the well-ordered ZZ morphology formed from toluene, the sample cast from CCl_4 consists of highly fragmented PS zig-zags and micelles which no longer forms smectic layers. In addition, SAED patterns show the PHIC domains to be randomly oriented. The sample cast from $CHCl_3$ shows a morphology intermediate to the toluene and CCl_4 samples.

3.6.4 Comparison with Theoretical Predictions

While some aspects of the self-assembly of the P(HIC-b-S) rod-coils are predicted by previous theories, the overall agreement between the experimentally observed morphologies and the theoretically predicted ones is poor. In particular, the monolayer and bilayer lamellar smectic A phases predicted by Semenov and Vasilenko [94] or the monolayer and bilayer "hockey-puck" phases predicted by Williams and Fredrickson to exist over much of the rod-rich portion of the phase diagram [97] are not observed at all in the P(HIC-b-S) rod-coil system over the entire range of volume fractions studied (f_{PHIC} = 0.42 to 0.98). In addition, predictions that the tilted smectic C phase should exist for $f_{rod} < 0.36$ by Semenov and Vasilenko or that a smectic C phase is favored for high coil volume fractions by Halperin [95, 96] are contrary to our experimental findings. Furthermore, previous papers [94-99] did not specifically address the possibility of rod-coil morphologies such as the ZZ or the AH morphologies. The LA morphology, however, is similar to the "needle" morphology first proposed by Raphael and de Gennes for dilute solutions of coil-rod-coil triblock copolymers [98, 99]. Raphael and de Gennes predicted that for large coil blocks, long needles would result in which the length (normal to the rod axis) would tend to infinity while the width (also normal to the rod axis) would remain finite and approximately equal to the thickness of the coil brush. Experimentally,

the length of the lenticular PHIC aggregates is indeed much longer (~10x) than their width. While some similarities exist between the previous rod-coil theories and the P(HIC-b-S) experimental results, clearly more sophisticated theories are needed.

Recent work by Gurovich [100] on the phase behavior of LC diblock copolymer melts near the spinodal shows some promising improvements to previous theories. In this work, the χN versus f_{LC} phase diagram for an LC-coil diblock copolymer is predicted. The LC nature of the A block is treated in the theory through an orientational interaction which is approximated by a self-consistent molecular field. Although similar in many ways to the classical phase diagram of coil-coil diblock copolymers developed by Leibler [29], this LC-coil phase diagram exhibits several important differences (see Figure 3.19). In particular, at a temperature above the order-disorder temperature, a disordered homogeneously mixed nematic melt is predicted for $f_{LC} > 0.27$. When cooled, the homogeneously mixed nematic phase undergoes microphase separation into a smectic phase for $0.27 < f_{LC} \lesssim 0.77$. In this composition range, three new orientationally ordered smectic phases separated by orientational phase transition are predicted. The three phases in order of increasing f_{LC} are characterized by a local director which is oriented parallel (smectic A), tilted (smectic C), and perpendicular (no name) to the layer normal, respectively.

Although Gurovich's theory is not strictly valid for rod-coil diblock copolymers, the experimental results for the P(HIC-b-S) system (see Figure 3.17) are qualitatively more consistent with his phase diagram than the other proposed rod-coil phase diagrams [94, 97]. In particular, smectic morphologies in which the director is tilted with respect to the IMDS normal are predicted to exist over a large composition range in the ordered phase. Similarly, the LA, ZZ, and AH morphologies are all microphase separated structures which are characterized by rod tilt. In addition, the ZZ and AH structures are both smectic phases which are characterized by different orientational order of the rod

block. In terms of the disordered state, Gurovich's prediction of a homogeneously mixed nematic phase below the spinodal also agrees well with the POM and nematic ellipsoid results assuming solvent affects the χ parameter in the same way as temperature.

(A)

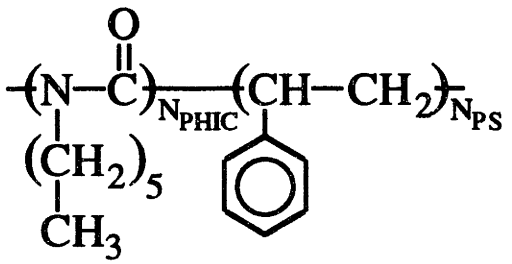

(B)

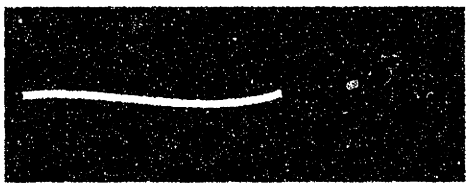

Figure 3.1 (A) Chemical formula of the P(HIC-b-S) rod-coil diblock copolymer. PHIC is the rigid rod block and PS the flexible coil block. The N_{PHIC} and N_{PS} values for the samples studied are listed in Table 3.2. (B) Schematic drawing of the rod-coil molecule in which the PHIC and PS blocks are depicted as a stiff rod-like chain and a Gaussian coil, respectively.

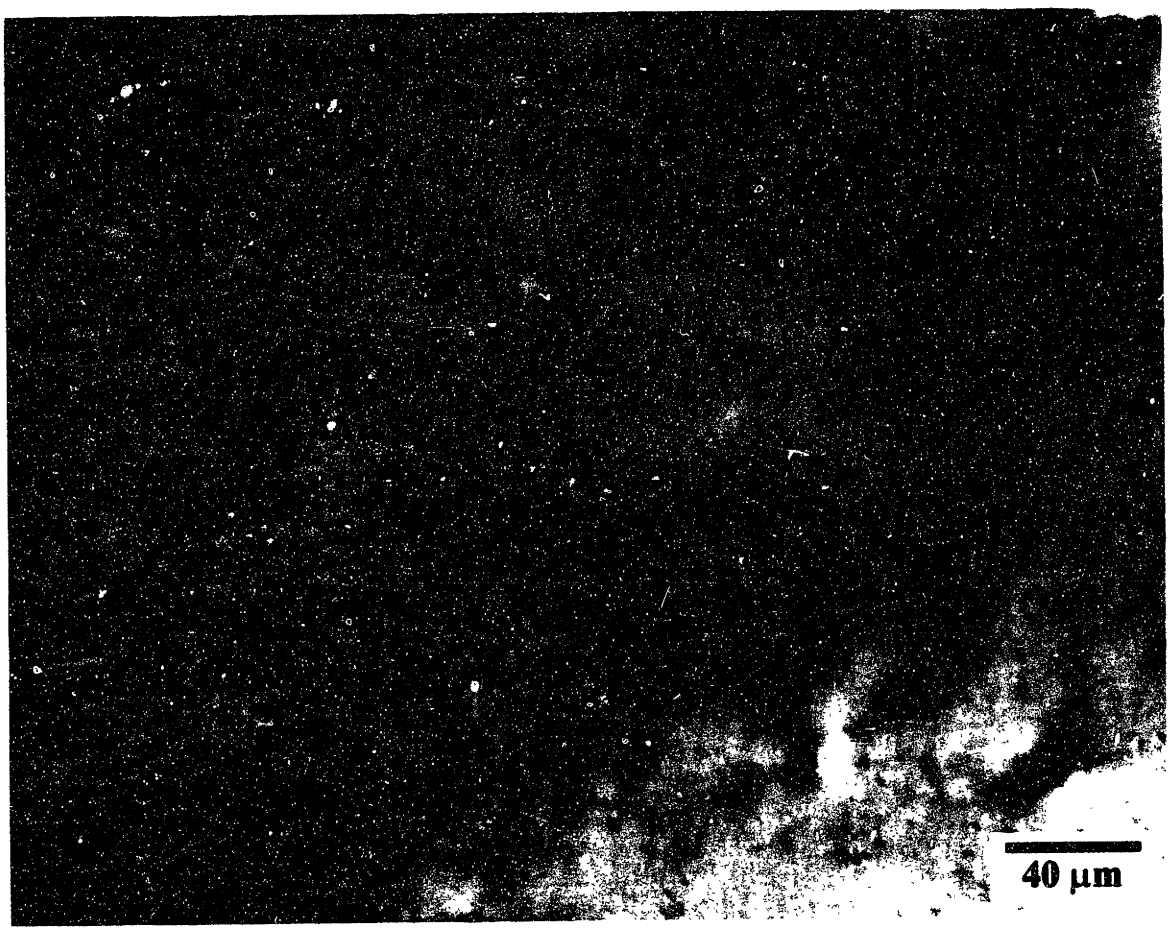

Figure 3.2 **Polarized optical micrograph of a concentrated solution of the rod–coil HS73/104 which shows a uniform birefringent texture confirming the presence of liquid crystallinity. The lyotropic behavior is particularly significant given the high PS content (f_{PS} = 0.58).**

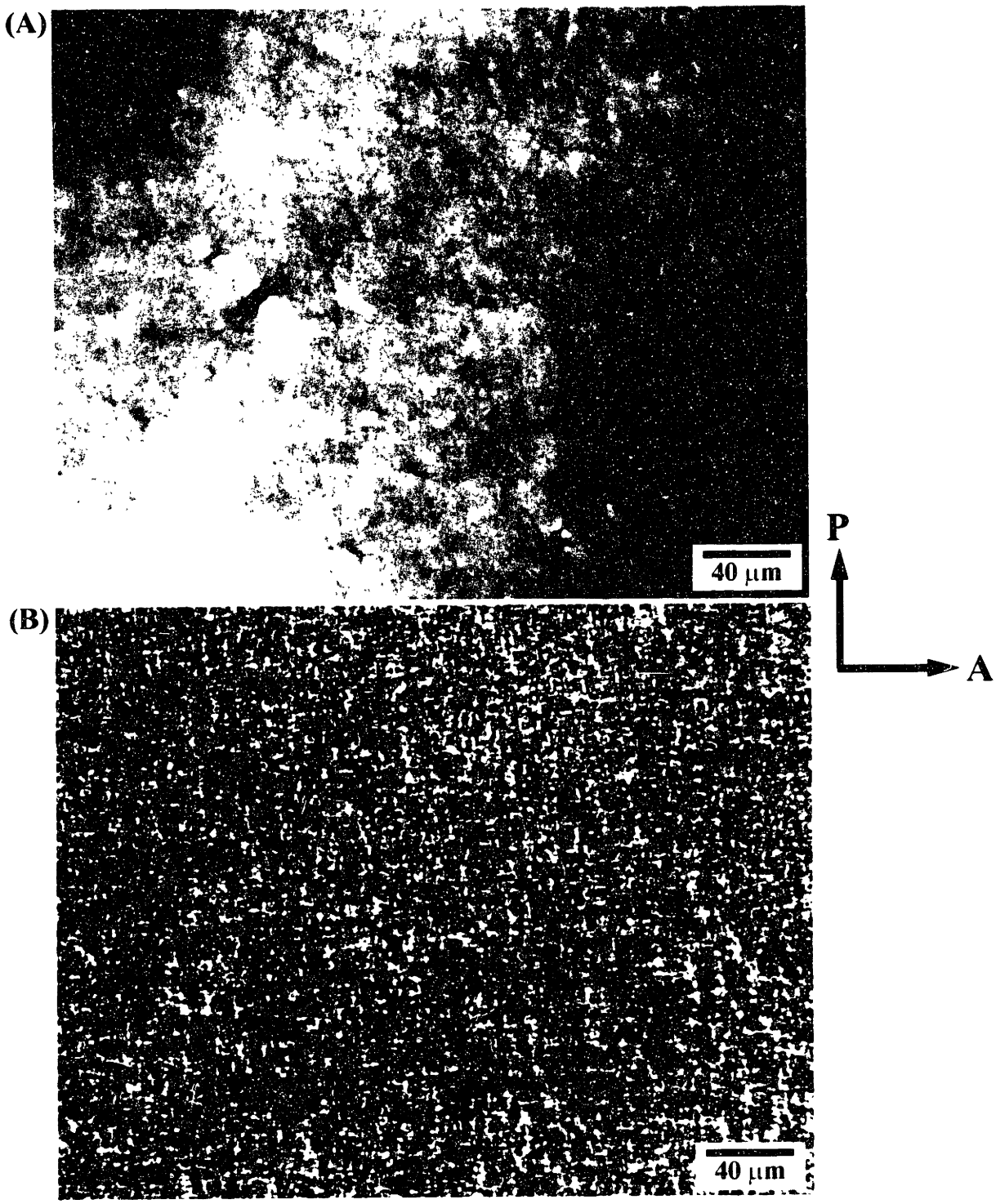

Figure 3.3 Polarized optical micrographs of concentrated solutions of the rod–coils (A) HS36/14 and (B) HS58/7. The birefringent textures are due to numerous randomly oriented overlapping grains ~5 μm or less in size.

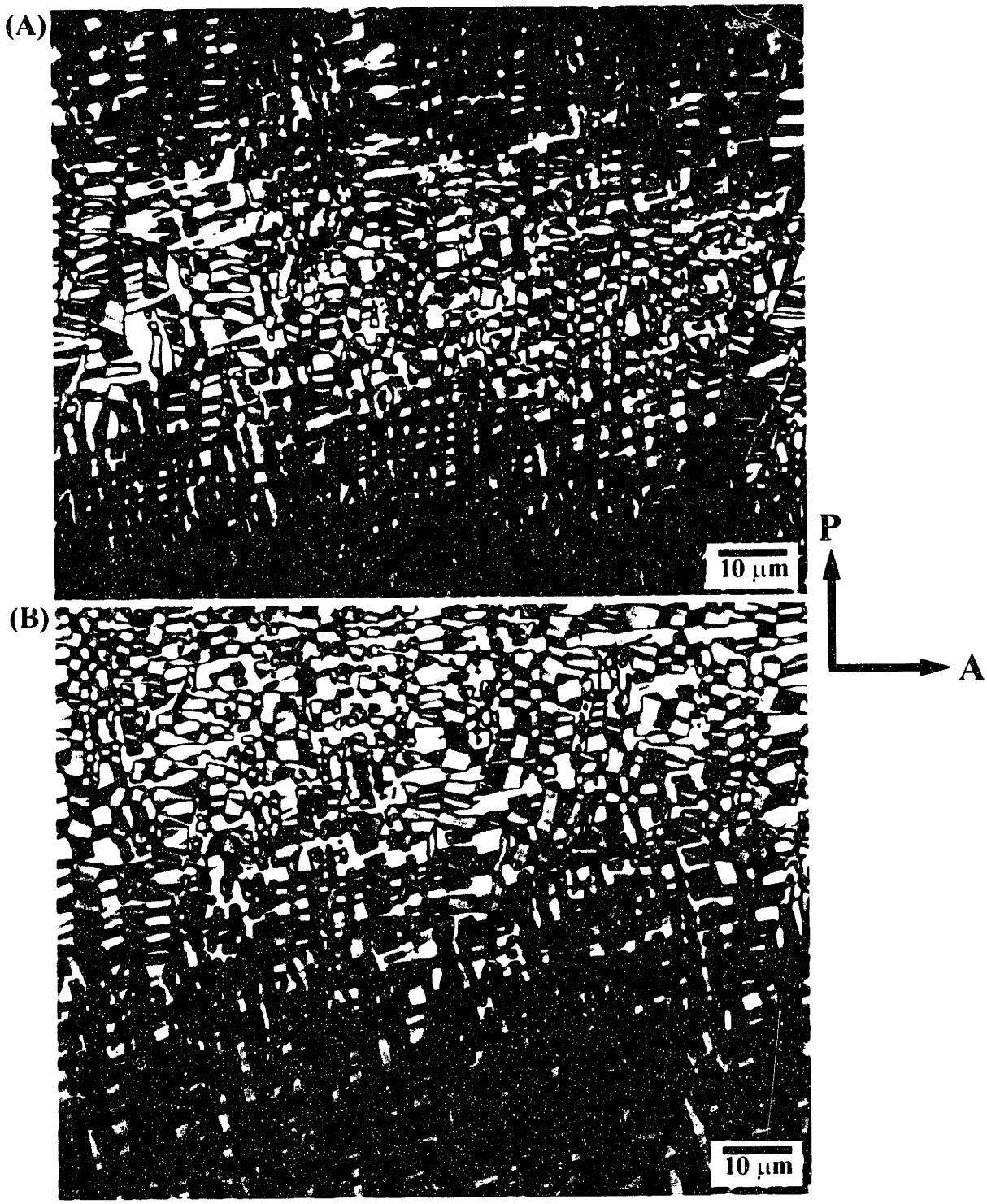

Figure 3.4 Polarized optical micrographs of concentrated solutions of the rod–coils (A) HS245/9 and (B) HS386/7. The highly anisotropic banded textures are characterized by distinct domains in which the local director adopts different orientations.

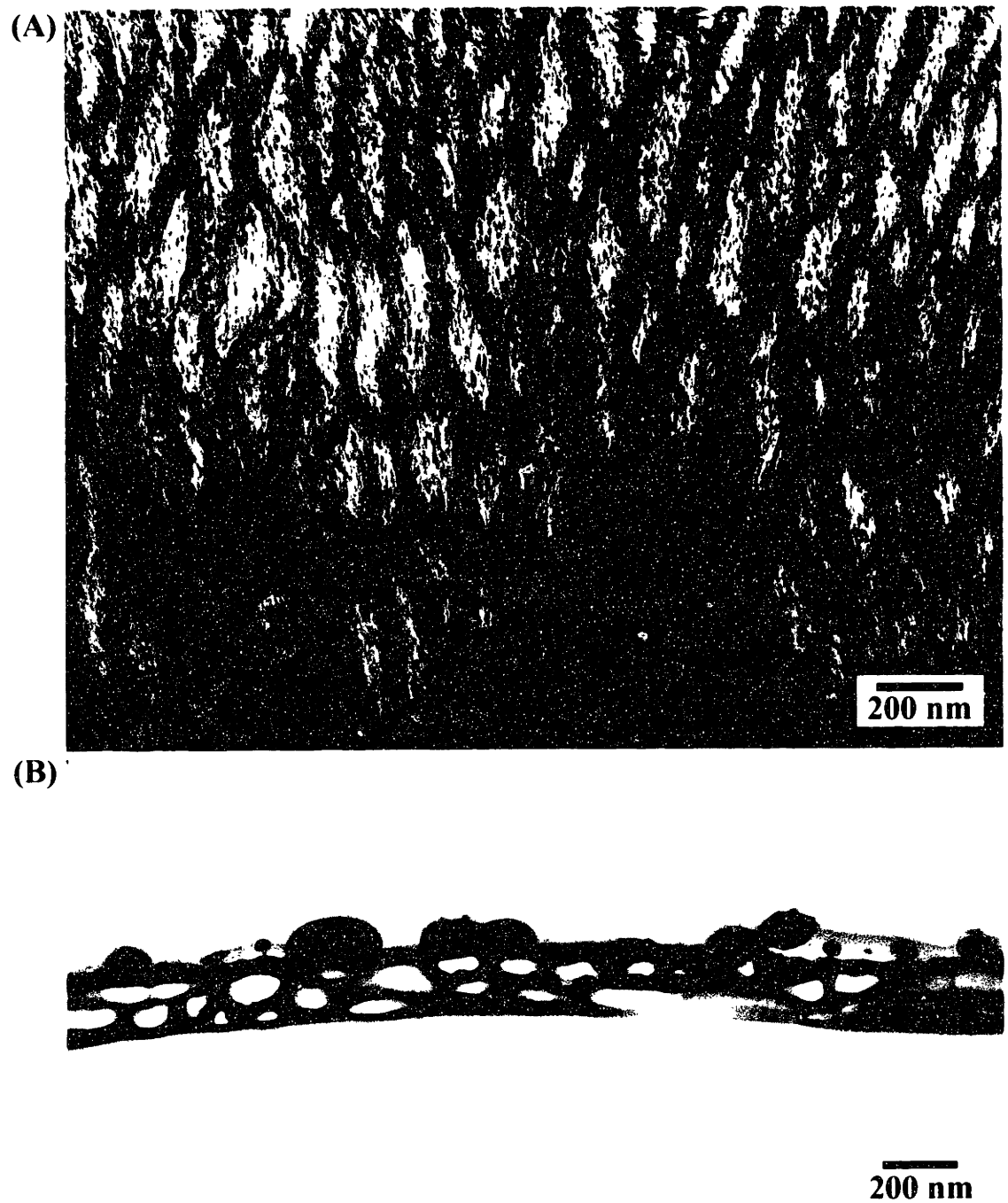

Figure 3.5 **Bright–field TEM micrographs showing a (A) plan view and a (B) cross–sectional view of the lenticular aggregate morphology formed by HS73/104 which has a rod volume fraction of $f_{PHIC} = 0.42$. The light and dark regions are the PHIC and the RuO_4 stained PS domains, respectively.**

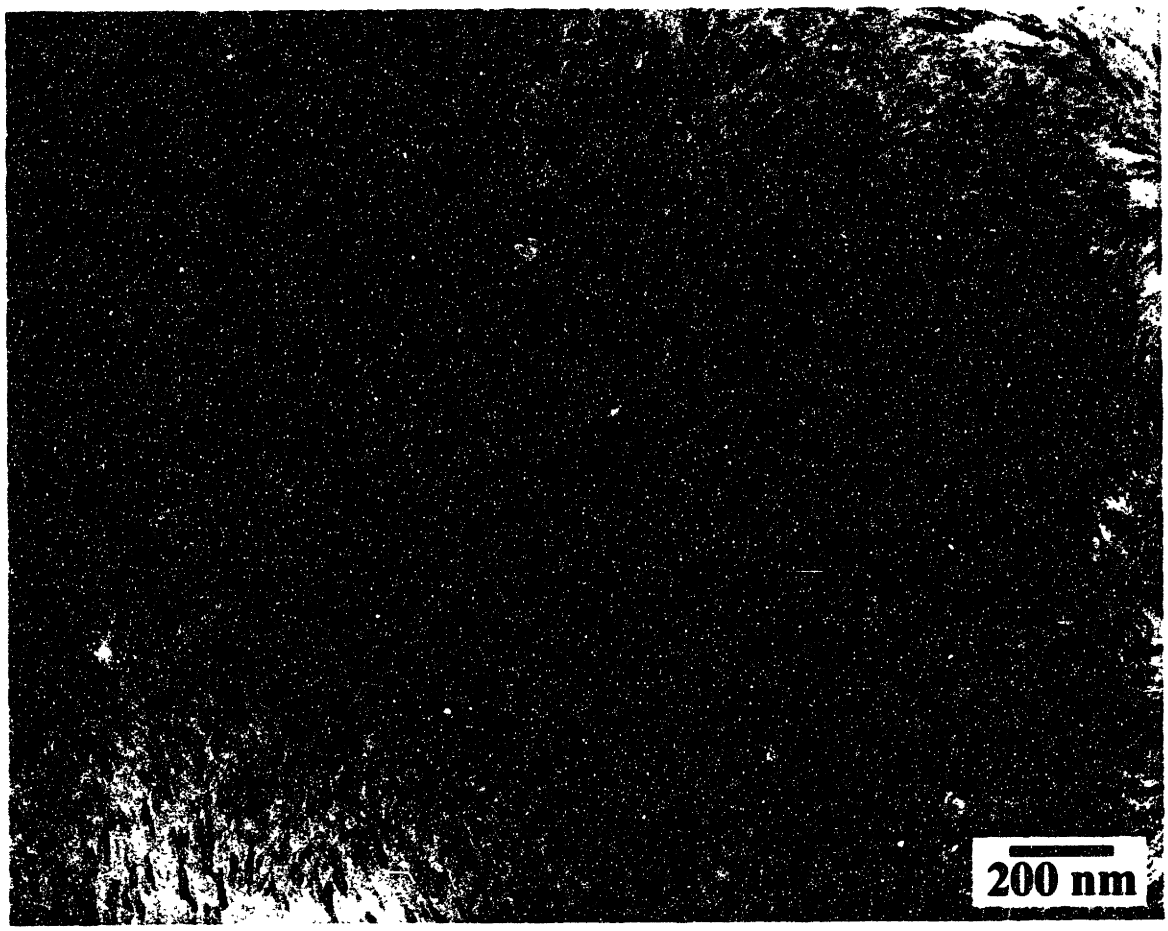

Figure 3.6 **Bright–field TEM micrograph of the nematic ellipsoid morphology formed in ultrathin films of HS73/104. The lighter regions are the PHIC domains while the darker elongated regions are the RuO_4 stained PS domains.**

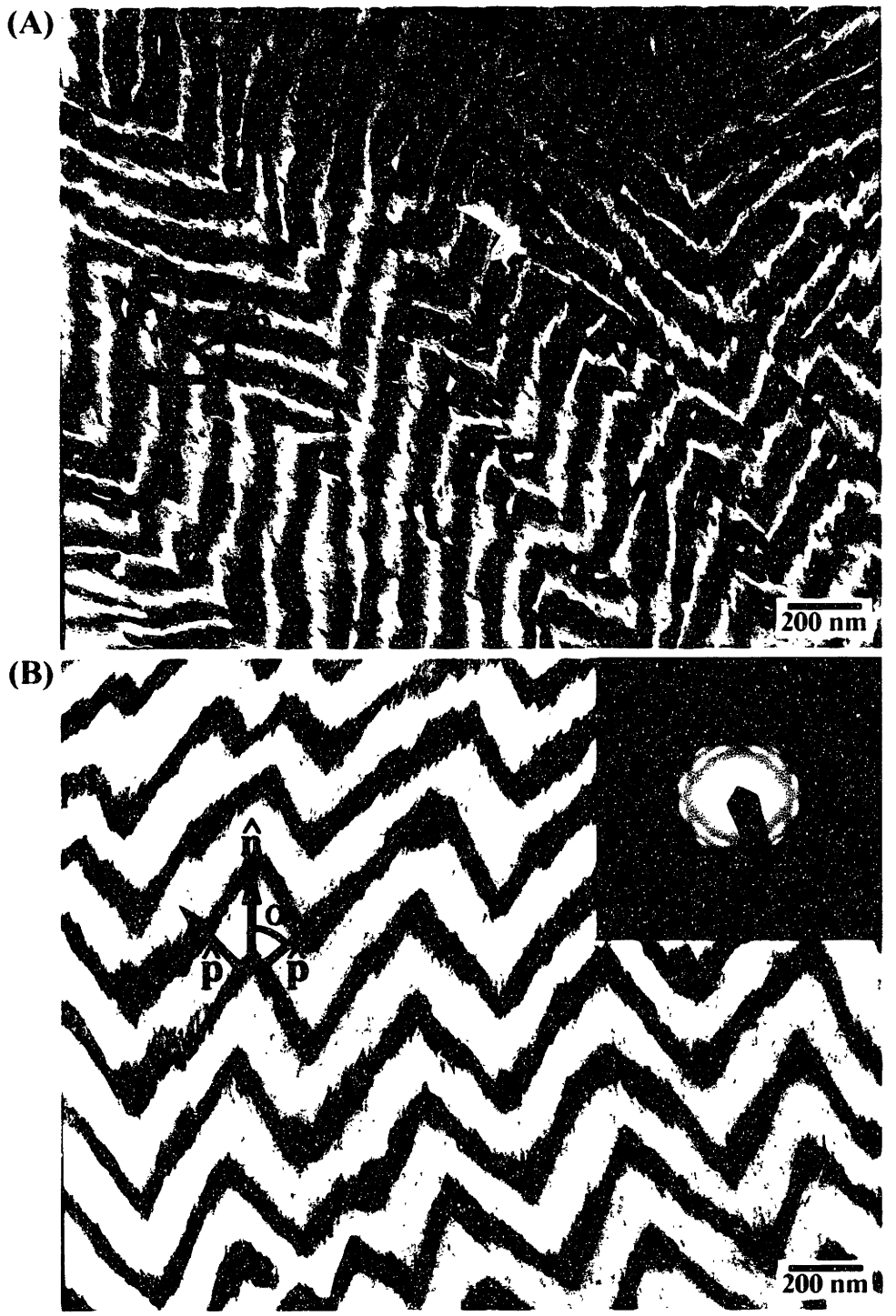

Figure 3.7 **Bright–field TEM micrographs of the zig–zag lamellar morphology formed by (A) HS36/14 and (B) HS58/7, which have rod volume fractions of f_{PHIC} = 0.73 and 0.90, respectively. The light and dark regions are the PHIC and the RuO_4 stained PS domains, respectively. The Figure 3.7b inset is a representative PHIC SAED pattern. The PHICchain axis and lamellar normals are denoted by $\hat{n}$ and $\hat{p}$, respectively.**

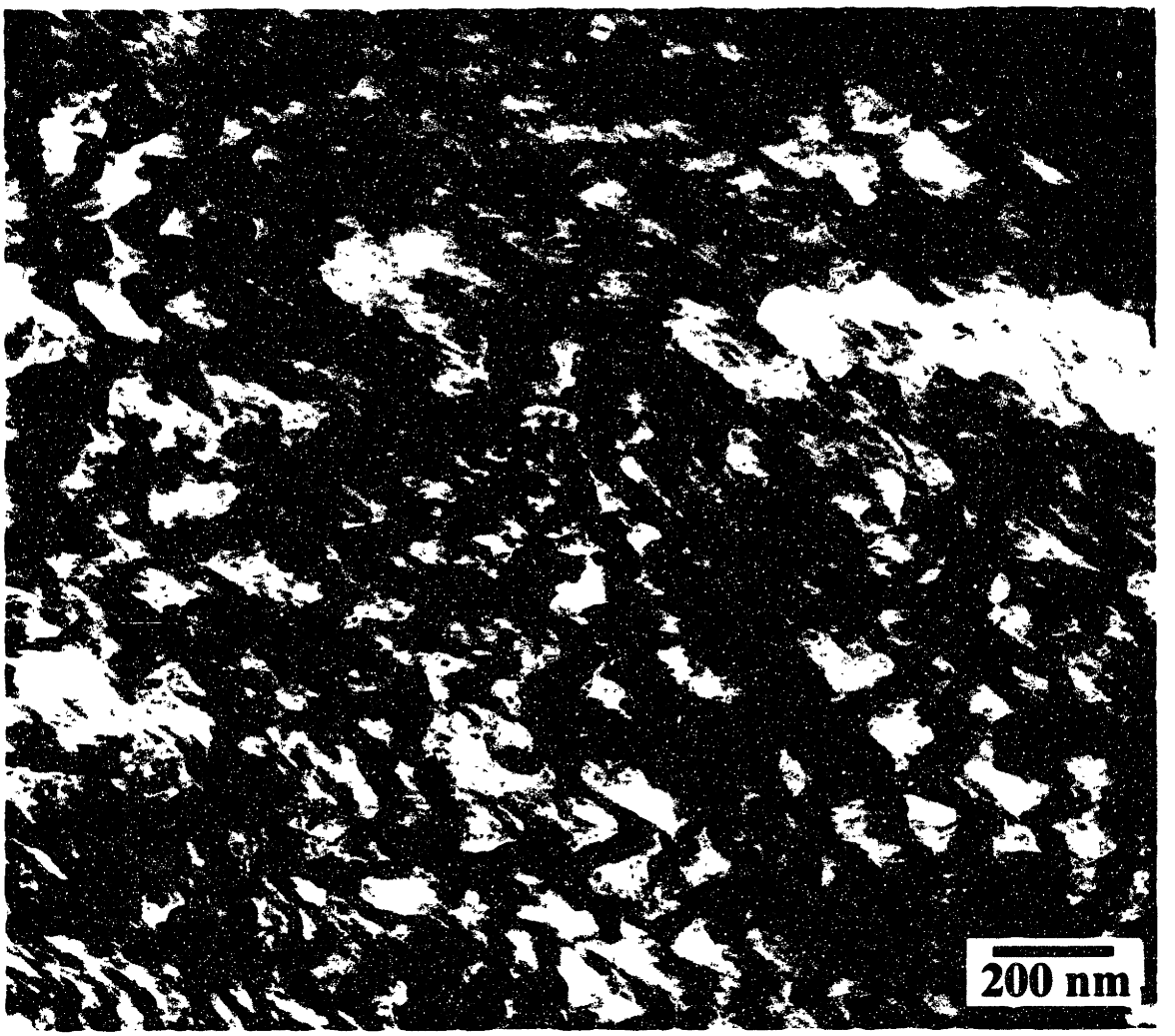

Figure 3.8 **Cross–sectional bright–field TEM micrograph of a bulk film of HS58/7 which shows the zig–zag lamellar morphology. The light and dark regions are the PHIC and RuO_4 stained PS domains, respectively.**

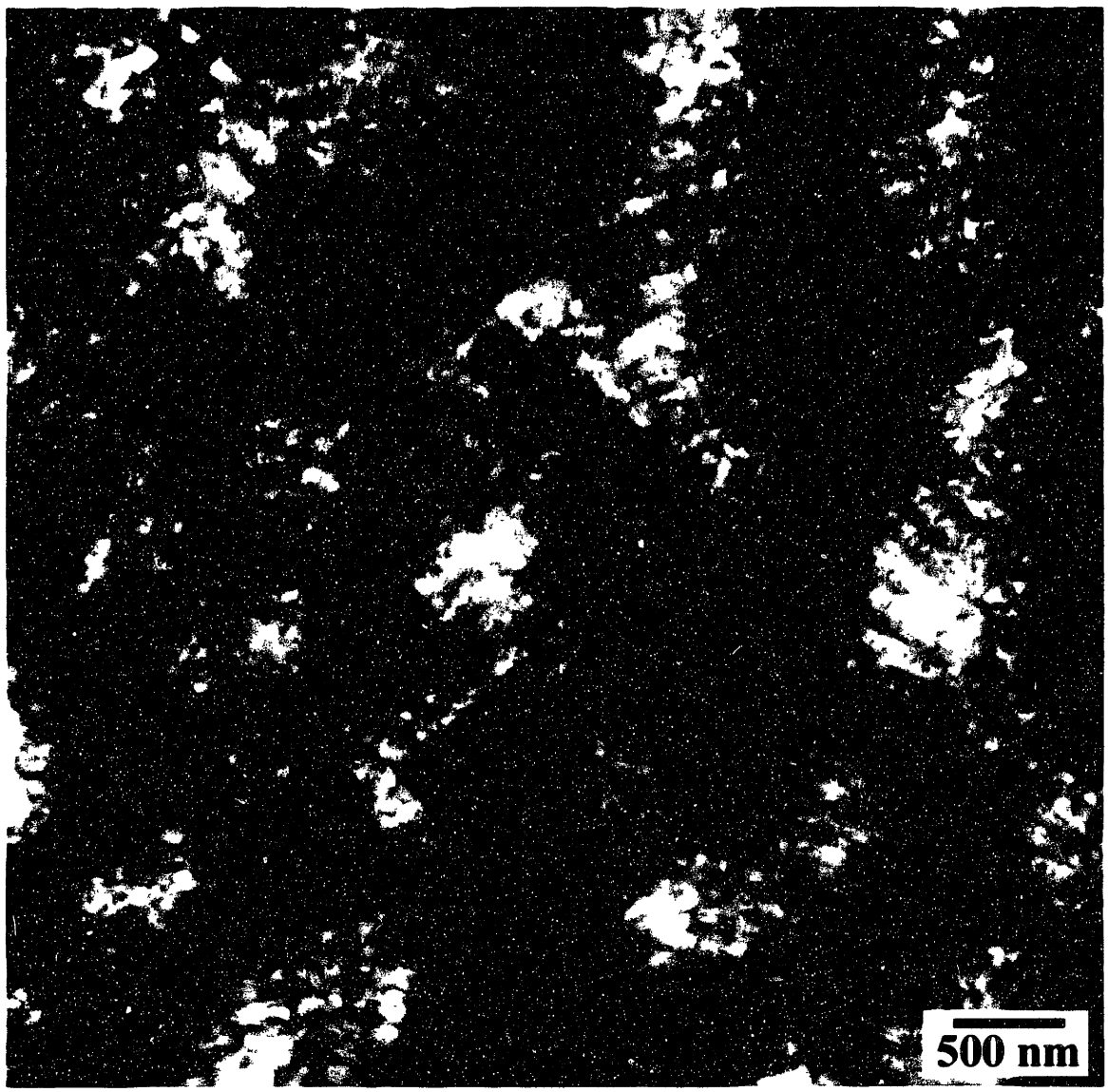

Figure 3.9 **Tapping mode AFM image of the zig–zag lamellar morphology formed by HS36/14. The arrows point out locations of packing defects within the crystalline PHIC domains.**

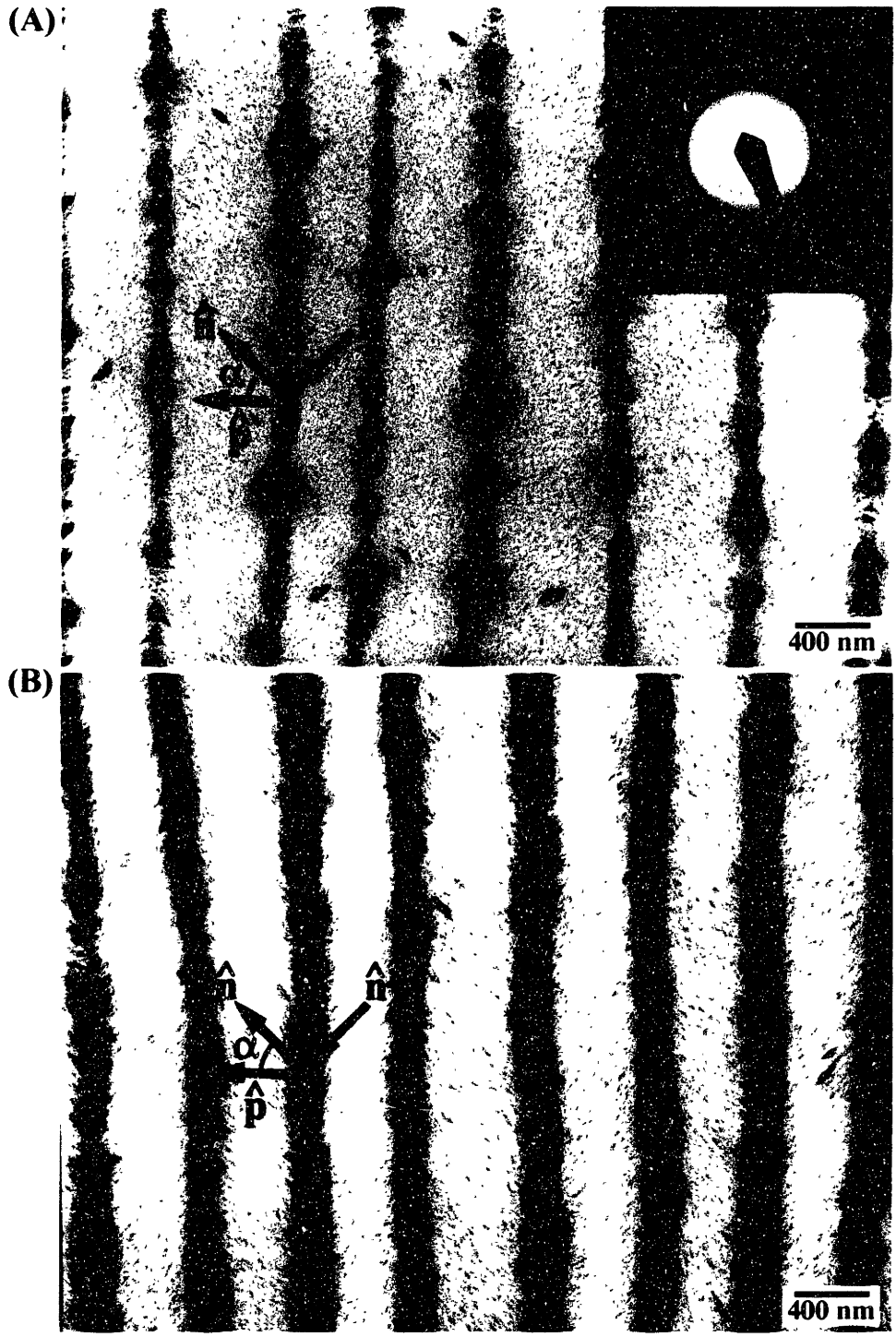

Figure 3.10 **Bright–field TEM micrographs of the arrowhead morphology formed by (A) HS245/9 and (B) HS386/7, which have rod volume fractions of f_{PHIC} = 0.96 and 0.98, respectively. The light and dark regions are the PHIC and the RuO_4 stained PS domains, respectively. The Figure 3.12a inset is representative PHIC SAED pattern for this structure. The PHIC chain axis and lamellar normals are denoted by $\hat{n}$ and $\hat{p}$, respectively.**

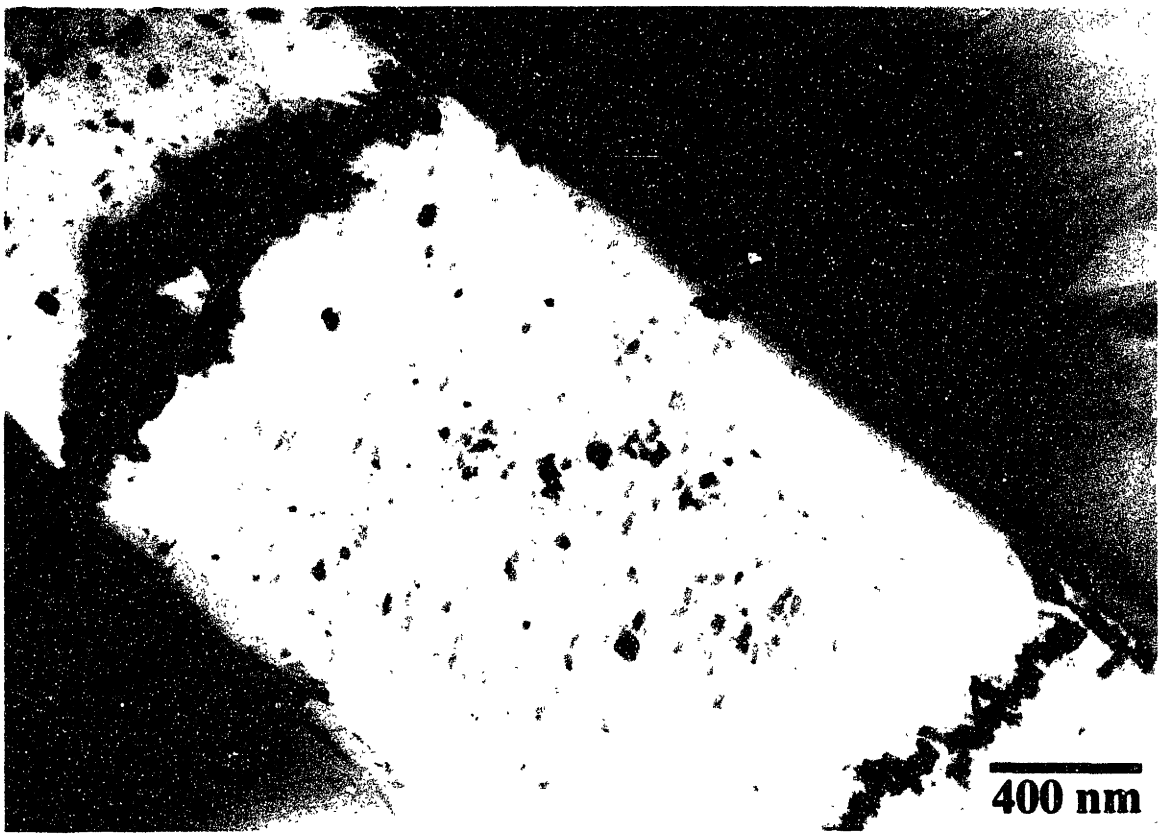

Figure 3.11 **Bright–field TEM micrograph showing a cross–sectional view of the arrowhead morphology formed by HS245/9. The light and dark regions are the PHIC and RuO_4 stained PS domains, respectively.**

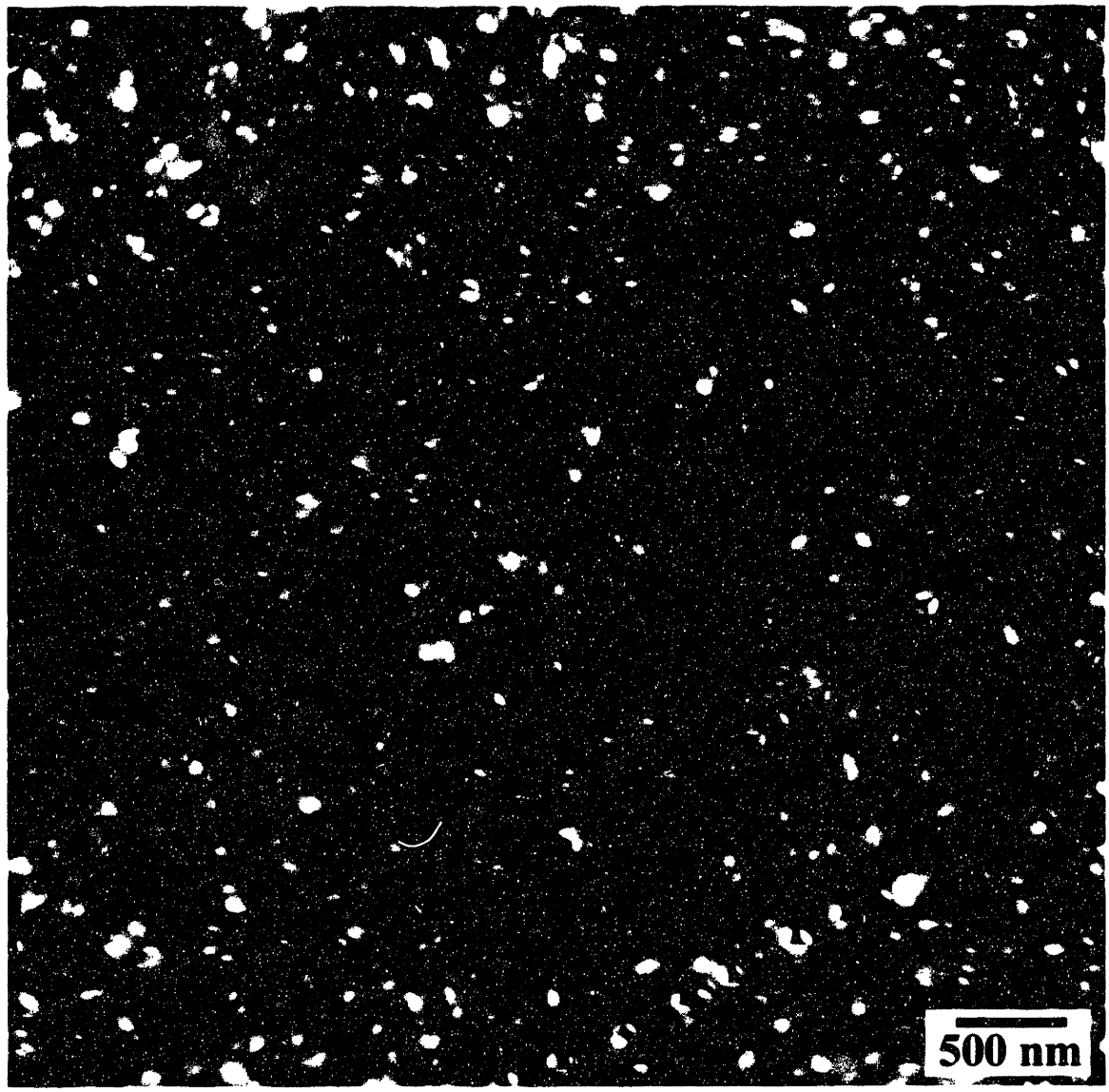

Figure 3.12 **Tapping mode AFM image of the arrowhead morphology formed by by HS245/9. The arrows point out locations of PS arrowheads.**

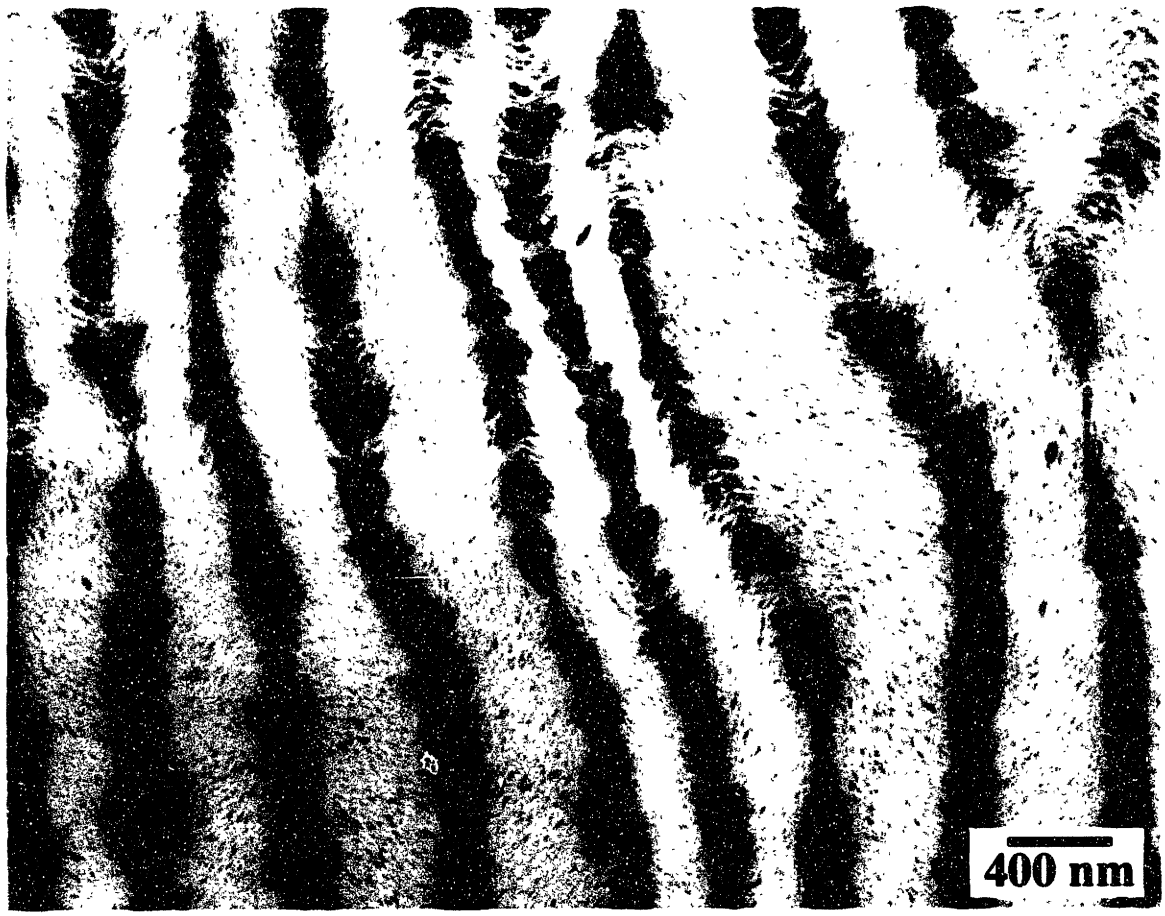

Figure 3.13 **Bright–field TEM micrograph of HS245/9 which shows the variation in domain size observed in some areas of the sample caused by polydispersity. The light and dark regions are the PHIC and RuO_4 stained PS domains, respectively.**

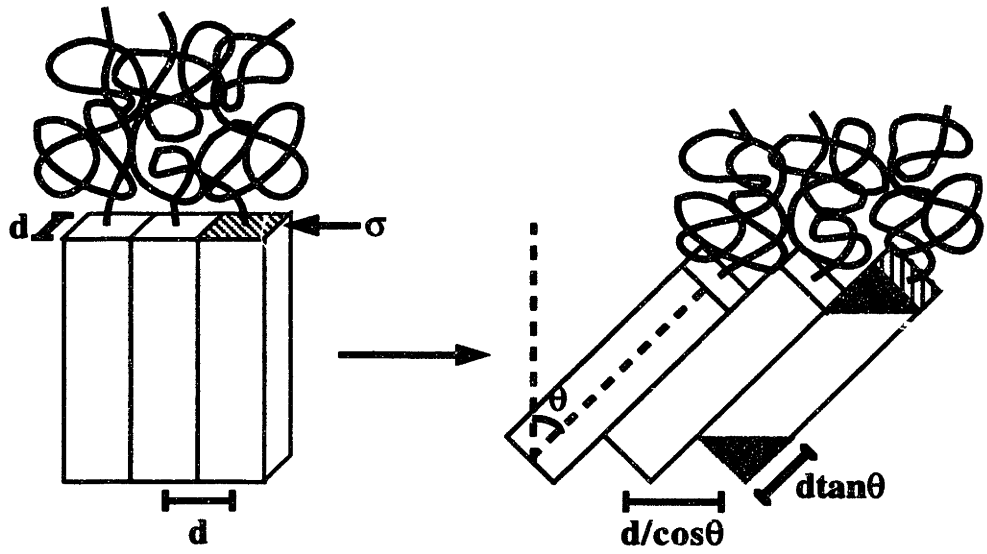

Figure 3.14 Diagram showing the effect of rod tilt on the interfacial area and the average separation between junctions. The striped area shows the area per rod-coil chain before tilt. The shaded area indicates the new surface area created after tilt.

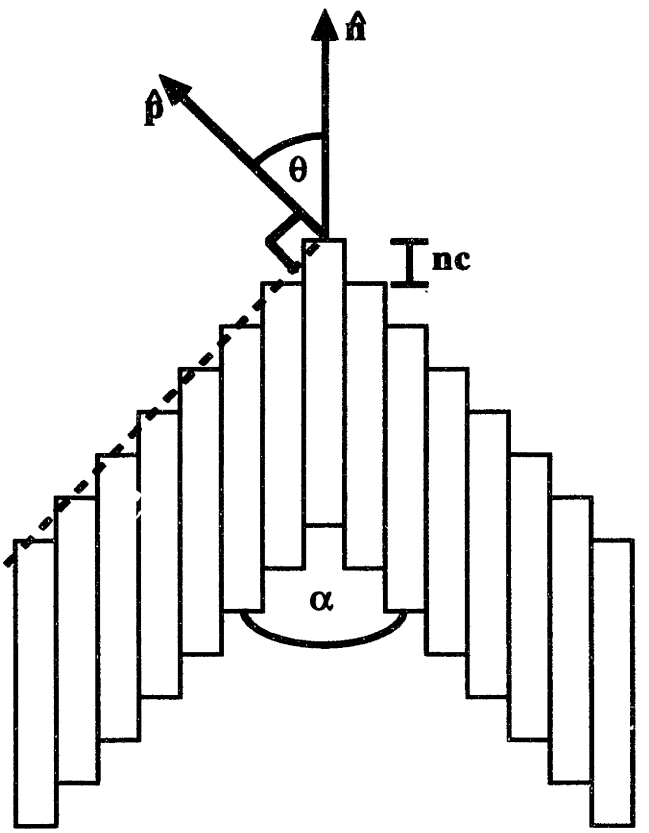

Figure 3.15 A diagram showing the quantization of the tilt angle θ and the zig-zag angle α which results from crystallization of the PHIC block. The tilt and zig-zag angles are quantized because the translation of adjacent unit cells along the chain axis must be an integral number of the c axis repeat distance in order to preserve translational symmetry of the PHIC crystal.

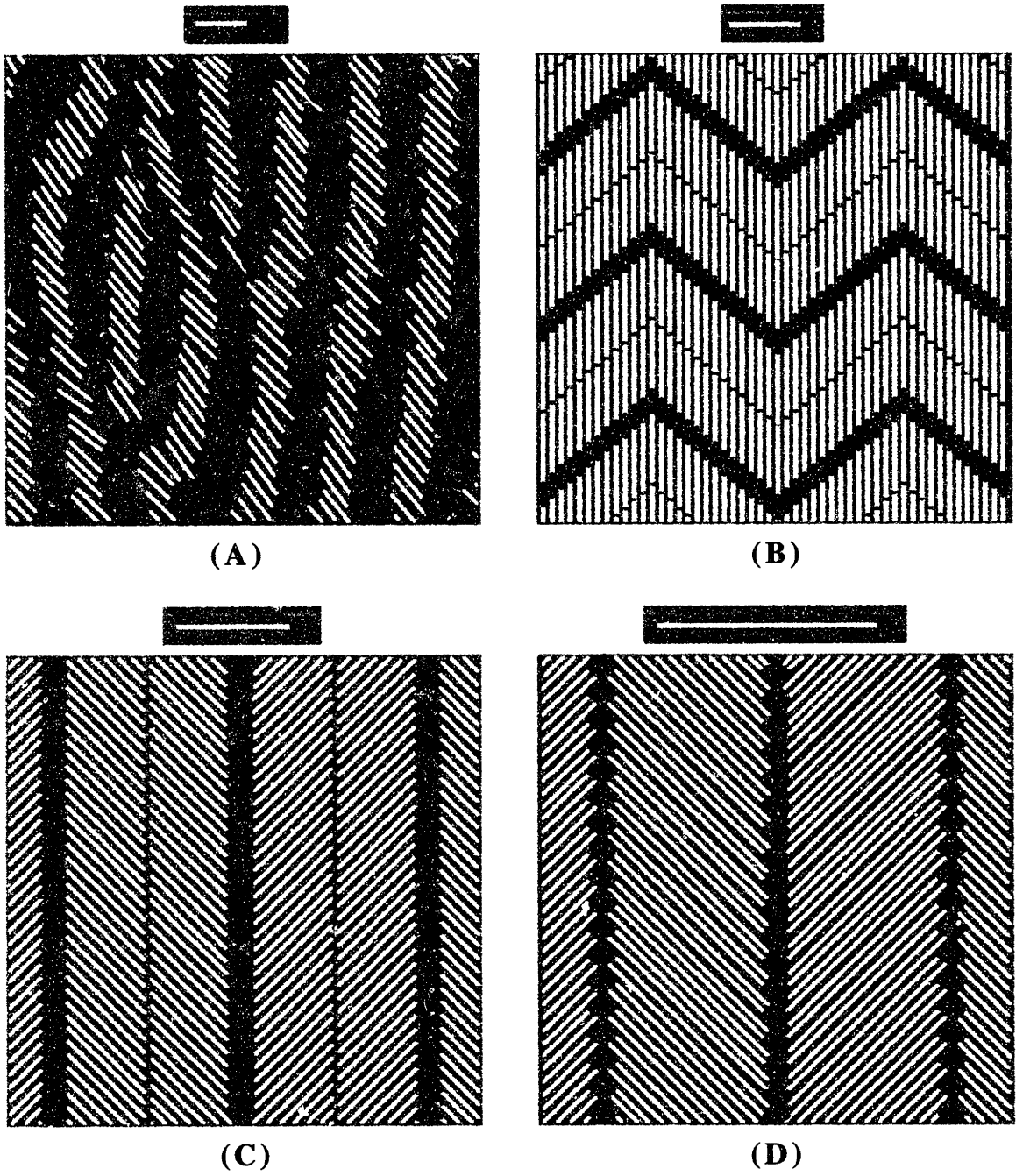

Figure 3.16 Schematic models showing the packing arrangement of the rod-coil chains in the three solid-state morphologies: (A) lenticular aggregate (LA), (B) zig-zag lamellar (ZZ), (C) bilayer arrowhead (AH) and (D) interdigitated arrowhead. The PHIC and PS blocks are represented by a white rod and a black ellipsoid, respectively.

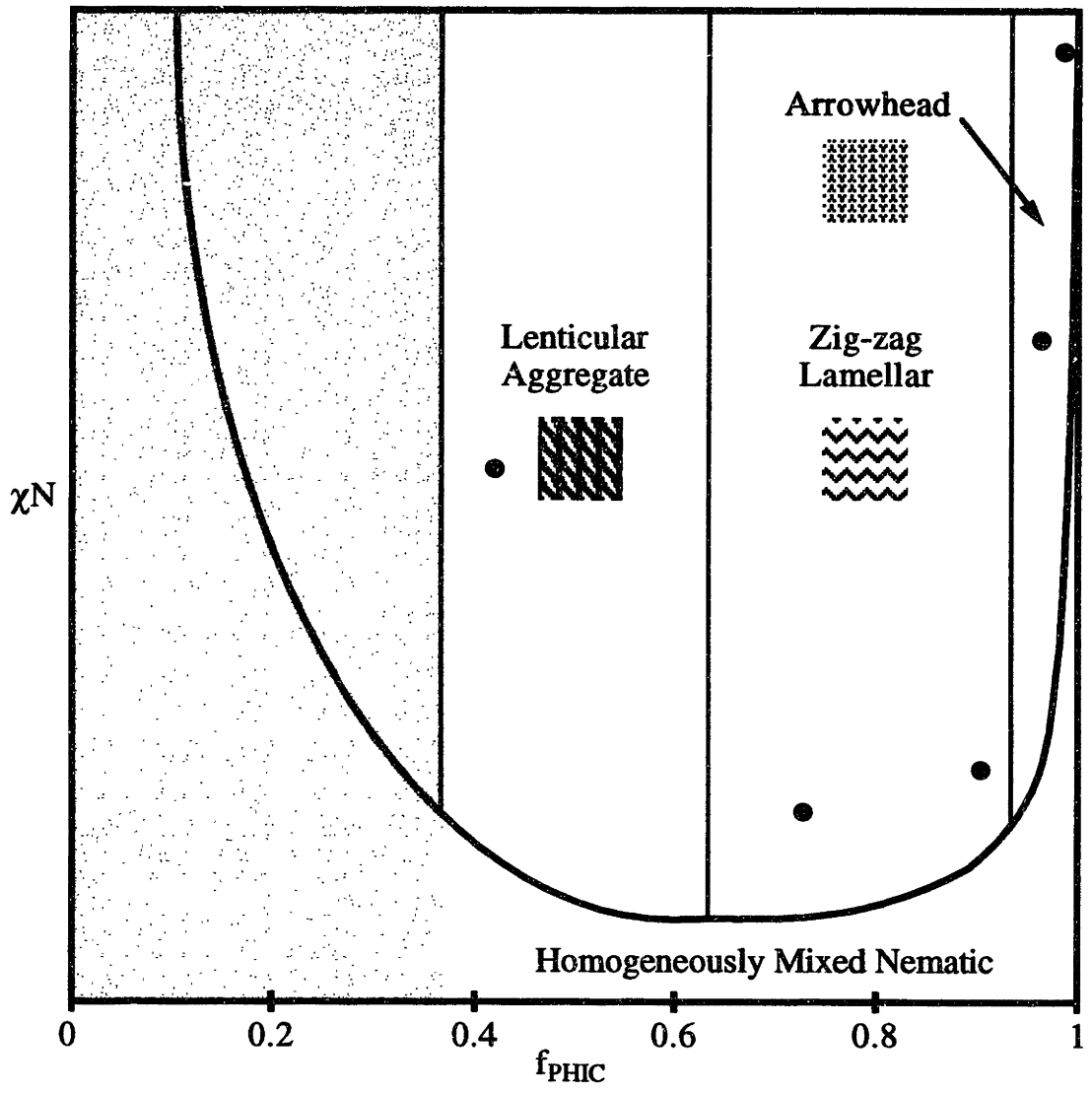

Figure 3.17 Morphology diagram for the P(HIC-b-S) rod-coil diblock copolymer system. The points correspond to the five synthesized rod-coils. The shaded region indicates the area of the morphology diagram not experimentally investigated. The vertical lines indicate approximate phase boundaries.

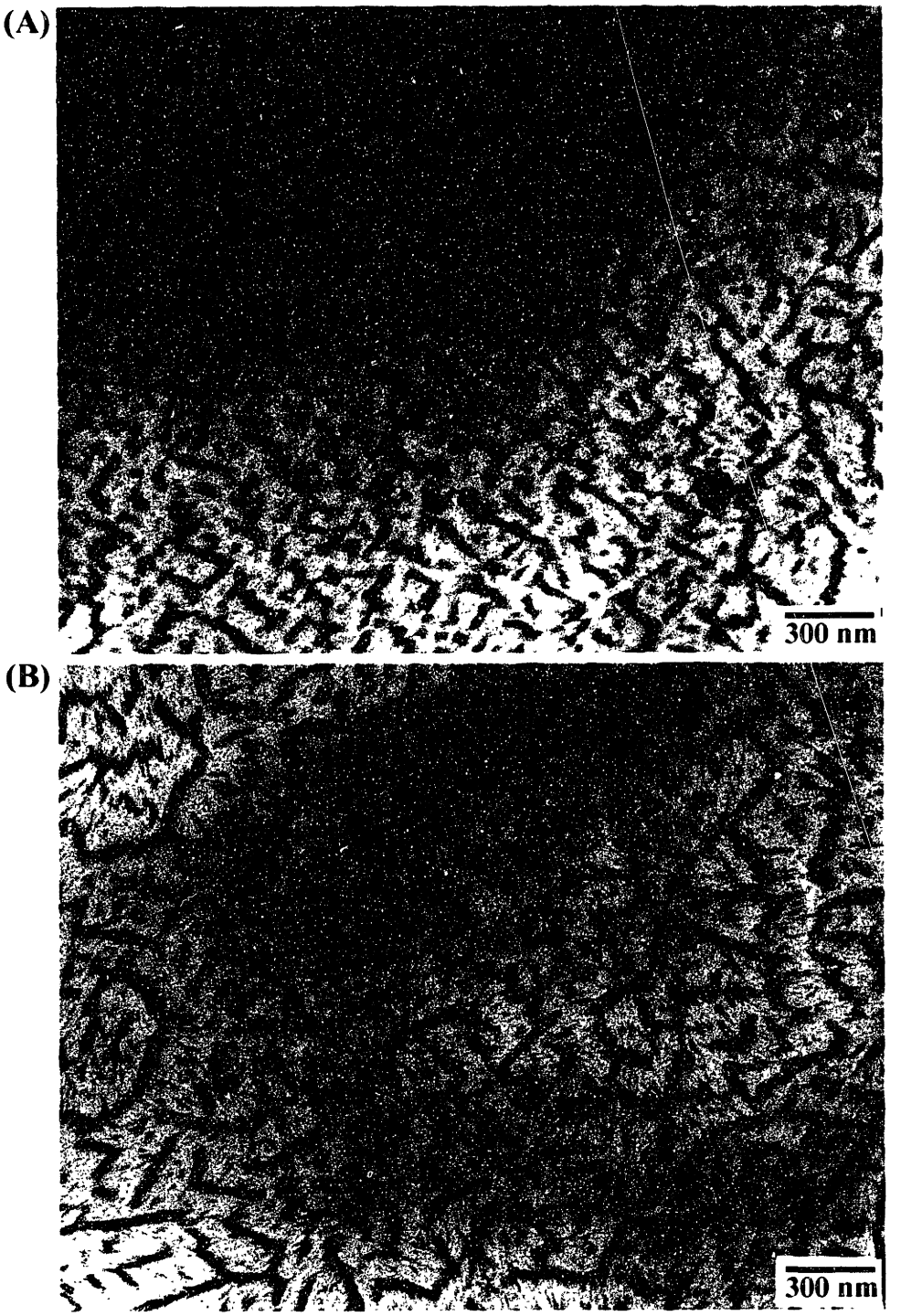

Figure 3.18 **Bright–field TEM micrographs of the rod–coil HS58/7 cast from (A) CCl_4 and (B) $CHCl_3$, respectively.**

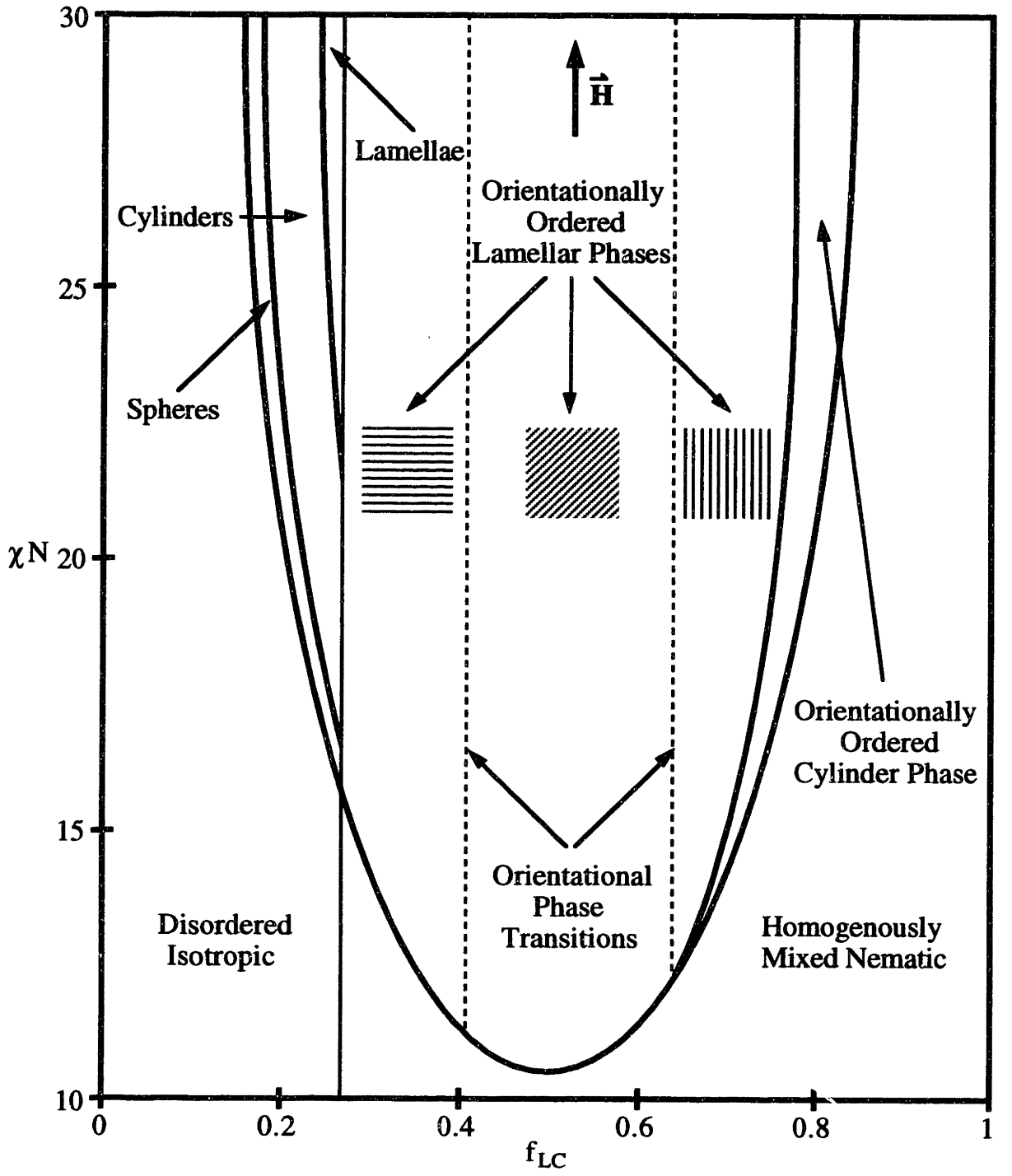

Figure 3.19 The morphology diagram predicted by Gurovich for a LC-coil block copolymer. The three schematics indicate the relative orientation of the lamellae with respect to the LC mean field in the different orientationally ordered lamellar phases. The region left of the vertical line obeys traditional coil-coil block copolymer behavior.

Chapter 4: Side-chain LC-Coil Block Copolymers

4.1 Introduction

So far, we have studied the morphologies formed by AB coil-coil and rod-coil diblocks, which represent the extreme cases of conformational symmetry and conformational asymmetry in diblock copolymers, respectively. Coil-coil diblocks have little or no conformational differences between blocks so their microdomain structures are controlled entirely by the physics of microphase separation. In contrast, rod-coil diblocks have the largest possible conformational difference between blocks and are dominated by the orientational ordering of the rod block. A second type of LC block copolymer is the AB side-chain LC-coil block copolymer. In these materials, the liquid crystalline block is composed of a flexible backbone with pendant LC mesogens which are attached to the backbone by flexible spacers. Because of the greater flexibility afforded the mesogens, these materials exhibit conformational differences between the A and B blocks which are intermediate to those of coil-coil and rod-coil diblocks. In addition, the formation of microdomain structures in these block copolymers is influenced by both microphase separation and the liquid crystallinity of the LC block. In this chapter, we describe the morphologies formed by a novel series of poly(isoprene LC-b-styrene), P(ILC-b-S), side-chain LC-coil block copolymers. The side-chain consists of an azobenzene mesogen connected to the isoprene backbone by a flexible $(CH_2)_5$ group. As we shall see in the P(ILC-b-S) system, microphase separation will precede the liquid crystal transition resulting in classical microdomain structures in which the LC block forms smectic A domains.

4.2 Background and Previous Work

4.2.1 Previous Experimental Work

Compared to coil-coil and even rod-coil diblock copolymers, side-chain LC-coil block copolymers are a new class of self-assembling materials which have only begun to be experimentally studied in recent years. The first side-chain LC-coil diblock was synthesized by Adams and Gronski in 1989 [113] by using a polymer-analogous esterification reaction to attach pendant cholesteryl groups to the 1,2-polybutadiene units of an anionically synthesized poly(1,2-butadiene-b-styrene) precursor. Using WAXD and TEM, the symmetric diblock was found to form a lamellar morphology in which the LC block formed a smectic mesophase below 203°C. Since then, several other studies on different side-chain LC-coil diblock and triblock copolymer systems have been carried out [114-121]. These studies included both nematic and smectic-forming LC blocks. Besides the familiar lamellar morphology, sphere and cylinder morphologies were also observed on both sides of the morphology diagram. The LC sphere and cylinder morphologies, however, were only observed for nematic LC blocks. Fischer et al. [119, 120] argued that smectic phases are not favored within spheres and cylinders because their characteristic radii are too small compared to the smectic layer spacing and can only be formed when the LC block is the majority component. In the studies by Fischer et al., however, the degree of polymerization of the LC blocks, which is known to significantly influence the mesophase type and order parameter, was extremely small (N_{LC} = 6 to 10).

4.2.2 Previous Theoretical Work

A statistical theory of the microphase separation of liquid crystalline diblock copolymer melts near the spinodal by Gurovich (see Chapter 3) is the only theoretical

work to date of relevance to side-chain LC-coil block copolymers [100]. In this theory, which is an extension of Leibler's original work [29], long range orientational order of the block copolymer segments is treated using the framework of Maier-Saupe theory via an orientational interaction which is approximated by a self-consistent molecular field **H** (which in general is different for the A and B blocks). For main-chain LC polymers, the monomer bonds tend to orient in the direction of the field. For side-chain LC polymers, the monomer bonds tend to orient perpendicular to the field. The molecular field influences the chain conformations of LC polymers so that they no longer obey Gaussian chain statistics. In addition, the radius of gyration for a LC block is now different parallel and perpendicular to the field. Ultimately, the liquid crystalline nature of the block copolymer chain results in a wave vector dependent effective composition, $\tilde{f}(\mathbf{Q})$. As for coil-coil diblock copolymers, a Landau expansion of the free energy per chain can be made in terms of a local order parameter $\Psi(\mathbf{r})$ for LC block copolymers. The $\chi\Psi^2$ term which describes the effective enthalpic repulsion between the A and B monomers is unaffected by the molecular fields and is the same as the coil-coil block copolymer term. All remaining terms in the expansion, however, which describe the loss in configurational entropy after microphase separation, must be modified by letting $f \rightarrow \tilde{f}(\mathbf{Q})$. By studying the topology of the resulting critical wave vector surfaces at the spinodal, Gurovich found that all liquid crystalline block copolymer melts fall into one of four universal classes whose phase behavior can be described by the parameters χN and $\tilde{f}(\mathbf{Q})$. Unfortunately, no predicted morphology diagrams were given for the case of a side-chain LC-coil diblock copolymer.

4.3 Synthesis and Characterization

Many factors, such as the molecular weight, volume fraction, length of the spacer, and phase behavior of the side-chain LC block, influence the microphase separated structures formed by side-chain LC-coil block copolymers. Systematic studies on model block copolymers are needed to fully understand how these factors are interrelated. A series of novel side-chain LC-coil diblock copolymers covering a wide range of composition (f_{PILC} = 0.20 to 0.82) were synthesized by Guoping Mao in the laboratory of Professor Chris Ober at Cornell University. These side-chain LC-coil diblocks had a PS coil block and a high molecular weight (relative to many of the previous studies) poly(isoprene LC) side-chain LC block (see Figure 4.1). The PI units (3 wt% 1,4-polyisoprene) of anionically synthesized P(I-b-S) diblock precursors were functionalized with azobenzene mesogens by polymer-analogous chemistry to produce the side-chain LC block copolymer. The azobenzene mesogens are connected to the backbone via a $(CH_2)_5$ flexible spacer group. Anionic polymerization of the P(I-b-S) precursors and nearly full conversion of the reactive pendant double bonds ensures that the final diblocks have narrow molecular weight distributions. In addition, the poly(isoprene LC-b-styrene), P(ILC-b-S), side-chain LC-coil block copolymers were designed to have nearly the same side-chain LC block molecular weights in order to minimize molecular weight dependent effects.

All of the chemicals needed in the synthesis of the side-chain LC-coils were purchased from Aldrich Chemical Company, Inc. (Milwaukee, WI) except where noted. Prior to use, the solvents tetrahydrofuran (THF) and toluene were dried by distilling from Na/benzophenone (deep purple color) under nitrogen after refluxing for at least 7 hours. Pyridine and hexane were distilled from CaH_2 after refluxing for 4 hours. The styrene monomer was purified by washing with 10% NaOH solution to remove inhibitor, stirring

over CaH_2 and di-butyl magnesium (bright greenish color) for 48 and 24 hours, respectively, and finally vacuum-distilled into a cold trap (-20°C) for storage. The isoprene monomer was distilled at room temperature over CaH_2, stirred with di-butyl magnesium at 0°C for 4 hours, and distilled into a cold trap for immediate use.

Anionic synthesis of the P(I-b-S) diblock copolymer precursors was carried out in the usual way. THF was first distilled into a 250 ml flask and cooled to -78°C using an isopropanol/dry ice cooling bath. Then the initiator sec-BuLi was added to the flask. Using a cannula, styrene monomer was added to the flask while vigorously stirring and allowed to polymerize. After a small amount of the PS was removed for characterization purposes, isoprene monomer was added to the flask and polymerized until completion. The living block copolymer was terminated with methanol, precipitated into methanol, and dried under vacuum. A hydroboration/oxidation reaction was used to convert the pendant double bonds on the PI units to hydroxyl groups which could be used to couple the azobenzene mesogens.

A standard synthetic approach reported in the literature [122] was used to make the 4-cyano-4'-hydroxyazobenzene mesogenic group. A flexible $EtOCO(O)(CH_2)_5$ spacer group was added to the mesogen by a William etherification reaction. Numerous studies have shown that the $(CH_2)_5$ group is the optimum length spacer for side-chain LC's [123]. Shorter spacers do not provide sufficient flexibility to the mesogen and prevent liquid crystallinity. When the number of methylene units is too large (>12), however, crystallization of the spacer group can occur [123]. KOH was used to deprotect the ester and produce an acid group which was converted to an acid chloride group using oxalyl chloride. A simple coupling reaction was finally used to attach the mesogenic groups onto the PI back bone producing the final P(ILC-b-S) side-chain LC-coil block copolymer. For means of comparison, a PILC homopolymer was synthesized as well using the same steps outlined above.

Gel permeation chromatography (GPC) and nuclear magnetic resonance (NMR) were used to determine the molecular weight and composition of each side-chain LC-coil block copolymer. GPC was performed in THF using a Waters 150 GPC equipped with a refractive index (254 nm) and UV detector (368 nm). A flow rate of 0.30 ml/min and four Ultrastyragel columns with mixed, 50 nm, 100 nm, and 1000 nm pore sizes were used. Mondisperse PS standards were used for column calibration. ^{1}H and ^{13}C NMR data were collected at 200 MHz or 400 MHz from a Varian instrument using $CDCl_3$ as the solvent. A relaxation time (T_1) of 12 seconds was used for all ^{1}H NMR characterization. Additional information about the thermotropic LC behavior of the side-chain LC-coil diblocks was obtained from thermograms measured with a Perkin-Elmer DSC 7. All characterization of the side-chain LC-coils was performed by Guoping Mao in Cornell University. The data obtained from GPC, NMR, and DSC are tabulated in Table 4.1.

Table 4.1 Molecular weight characterization and smectic A-isotropic transition data for the P(ILC-b-S) diblocks, obtained from GPC, NMR, and DSC. Data courtesy of Guoping Mao.

Sample	Total M_w (g/mol)	M_w/M_n	M_{PILC} (g/mol)	N_{PILC}	f_{PILC}	M_{PS} (g/mol)	N_{PS}	Sm A-Isotropic Transition (°C)
ILC-S29/107	124,000	1.07	29,000	72	0.20	107,000	1029	202
ILC-S55/176	192,000	1.13	55,000	136	0.22	176,000	1692	179
ILC-S78/176	223,000	1.15	78,000	193	0.29	176,000	1692	185
ILC-S60/66	93,000	1.12	60,000	148	0.45	66,000	635	157
ILC-S62/59	96,000	1.10	62,000	153	0.49	59,000	567	158
ILC-S43/13	48,000	1.10	43,000	106	0.75	13,000	125	208
ILC-S72/14	75,000	1.24	72,000	178	0.82	14,000	135	188
ILC78	68,000	1.15	78,000	168	1.00	-----	-----	176

The P(ILC-b-S) side-chain LC-coil block copolymers are designated ILC-Sx/y, where x and y are the M_w of the PILC and PS blocks in units of 1 kg/mol, respectively. The total molecular weights and polydispersities listed in columns 2 and 3 were determined relative to a PS standard. Before undergoing the coupling reaction, all of the precursor P(I-b-S) diblocks were observed to have narrow molecular weight distributions with polydispersities less than or equal to 1.07. After attachment of the side-chain LC mesogens, however, the molecular weight distributions become somewhat broader. The polydispersity is expected to increase more for the diblocks with a higher f_{PILC} because the probability of side reactions is greater during the coupling reaction. The side-chain LC block molecular weights listed in column 4 were calculated from NMR data and the PS block molecular weights (see column 7) obtained from GPC. A comparison of the experimentally determined side-chain LC molecular weights with those predicted from the known PI block molecular weights assuming complete conversion of the pendant hydroxyl groups shows that, on average, 97% of the PI units have side-chain LC mesogens. The volume fraction of the diblocks, f_{PILC}, (see column 6) were calculated using the density of PILC, 1.15 g/cm^3., which was determined using a series of NaI-H_2O solutions (densities 1.0 to 1.4 g/cm^3) and ethylene glycol (1.113 g/cm^3).

4.4 Sample Preparation

Two kinds of samples were prepared in order to study the P(ILC-b-S) side-chain LC-coil diblock copolymers. Oriented samples of the side-chain LC-coil diblocks and the PILC homopolymer were made for wide-angle X-ray diffraction (WAXD) studies in order to determine the LC mesophases. Pieces of the diblock or homopolymer were placed on a glass slide and heated above the glass transition temperature of both blocks

(~110°C) using a hotplate. To make oriented films (~200 μm thick), the melt was sheared with a spatula to create a macroscopically aligned monodomain and then cooled slowly to freeze in the orientation. In addition to oriented films, tweezers were used to pull fiber (~100 μm in diameter) samples from the melt. Such fibers displayed uniaxial symmetry along the fiber axis.

Unoriented bulk samples of the side-chain LC-coil diblocks were made for TEM and small-angle X-ray diffraction (SAXD) studies of the microdomain structures as well. Films (final thickness ~1 mm) were cast in covered ceramic crucibles from 5 wt% solutions in toluene and allowed to evaporate slowly for one week. The as-cast films were placed in a vacuum oven at room temperature for two days to remove residual solvent. The samples were then annealed at 145°C for four days in a vacuum oven to improve long range order of the morphology. The annealing temperature of 145°C was high enough (~40°C) above the glass transition of the PS block to allow sufficient mobility of the chains but still within the smectic A phase of the PILC block. For SAXD studies, the films were used without further processing. For TEM studies (see sample preparation of bulk rod-coil samples in Chapter 3), small pieces of the P(ILC-b-S) films were cut off and prestained in RuO_4 vapors for 15-20 minutes to protect the samples. The prestained pieces were then embedded in epoxy monomer and cured overnight at 80°C to produce blocks which were suitable for cross-sectional microtomy. Thin sections were microtomed, stained in RuO_4 a second time for 15-20 minutes (RuO_4 preferentially stains the PS block), and carbon coated prior to examination as described previously in Chapter 2 and 3.

4.5 Experimental Techniques

A number of techniques were used to study the liquid crystalline mesophases and the microphase separated morphologies formed by the P(ILC-b-S) side-chain LC-coil diblock copolymers. Polarized optical microscopy (POM) of the PILC homopolymer and P(ILC-b-S) diblocks was performed under crossed polarizers using a Nikon optical microscope equipped with a Mettler hotstage and temperature controller. Small pieces of the samples were placed between glass slides and heated into the melt state. A glass cover slip was then used to press the sample into a uniform thickness film. The films were observed at temperatures ranging from room temperature to temperatures above the smectic A-isotropic transition.

WAXD and SAXD were used to investigate the mesophase and the microphase separated morphologies of the side-chain LC-coils and the mesophase of the PILC homopolymer. WAXD patterns were primarily obtained using a sealed tube Enraf Nonius X-ray diffractometer operated at 40 kV employing Ni-filtered 1.54 Å CuKα X-rays. WAXD patterns were recorded using a Statton camera equipped with a film cartridge. A CaF_2 (d = 3.155 Å) standard was used for calibration. SAXD and some WAXD patterns were measured at the Cornell High Energy Synchrotron Source (CHESS) using $\lambda = 0.899$ Å X-rays. X-ray patterns were recorded with two dimensional CCD detectors or Fuji image plates.

Bright field transmission electron microscopy (TEM) was used to examine the microphase separated morphologies formed by the side-chain LC-coil diblock copolymers in real-space. Bulk samples were studied using a JEOL 200CX operated at either 100 kV or 200 kV depending on the contrast present in each sample. Typically, condenser aperture #2 (300 μm), spot size #3, and objective aperture #4 (40 μm) were used during routine operation. In contrast to the cross-sectional thin films examined in

Chapter 2 or the ultrathin rod-coil samples studied in Chapter 3, the P(ILC-b-S) microtomed sections did not undergo significant deformation or mass loss in the electron beam. Beam damage, however, may have resulted in a loss of liquid crystalline or crystalline order within the PILC domains which were not observed by electron diffraction.

4.6 Results and Discussion

4.6.1 Side-chain LC-Coil Mesophases

Thin films of all the P(ILC-b-S) side-chain LC-coil block copolymers and the PILC homopolymer were observed by POM to become highly birefringent when cooled from the isotropic melt. These results confirm that the PILC block is a thermotropic LC despite the presence of the flexible PS block which for ILC-S29/107, ILC-S55/176, and ILC-S78/176 is greater than 100,000 g/mol. The specific mesophase formed by the PILC homopolymer was determined from WAXD patterns of oriented fiber samples (see Figure 4.2). Figure 4.2 shows a set of Bragg reflections resulting from a smectic layered structure (oriented along the fiber axis which is denoted by the arrow) with a layer spacing of 31 Å and two broad peaks which are due to the 4.4 Å (average) side-to-side packing distance of the mesogens within each layer. Because the layer reflections are oriented at 90° to the two broad peaks, the LC mesophase can be identified as the smectic A phase. The experimentally determined 31 Å smectic A layer spacing shows fair agreement with molecular modeling calculations of the fully extended side-group length, done by Guoping Mao using the software package Chem3D, which predict 26.8 Å. The discrepancy between the measured and predicted smectic A layer spacing is most likely caused by the presence of the flexible polyisoprene backbone which must also be

accommodated within the PILC domains and is expected to increase the distance between adjacent smectic A layers. In addition, Figure 4.2 shows that the PILC backbone was oriented along the fiber axis. WAXD was also used to investigate the mesophases formed by the P(ILC-b-S) side-chain LC-coil diblocks. In all cases, a smectic A mesophase was also observed with the same layer spacing of 31 Å. The smectic A-isotropic transition temperatures obtained from DSC for the P(ILC-b-S) diblocks are shown in the far right column of Table 4.1.

4.6.2 Side-chain LC-Coil Microdomain Morphologies

TEM and SAXD were used to investigate the microphase separated morphologies formed by the P(ILC-b-S) diblocks. The side-chain LC-coils ILC-S29/107 and ILC-S55/176 (f_{PILC} = 0.20 and 0.22, respectively), which have a minority PILC block, both form a microphase separated morphology consisting of hexagonally packed PILC cylinders surrounded by a PS matrix (see Figures 4.3a and 4.3b). The average domain sizes and PILC cylinder radii measured from TEM for ILC-S29/107 and ILC-S55/176 are 33 nm and 6 nm and 72 nm and 16 nm, respectively. The formation of a PILC cylinder morphology is expected for these volume fractions when compared to the cylinder composition range observed for typical P(S-b-I) diblock copolymers (f_{PS} = 0.17 to 0.28 or f_{PI} = 0.23 to 0.34) [9]. The PILC cylinder morphologies formed by ILC-S29/107 and ILC-S55/176, however, are the first observation of a smectic A minority LC component cylinder morphology in side-chain LC-coil block copolymers and contradict the predictions of Fischer et al. The higher degree of polymerization in the side-chain LC block has resulted in a smectic A phase rather than a nematic phase. A one dimensional line scan of a two dimensional SAXD pattern of ILC-S55/176 showed Bragg peaks in the ratio $1:\sqrt{3}:\sqrt{4}:\sqrt{7}$ which is characteristic of hexagonally packed cylinders. The domain

size and cylinder radius (based on volume fraction) measured from SAXD were 76 nm and 19 nm, respectively, which agrees well with TEM values. The location of the first zero in the cylinder form factor also yielded a value of the cylinder radius which agreed well with the value calculated from the volume fraction, f_{PILC}.

The side-chain LC-coil ILC-S78/176 (f_{PILC} = 0.29), which also has a minority PILC block, forms what appears to be a poorly ordered bicontinuous microphase separated morphology (see Figure 4.4). In contrast to bulk samples of cylinders or lamellae which typically have grains oriented in all directions, the same morphology is observed over the entire ILC-S78/176 sample. The observation of a bicontinuous structure at f_{PILC} = 0.29 is consistent with the volume fraction range in which the bicontinuous cubic morphologies have been observed in P(S-b-I) diblocks (f_{PS} = 0.28 to 0.34 or f_{PI} = 0.34 to 0.38). Given that ILC-S78/176 is the highest molecular weight side-chain LC-coil, the possibility exists that the bicontinuous morphology is actually a kinetically trapped nonequilibrium microdomain structure. The SAXD pattern obtained for ILC-S78/176 indicated a lack of long range order and was characterized by a single broad peak with a shoulder at higher Q. No definitive structural data could be extracted from the pattern.

Samples ILC-S60/66 and ILC-S62/59 (f_{PILC} = 0.45 and 0.49), respectively), which have nearly symmetric compositions, both form a microphase separated lamellar morphology consisting of alternating PILC and PS layers (see Figure 4.5 for ILC-S60/66 only). The average lamellar domain size obtained from TEM for ILC-S60/66 of 63 nm agrees well with the value determined from SAXD of 60 nm (L_{PILC} = 27 nm, L_{PS} = 33 nm). The lamellar domain size for ILC-S62/59 was determined from SAXD to be 59 nm (L_{PILC} = 29 nm, L_{PS} = 30 nm). SAXD patterns of both lamellar-forming side-chain LC-coils showed Bragg peaks with the characteristic ratio 1:2:3:4 expected for the lamellar morphology.

Samples ILC-S43/13 and ILC-S72/14 (f_{PILC} = 0.75 and 0.82), respectively), which each have a minority PS block, both form a microphase separated morphology consisting of hexagonally packed PS cylinders surrounded by the PILC matrix (see Figures 4.6a and 4.6b). The average domain sizes and PS cylinder radii measured from TEM for ILC-S43/13 and ILC-S72/14 are 32 nm and 8 nm and 38 nm and 8 nm, respectively. The formation of a PS cylinder morphology is expected for these volume fractions when compared to the cylinder composition range observed for typical P(S-b-I) diblock copolymers (f_{PS} = 0.66 to 0.77 or f_{PI} = 0.72 to 0.83). One dimensional line scans of SAXD patterns of ILC-S43/13 and ILC-S72/14 confirmed a hexagonally packed microdomain structure with Bragg peaks in the ratio $1:\sqrt{3}:\sqrt{4}:\sqrt{7}$. For ILC-S43/13 and ILC-S72/14, domain size and cylinder radius (based on volume fraction) measured from SAXD were 33 nm and 9 nm, and 38 nm and 8 nm respectively, which agrees quite well with TEM values. The morphologies and domain sizes for the side-chain LC-coil diblock copolymers obtained from TEM and SAXD are summarized in Table 4.2

Table 4.2 Summary of the morphologies and domain sizes for the side-chain LC-coil diblock copolymers obtained from TEM and SAXD.

Sample	f_{PILC}	Morphology	D_{TEM} (nm)	D_{SAXD} (nm)	R_{TEM} (nm)	R_{SAXD} (nm)
ILC-S29/107	0.20	PILC Cylinders	33	-----	6	-----
ILC-S55/176	0.22	PILC Cylinders	72	76	16	19
ILC-S78/176	0.29	*Chaotic Bicontinuous (?)*	-----	-----	-----	-----
ILC-S60/66	0.45	Lamellae	63	60, (D_{PILC}/D_{PS} :27/33)		
ILC-S62/59	0.49	Lamellae	-----	59, (D_{PILC}/D_{PS} :29/30)		
ILC-S43/13	0.75	PS Cylinders	32	33	8	9
ILC-S72/14	0.82	PS Cylinders	38	38	8	8

We thus find that the P(ILC-b-S) side-chain LC-coil block copolymers cast from solution form microphase separated morphologies which are more-or-less like the classical microdomain structures formed by traditional coil-coil block copolymers. The liquid crystallinity of the PILC block has not changed the morphology diagram significantly or produced any new microdomain structures. Unlike coil-coil block copolymers, however, the side-chain LC-coil block copolymers are able to self-assemble on two length scales. Within the PILC microdomains, the side-chain LC mesogens form a confined smectic A mesophase as shown by DSC and X-ray diffraction. How are the mesogens aligned with respect to the microdomain structure? SAXD of a macroscopically oriented film of ILC-S60/66 (see Figure 4.7) shows a set of inner Bragg reflections resulting from the lamellae and a pair of outer reflections resulting from the smectic A mesophase. Although the two reflections from the smectic A layer spacing are

quite broad, they are clearly oriented 90° to the lamellar reflections. As a result, the SAXD pattern conclusively shows that the side-chain LC mesogens have a homogeneous boundary condition with respect to the IMDS and are oriented in the direction of the lamellae.

Using the WAXD, SAXD, and TEM results for the P(ILC-b-S) diblocks, we can construct schematic molecular models for the cylinder and lamellar morphologies which illustrate how the side-chain LC-coil chains pack together (see Figure 4.8). By knowing the geometry of a given microdomain morphology and the orientation of smectic A layers within the PILC domains, the average number of side-chain LC mesogens per diblock copolymer chain can be calculated as an independent way of checking the schematic models. For these calculations, the area per chain at the IMDS must be calculated. The following expressions,

$$\sigma_{cyl} = \frac{2M_A}{R_{cyl}\rho_A N_{AV}} = \frac{2M_B(1-f_B)}{R_{cyl}\rho_B f_B N_{AV}}, \qquad (4.1)$$

$$\sigma_{lam} = \frac{2M_A}{D\rho_A f_A N_{AV}} = \frac{2M_B}{D\rho_B f_B N_{AV}}, \qquad (4.2)$$

which are easily derived, are applicable to AB diblock copolymers forming A cylinders and lamellae, respectively. The M_i, ρ_i, and f_i (where i = A or B) are the molecular weights, densities, and volume fractions of each block, respectively. R_{cyl}, D, and N_{AV} are the cylinder radius, lamellar domain spacing, and Avogadro's number, respectively. Besides the area per chain at the IMDS, the smectic A layer spacing of 31 Å and the lateral distance between mesogens of 4.4 Å are used in the calculations. The results of the calculations for the P(ILC-b-S) cylinder and lamellar morphologies are tabulated in Table 4.3.

Table 4.3 Summary of the actual (equal to the degree of polymerization of the PILC block) and calculated (from TEM and SAXD data) values of the number of side-chain LC mesogens per chain.

Sample	Morphology	σ_{TEM} (nm^2)	σ_{SAXD} (nm^2)	N_{PILC}^{TEM}	N_{PILC}^{SAXD}	N_{PILC}
ILC-S29/107	PILC Cylinders	14.00	-----	70	-----	72
ILC-S55/176	PILC Cylinders	9.90	8.40	130	130	136
ILC-S60/66	Lamellae	6.10	6.40	-----	140	148
ILC-S62/59	Lamellae	-----	6.20	-----	150	153
ILC-S43/13	PS Cylinders	5.20	4.60	100	100	106
ILC-S72/14	PS Cylinders	5.60	5.60	170	170	178

The close agreement between the actual and calculated values of the number of side-chain LC mesogens per diblock chain provides further support that the proposed schematic chain packing models of the P(ILC-b-S) morphologies are indeed correct.

4.6.3 Formation of Side-chain LC-Coil Morphologies

A rigorous theory which adequately explains the equilibrium microdomain structures in side-chain LC-coil block copolymers has yet to be developed. The experimentally observed morphologies, however, may be a direct reflection of the process by which they were formed. All of the side-chain LC-coil morphologies were essentially classical cylinder or lamellar microdomain morphologies. Unlike the P(HIC-b-S) rod-coils in which the rod block dominated self-assembly, the smectic A-forming PILC block did not impart any long range orientational order to the side-chain LC-coil morphologies. These characteristics suggest that when the P(ILC-b-S) diblocks are cast

from solution, microphase separation into PILC and PS microdomains occurs first and is then followed by an isotropic-smectic A LC transition which takes place within the confined solvent swollen PILC domains. Based on this proposed pathway and the experimental results, a schematic strong segregation limit morphology diagram in the variables χN and f_{PILC} can be constructed for the P(ILC-b-S) side-chain LC-coil system (see Figure 4.9). The points indicate the locations of the seven side-chain LC-coil diblock copolymers scaled relative to their total molecular weights. The phase boundaries are approximate. Essentially, only lamellar and hexagonally packed cylindrical morphologies are experimentally observed over the ordered region of the morphology diagram. The morphology diagram shown in Figure 4.9 assumes that the PILC block has already undergone its isotropic-smectic A transition. In reality, the isotropic-smectic A transition depends on the PILC block molecular weight, the microdomain structure, and f_{PILC}. As a result, a single universal morphology diagram is strictly no longer possible. However, in practice, one should be able to determine the morphology of the side-chain LC-coil given its molecular weight and composition.

(A)

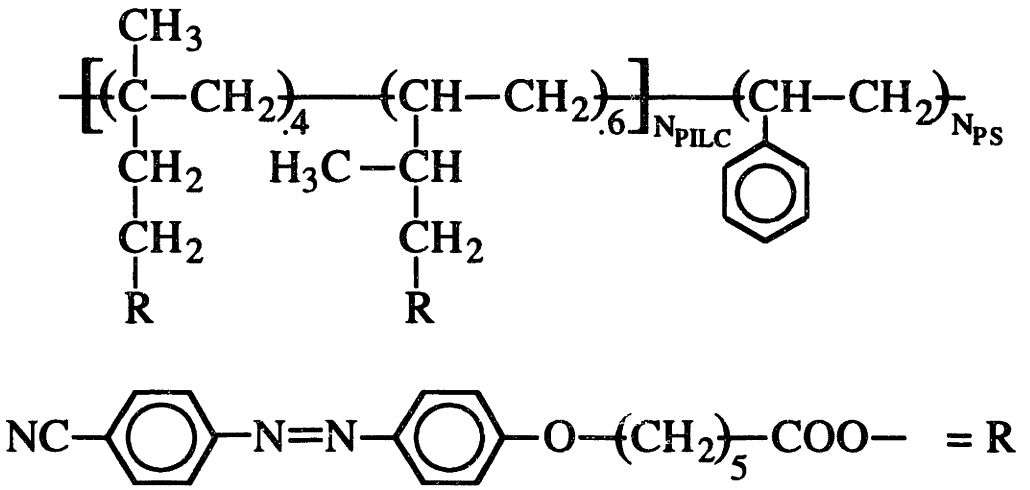

(B)

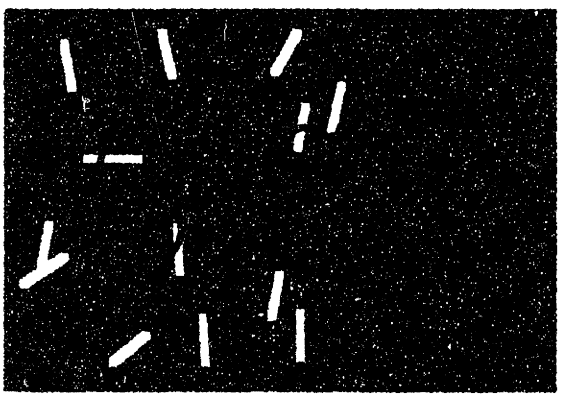

Figure 4.1 (A) Chemical formula of the P(ILC-b-S) side-chain LC-coil diblock copolymer. PILC is the LC block and PS the flexible coil block. The N_{PILC} and N_{PS} values for the samples studied are listed in Table 4.1. (B) Schematic drawing of the side-chain LC-coil molecule in which the PILC and PS blocks are depicted as a flexible chain polymer with pendant mesogens and a Gaussian coil, respectively.

Figure 4.2 **WAXD pattern obtained from an oriented fiber sample of ILC78 which shows a smectic A mesophase oriented along the fiber axis (arrow). The inner Bragg reflections indicate a smectic arrangement of the mesogens with a layer spacing of 31 angstroms. The two outer peaks show that the mesogens are oriented normal to the layers and have a side–to–side packing distance of 4.4 angstroms.**

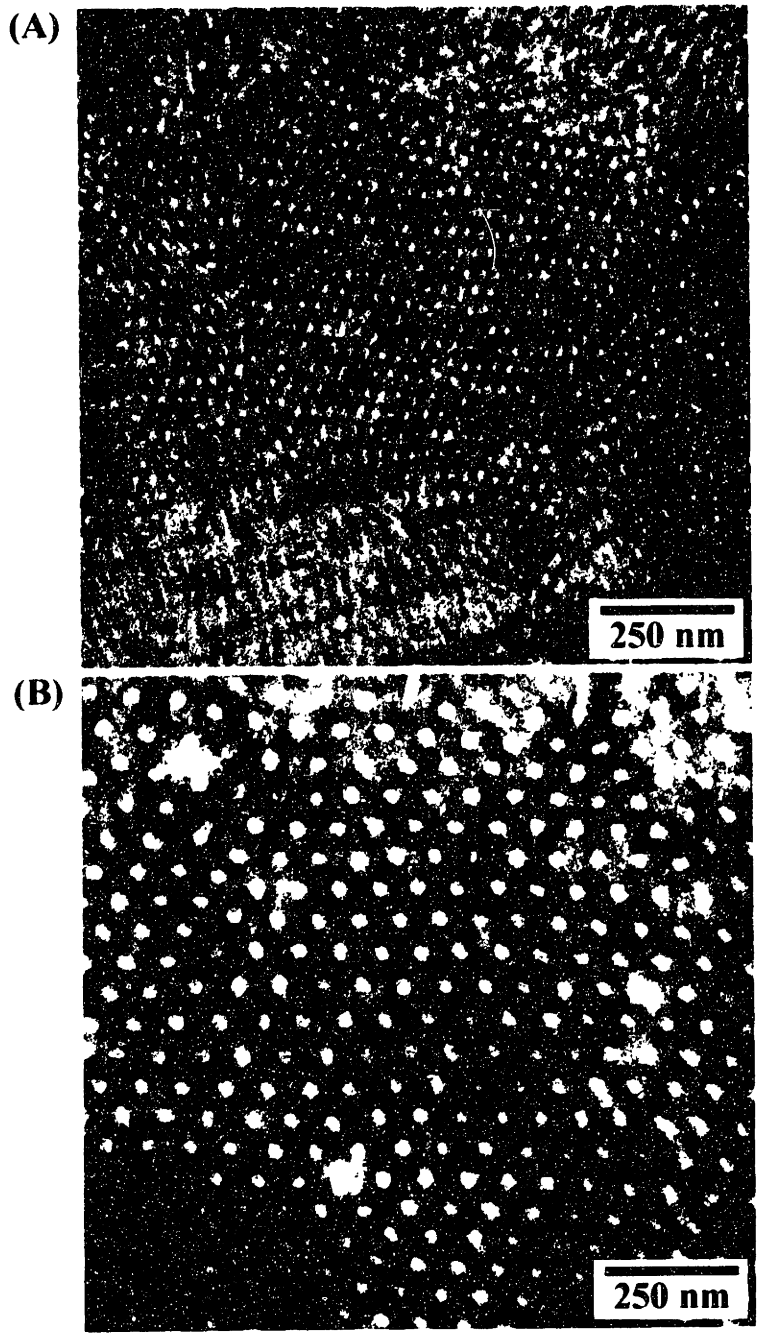

Figure 4.3 **Bright–field TEM micrographs of the cylinder morphologies formed by the P(ILC–b–S) side–chain LC–coils (A) ILC–S29/107 and (B) ILC–S55/176, which have PILC volume fractions of $f_{PILC} = 0.20$ and 0.22, respectively. The light and dark regions are the PILC and RuO_4 stained PS domains, respectively.**

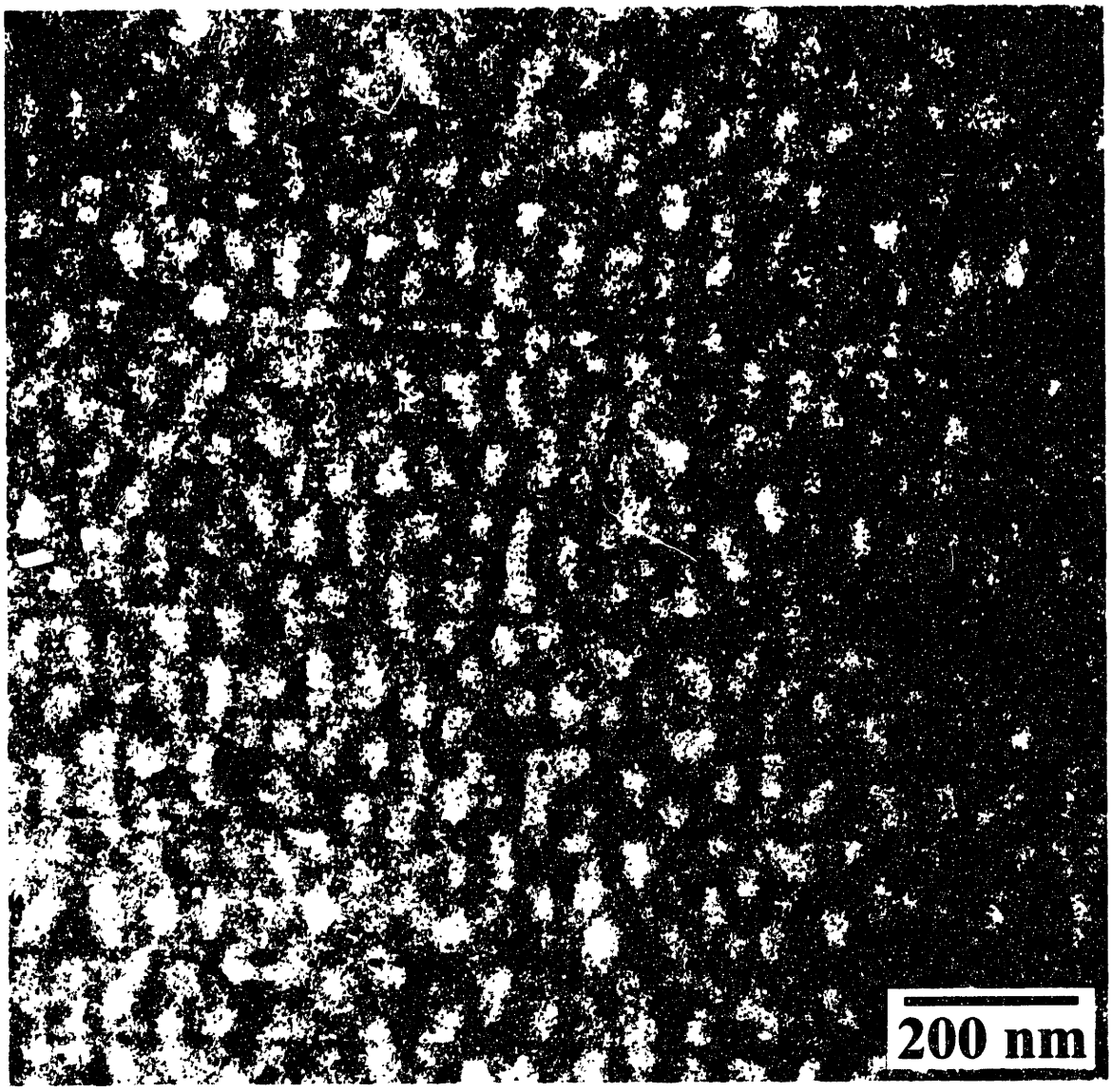

Figure 4.4 **Bright–field TEM micrograph of the bicontinuous morphology formed by the P(ILC–b–S) side–chain LC–coil ILC–S78/176 which has a PILC volume fraction of $f_{PILC} = 0.29$. The light and dark regions are the PILC and RuO_4 stained PS domains, respectively.**

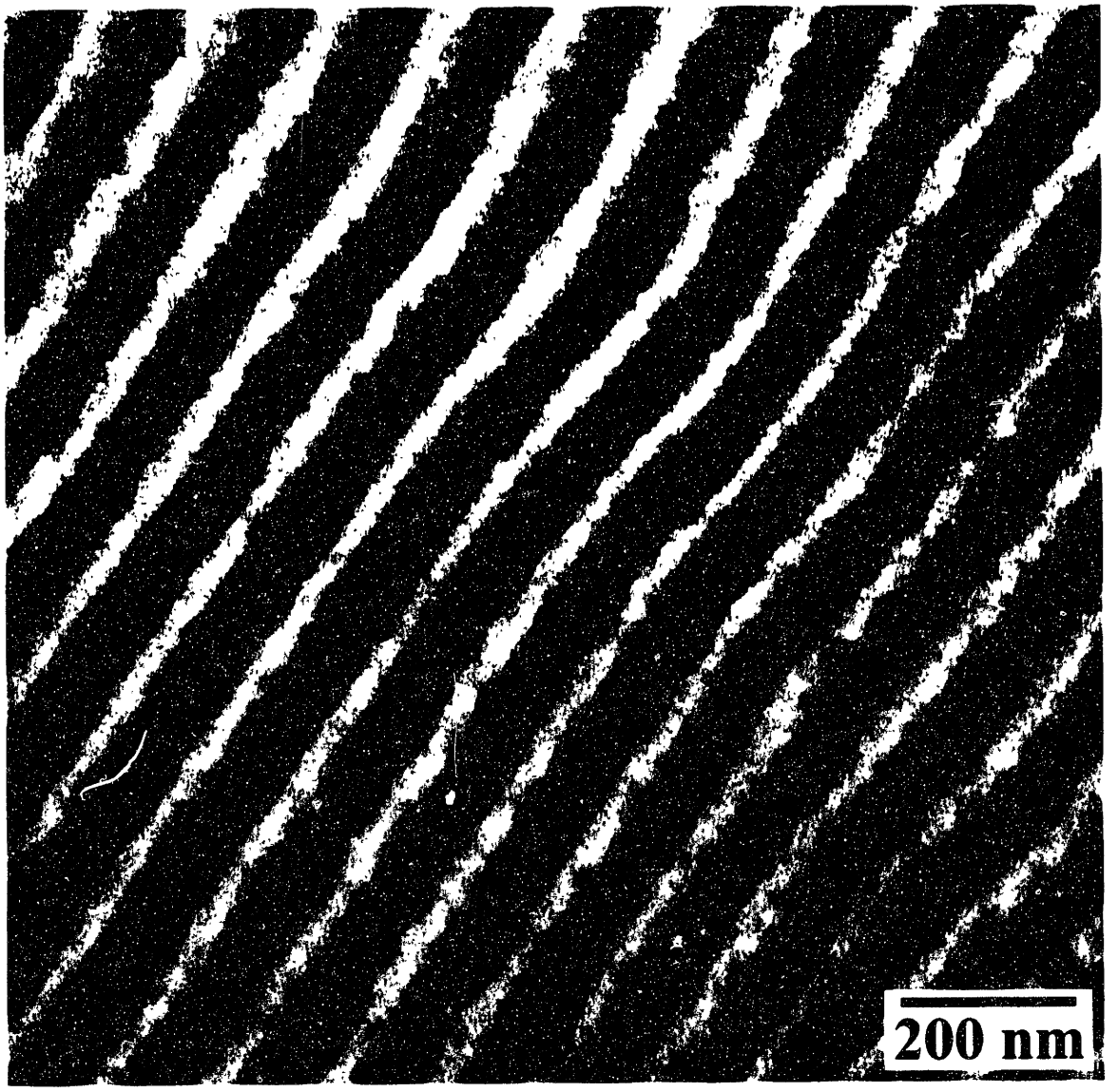

Figure 4.5 **Bright–field TEM micrograph of the lamellar morphology formed by the P(ILC–b–S) side–chain LC–coil ILC–S60/66 which has a PILC volume fraction of $f_{PILC} = 0.45$. The light and dark regions are the PILC and RuO_4 stained PS domains, respectively.**

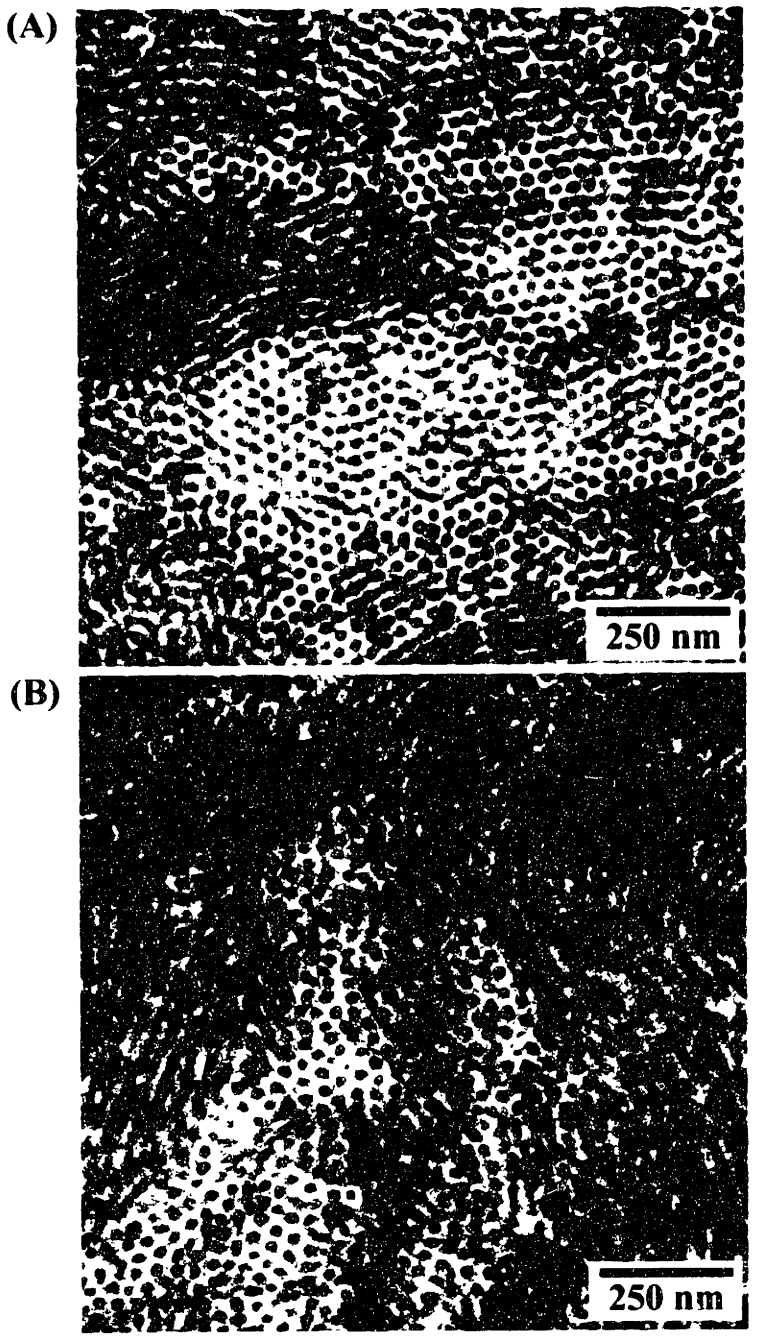

Figure 4.6 **Bright–field TEM micrographs of the cylinder morphologies formed by the P(ILC–b–S) side–chain LC–coils (A) ILC–S43/13 and (B) ILC–S72/14, which have PILC volume fractions of $f_{PILC} = 0.75$ and 0.82, respectively. The light and dark regions are the PILC and RuO_4 stained PS domains, respectively.**

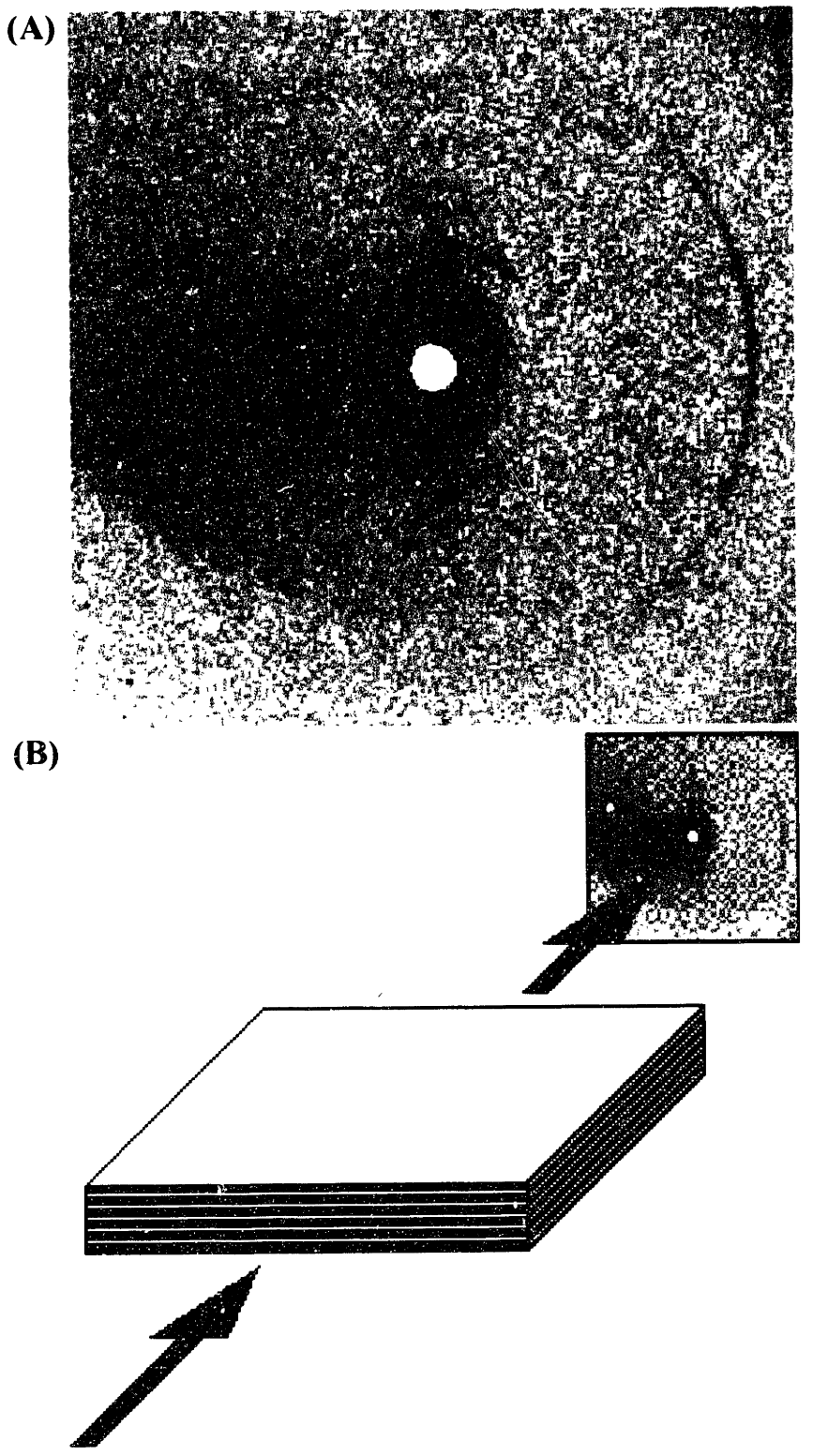

Figure 4.7 **(A) SAXD pattern of a macroscopically oriented film of ILC–S60/66. (B) Schematic diagram of the orientation of the film with respect to the X–ray beam.**

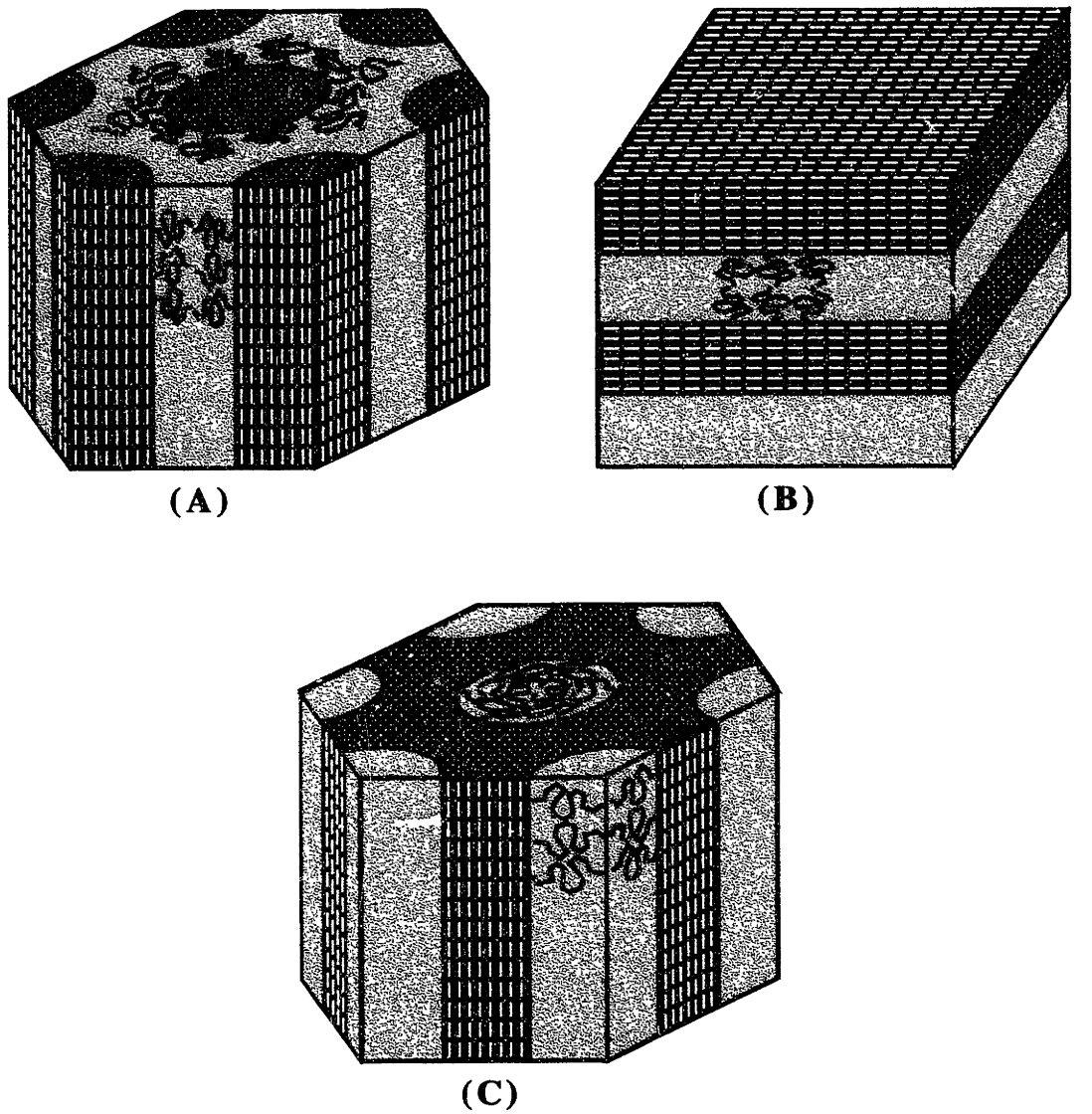

Figure 4.8 Schematic models showing the packing arrangement of the side-chain LC-coil chains in the (A) PILC cylinders, (B) lamellar, and (C) PS cylinder morphologies. In the figures, only the mesogens (white) of the PILC block are shown. A representative number of PS (black) chains are also drawn.

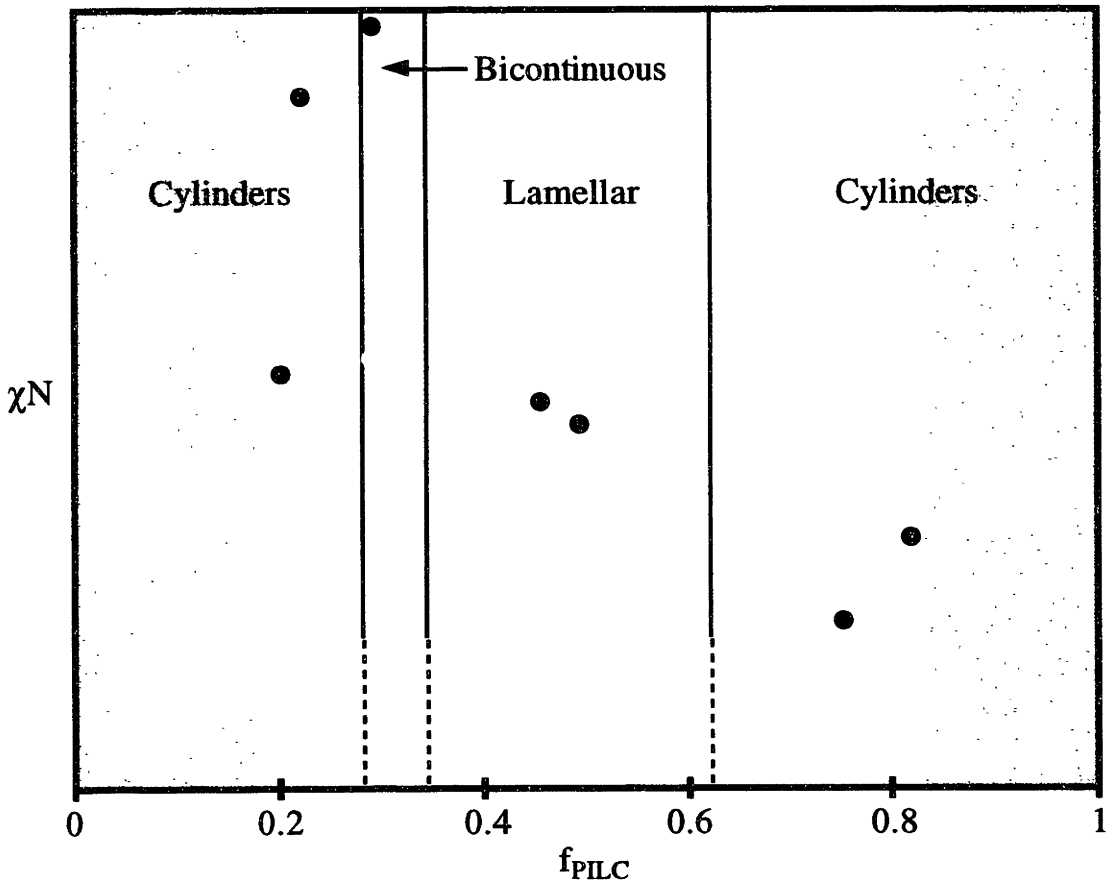

Figure 4.9 Morphology diagram for the P(ILC-b-S) side-chain LC-coil diblock copolymer system. The points correspond to the seven synthesized diblocks. The shaded areas indicate regions of the morphology diagram which have not been experimentally investigated. The vertical lines indicate approximate phase boundaries in the SSL.

Chapter 5: Predicting the Morphology and Optical Properties of LC-Coil Block Copolymers Using Symmetry

5.1 Introduction

In Chapters 3 and 4, we saw that a LC block affects the morphology of a block copolymer differently depending on the particular nature of the LC component. In the rod-coil system, the morphology diagram was drastically altered from the equilibrium morphology diagram found for coil-coil diblock copolymers. Some morphologies remained, new ones appeared, and others were completely absent. In contrast, for the side-chain LC-coil block copolymers, the morphology diagram was only slightly perturbed from the coil-coil block copolymer morphology diagram. Phase boundaries were shifted, and some morphologies appeared to be absent but no new microstructures were discovered. The morphologies presented in Chapters 3 and 4 represent only two particular LC-coil block copolymer systems. A multitude of different LC block copolymer systems have yet to be synthesized and investigated which will, undoubtedly, exhibit differing microstructures. In Chapter 5, a framework is developed which allows LC-coil block copolymers to be studied in a systematic way. By knowing the symmetry groups of both the traditional microdomain morphologies and the liquid crystal phases, the preferred anchoring conditions of the LC block at the IMDS, and the likelihood of any defects within the LC domains, one can make general predictions about the most probable morphologies a LC block copolymer can form. In addition, the symmetry framework can also be used to directly determine the optical properties of a particular LC block copolymer morphology. As concrete examples, the nematic LC-coil and smectic A LC-coil diblock copolymer systems are examined using the framework and the

conclusions compared with the results of the P(HIC-b-S) and P(ILC-b-S) research. The underlying principles, however, can be applied to any LC block copolymer system.

5.2 General Principles

5.2.1 Classical Microdomain Structures and LC Phases

As we saw in Chapters 3 and 4, the morphology formed by a LC block copolymer combines structural features of both traditional block copolymers and liquid crystals. As a consequence, symmetries common to both the microphase separated morphology and the liquid crystal are present in the ultimate equilibrium structure. Like any self-assembling block copolymer, an AB LC-coil block copolymer will microphase separate into a periodic microstructure that reflects the two inherent molecular length scales of the block copolymer chain, $\sqrt{\overline{r_A^2}}$ and $\sqrt{\overline{r_B^2}}$. The particular morphology, however, will depend on the composition and the degree of segregation in a much more complicated way than that of a coil-coil diblock copolymer. Even so, the classical microdomain structures previously observed for coil-coil diblocks (lamellae, hexagonally-packed cylinders, and BCC spheres) are still good candidate morphologies because they can partition space efficiently and are spatially periodic. As was discussed in Chapter 2 (see Table 2.2), these morphologies have one, two, or three dimensional translational order and can be described by well defined symmetry properties.

In addition to being a block copolymer, a LC-coil also has a LC block which can form liquid crystalline phases. Liquid crystalline materials, due to their shape anisotropy, possess orientational order. Although they lack full three-dimensional translational order, liquid crystals still possess well defined symmetry properties. In 1922, Friedel proposed the original classification of liquid crystalline materials [124]. The classical LC phases

are the nematic, the cholesteric (twisted nematic or nematic*), and the smectic. In a nematic liquid crystal, the molecules, on average, are oriented along a common direction called the director $\hat{\mathbf{n}}$ (see Figure 5.1a). The corresponding group of symmetries therefore includes all (continuous) translations, an ∞-fold rotation axis parallel to the average director, an infinite set of 2-fold axes perpendicular to the director, an infinite set of mirror planes parallel to the director, and a mirror plane perpendicular to the director. In addition, inversion centers are located at the intersections of the 2-fold axes and the mirror planes. The point group symmetry of the nematic phase is continuous and equal to $\frac{\infty}{m}$m m everywhere.

The twisted nematic phase is formed by chiral molecules and is similar to the nematic phase in that the molecules locally orient along a common director. However, the presence of a net dipole on each molecule and the shape anisotropy of the molecule induces the overall director to twist in a helical pattern (see Figure 5.1b) so as to cancel the total far field dipole moment for the material as a whole and increase the packing density. Unlike the nematic phase, however, the twisted nematic phase possesses one dimensional translational symmetry along the axis of precession with a translation vector equal to the half the pitch ($\hat{\mathbf{n}} = -\hat{\mathbf{n}}$). In addition, two-fold rotation axes perpendicular to the helical axis and parallel with the local director exist at every point. The resulting point group symmetry of the twisted nematic phase is simply 2 and is also continuous.

In the smectic LC phase, the molecules stack in layers which possess long-range one-dimensional translational order (with an interlayer spacing of d) normal to the layers. Since liquid crystals were first discovered, many types of smectic phases have been observed and classified (e.g. smectic A, B, C, C*, F, I, L, and O). The smectic A, C, C*, and O phases differ primarily in the way the molecules are oriented with respect to the layer normal. In the smectic B, F, I, and L phases (also known as the hexatic phases), however, the molecules also possess positional order within layers in terms of their side-

to-side packing. The hexatic phases are essentially three dimensional crystals with finite long range order. Of the smectic phases listed above, only the smectic A, C, C*, and O phases have any relevance to the thesis. As a result, we will limit our discussion of the symmetries of smectic liquid crystals to these phases alone.

In the smectic A phase, the average director coincides with the layer normals and the centers of gravity of the molecules are ordered within the layer with a liquid-like side-to-side packing (see Figure 5.2a). Mirror planes are located everywhere parallel to the layer normal. Mirror planes perpendicular to the layer normal are located between layers and at the midpoints of each layer. Rotational symmetries consist of ∞-fold rotation axes everywhere parallel to layer normal and 2-fold rotation axes perpendicular to the layer normal located between each layer and at the midpoint of each layer. Inversion centers are located at the intersection of the two-fold axes and the mirror planes, which are parallel to the average director. The highest point group symmetry of the smectic phase is $\frac{\infty}{m}$m m.

In the smectic C and C* phases, the molecules still have liquid-like packing within layers but the director is now tilted by a fixed angle with respect to the layer normal (see Figures 5.2b and 5.2c). For chiral molecules which form the smectic C* phase, the director undergoes a further helical precession about the layer normal from layer to layer. In comparison with the smectic A phase, the smectic C phase has only 2-fold rotation axes which are perpendicular to both the layer normal and the director and are located between each layer and at the midpoint of each layer. In addition, only one mirror plane perpendicular to the 2-fold axes exists. Because of the chiral nature of the smectic C* phase, only the 2-fold axes remain. As a result, the highest point group symmetries for the smectic C and C* phases are $\frac{2}{m}$ and 2, respectively.

While very similar to the smectic C, the smectic O phase is a more complicated structure (see Figure 5.2d) in which the director undergoes a reorientation from layer to

layer. The chevron-like arrangement of molecules gives rise to 2-fold rotation axes, with perpendicular mirror planes, located at the midpoints of each layer which are perpendicular to both the layer normal and the director. Additional 2-fold axes are oriented perpendicular to the first set of 2-fold axes but are located in between layers. The alternating nature of the smectic O structure gives rise to 2_1 screw axes parallel to the layer normal. Mirror planes perpendicular to the screw axes are also located in between layers. The highest point group symmetry of the smectic O phase is thus $\frac{2}{m}\frac{2}{m}\frac{2}{m}$. The symmetry characteristics for all the LC phases discussed above are summarized in Table 5.1.

Table 5.1 Summary of the space groups, highest point group symmetries, and type of translational order which characterize the common liquid crystal phases.

LC Phase	Space Group	Highest Point Group	Translational Order
Nematic	$P\frac{\infty}{m}mm$	$\frac{\infty}{m}mm$	Continuous
Nematic*	P2	2	1D
Smectic A	$P\frac{\infty}{m}mm$	$\frac{\infty}{m}mm$	1D
Smectic C	$P\frac{2}{m}$	$\frac{2}{m}$	1D
Smectic C*	P2	2	1D
Smectic O	$P222_1$	$\frac{2}{m}\frac{2}{m}\frac{2}{m}$	1D
Columnar	$P\frac{6}{m}mm$	$\frac{6}{m}\frac{2}{m}\frac{2}{m}$	2D

The LC phases discussed above are typically formed by rod-shaped molecules. Plate-like molecules also have shape anisotropy which allows them to form a discotic nematic LC phase as well as columnar LC phases which possess two dimensional

translational order. In the columnar phases (see Table 5.1), the plate-like molecules stack in columns which are themselves arranged in two dimensional crystal lattices.

Given the above discussion on the symmetries of the classical microdomain structures and the liquid crystal phases, a general statement can be made about LC-coil block copolymers. A LC-coil block copolymer will be able to form a classical microdomain structure as long as the point group symmetry of the LC phase within the LC domains is sufficient to maintain overall translational symmetry of the morphology. Thus on symmetry considerations alone, one would also predict LC block copolymers to form microdomain structures in which the LC phase maximizes the overall point group symmetry of the morphology.

5.2.2 The IMDS, Anchoring Conditions, and Defects

Understanding the symmetries of the classical microdomain structures and the LC phases is extremely useful but does not provide the entire picture. Only when symmetry arguments are combined with knowledge of the intermaterial dividing surface (IMDS), anchoring conditions of the LC block at the IMDS, and any defects within the LC domains can we make reliable predictions about the morphologies a LC-coil block copolymer may form. In strongly segregated microphase separated LC-coil block copolymers, the composition profile across the interface is quite narrow. As a result, the interfacial region between the LC and coil domains can be well-represented by an IMDS (see Figure 5.3), which shares the same translational symmetries as that of the microdomain structure. The shape of the IMDS can be described by its mean (H) and Gaussian (K) curvatures. Minimal (H = 0) and constant mean curvature surfaces have been found to be good candidate models for the IMDS of observed microdomain structures [22].

Three fundamental descriptors determine the shape of the IMDS adopted by a LC-coil block copolymer: the preferred interfacial curvature, the interfacial area per molecule, and the average microdomain size (of each block). All three of these quantities are interrelated through the molecular weight and volume of each block and are often frustrated in the compromise structures that form. For example, in coil-coil diblocks, the preferred interfacial area of a block varies with the block $M_w^{1/3}$, whereas, in rod-like liquid crystalline blocks, the cross sectional area per block is independent of molecular weight. The preferred interfacial curvature at the IMDS, in turn, is determined by the mismatch in the volume and preferred interfacial area of each block. In addition, in strongly segregated coil-coil diblocks, domain dimensions, which also influence interfacial curvature, scale with $M_w^{2/3}$ whereas for a rod-like block, domain dimensions are proportional to M_w^1.

The director field within a LC microdomain typically has a preferred orientation with respect to the IMDS which results in either homogeneous (parallel) or homeotropic (perpendicular) anchoring conditions. In many cases, the translational symmetry of the overall morphology and the particular anchoring conditions of the LC block can be satisfied by more than one configuration of the director with respect to the IMDS. One example of this situation arises for LC cylinders which obey homogeneous anchoring conditions. In such cases, the LC director will prefer to be parallel to the tangent direction of the normal section which is characterized by the largest radius of curvature because this orientation minimizes local distortions of the director field. At any given point on the IMDS, a normal section is given by the intersection of a normal plane (a plane containing the normal vector at that point) with the IMDS. This constraint becomes increasingly important as the LC domain size becomes smaller in comparison to the characteristic size of the LC block (end-to-end distance for rod-coils and mesogen length for side-chain LC-coils).

Microdomain structures that have a highly curved IMDS such that the normal to the surface varies in a three dimensional manner cannot always accommodate the LC director field without the creation of periodic defects and/or boundary regions of disordered material. The particular architecture of a LC block copolymer becomes important. LC blocks with small mesogenic units connected by flexible spacers (either main-chain or side-chain) allow more freedom for the mesogens to better align with the IMDS and uniformly fill domains of variable thickness and orientation. In contrast, LC block copolymers containing rod-like blocks experience significant packing frustration in microdomain structures characterized by a highly curved IMDS. In addition, for flexible spacer-containing LC blocks, most of the mesogenic units are not adjacent to the IMDS (particularly for high MW blocks) whereas, for the rod-like LC blocks, every mesogenic block is directly coupled to the IMDS.

The inability of the LC block to pack into certain microdomain geometries can result in prohibitively high energetic penalties which suppress the formation of the LC state. For example, consider how an interconnected microdomain structure (such as a bicontinuous cubic morphology, see Figure 5.4a) influences a minority component side chain-LC block. While the flexible spacer and flexible backbone chain allow the mesogens to follow the contours of the labyrinthine networks, the anchoring condition of the mesogen with respect to the A/B interface can only be maintained by the incorporation of point defects arrayed periodically in space (see Figure 5.4b). The possibility exists that certain microdomain geometries can never form in LC diblock copolymers due to the excessive Frank curvature elasticity energy penalties imposed by the required defects. As a result, in addition to maintaining translational symmetry and the anchoring conditions of the LC block, a LC block copolymer tends to form microdomain structures which also minimize the creation of periodic line and point defects within the LC domains. Of course, the presence of defects depends greatly on the

particular system considered. In chiral liquid crystals, "blue phases" which consist of periodic arrays of defect lines have been observed previously [125].

5.3 Morphology and Optical Property Classification Scheme

5.3.1 Nematic LC-Coil Block Copolymers

Having laid out the general principles behind a LC-coil block copolymer symmetry framework, we can now apply the framework to our first example, a nematic LC-coil block copolymer. The most probable morphologies formed by a nematic LC-coil block copolymer and their corresponding optical properties were determined using the following guidelines:

Step 1: Choose a particular microdomain morphology

Step 2: Determine if the LC block is the minority or majority component

Step 3: Determine if the LC block obeys homogeneous or homeotropic anchoring conditions at the IMDS

Step 4: Determine the orientation of the LC director within the microdomain morphology which simultaneously satisfies the anchoring conditions at the IMDS, results in the highest point group symmetry of the composite morphology, and creates the fewest number of point or line defects within the LC domains

Step 5: Determine the space group of the composite morphology and use Table 2.1 and Table 2.2 to deduce the corresponding optical class

Step 6: In most cases, Table 2.3 can then be used to calculate the principal refractive indices in the long wavelength limit

Table 5.2 lists the most probable morphologies predicted for an AB nematic LC-coil block copolymer using the above classification scheme. For each morphology, the space group, optical class, expressions for the principal refractive indices, and a description of the defects in the LC domains (if any) are listed. Schematic diagrams for each of these morphologies can be found in Figures 5.5a to 5.5g.

Table 5.2 Summary of the space group, optical class, expressions for the principal refractive indices, and defects present in the LC domain for the nematic LC-coil block copolymer morphologies predicted using the LC block copolymer symmetry framework.

LC Anchoring Conditions	Lamellar	A (LC) Cylinders	B (Coil) Cylinders	A (LC) Spheres	B (Coil) Spheres
Homogeneous Nematic	$P\frac{2}{m}mm$	$P\frac{6}{m}mm$	$P\frac{6}{m}mm$		
	Biaxial	Uniaxial	Uniaxial		
	$n_x=n_o(n_o^A, n_B)$ $n_y=n_o(n_e^A, n_B)$ $n_z=n_e(n_o^A, n_B)$	$n_o=n_o(n_o^A, n_B)$ $n_e=n_e(n_e^A, n_B)$	$n_o=n_o(n_B, n_o^A)$ $n_e=n_e(n_B, n_e^A)$		
	No defects	No defects	No defects		
Homeotropic Nematic	$P\frac{\infty}{m}m$	$P\frac{6}{m}mm$	$P\frac{6}{m}mm$	$Im\bar{3}m$	
	Uniaxial	Uniaxial	Uniaxial	Isotropic	
	$n_o=n_o(n_o^A, n_B)$ $n_e=n_e(n_e^A, n_B)$	$n_o=n_o(\overline{n_A}, n_B)$ $n_e=n_e(n_o^A, n_B)$	$n_o=n_o(n_B, \overline{n_A})$ $n_e=n_e(n_B, n_o^A)$	$n=n(\overline{n_A}, n_B)$	
	No defects	+1 defects in cylinder centers	-1/2 defects at Wyckoff 2b sites	Point defects in sphere centers	

The principal refractive indices for each morphology can be calculated using the expressions in Table 5.2 by substituting the indices in parentheses for the values of n_A and n_B, respectively, which appear in the EMT equations listed in Table 2.3 for a given microdomain morphology. The expressions in Table 5.2 were derived assuming that the optically uniaxial nematic LC A block is characterized by n_o^A and n_e^A and the coil B block by a single isotropic refractive index n_B, respectively. In the above expressions, $\overline{n_A}$ is the effective refractive index of the nematic LC block which is obtained by averaging over all orientations of the LC director. The effective refractive index can be calculated exactly according to the following relations,

$$\overline{n_A}(n_o^A>n_e^A) = \frac{\sqrt{n_o^{A2} - n_e^{A2}}}{\tan^{-1}\sqrt{\frac{n_o^{A2} - n_e^{A2}}{n_e^{A2}}}},$$

$$\overline{n_A}(n_o^A<n_e^A) = \frac{\sqrt{n_e^{A2} - n_o^{A2}}}{\tanh^{-1}\sqrt{\frac{n_e^{A2} - n_o^{A2}}{n_e^{A2}}}}. \qquad (5.1)$$

A useful approximation for the effective refractive index which can be obtained from a Taylor expansion of Equation 5.1 around either n_o^A or n_e^A is $\overline{n_A} \approx (2n_o^A + n_e^A)/3$. As an example, to calculate the principal refractive indices of the cylinder morphology with a majority nematic LC component which obeys homogeneous boundary conditions, one would evaluate the expressions for the ordinary and extraordinary refractive indices listed in Table 2.3 for the cylinder morphology with n_A -> n_B and n_B -> n_o^A and n_A -> n_B and n_B -> n_e^A, respectively.

Of the morphologies listed in Table 5.2, the lamellar morphologies and the two cylinder morphologies for homogeneously aligned nematic LC blocks are the most likely

to be formed. These morphologies satisfy the anchoring conditions without creating defects within the LC domains. The remaining cylinder and LC sphere morphologies are less probable because they involve the incorporation of point or line defects within either the spherical LC domain or the LC cylinders, respectively. For nematic LC-coil block copolymers, the defects confined to the LC domains cause highly localized distortions of the director field which increase the Frank elasticity energy (resulting from bend, twist, and splay) and thus the energy of the entire system.

The predictions made above for a nematic LC-coil block copolymer can be directly compared to the P(HIC-b-C) rod-coil block copolymer morphologies discussed in Chapter 3. PHIC, itself, is known to be a lyotropic nematic LC polymer. In addition, the PHIC block is a main-chain rodlike polymer directly connected to the PS block by a single junction point. Homogeneous alignment of the PHIC block would result in severe distortion of the coil block and is thus highly unlikely. Therefore, a priori, homeotropic anchoring conditions are expected. As discussed above, the lamellar morphology is the most likely predicted microstructure for the P(HIC-b-S) rod-coil system. With the exception of the LA morphology (f_{PHIC} = 0.42), the remaining P(HIC-b-S) rod-coil morphologies (f_{PHIC} = 0.73 to 0.98) were indeed lamellar structures. No cylinder, sphere, or bicontinuous cubic structures were observed. The LA morphology does not fall precisely into one of the traditionally observed microdomain structures because it lacks translational symmetry, which suggests that it may be a nonequilibrium structure or a consequence of polydispersity effects. Statistically speaking, however, the LA morphology has the same symmetries as the nematic phase and can be assigned the space group $P\frac{\infty}{m}m\,m$ with uniaxial optical properties.

The symmetry framework failed to predict rod tilt which was present in all the P(HIC-b-S) rod-coil morphologies. Modeling the PHIC block as a nematic LC with homeotropic boundary conditions was clearly too restrictive. However, if the anchoring

conditions are relaxed and the framework is applied to smectic C LC-coil and smectic O LC-coil block copolymer systems, layered structures similar to the ZZ and AH morphologies are predicted. The zig-zag lamellar, and arrowhead morphologies have the space groups $P\frac{2}{m}$, and $P2_12_12_1$, respectively. As a result, in the long wavelength limit, each of these morphologies has biaxial optical properties where $n_x = n_o(n_o^A, n_B)$, $n_y = n_o(n_A(\pi/2-\theta), n_B)$, and $n_z = n_e(n_A(\theta), n_B)$ for these lamellar structures. In these relations, θ is the tilt angle of the PHIC rods in the various morphologies and $n_A(\varphi) = \left(\frac{\sin^2\varphi}{n_o^{A2}} + \frac{\cos^2\varphi}{n_e^{A2}}\right)^{-\frac{1}{2}}$. In reality, however, given its large domain size, the AH morphology is a one dimensional photonic crystal in which each PHIC domain is a homogeneous layer. The PS block will not influence the optical properties significantly given its low volume fraction.

5.3.2 Smectic A LC-Coil Block Copolymers

Smectic A LC-coil block copolymers are the second LC block copolymer system we will investigate using the symmetry framework. Since the smectic A phase shares the same point group symmetry as the nematic phase, the predicted morphologies are essentially the same as those listed in Table 5.2 except for one difference. Besides the tendency for the molecules to align themselves along the director, in smectic A liquid crystals, bend and twist distortions of the director are energetically much more costly than splay distortions because of the additional constraint that the director be normal to the layers [126]. As a result, distortions which result in changes of the equilibrium layer spacing d are highly unfavorable.

The most probable morphologies predicted for smectic A LC-coil block copolymers are still the two lamellar morphologies and the cylinder morphologies for homogeneous alignment of the smectic A LC. The cylinder and LC sphere morphologies

for homeotropic alignment of the smectic A LC, which have line or point defects within the LC domains, are plausible but less likely structures. In these morphologies, especially the coil cylinder morphology, conceivably, a smectic A-nematic transition could be induced by the confinement and boundary conditions in order to relieve layer deformation. In terms of optical properties, smectic A liquid crystals are uniaxial materials and can also be characterized by an ordinary and extraordinary refractive index n_o^A and n_e^A, respectively. As a result, the expressions for the principal refractive indices of the various morphologies will be identical to those found for nematic LC-coil block copolymers. Table 5.3 summarizes the results obtained for an AB smectic A LC-coil block copolymers. Schematic diagrams for each of these morphologies can be found in Figures 5.6a to 5.6g.

Table 5.3 Summary of the space group, optical class, expressions for the principal refractive indices, and defects present in the LC domain for the smectic A LC-coil block copolymer morphologies predicted using the LC block copolymer symmetry framework.

LC Anchoring Conditions	Lamellar	A (LC) Cylinders	B (Coil) Cylinders	A (LC) Spheres	B (Coil) Spheres
Homogeneous Smectic A	$P\frac{2}{m}mm$	$P\frac{6}{m}mm$	$P\frac{6}{m}mm$		
	Biaxial	Uniaxial	Uniaxial		
	$n_x=n_o(n_o^A, n_B)$ $n_y=n_o(n_e^A, n_B)$ $n_z=n_e(n_o^A, n_B)$	$n_o=n_o(n_o^A, n_B)$ $n_e=n_e(n_e^A, n_B)$	$n_o=n_o(n_B, n_o^A)$ $n_e=n_e(n_B, n_e^A)$		
	No defects	No defects	No defects		
Homeotropic Smectic A	$P\frac{\infty}{m}m$	$P\frac{6}{m}mm$	$P\frac{6}{m}mm$	$Im\bar{3}m$	
	Uniaxial	Uniaxial	Uniaxial	Isotropic	
	$n_o=n_o(n_o^A, n_B)$ $n_e=n_e(n_e^A, n_B)$	$n_o=n_o(\overline{n_A}, n_B)$ $n_e=n_e(n_o^A, n_B)$	$n_o=n_o(n_B, \overline{n_A})$ $n_e=n_e(n_B, n_o^A)$	$n=n(\overline{n_A}, n_B)$	
	No defects	+1 defects in cylinder centers	-1/2 defects at Wyckoff 2b sites	Point defects in sphere centers	

Good agreement is found between the morphologies predicted in Table 5.3 and the experimentally observed P(ILC-b-S) side-chain LC-coil block copolymer morphologies discussed in Chapter 4. The PILC homopolymer, which has pendant side-chain azobenzene mesogens separated from the isoprene backbone by a flexible $(CH_2)_5$ sequence, is a thermotropic liquid crystal which exhibits a smectic A phase at room

temperature. In addition, as we saw in Chapter 4, the PILC block exhibits homogeneous boundary conditions at the IMDS. Therefore, the lamellar and cylinder morphologies listed in the first row of Table 5.3 are the most probable morphologies predicted for the P(ILC-b-S) system. With the exception of the morphology observed at $f_{PILC} = 0.29$, which is most likely a nonequilibrium bicontinuous structure, the remaining morphologies which span the range $f_{PILC} = 0.20$ to 0.82 are all classical lamellar or cylinder microdomain structures. The homogeneous alignment of the mesogens with respect to the IMDS in the microdomain structures was confirmed by SAXD for the lamellar morphology and further supported by calculations (for all the samples except the bicontinuous morphology) which correctly predicted the number of mesogens per block copolymer chain based only on the geometry of the morphology. As predicted in Table 5.3, no sphere or bicontinuous cubic morphologies were observed. The corresponding optical properties and principal refractive indices of the P(ILC-b-S) morphologies are expected to also be well described by the relations listed in Table 5.3.

While the two examples given above are by no means exhaustive, they help illustrate how the framework developed in this chapter can be used to predict, in a logical and relatively intuitive way, the most probable equilibrium microstructures and optical properties of newly synthesized LC block copolymer materials. The discussion presented in Chapter 5 has also helped give insight into how a liquid crystalline block can influence the ultimate microstructure and optical properties of a block copolymer, particularly for the cases of a rod-coil and side-chain LC-coil block copolymer. Namely, LC block copolymers are seen to form microdomain structures which have point group symmetries commensurate with those of the LC block and which result in the creation of the fewest defects within LC domains.

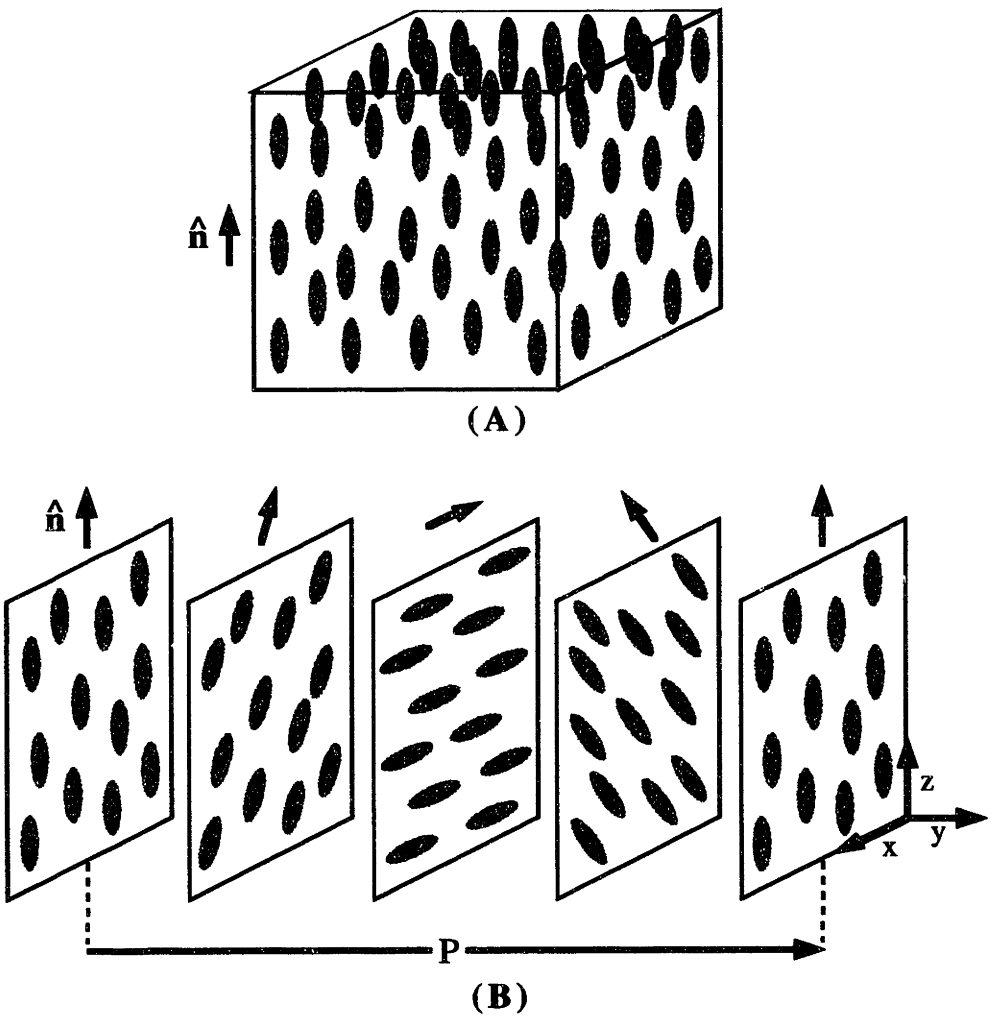

Figure 5.1 Schematic diagrams of the positions and orientations of liquid crystal molecules in the (A) nematic and (B) twisted nematic phases. The orientation of the local director is indicated by the arrows. P is the pitch of the twisted nematic phase.

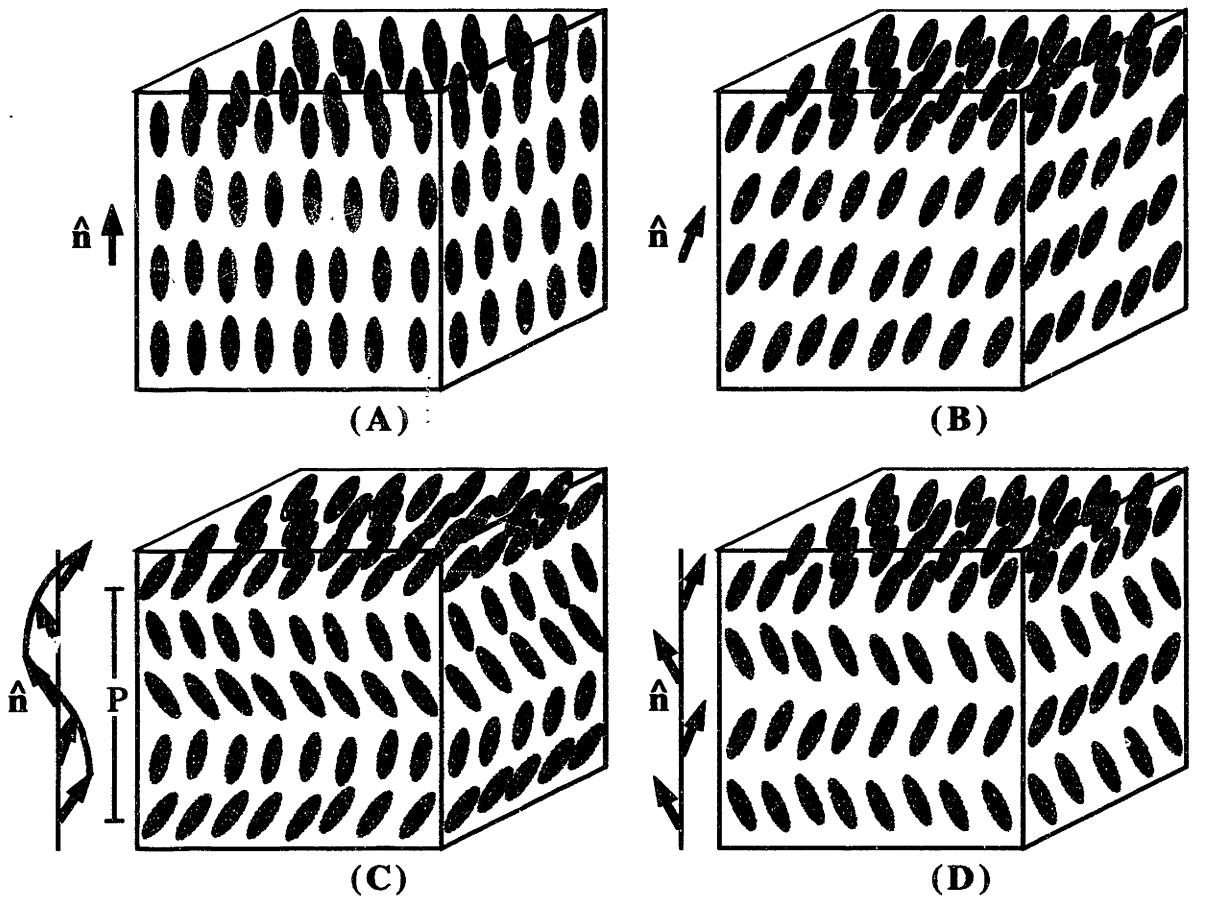

Figure 5.2 Schematic diagrams of the positions and orientations of liquid crystal molecules in the (A) smectic A, (B) smectic C, (C) smectic C*, and (D) smectic O phases. The orientation of the local director is indicated by the arrows. P is the pitch of the smectic C* phase.

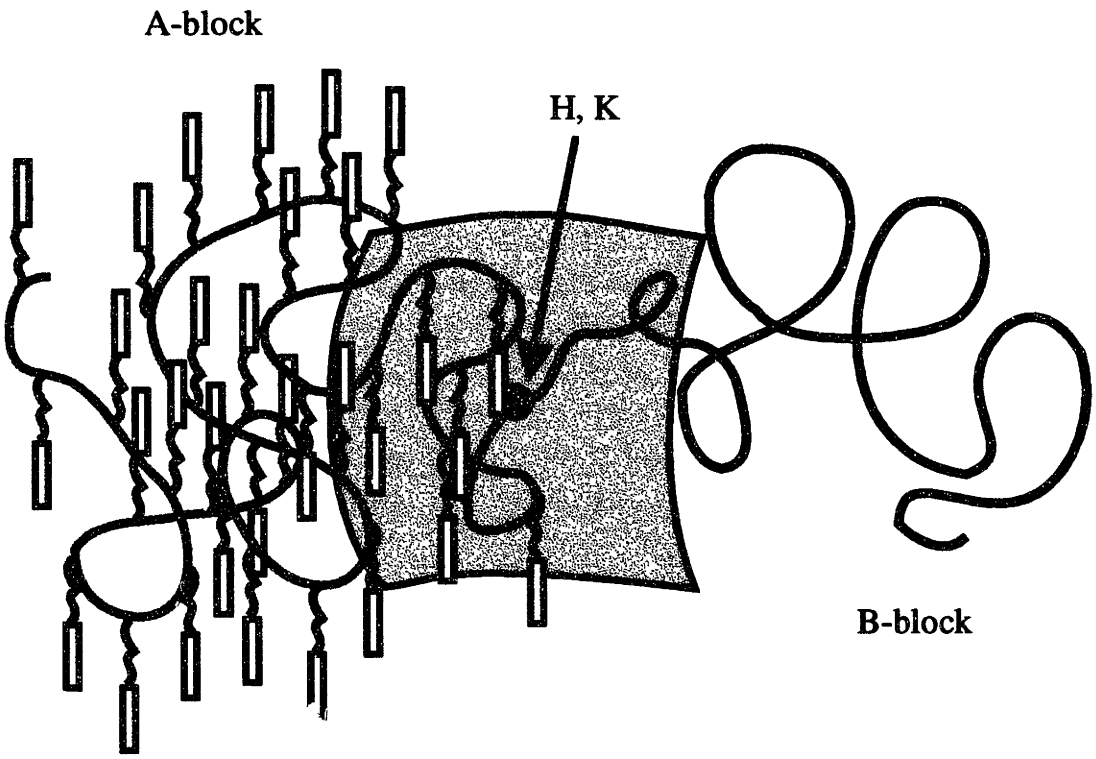

Figure 5.3 Schematic diagram of the IMDS (gray) for the case of an AB side-chain LC-coil diblock copolymer. $H = (C_1 + C_2)/2$ and $K = C_1 C_2$ where C_1 and C_2 are the principal curvatures.

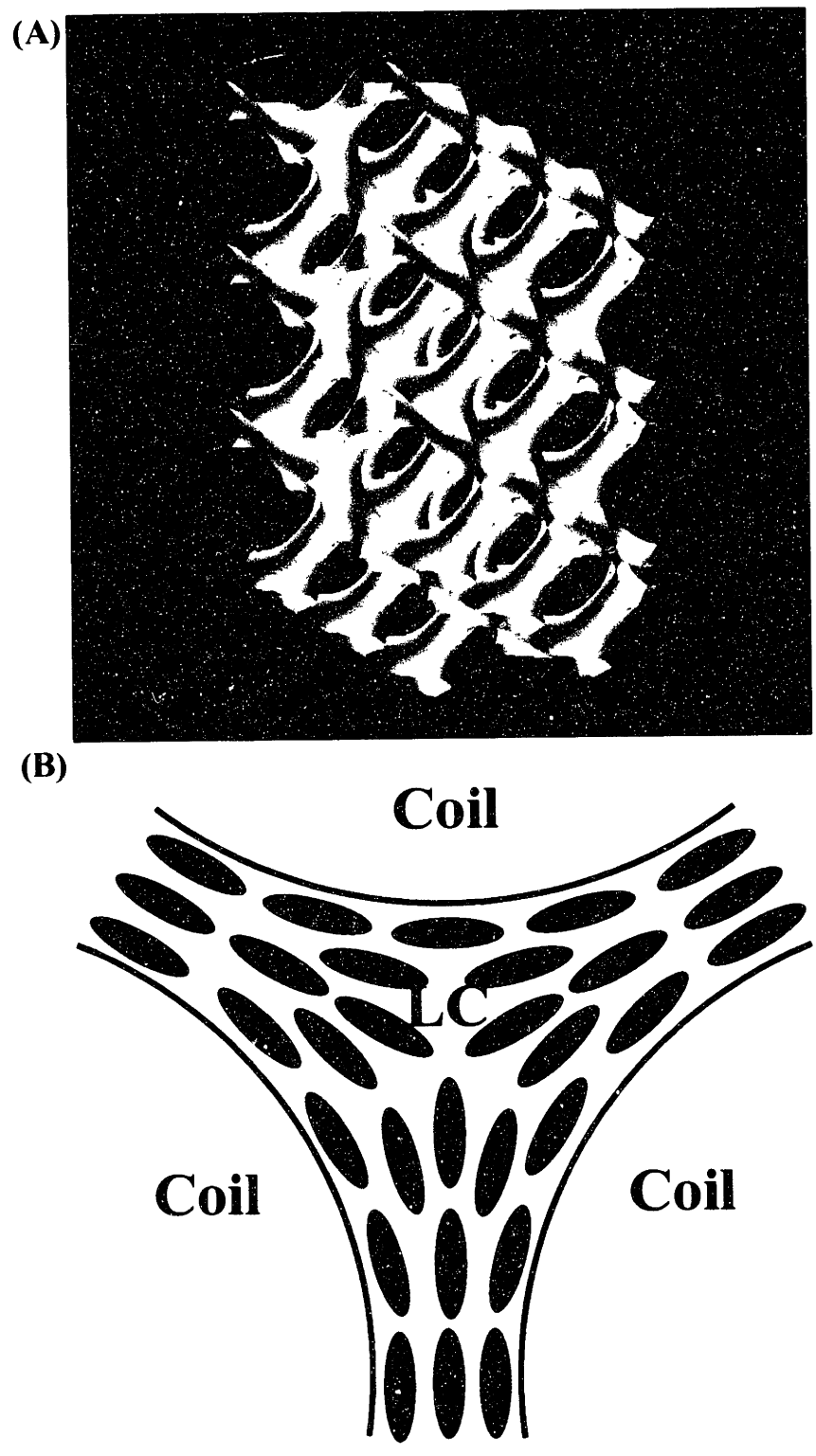

Figure 5.4 **(A) 3D graphical depiction of the double gyroid IMDS surface for a volume fraction of 37.5% LC block. (B) Cross–sectional schematic of a node in the labyrinthine LC network showing an orinetational defect.**

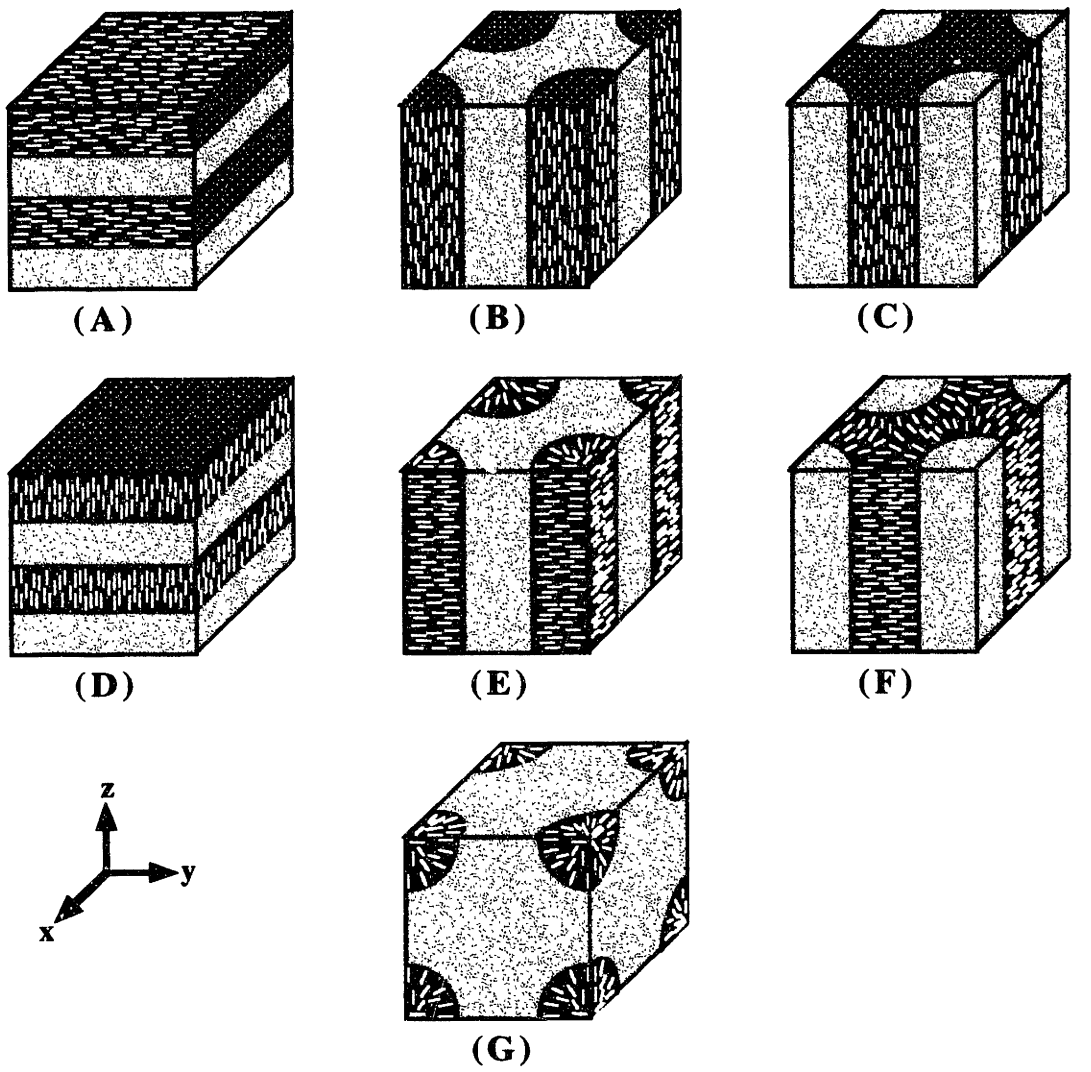

Figure 5.5 Schematic diagrams of the nematic LC-coil block copolymer morphologies predicted using the LC block copolymer symmetry framework: (A) lamellae, (B) LC cylinders, (C) coil cylinders for homogeneous anchoring conditions and (D) lamellae, (E) LC cylinders, (F) coil cylinders, and (G) LC spheres for homeotropic anchoring conditions.

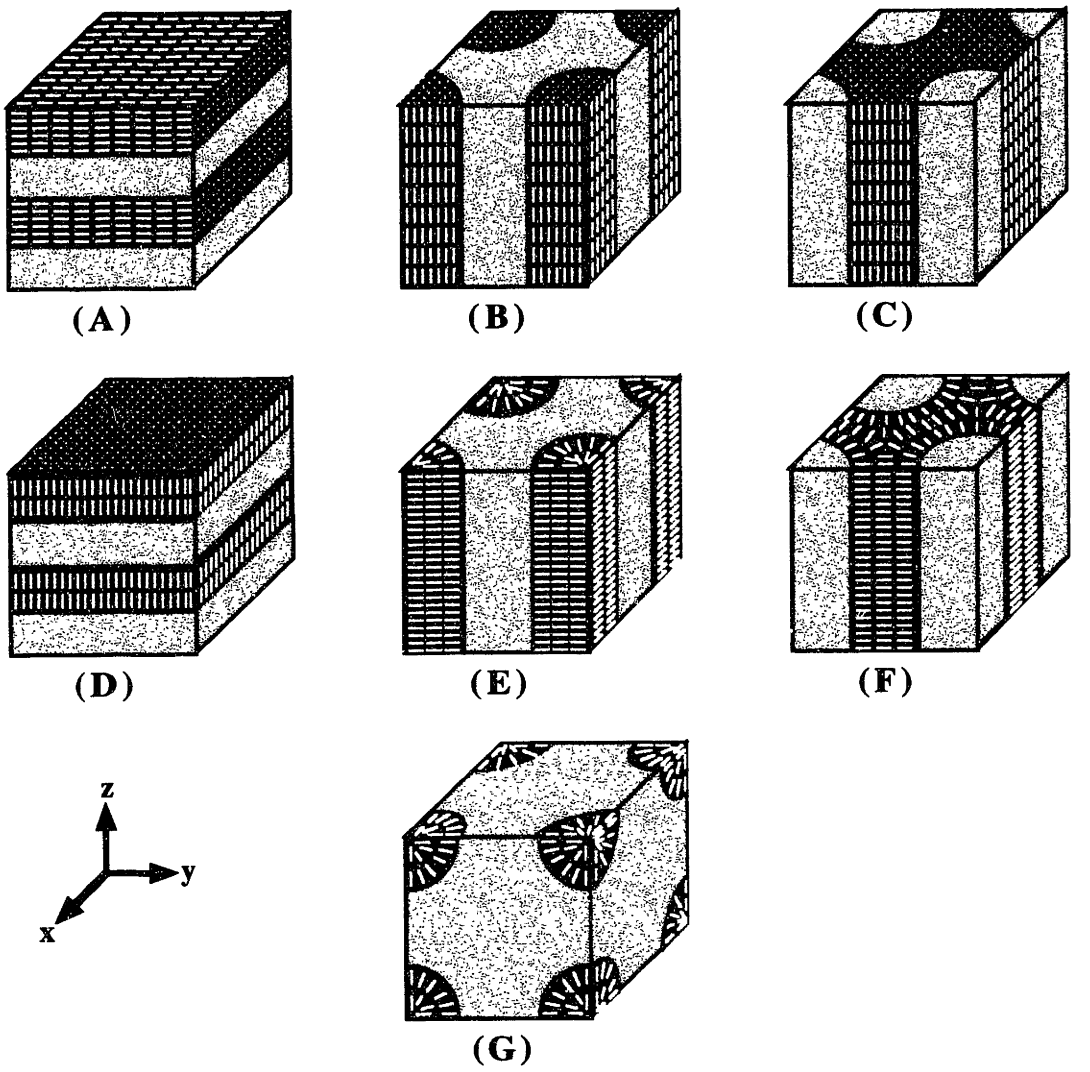

Figure 5.6 Schematic diagrams of the smectic A LC-coil block copolymer morphologies predicted using the LC block copolymer symmetry framework: (A) lamellae, (B) LC cylinder, (C) coil cylinders for homogeneous anchoring conditions and (D) lamellae, (E) LC cylinders, (F) coil cylinders, and (G) LC spheres for homeotropic anchoring conditions.

Conclusions and Future Work

The goal of this thesis was to understand the influence of a liquid crystalline block on the morphology and optical properties of block copolymers. For the most part, this goal was successfully accomplished. In Chapter 2, a discussion of the morphologies and optical properties of traditional coil-coil block copolymers was given which served as a foundation and starting point from which to build upon in the later chapters. While the morphologies of coil-coil diblocks and the reasons for their formation are well known, the optical properties of spatially periodic microphase separated block copolymer morphologies has, for the most part, gone unexplored. The section in Chapter 2, which deals with the long wavelength optical properties of coil-coil block copolymers, thus provides a new and systematic way of classifying and predicting the optical properties of coil-coil block copolymer microdomain structures using symmetry and effective medium theory (EMT). Although the EMT expressions for the various microstructures are quite sufficient for computational purposes, the specific expressions given for the cylinder, sphere, and bicontinuous cubic morphologies are approximate. Future work could focus on the derivation of rigorous expressions for the principal refractive indices of these morphologies.

In addition, the section on the short wavelength properties of block copolymers was only a brief overview of the principles behind photonic crystals. For large domain size block copolymer morphologies, photonic band gap calculations have to be performed in order to be able to accurately predict how light propagates through such structures. The section given on block copolymer waveguides is a good example of the potentially new optical properties self-assembling block copolymer materials can exhibit. The work presented in this section was the first investigation of the optical waveguiding properties of lamellar-forming block copolymers. Theoretical calculations showed that for certain

layered diblock and triblock copolymer waveguide structures with large domain sizes (D > $\lambda/3$), light can be controlled and made to propagate in all or some of the high index layers. Future researchers can extend the current work to the other morphologies: cylinder, sphere, and even the bicontinuous cubics. Experimentally, a determined effort was made to actually make block copolymer waveguides using an ultrahigh molecular weight P(S-b-I) diblock. However, well-ordered macroscopically aligned lamellar films were not possible despite the use of a number of different processing methods. Future researchers, however, are strongly encouraged to look into different processing conditions and block copolymer systems, coil-coil, rod-coil, LC-coil, LC-LC, etc... which may turn out to be better waveguide materials than the P(S-b-I) system.

In Chapter 3, the influence of a lyotropic nematic rodlike polymer block on the microphase separated morphologies formed by block copolymers was investigated. The P(HIC-b-S) rod-coil diblock copolymers, which ranged in volume fraction from f_{PHIC} = 0.42 to 0.98, were observed by TEM and SAED to form three novel orientationally ordered microstructures with domain sizes ranging from 10's to 100's of nanometers. In all of the microphase separated morphologies, the rod block exhibited liquid crystallinity and was tilted at a large angle with respect to the IMDS. The significantly different cross-sectional area per chain of the rod and coil blocks at the IMDS induces the rods to tilt when the rod-coil chains pack in the solid-state. In the P(HIC-b-S) system, the tilt angle which is adopted minimizes the total free energy of the system subject to the preservation of three dimensional crystallinity in the PHIC domains. The extreme conformational asymmetry between the rod and the coil blocks causes these materials to first undergo an isotropic-nematic transition and then the microphase separation transition as solvent evaporates. The observed phase behavior of the P(HIC-b-S) rod-coils qualitatively agrees with that predicted for an LC-coil block copolymer by a statistical theory recently developed by Gurovich.

Many possibilities, however, exist for extending the current work. Most importantly, more P(HIC-b-S) rod-coils need to be synthesized to fill in the morphology diagram especially for coil-rich compositions. According to Gurovich, for sufficiently low rod content, rod-coils are expected to behave like traditional coil-coil block copolymers forming classical microdomain structures of spheres, cylinders, and lamellae. A molecular weight series synthesized at fixed composition would also be of interest for studying the domain size versus molecular weight scaling relationships for both the coil and the rod domains. Given the small area per chain favored by the rod block, the coil block is expected to be highly stretched in comparison to typical coil-coil diblock copolymers. The issue of rod tilt could be better studied if the rod blocks did not crystallize. As a result, in the future, researchers could synthesize a rod block using both PHIC and poly(octyl isocyanate), for example, to prevent crystallization. In addition, the equilibrium phase behavior of rod-coils could be better studied with a thermotropic liquid crystalline rod block because high temperature annealing could be employed. Since rod-coils are a relatively new type of block copolymer, their blend behavior is a completely unexplored area of research as well. No theoretical studies have ever predicted the phase behavior of rod-coils blended with rod or coil homopolymers. Unlike traditional block copolymer/homopolymer blends, in rod-coil/coil homopolymer blends, entropic effects dominate and homopolymers may macrophase separate, even for low concentrations. So far we have been discussing possible extensions of the rod-coil work presented in this thesis. The synthesis of new block copolymer architectures, however, as with coil-coil diblocks, will undoubtedly open up whole new research opportunities. The phase behavior of rod-coil-rod triblock or rod-rod diblock copolymers, just to mention a few cases, is expected to be significantly different from that of rod-coils.

In Chapter 4, the morphologies formed by a P(ILC-b-S) side-chain LC-coil block copolymer were studied. The volume fraction in these diblocks ranged from $f_{PILC} = 0.20$

to 0.82. The LC block consisted of a flexible PI backbone which had an azobenzene mesogen attached to every pendant double bond of the PI monomer via flexible spacers. WAXD experiments showed that the PILC block formed a smectic A mesophase in every diblock copolymer. TEM and SAXD showed that the side-chain LC-coils formed classical coil-coil microdomain structures with the exception of one nonequilibrium bicontinuous structure. Within the PILC domains, however, the azobenzene mesogens formed a smectic A mesophase with homogeneous anchoring conditions with respect to the IMDS. The multiple length-scale organization displayed in these morphologies suggests that the microphase separation transition occurs prior to the isotropic-smectic A transition when solvent evaporates.

While the morphology diagram of the P(ILC-b-S) system is fairly complete, definite gaps in composition exist near the bicontinuous cubic and sphere compositions. These morphologies are particularly interesting because they place severe packing constraints on a smectic A mesophase. For example, the smectic A mesophase could be forced to form a nematic phase or even an isotropic phase within spheres of the PILC component. A more detailed study of the orientation of the mesogen and smectic A layers with respect to the IMDS of the cylinder-forming samples should be carried out using SAED and SAXS of macroscopically aligned samples. The isotropic-smectic A transition temperature should also be measured as a function of solvent concentration in order to obtain more information about the path by which the side-chain LC-coil morphologies form. In addition, different (preferential) solvents can be used in casting the side-chain LC-coils to see whether the isotropic-smectic A transition can be made to occur prior to the microphase separation transition.

Besides bulk studies, thin film samples of the side-chain LC-coils would be of significant interest in determining which block preferentially segregates to the air surface. Thermodynamically, the PILC block with its pendant azobenzene mesogens is expected

to segregate to the air surface because it experiences a smaller loss in conformational entropy in comparison to the coil block. Thin films of the side-chain LC-coil diblocks are also interesting from an optical point of view. The azobenzene mesogen undergoes a cis-trans isomerization with irradiation by UV light. As a result, in a microphase separated P(ILC-b-S) morphology, the optical properties of the PILC domains can be significantly changed using UV light. This effect could potentially be exploited in oriented lamellar films of the side-chain LC-coils (for example) to make switchable waveguides.

Finally, in Chapter 5, a framework was developed to help understand and predict the influence of a LC block on the morphologies and optical properties of LC-coil block copolymers. Knowing only the symmetries of the classical microdomain structures, the symmetries of the liquid crystalline phases, the composition of the block copolymer, and the preferred anchoring conditions of the LC block at the IMDS, general predictions can be made as to what the most likely structures will be. In addition to maintaining translational symmetry and obeying the preferred anchoring conditions of the LC block, the most probable structures tend to preserve the highest point group symmetry which is common to both the microdomain structure and the LC mesophase. Structures which require the incorporation of a periodic arrays of defects to satisfy the anchoring conditions are less energetically favorable. However, the stability of a periodic array of defects is highly dependent on the elastic constants and how big the LC domain is in comparison to the liquid crystalline block. The elastic constants are themselves dependent on temperature and solvent quality. Thus by adjusting temperature, solvent concentration, and molecular weight, one could conceivably tailor the types and locations of periodic defects in a microphase separated LC block copolymer. Changes in the space group of a LC block copolymer could thus be achieved without the need for large-scale structural rearrangement of microdomains, which has possible optical uses.

The symmetry framework was found to predict morphologies which showed good agreement with those observed for the rod-coil and side-chain LC-coil systems. Future research, however, could focus on the synthesis of more complicated LC block copolymers such as a smectic C LC-coil or smectic C* LC-coil series. According to the symmetry framework, these types of LC block copolymers are only expected to form lamellar structures. The conceptual framework developed in Chapter 5 is also useful for predicting the optical properties of LC block copolymers in the long wavelength limit. Since the space group of a particular structure is determined from the framework, so too is the macroscopic optical class (isotropic, uniaxial, or biaxial) of a given morphology. Once the optical class is known, appropriate EMT expressions can be used to obtain the principal refractive indices. Relatively straightforward experiments on single crystal samples could be carried out in the future to verify the long wavelength optical properties of LC block copolymers. Short of a full statistical theory of microphase separation in LC-coil block copolymers, the framework developed in Chapter 5 provides a relatively simple and intuitive way of making a reliable prediction of what morphology a LC block copolymer will adopt and what its optical properties will be.

Appendix 1: Asymmetric Slab Waveguide

A good model for understanding the behavior of dielectric waveguides is the asymmetric slab waveguide. An asymmetric slab waveguide (see Figure A1.1) is a three layer dielectric system consisting of a film, with refractive index n_1, deposited between a semi-infinite substrate and superstrate of lesser refractive index, n_0 and n_s, respectively. For an asymmetric slab waveguide, a continuum of modes exists in which light is able to propagate through the structure. However, for optical waveguiding purposes, only the normal modes of the waveguide in which the propagating light is confined solely within the middle layer are of interest. Classical ray optics can be used to explain the existence of the waveguide modes in an intuitive manner using Snell's law of refraction and the phenomena of total internal reflection. In this approach [59, 56], propagating light waves are represented by lines or rays which are perpendicular to the surfaces of constant phase. As the light rays travel through the slab waveguide, they must obey Snell's law at the superstrate and substrate interfaces,

$$n_s \sin\theta_s = n_1 \sin\theta_1, \qquad \text{(A1.1)}$$

$$n_0 \sin\theta_0 = n_1 \sin\theta_1, \qquad \text{(A1.2)}$$

where the various angles and indices are defined in Figure A1.2. If $n_1 > n_0$ or n_s, θ_0 and θ_s are always larger than θ_1. As θ_1 is increased at each interface, eventually θ_s and θ_0 will equal $\pi/2$ for different values of $\theta_1 < \pi/2$. When this condition is satisfied, the light rays will total internally reflect. In other words, no transmitted light will exist in the superstrate or substrate when light is totally internally reflected in the film and the light is effectively confined to guide in the film layer. The two criteria for total internal

reflection at each interface, $\theta_1 > \sin^{-1}(n_s/n_1) = \theta_{c,\,s}$ and $\theta_1 > \sin^{-1}(n_0/n_1) = \theta_{c,\,0}$, can be combined into a single condition for the film as a whole, $\pi/2 > \theta_1 > \sin^{-1}(n_0/n_1)$.

Not all rays satisfying the total internal reflection condition are waveguide modes, however. Light which totally internally reflects must also constructively interfere with itself upon reflection from both interfaces. This phase condition is illustrated in Figure A1.3. Only two rays are pictured for simplicity. In order for these two rays to constructively interfere with each other, the points C and A on the same phase front at an initial time must still be in phase at a later time when C and A have traveled to D and B, respectively. In addition to undergoing a path length difference, the ray CD also suffers two phase shifts because of reflections at the superstrate and substrate interfaces. The total phase difference between the two rays must be a multiple of 2π and satisfies the following relation,

$$2k_0 n_1 d\sin\theta_1 + \Phi_0 + \Phi_s = 2m\pi. \qquad \text{(A1.3)}$$

In Equation A1.3, k_0 is the magnitude of the wave vector in free space and Φ_0 and Φ_s are the phase shifts at the substrate and superstrate, respectively, which are expressible in terms of the angle, θ_1, and refractive indices of the three layers [56]. Equation A1.3 is called the eigenvalue equation and can be used to determine the characteristic angles of the waveguide modes. Each mode is characterized by a mode number m and can be thought of as a standing wave with m+1 maxima which corresponds to a light ray that zig-zags inside the film at an angle θ_1. Higher order modes have smaller angles and undergo a greater number of reflections as shown in Figure A1.4.

In the above discussion, the waveguide modes of an asymmetric slab waveguide were obtained intuitively using classical ray optics. However, for a rigorous solution of

the asymmetric slab waveguide, Maxwell's equations (see Equations 2.10 to 2.13) must be solved in each region to obtain a complete description of the guided normal modes [59, 56]. The normal modes can then be used to calculate the optical field distribution of each mode, the electric and magnetic field profiles across the waveguide, and mode angles. If we only consider the TE (transverse electric) modes, Figure A1.1 shows that the electric and magnetic field will have the components $\mathbf{E} = (0, E_y, 0)$ and $\mathbf{B} = (B_x, 0, B_z)$. Assuming each guided mode is a propagating mode in the $\hat{z}$ direction, we can simplify the analysis further by assuming the familiar time and z dependence of $e^{i(\omega t - \beta z)}$ where β is the z-component of the wave vector for a given mode. Dividing β by k_0 yields the propagation constant, n_{eff}, which is inversely proportional to the velocity of the mode. Manipulation of Maxwell's equations using these simplifications yields the one dimensional reduced wave equation,

$$\frac{\partial^2 E_y^i}{\partial x^2} + k_o^2\left(n_i^2 - n_{eff}^2\right)E_y^i = 0, \qquad \text{(A1.4)}$$

where i = 0, 1, or s. From the solutions of Equation A1.4, the TE guided modes can be obtained. The resulting solutions of E_y in the three regions will have the form,

$$E_y^s = A_0 B_1 \exp\left[-k_s(x - d)\right] \qquad x \geq d, \qquad \text{(A1.5)}$$

$$E_y^1 = A_0\left[\cos(k_1 x) + T_0 \sin(k_1 x)\right] \qquad d \geq x \geq 0, \qquad \text{(A1.6)}$$

$$E_y^0 = A_0 \exp\left[k_0 x\right] \qquad x \leq 0, \qquad \text{(A1.7)}$$

where $B_1 = \cos(k_1 d) + T_0 \sin(k_1 d)$ and $T_0 = k_0/k_1$. The electric field amplitude coefficient, A_0, is a normalization constant defined such that the total power contained in

each mode is equal to 1 W/μm. The corresponding expressions for B_x and B_z can be obtained using Maxwell's equations. The final requirement that the tangential field components, E_y and B_z, be continuous at the two interfaces yields the equation,

$$k_1 d - \tan^{-1}\left(\frac{k_s}{k_1}\right) - \tan^{-1}\left(\frac{k_0}{k_1}\right) = m\pi, \qquad \text{(A1.8)}$$

where k_0, k_1, and k_s are functions of n_{eff} (see Equation 2.37). Equation A1.8 is identical to the eigenvalue equation, Equation A1.3, derived earlier. Each n_{eff} satisfying Equation A1.8 is an eigenvalue corresponding to a guided mode with mode number m. Figure A1.5 shows the solutions of the eigenvalue equation corresponding to a 1.5 μm polystyrene film on quartz for a wavelength of 488 nm. From the n_{eff}'s, the optical field distribution in the waveguide for each mode can be easily calculated using Equations A1.5 to A1.7 (see Figure A1.6).

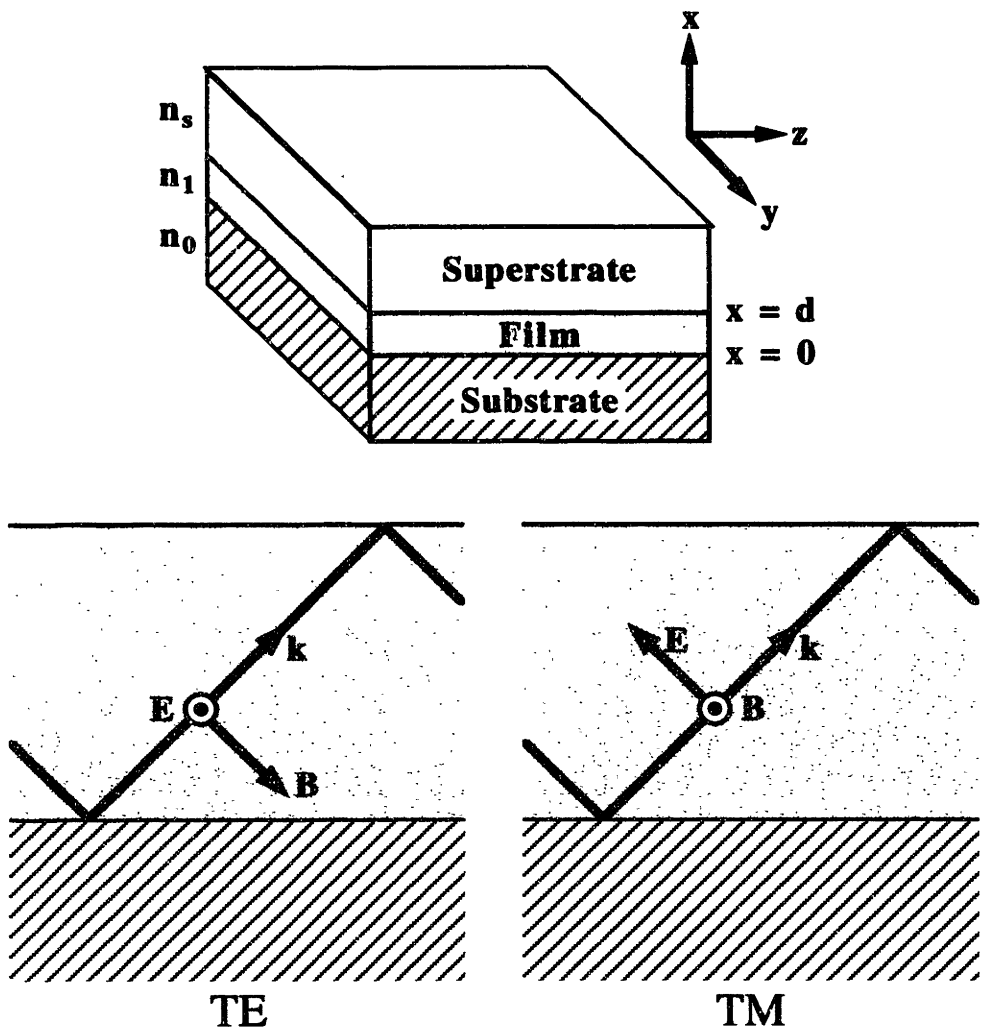

Figure A1.1 Schematic diagram of the asymmetric slab waveguide which shows the propagation direction and the orientation of the electric and magnetic field vectors for transverse electric (TE) and transverse magnetic (TM) modes.

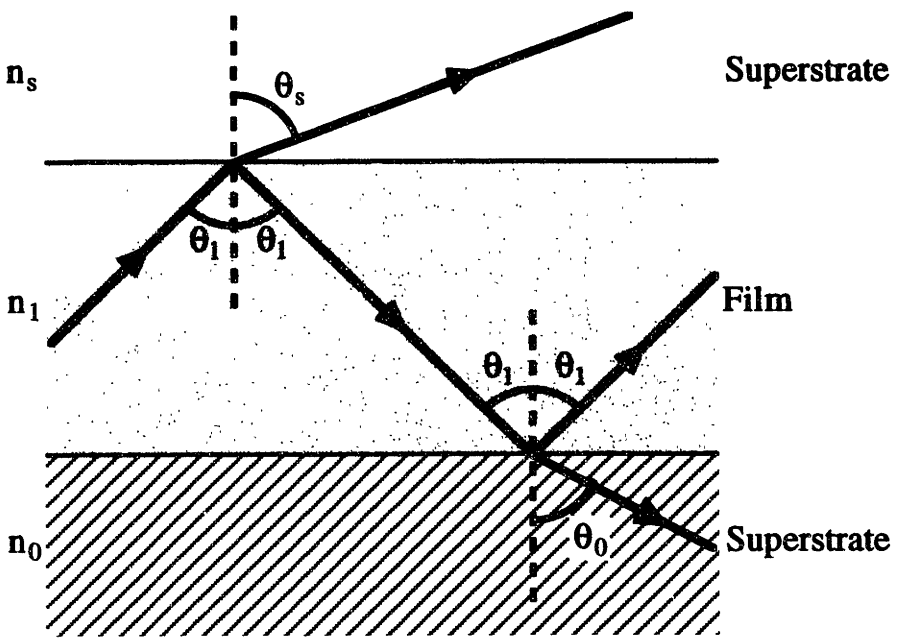

Figure A1.2 Schematic diagram of the refraction of light at the superstrate and substrate interfaces.

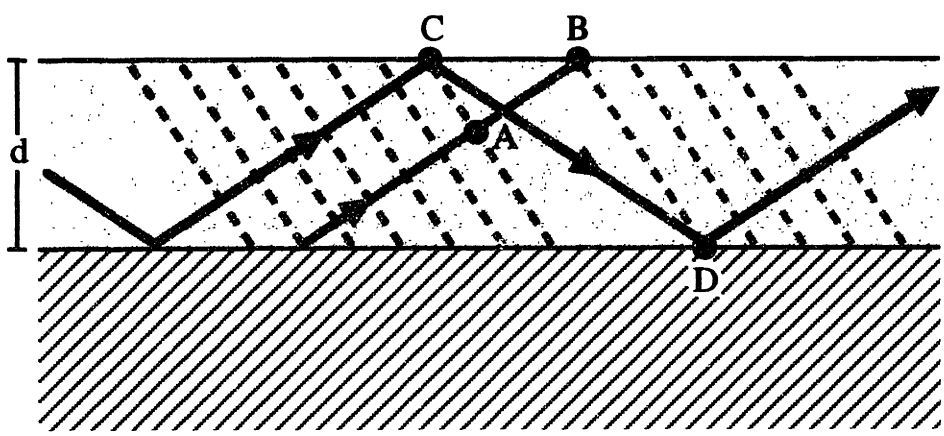

Figure A1.3 Graphical illustration of the phase condition which must be satisfied for waveguide modes.

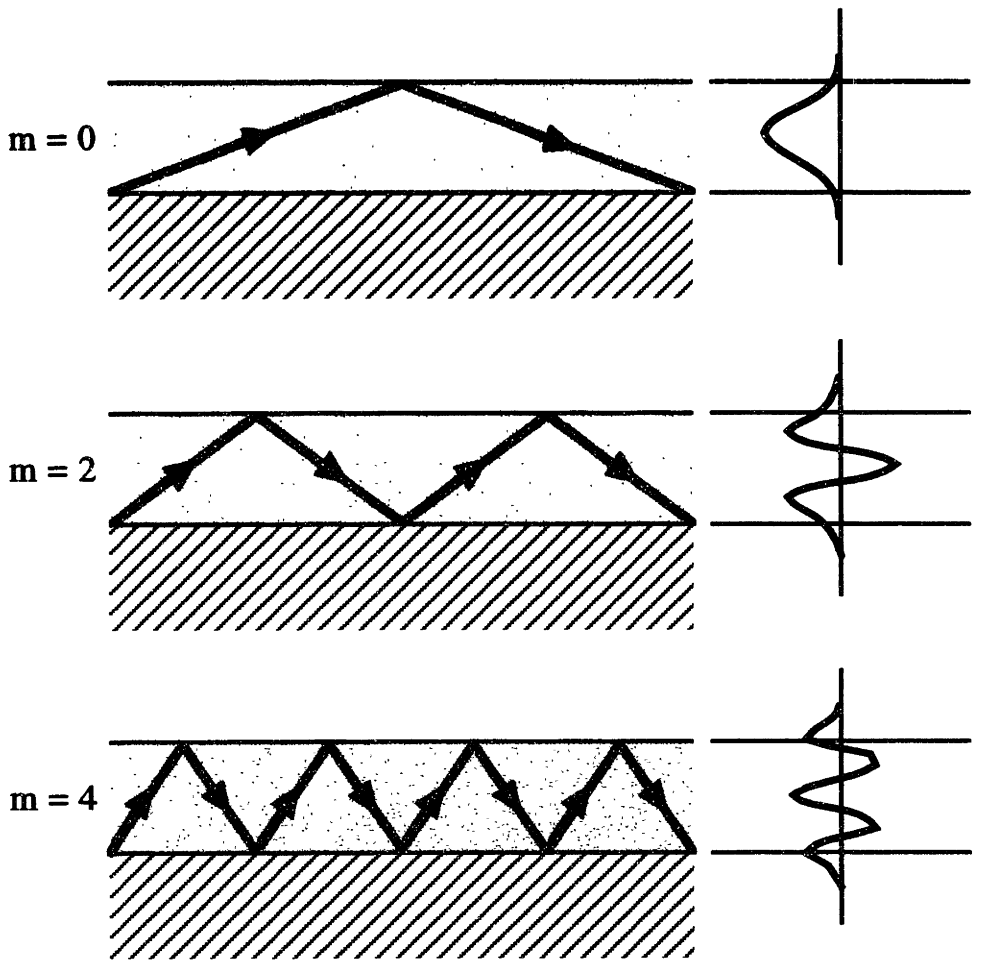

Figure A1.4 Ray optics representation of the waveguide modes showing their angles of reflection and electric field profiles.

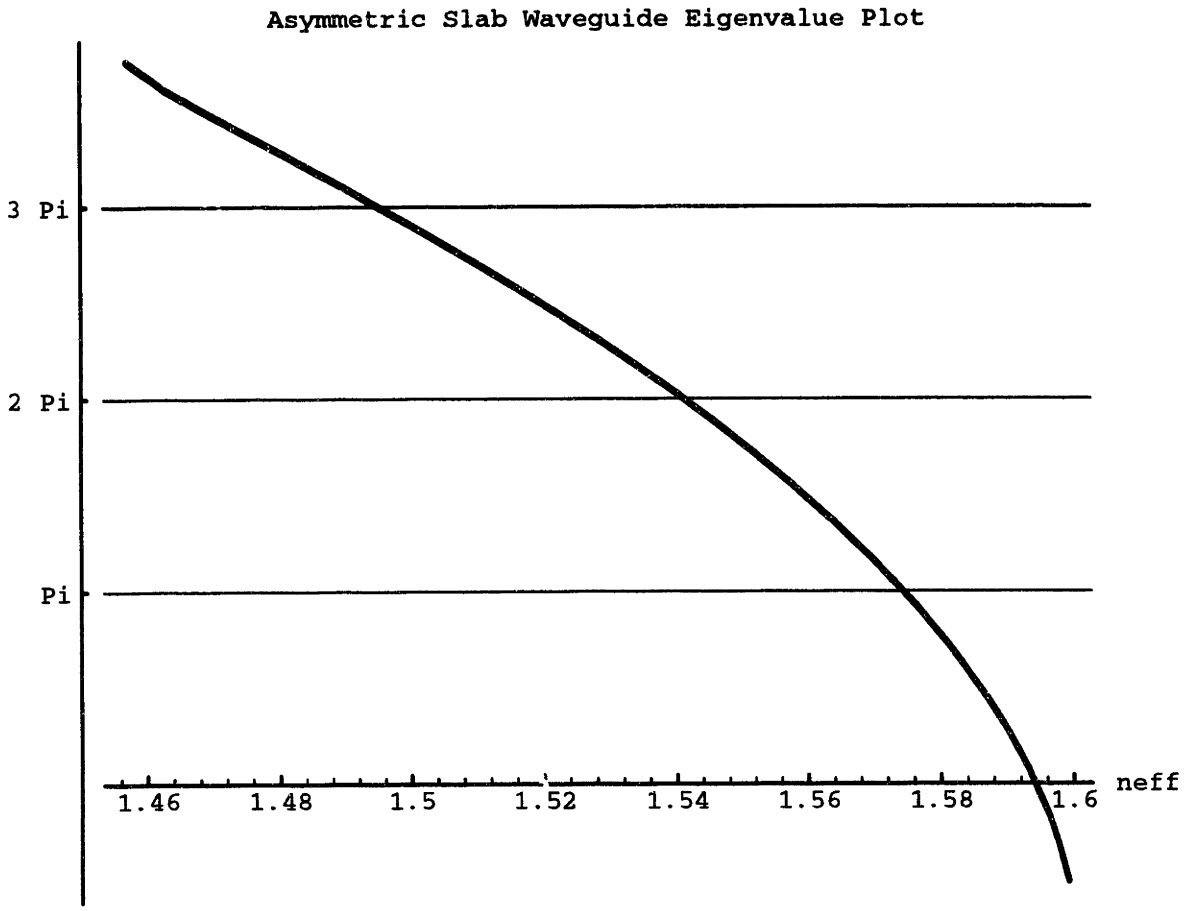

Figure A1.5 Graphical solution of the eigenvalue equation for a PS asymmetric slab waveguide.

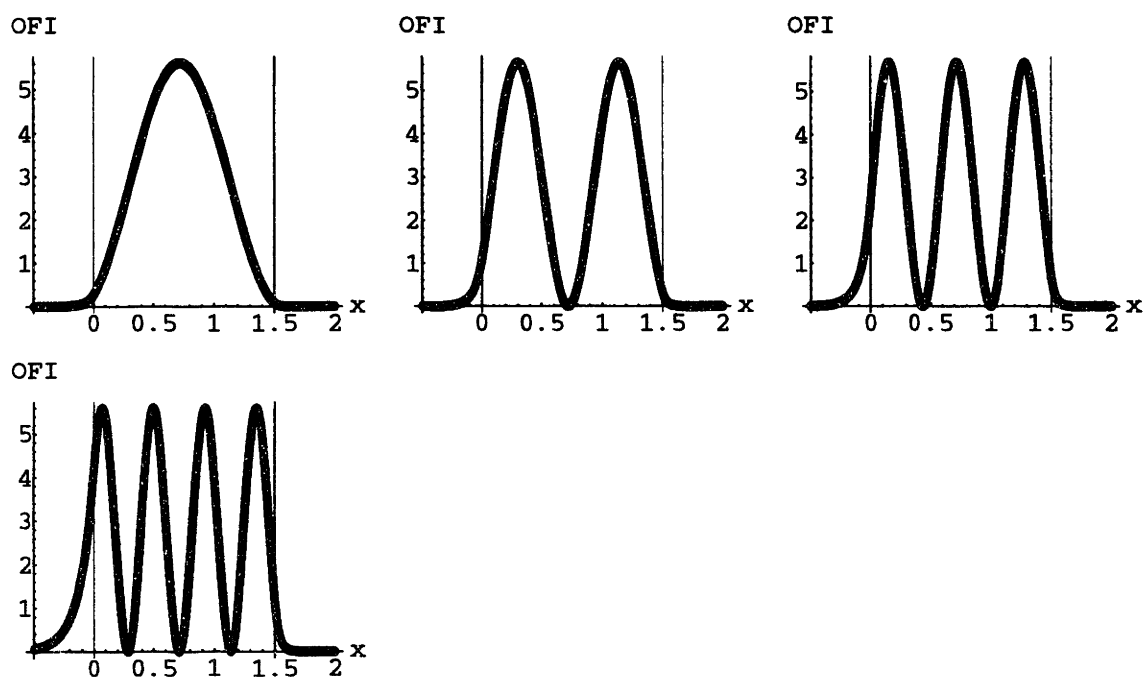

Figure A1.6 Optical field intensity distribution plots for the four TE modes of the PS slab waveguide.

Appendix 2: Spin Coating

The process of spin coating is widely used in industry to make thin polymer films with uniform thickness and low surface roughness. Typically, films with thicknesses ranging from 10 nm to several microns can be easily cast from solution using this method. Despite the widespread use of spin coating, a complete theory of the process still does not exist. The main features and key variables which affect the process, however, are well understood [127, 128]. Spin coating is a nonequilibrium process which involves flow of material and mass transfer. A complicated competition between centrifugally driven thinning of the liquid film and concentration driven evaporation of solvent determines the final film thickness and uniformity. The spin coating process can be divided into four main stages: deposition, spin-up, spin-off, and evaporation of solvents (see Figure A2.1).

In the deposition stage, the liquid or solution is applied to the surface of the substrate where a portion of the solution immediately wets the substrate. Most or all of the air that covered the substrate initially is displaced by the liquid. Deposition is followed by the spin-up stage where the substrate is rotated and accelerated to its final rotational speed in times typically less than a second. The substrate is usually held by vacuum onto a chuck which in turn is attached to the motor shaft. The viscous nature of the polymer solution allows the centrifugal force of the substrate to be transmitted to the solution. During the spin-off stage, the motor reaches its final rotational speed. Any excess solution is removed radially from the substrate by centrifugal force. Successive waves or fronts of solution develop and travel radially outward leaving a uniform film behind them. The film continues to thin by this process until the viscosity of the film increases to such a point that the remaining solution behaves like a solid. After this point, solvent evaporation dominates. During this complex process, two factors control the rate

at which solvent evaporates. The chemical potential difference of the solvent between the film and the air immediately above the film provides the main driving force for evaporation. Second, the rate of evaporation is limited by the diffusion or mass transport of the solvent through the gas layer between the film and the bulk air flowing above the film. Solvent evaporation during this stage becomes a steady state process which thins the film normal to the surface until nearly all the residual solvent is gone.

The spin-off and solvent evaporation stages have been found to affect the thickness and surface roughness of the final film the most. The factors which play the most important role are initial solution concentration, final rotational speed, the weight-averaged molecular weight of the polymer, the solvent quality, and solvent evaporation rate [129, 130]. As expected, film thickness increases with increasing solution concentration, slower rotation speed, higher molecular weight, and solvent volatility. Films with low surface roughness result when the initial solution concentration and solvent quality are such that the polymer chains are entangled.

Spin coating of the samples discussed in this thesis was performed on a Headway spin coater equipped with a 5.5 inch bowl and an EC101 DC motor which was capable of spin speeds between 50 and 10,000 rpm. Sample variability due to the spin coating process was minimized by standardizing the spinning conditions. The substrate was first flooded with a specified aliquot of the polymer solution (typically 100 μL to 400 μL) for 10 seconds prior to spinning. During this step, any preferential absorption of the block copolymer chains to the substrate would help bias the self-assembly process. The substrate was then accelerated to a final spin speed of 5000 rpm which was maintained for 20 seconds. The 20 second spin time was sufficient to remove nearly all the solvent. For a given molecular weight polymer, the final film thickness was controlled by adjusting the initial solution concentration. One can also change film thickness by fixing the concentration and adjusting spin speed.

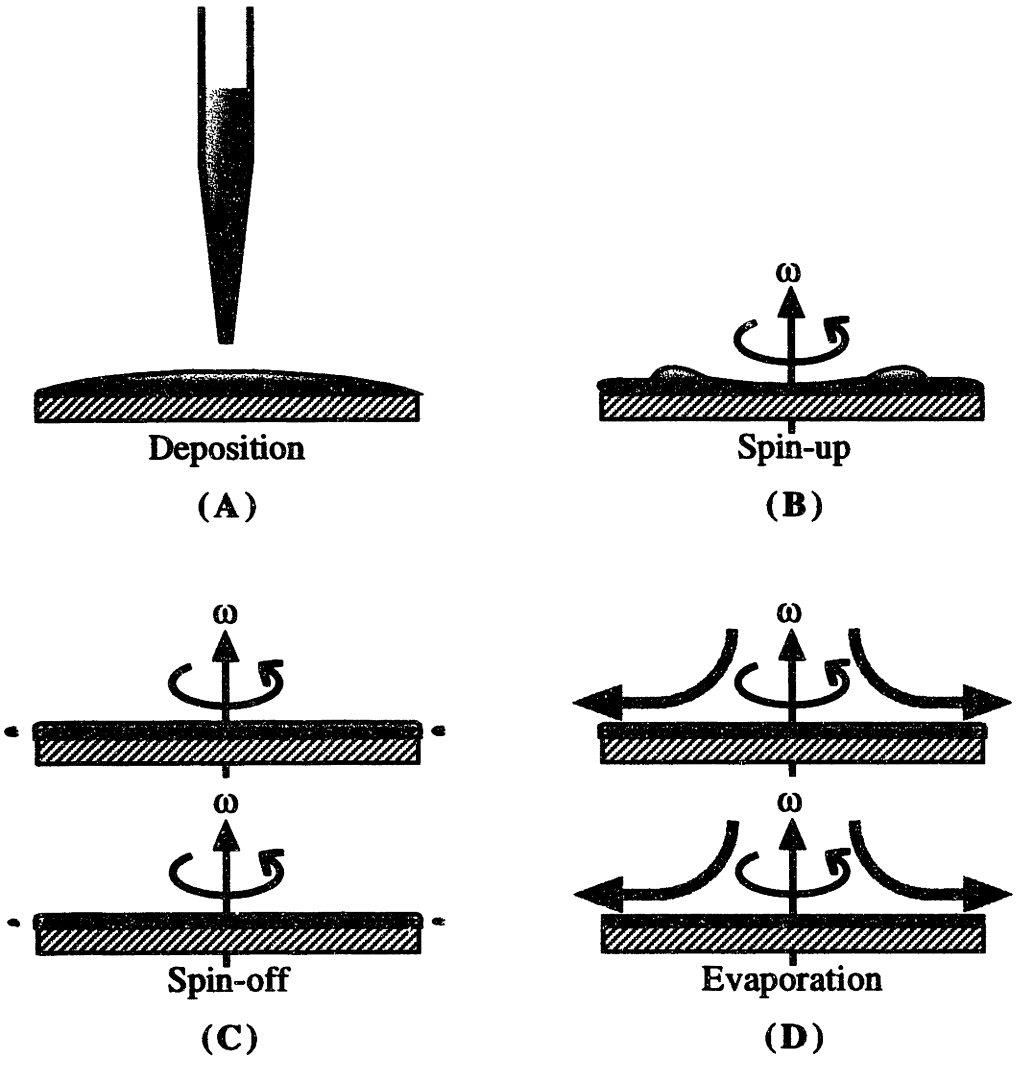

Figure A2.1 Schematic diagrams of the four stages of spin coating: (A) deposition, (B) spin-up, (C) spin-off, and (D) evaporation.

Appendix 3: Ellipsometry and its Applications to Anisotropic Films

Optical ellipsometry is defined as the measurement of the state of polarization of polarized light. By measuring the state of polarization of light before and after it is reflected from a thin film or bare substrate, one can obtain information about the optical constants of the sample. Polarized light incident upon a surface between two media (of refractive index n_0 and n_1) can always be decomposed into two mutually orthogonal components called the s and p waves, which are perpendicular and parallel to the plane of incidence, respectively. The plane of incidence is defined by the incident wave vector and the vector normal to surface (see Figure A3.1). When polarized light undergoes reflection from a surface, its state of polarization is changed (i.e. its amplitude and phase) differently depending on whether it is s or p polarized. These changes are summarized by the Fresnel complex-amplitude reflection coefficients,

$$r_s = \frac{n_1\cos\Phi_1 - n_0\cos\Phi_0}{n_1\cos\Phi_1 + n_0\cos\Phi_0} = |r_s| e^{i\delta_s}, \qquad \text{(A3.1)}$$

$$r_p = \frac{n_0\cos\Phi_1 - n_1\cos\Phi_0}{n_0\cos\Phi_1 + n_1\cos\Phi_0} = |r_p| e^{i\delta_p}, \qquad \text{(A3.2)}$$

where Φ_0 and Φ_1 are the angles of incidence and refraction, respectively. The real part of each expression is the ratio of the electric field amplitudes of the reflected to incident waves. The δ_i are the phase shifts which take place upon reflection. In ellipsometry, what is measured is the ratio of the reflection coefficients,

$$\rho = \tan\Psi e^{i\Delta} = \frac{r_p}{r_s}. \qquad \text{(A3.3)}$$

In particular, the two ellipsometric angles Ψ and Δ which determine the differential changes in amplitude and phase, respectively, are measured. Once the two ellipsometric angles are known, Equation A3.3 can be used to calculate the refractive index of the bare substrate (assuming the angles of incidence and n_1 are known) using the relation [131],

$$n_0 = n_1 \tan\Phi_1 \sqrt{1 - \frac{4\rho}{(1+\rho)^2} \sin^2\Phi_1} \,. \qquad \text{(A3.4)}$$

To measure the refractive indices and thickness of a thin dielectric film, such as a block copolymer film, the reflection coefficients must be modified. In particular, the overall complex reflection coefficients must be substituted into Equation A3.3. We will treat the more general case of a three layer system (see Figure A3.2) consisting of an optically uniaxial film (optic axis normal to the film) characterized by n_{1o} and n_{1e} located between a semiinfinite substrate (n_0) and superstrate (n_2) which is of particular relevance to oriented lamellar block copolymer films. The same expressions can be used for an isotropic thin film by setting $n_{1o} = n_{1e}$. The expressions for the overall reflection coefficients of the s and p polarized light are given by the following expressions [131],

$$R_s = \frac{r_s^{12} + r_s^{01} e^{-2i\beta_s}}{1 + r_s^{12} r_s^{01} e^{-2i\beta_s}}, \qquad \text{(A3.5)}$$

$$R_p = \frac{r_p^{12} + r_p^{01} e^{-2i\beta_p}}{1 + r_p^{12} r_p^{01} e^{-2i\beta_p}}, \qquad \text{(A3.6)}$$

where

$$r_s^{01} = \frac{-n_0\cos\Phi_0 + \sqrt{n_{1o}^2 - n_0^2\sin^2\Phi_0}}{n_0\cos\Phi_0 + \sqrt{n_{1o}^2 - n_0^2\sin^2\Phi_0}}, \tag{A3.7}$$

$$r_s^{12} = \frac{n_2\cos\Phi_2 - \sqrt{n_{1o}^2 - n_2^2\sin^2\Phi_2}}{n_2\cos\Phi_2 + \sqrt{n_{1o}^2 - n_2^2\sin^2\Phi_2}}, \tag{A3.8}$$

$$r_p^{01} = \frac{-n_{1o}n_{1e}\cos\Phi_0 + n_0\sqrt{n_{1e}^2 - n_0^2\sin^2\Phi_0}}{n_{1o}n_{1e}\cos\Phi_0 + n_0\sqrt{n_{1e}^2 - n_0^2\sin^2\Phi_0}}, \tag{A3.9}$$

$$r_p^{12} = \frac{n_{1o}n_{1e}\cos\Phi_2 - n_2\sqrt{n_{1e}^2 - n_2^2\sin^2\Phi_2}}{n_{1o}n_{1e}\cos\Phi_2 + n_2\sqrt{n_{1e}^2 - n_2^2\sin^2\Phi_2}}, \tag{A3.10}$$

$$\beta_s = \frac{2\pi d}{\lambda}\sqrt{n_{1o}^2 - n_2^2\sin^2\Phi_2}, \tag{A3.11}$$

$$\beta_p = \frac{2\pi d}{\lambda}\frac{n_{1o}}{n_{1e}}\sqrt{n_{1e}^2 - n_2^2\sin^2\Phi_2}. \tag{A3.12}$$

A simultaneous determination of n_{1o}, n_{1e}, and d is not possible with only two ellipsometric angles Ψ and Δ. As a result, in order to determine the optical constants of an anisotropic film given the substrate and superstrate indices, one must perform ellipsometric measurements at multiple angles of incidence. Although only two different measurements are needed, a greater number of Ψ and Δ values will improve precision and accuracy. A nonlinear least-squares fit of the data can then be performed using n_{1o}, n_{1e}, and d as the fitting parameters. For the lamellar diblock copolymers examined in this thesis, the birefringence was small ($\Delta n \lesssim 10^{-3}$). As a result, the block copolymer films could be approximated as isotropic.

So far we have discussed how to calculate the optical constants of bare substrates and thin films using the ellipsometric angles obtained from the ellipsometer. We will

now briefly describe how these angles are measured experimentally. Figure A3.3 shows a schematic diagram of the setup used in the ellipsometry experiment. The specific ellipsometer used in this thesis was a photometric ellipsometer. In photometric ellipsometry, the polarizer and compensator are set at a fixed angles P and C relative to the plane of incidence, respectively. The elliptically polarized light is then reflected off the surface of the sample into a rotating analyzer. The periodic transmitted light intensity, which is a function of the analyzer angle A, is detected by a photodetector and can be expressed in the form,

$$I(A) = \bar{I}[1 + \alpha \cos 2A + \beta \sin 2A], \qquad \text{(A3.13)}$$

where $\bar{I}$ is the average detected signal over one full rotation of the analyzer. The coefficients α and β are obtained by Fourier analyzing the transmitted intensity. These coefficients are used to calculate the ellipsometric angles Ψ and Δ according to the foll. .g expression [131],

$$\tan\Psi e^{i\Delta} = \frac{(1+\alpha)}{\beta \pm i\sqrt{1-\alpha^2-\beta^2}} \times \frac{\tan C + \rho_c \tan(P-C)}{1-\rho_c \tan C \tan(P-C)}, \qquad \text{(A3.14)}$$

where ρ_c is the relative transmittance of the compensator.

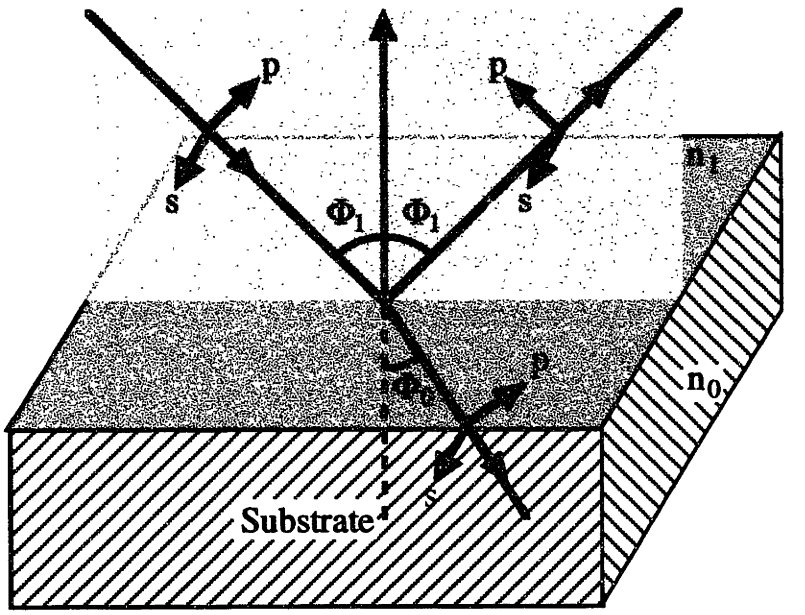

Figure A3.1 Schematic diagram illustrating the reflection of polarized light at a surface between two media. Any polarized light can be decomposed into a s component perpendicular to and a p component parallel to the plane of incidence (shaded), respectively.

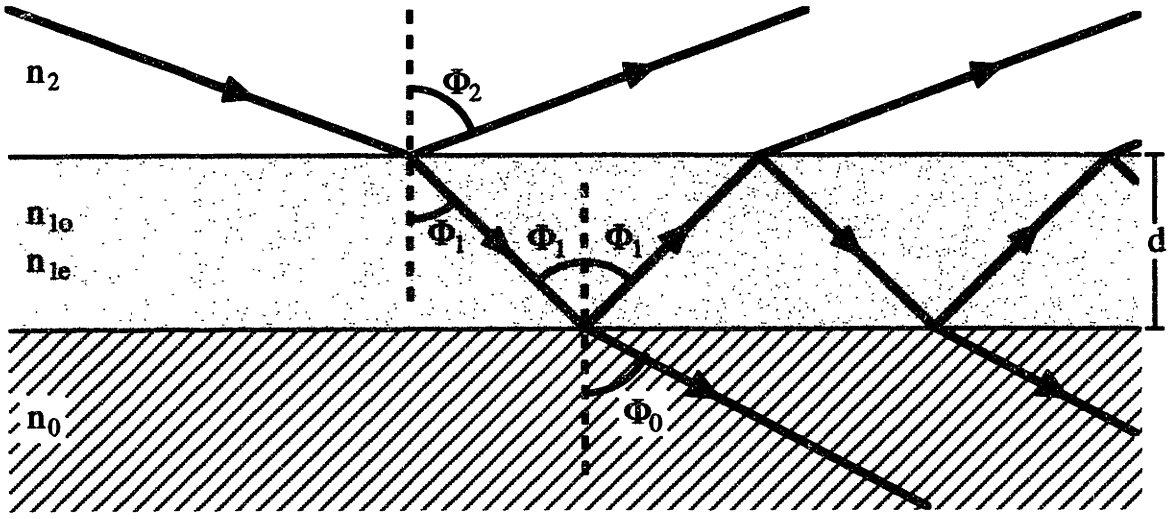

Figure A3.2 Schematic diagram of a three layer substrate/film/ambient system in which the film layer is optically uniaxial with its optic axis normal to the film.

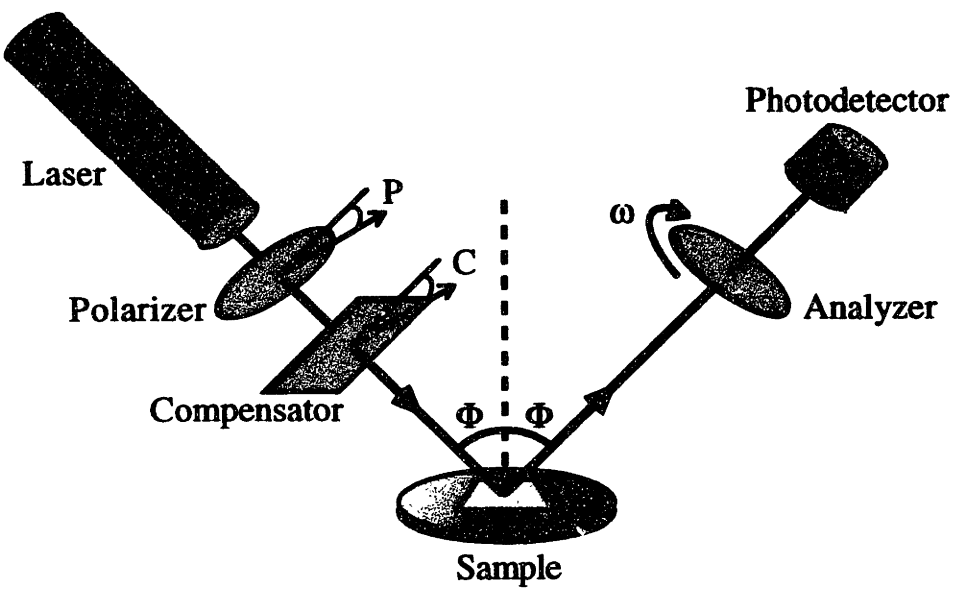

Figure A3.3 Schematic diagram of a photometric ellipsometer.

Appendix 4: Prism Coupling

Prism coupling is an integrated optics technique [57, 58] which, by probing the waveguide modes of thin dielectric films, can be used to obtain the refractive index and film thickness. The general principles behind the technique will now be described. A thin film sample mounted on a substrate is brought into intimate contact with the base of a high index prism by means of a pneumatically-operated coupling piston (see Figure A4.1). A small air gap exists between the prism and the surface of the thin film sample which is essential for prism coupling to work. A laser beam is made incident on the base of the prism as shown in Figure A4.1. Because the prism has a higher refractive index (n_p) than the air, the light undergoes total internal reflection at the air-prism interface. In addition, the prism is typically cut at an angle α so that light is totally internally reflected for all angles of incidence, θ_p. As a result, in the air gap, the light takes the form of an evanescent wave or decaying exponential. For most incident angles, the intensity of the light which is reflected from the prism base is nearly unity. But for certain discrete angles of incidence, the light is able to tunnel through the air gap and excite resonances in the film layer causing a significant drop in the reflected light intensity. These resonances coincide with the propagating waveguide modes of the film. For air gaps greater than 200 nm, the waveguide modes are unaffected by the presence of the prism. The angles of incidence at which the waveguide modes occur can be used to calculate the n_{eff}'s of the modes according to the following expression [76].

$$n_{eff} = n_p \sin\left[\alpha + \sin^{-1}\left(\frac{\sin\theta_p}{n_p}\right)\right] \qquad \text{(A4.1)}$$

Thus, by measuring the reflected light intensity one can measure the waveguide modes of a thin film. However, once the experimentally determined n_{eff}'s are known, one can also calculate the refractive index and film thickness through a least-squares minimization routine which employs the eigenvalue equation, Equation A1.8. Standard methods for this procedure are outlined in the literature [132, 133].

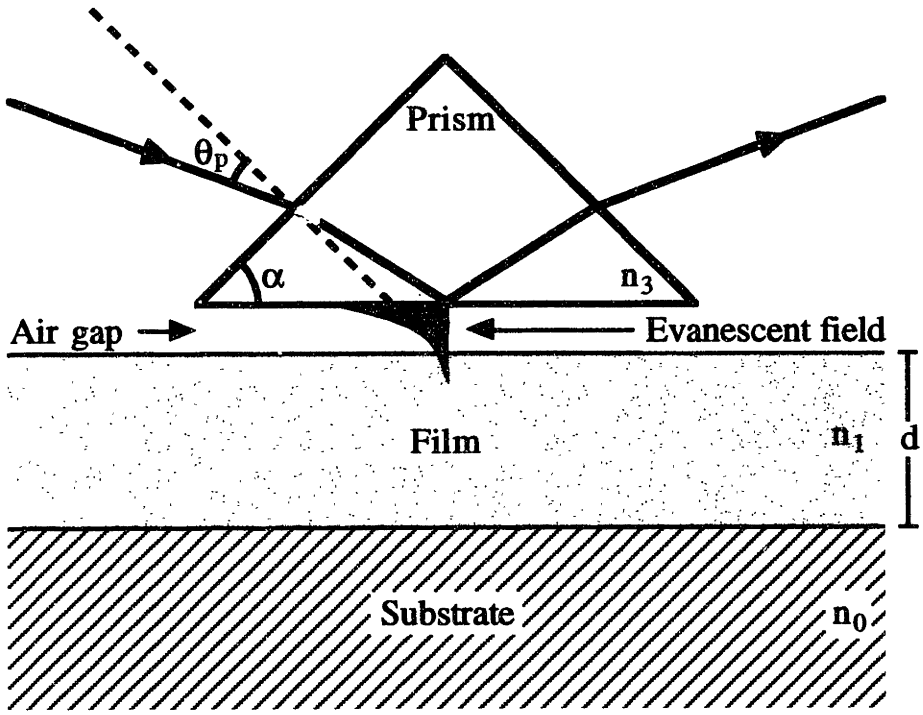

Figure A4.1 Schematic diagram of prism coupling.

Appendix 5: GPC Characterization of Rod-Coils

Raw gel permeation chromatography (GPC) chromatograms of all the rod-coil diblock copolymers were processed and analyzed to obtain total molecular weights, polydispersities, and weight fractions of PS homopolymer relative to a PS standard. The GPC chromatograms of detector response, $f(V_e)$, which were plots of differential refractive index vs. elution volume V_e on graph paper, were converted to numerical form by hand reading points along the curves at 0.5 ml intervals. The measured $f(V_e)$ for each rod-coil was then converted to weight-fraction molar mass distributions w(M) according to the procedure outlined by Young [134]. In order to carry out this conversion, the relationship between molar mass M and V_e was needed. This data was provided by a GPC calibration curve obtained from Dr. Lewis Fetters at Exxon Research and Development using PS standards which gave numerically logM vs. V_e. The calibration curve was numerically fit using a fourth-order polynomial in order to obtain an analytical expression. Using a program written in Mathematica, w(M) was obtained numerically at discrete points with the following expression.

$$w(M) = -\left(\frac{f(V_e)}{A}\right)\left(\frac{dV_e}{d\ln M}\right)\left(\frac{1}{M(V_e)}\right) \qquad \text{(A5.1)}$$

In Equation A5.1, A is a normalization factor which was determined by calculating the area under the $f(V_e)$ curve. The first term is obtained from the GPC chromatograms and the remaining two from the calibration curve. Once the w(M) was known for each rod-coil, the molar mass averages were easily computed numerically using the standard equations.

$$\overline{M}_n = \left[\int_0^\infty \frac{w(M)}{M} dM \right]^{-1} \qquad \text{(A5.2)}$$

$$\overline{M}_w = \int_0^\infty w(M)\, M\, dM \qquad \text{(A5.3)}$$

Before the weight fraction of PS homopolymer was calculated, the homopolymer regions of each $f(V_e)$ curve were corrected by dividing by a factor of two since the differential refractive index of PS is known to be about twice that of PHIC [135]. The PS weight fractions were then calculated by taking the ratio of the integral of w(M) over the homopolymer peak to the integral over the entire w(M). The homopolymer peaks were always well separated from the rod-coil distributions so that well defined limits of integration could be chosen.

Appendix 6: Force Modulation Microscopy

Introduction

AB block copolymers microphase separate to form ordered structures due to the mutual repulsion of the dissimilar blocks and the constraints imposed by the connectivity of the A and B blocks. Traditionally, transmission electron microscopy (TEM) has been used to study the bulk and near-surface morphologies (in cross-section) of block copolymers. For TEM, however, samples normally must be preferentially stained to achieve sufficient electron density contrast between the A and B blocks. The sample preparation needed for TEM can also be quite involved due to the microtomy necessary to achieve thin sections [136]. In addition, many block copolymers can experience significant beam damage which can result in image artifacts. The relatively new technique of low voltage high resolution scanning electron microscopy (LVHRSEM), which requires much less sample preparation than TEM, has also been used to study the near-surface domain structure of block copolymers [137]. While LVHRSEM is a promising tool for directly studying the surface morphology of block copolymers, samples must still be preferentially stained. In addition, because LVHRSEM utilizes an electron beam, samples can only be imaged under high vacuum and beam damage of samples can occur.

More recently, contact mode atomic force microscopy (AFM), which has excellent lateral and height resolution, was used to study the morphology of microphase separated block copolymers at free surfaces [138-140]. In the studies by Schwark et al. [138] and Annis et al. [139], solution cast samples of various poly(styrene-b-butadiene), P(S-b-B), diblock copolymers were investigated. In particular, diblock copolymers which form the lamellar and sphere (PB) morphologies in the bulk were studied. In all

the samples, the lower surface tension PB block was found to form a thin (~5 nm thick) layer which covered the entire free surface of the sample. For samples which exhibited regions of lamellae perpendicular or nearly perpendicular to the free surface, the presence of the PB surface layer resulted in a periodic surface morphology in which the peaks and valleys corresponded to the PS and PB domains, respectively. The peak to valley height as measured by AFM was found to vary between 1.5 nm and 4 nm dependent on the orientation of the lamellae with respect to the surface. In contrast to these studies, Collin et al. [140] studied the evolution of the surface morphology of spin coated lamellar-forming poly(styrene-b-n-butyl methacrylate), P(S-b-BMA), diblock copolymer films as a function of annealing time. Previous studies have shown that in these films, the microphase separated lamellae are oriented parallel to the substrate after annealing. As a result, if the initial film thickness is not equal to an integer multiple of the lamellar period (for symmetric boundary conditions), upon annealing, the films form islands or holes having heights equal to the lamellar period. By measuring the time dependent root-mean-square roughness of the films with AFM, Collin et al. were able to monitor the kinetics of island coarsening.

AFM has many advantages over TEM and LVHRSEM. Unstained samples can be imaged under ambient conditions with virtually no preparation. In addition, under proper operating conditions, the force (a few nN's) exerted by the cantilever tip is not great enough to cause permanent plastic deformation of the sample and stable imaging of the same area can be performed for hours. However, with the use of stiff cantilevers and large contact forces, deliberate deformation of the sample can be achieved through plowing or nanoindentation of the sample surface [141]. Contact mode AFM, however, does have drawbacks. Contact mode can only be used to study relatively smooth block copolymer samples which exhibit height variations commensurate with the morphology of interest. Height variations in block copolymer samples can arise from two sources.

The thermodynamics of microphase separation in the presence of a free surface can result in natural variations in the topography which are indicative of the underlying near-surface morphology, as demonstrated in references 138-140. For samples which have been fractured to expose the internal microphase separated morphology, differences in the mechanical properties of the blocks can sometimes give rise to an effective variation in height along the crack plane during deformation which mirrors the block copolymer morphology. In each case, the height variations are small, on the order of 5 nm. As a result, any significant roughness present in the sample with a periodicity similar to the domain spacing of the block copolymer can easily obscure the morphology. As well, there is no *a priori* connection between height features and chemical identity of the blocks.

In recent years, force modulation microscopy (FMM), a variation of contact mode AFM, has been developed [142]. FMM relies on differences in elasticity across the sample as the contrast mechanism rather than height differences. FMM has already been successfully demonstrated on mixed Langmuir-Blodgett films, composites, and polymer blends [142-148] which had structures ranging from hundreds of angstroms to several microns. In contrast, microphase separated block copolymers typically have domain sizes of 10 nm-50 nm. FMM is ideally suited to studying block copolymers because of its unprecedented lateral resolution and sensitivity to elasticity differences. To the best of our knowledge, block copolymers have not been studied before using this technique. In this appendix, the technique of FMM is successfully used to reveal the morphology of actual block copolymer samples. These studies show that FMM, which is a non-destructive technique requiring little sample preparation, can be used to study the near-surface morphology of block copolymers with resolutions equal to or better than those obtainable from TEM or LVHRSEM studies.

Principles and Experiment

In conventional contact mode AFM [149], a sharp tip (radius of curvature of ~10 nm-20 nm) mounted on a flexible cantilever is brought into contact with the sample. The sample which is mounted on a piezoelectric tube is then scanned at a certain rate in a xy raster scan. During the scan, the force between the tip and the sample (or cantilever deflection) is kept constant through a feedback loop which continuously monitors the deflection (input to the feedback loop) of the cantilever (a laser beam is reflected off the back of the cantilever into a segmented photodiode) and adjusts the height of the sample accordingly by applying a z motion (output of the feedback loop) to the piezoelectric tube. These z height adjustments along with their xy coordinates are used to form a topographic image of the sample. In recent years, tapping mode AFM, a variation of contact mode AFM has been developed [107]. In tapping mode AFM, the cantilever is oscillated near its resonant frequency by a small piezoelectric bimorph and has a characteristic rms amplitude of oscillation. In contrast to contact mode AFM, the tip is only in contact with the sample at the lowest point of its oscillation which reduces sample damage and minimizes the effect of lateral forces on the tip. As the oscillating tip is scanned along the sample, the feedback loop continually adjusts the z position of the piezoelectric tube so that the cantilever maintains a constant rms amplitude (typically 75% to 85% of the maximum rms amplitude). The height adjustments along with their xy coordinates are used to form the topographic image of the sample just as in contact mode AFM. In FMM, an additional sinusoidal modulation, whose amplitude is ~20 nm, is applied to either the sample position [142] or the cantilever position [150] while the tip, which is in contact with the surface, is scanned across the sample surface. The applied modulation of the tip or sample position results in a modulation of the applied contact force and of the cantilever deflection which is detected by the segmented photodiode.

The average cantilever deflection is now used as the input signal into the feedback loop as in conventional contact mode AFM to maintain a constant average applied force. The rms amplitude of the cantilever deflection, however, can be used to obtain information on the mechanical properties of the sample. For a given amplitude modulation, the resulting rms cantilever deflection for a soft material will be less than that for a hard material. As a result, the measured rms amplitude at each point in the scan along with the corresponding xy coordinates can be used to obtain an image of the surface in which contrast is achieved through relative differences in elasticity across the sample surface.

The particular method of FMM used in this study was slightly different from the one described above. A Digital Instruments, Inc. Nanoscope III controller and Multimode AFM was operated in tapping mode using the interleaved mode. When the interleaved mode is used, the piezoelectric scanner performs twice as many scan lines for a given area, displaying separate images for the odd and even numbered scan lines. The scan conditions and feedback parameters, however, can be adjusted independently for the odd (main) and even numbered (interleaved) scan lines. As a result, different sample information can be displayed simultaneously such as height and elasticity. The main scan was used to display the height information obtained using tapping mode AFM (see Figure A6.1a). To obtain the force modulation image, a feature called lift mode was employed during the interleaved scan. In lift mode, the feedback loop for the interleaved scan line is disabled and the oscillating tip tracks the surface at a user specified distance above or below the topography acquired during the previous main scan line (see Figure A6.1b). Modulation of the cantilever position is achieved by oscillating the bimorph at its resonant frequency. The resulting rms deflection of the cantilever is obtained from the normalized photodiode difference signal, (U-L)/(U+L), which is offset to zero, rectified, and low-pass filtered (U = upper detector, L = lower detector). The Nanoscope III software converts this rms deflection signal into a gray scale value where stiffer regions,

which result in a larger rms cantilever deflection, appear as darker areas. Operating the interleaved force modulation scan using lift mode has the key advantage of decoupling the height from the elasticity information, which is not possible with traditional force modulation techniques.

The FMM was done under ambient conditions using 226 μm long etched silicon cantilever substrates having spring constants ranging from 1.7 to 4.3 N/m. To obtain the height and force modulation images, the cantilever was oscillated at ~70 kHz near its resonant frequency and the bimorph at ~8 kHz near its resonant frequency. During the interleaved force modulation scans, negative lifts ranging from -12 nm to -20 nm were employed. Under these conditions, the average contact force exerted on the sample by the tip was approximately 15 nN. Height and force modulation images ranging from 1x1 μm^2 to 2.5x2.5 μm^2 in size were obtained at scan rates per line of 1-2 Hz.

Three model block copolymer samples were investigated in this study. The first sample was an unannealed poly(styrene-butadiene-styrene), P(S-B-S), triblock copolymer film fabricated from a 40 wt% toluene solution using the 'roll-casting' technique [151, 152]. The cylinder-forming triblock copolymer was synthesized by Dexco Polymers and had a total molecular weight of 73,400 g/mol and a PS fraction of 29.2%. The roll-casting process yields nearly single crystal films in which the hexagonally packed PS cylinders are macroscopically oriented in the flow direction. The roll-cast samples were cut perpendicular to the oriented cylinders with a razor blade prior to imaging to expose a fresh surface of the internal morphology. The second sample consisted of 290 nm thick unannealed and annealed poly(styrene-b-methyl methacrylate), P(S-b-MMA), diblock copolymer thin films spin coated from a 6.2 wt% solution in toluene at 5000 rpm onto glass cover slips. For annealing, samples were placed in a vacuum oven at 170°C for five days. The lamellar-forming P(S-b-MMA) diblock copolymer was synthesized by Polymer Labs and had a total molecular weight of 107,800 g/mol and a PS fraction of

47.3%. The third sample was an ultrathin film of a poly(styrene-b-hexyl isocyanate), P(HIC-b-S), rod-coil diblock copolymer cast from a dilute 0.05 wt% solution in toluene onto a carbon coated mica sheet. The synthesis and morphology of this rod-coil diblock copolymer (HS58/7) have been discussed previously in Chapter 3.

Results and Discussion

The typical lateral resolution achievable with FMM on block copolymer samples is shown (see Figure A6.2) in the 0.6x0.6 μm^2 height and force modulation images obtained for the unstained P(S-B-S) roll-cast samples. The left and right images, Figures A6.2a and A6.2b, correspond to the height image obtained with tapping mode AFM and to the force modulation image obtained from the interleaved scan using negative lift, respectively. The particular triblock copolymer studied is known to form a near-single-crystal morphology consisting of PS cylinders in a PB matrix from previous cross-sectional TEM [153] and SAXS [154] experiments. Figure A6.2a shows that the exposed fresh cut surface of the roll-cast sample is relatively rough and has height variations of ~16 nm over the area of the scan. A closer inspection, however, reveals the presence of a faint periodic hexagonal lattice of PS cylinders which are seen to protrude above the surface of the film by about 1.5-3 nm. The different mechanical properties of PS and PB most likely give rise to this topography when the sample was cut with the razor blade. In comparison to the height image, the regular two dimensional array of cylinders is more easily recognizable in the elasticity image, Figure A6.2b, due to the large stiffness contrast between PS and PB. As expected, the glassy PS cylinders appear dark in Figure A6.2b indicating that they are stiffer than the surrounding rubbery PB matrix. The inset to Figure A6.2b is a digital fast Fourier transform (FFT) of a 0.3x0.3 μm^2 area within the image and confirms the hexagonal packing of the PS cylinders. In particular, the FFT is a

hexagonal pattern which has been stretched in the vertical direction. In unannealed roll-cast films, asymmetry in the cylinder morphology has been shown to be a direct result of the roll-casting process. Additional asymmetry can also result from either plastic deformation experienced during cutting and/or a fracture surface not exactly perpendicular to the cylinder axis. The 23.3±1.1 nm d-spacing obtained from the smallest Bragg peak agrees well with the 24.0 nm d-spacing measured with SAXS. In addition, the measured average PS cylinder diameter of 13 nm is the same within error to the cylinder diameter obtained from cross-sectional TEM measurements and that calculated from simple volume fraction considerations assuming the 24 nm d-spacing. The roll-cast sample demonstrates that FMM can be used to study the internal morphologies of traditional coil-coil block copolymers in which one block is glassy and one is rubbery. In addition, the method of FMM used in this study successfully decouples topographic information from elasticity information.

The height and force modulation images shown in Figure A6.2 were obtained less than ~10 minutes after the internal surface of the roll-cast samples were exposed to the air using the razor blade. Both the elasticity contrast and the height contrast arising from the oriented PS cylinders were found to disappear after prolonged imaging with FMM. Images of previously unscanned areas on the same sample also showed an absence of height or elasticity contrast which ruled out the possibility of sample damage as a source of the loss in contrast. PB has a lower surface tension with the air than PS. Consequently, the evolution of the fracture surface with time indicates a migration of the PB block over the surface which covered the exposed PS domains and obscured the presence of the underlying morphology. The migration of the PB block is thermodynamically driven and reduces the free energy of the higher energy PS-air surfaces [138]. The process is further facilitated by the fact that PB is rubbery at room temperature and is the majority component. Typically, the total loss of elasticity contrast

between the PS cylinders and the PB matrix took place within 30 minutes after cutting. Although not carried out in this study, the technique of FMM could easily be used to study migration phenomena of this type.

While FMM is ideally suited to studying glassy/rubbery block copolymer morphology, the technique is also able to detect much smaller elasticity differences. Height and force modulation images of the as spun P(S-b-MMA) thin film are shown in Figures A6.3a and A6.3b for a scan size of 1x1 μm^2, respectively. Both images reveal a chaotic bicontinuous morphology consisting of interconnected PS and PMMA channels which results from the rapid solvent evaporation caused by the spin coating process. The two images, however, are significantly different in a number of ways. The height image shows both a gradual variation in the height of the P(S-b-MMA) film, which causes some areas of the scan to appear brighter and others darker, and ~4.5 nm pseudoperiodic height variations due to the microphase separated morphology which have an approximate domain size of 47 nm. In contrast, only the variation in elasticity across the sample resulting from the relative differences in the stiffness of the microphase separated PS and PMMA domains is apparent in the elasticity image. Although under ambient conditions and at the 8 kHz frequency of loading used in this study both PMMA and PS are glassy polymers, PMMA has been shown in a number of studies [155-158] to be stiffer than PS by a factor ranging from 1.1 to 1.5. Consequently, the dark areas in the elasticity image and the lower areas in the height image correspond to the stiffer PMMA domains.

Figures A6.4a and A6.4b show similar height and force modulation images obtained for the annealed P(S-b-MMA) film for a scan size of 1x1 μm^2, respectively. Because PS has a lower surface tension with air, annealing causes the PS block to migrate over the surface of the sample covering the PMMA domains [60]. In comparison to the unannealed sample, the height features present in Figure A6.4a are due mainly to the overall surface roughness of the film. In addition, the faint height variations associated

with the microphase separated morphology are only 8 Å in amplitude. As a result, the surface roughness tends to obscure the microstructure making the block copolymer morphology not readily apparent. The elasticity image (see Figure A6.4b), however, does show the alternating PS and PMMA domains of the lamellar morphology. The elasticity contrast present in the annealed sample is only about 1/3 that of the unannealed sample which is consistent with a thin PS surface layer. The characteristic domain spacing of the annealed morphology obtained from Figure A6.4b is found to be ~55 nm. Although this value is significantly larger than that measured for the unannealed sample, spin coating of diblock copolymers has been shown to produce chaotic morphologies with domain sizes much smaller than their equilibrium spacings [159]. The domain spacing of the annealed sample, however, does agree well with the equilibrium bulk domain spacing measured with SAXS of 55.3 nm. The P(S-b-MMA) samples show that FMM is well suited to studying the near-surface morphologies of block copolymer thin films even when both blocks of the copolymer are glassy.

Measuring the sizes of individual domains using conventional contact mode AFM or TEM is not always a straightforward process. For AFM, the local topography does not always correspond directly to the microphase separated morphology. For TEM, staining, microtomy, beam damage, and sample tilt can all lead to incorrect domain spacing measurements. FMM, however, is much better suited to measurements of domain size. In a strongly segregated block copolymer, the elasticity measured at any given point is directly correlated to the composition of the material being probed by the tip. As a result, the force modulation image gives a true representation of the microphase separated morphology. Height and force modulation images for the P(HIC-b-S) rod-coil block copolymer thin film are shown in Figures A6.5a and A6.5b for a scan size of 2.5x2.5 μm^2, respectively. Both Figures A6.5a and A6.5b show the alternating "zig-zag" lamellar structure of PS and PHIC domains discussed previously in Chapter 3 using

bright field TEM and electron diffraction. From the height image, the amorphous PS domains are found to be ~7 nm lower than the surrounding PHIC rod domains. Height profiles obtained from slices vertical to the sample plane show that many of the height depressions present throughout the scan result from local packing defects within the PHIC domains and are only ~3 nm in depth. Unlike the previous two samples, the morphology of the P(HIC-b-S) thin film in Figure A6.5a is not significantly obscured by any surface roughness across the scan area. In this case, the elasticity image, Figure A6.5b, shows essentially the same morphology. While PHIC is known to be a rigid rod [101, 102], it adopts an 8_3 helical conformation (see Appendix 7) in which the paraffin-like pendant hexyl groups surround the PHIC backbone. Consequently, the glassy PS domains are stiffer than the PHIC domains and appear dark in the elasticity image. The average PHIC domain spacing measured from the elasticity image, 177 nm, agrees well with the 180 nm value obtained from TEM. In contrast, the average width of the PS domains obtained from the elasticity image is found to be 15 nm, which is significantly lower than the average value obtained previously using TEM of 25 nm. The value of the PS domain size obtained using FMM is likely a more accurate value of the actual domain size. Swelling effects resulting from the RuO_4 staining of the PS and the effect of sample tilt on the finite thickness samples could easily explain the larger values of the PS domain size measured previously by TEM. These results show a major advantage of FMM over other existing microscopy techniques. Namely, for a given sample, block copolymer domain sizes can be accurately measured using FMM entirely bypassing the need for heavy metal staining or for microtomy which can lead to errors induced through sample preparation.

In addition to the uses of FMM in studying block copolymer morphology demonstrated in this appendix, FMM has the potential to be used in a number of other applications. As mentioned earlier, FMM can be used to study kinetic phenomena such

as the migration of polymers over surfaces. Depending on the glass transition temperatures of the individual blocks or homopolymers, temperature stages could be used to conduct in-situ migration studies of both pure block copolymers and block copolymer/homopolymer blends. In a pure block copolymer, the lower surface tension block would be tethered to the intermaterial dividing surface (IMDS) and migration would be hindered. In a blend, however, no such anchoring of the homopolymer chains would be present allowing the homopolymer to freely diffuse. In addition, FMM could be used to study surface reconstruction in block copolymers. The presence of a free surface perturbs the free energy of the block copolymer near the surface. As a result, a different equilibrium morphology may be preferred at the surface than is present in the bulk block copolymer. Bulk samples could be fractured to expose the internal morphology and studied with FMM as a function of time or temperature as the surface morphology evolved. The elasticity at a given point on the microphase separated block copolymer sample is dependent on the local composition and the amount of loading. As a result, FMM could be used to study the lateral composition profile near the interfacial region between block copolymer domains (rubbery/glassy, noncrystalline/crystalline, ...etc.). The effect of the degree of segregation on the interfacial width could also be investigated. By varying the amount of modulation applied to the sample, information on the vertical composition could be obtained (i.e. thicknesses of surface layers). In the future, as the complex interaction between the tip and sample is better understood and reliable calibration standards for FMM are developed, exact values of the modulus at any point in the scan may be achievable. Thus, the modulus of a given polymer confined within a strongly segregated block copolymer domain, which is likely to be significantly different from that of the free homopolymer, could be measured. In addition, the influence of architecture, morphology, and molecular weight on the modulus could be studied. With advances in force modulation microscope design, a dynamic mechanical

analysis of block copolymers and semicrystalline homopolymers on the molecular scale could also be possible.

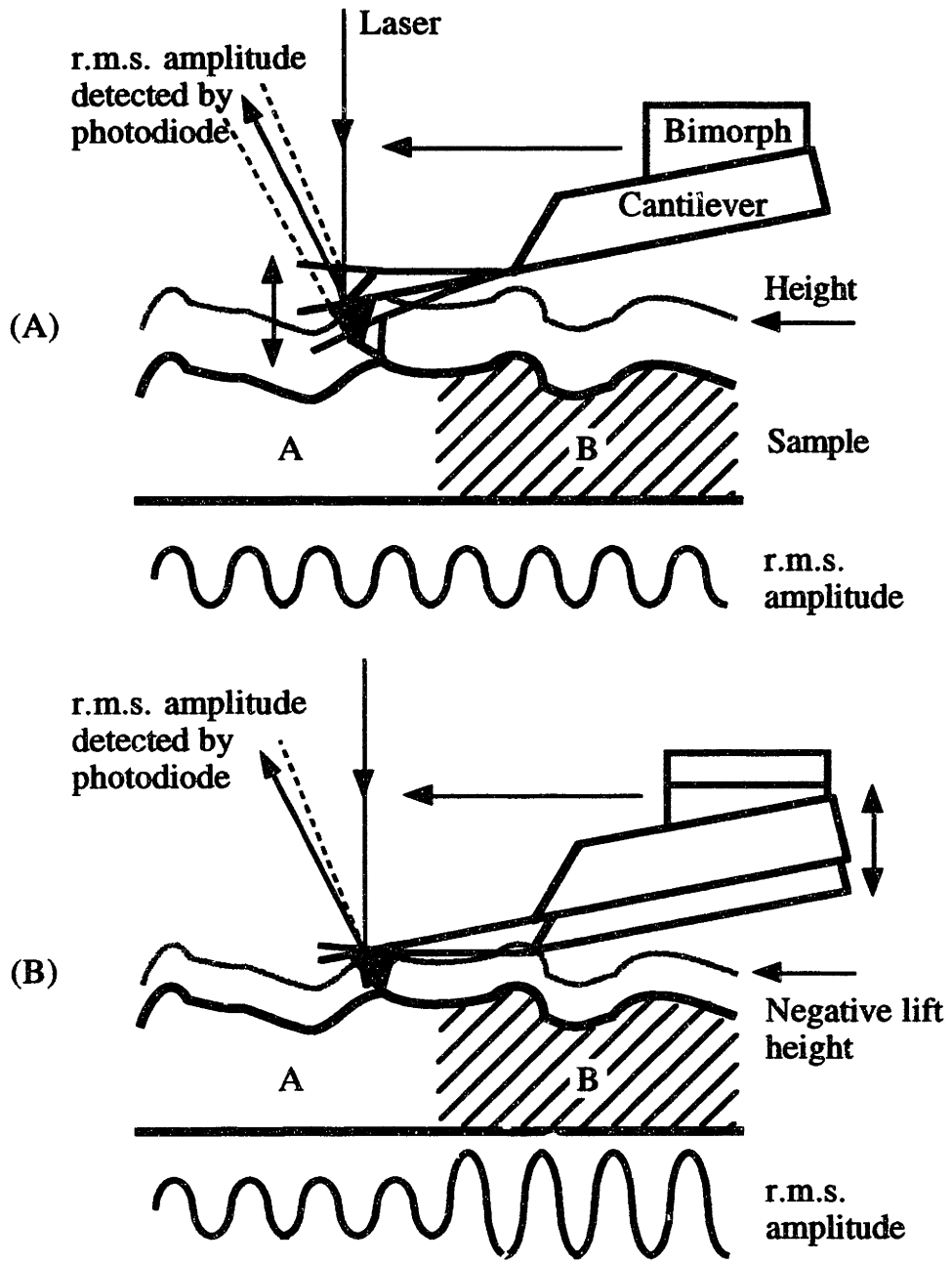

Figure A6.1 (A) Schematic diagram illustrating how the height images are acquired using tapping mode AFM during the main scan. In tapping mode, the cantilever is oscillated at its resonant frequency of ~70 kHz while the feedback loop keeps the r.m.s. amplitude constant. (B) Schematic diagram illustrating how the elasticity images are acquired in the interleaved scan using FMM with negative lift mode. During the interleaved scan, the cantilever is oscillated at the bimorph resonant frequency of ~8 kHz. The detected r.m.s. amplitude of the cantilever is a measure of the local surface elasticity of the sample. In the diagram, material B is stiffer and results in a greater r.m.s. amplitude.

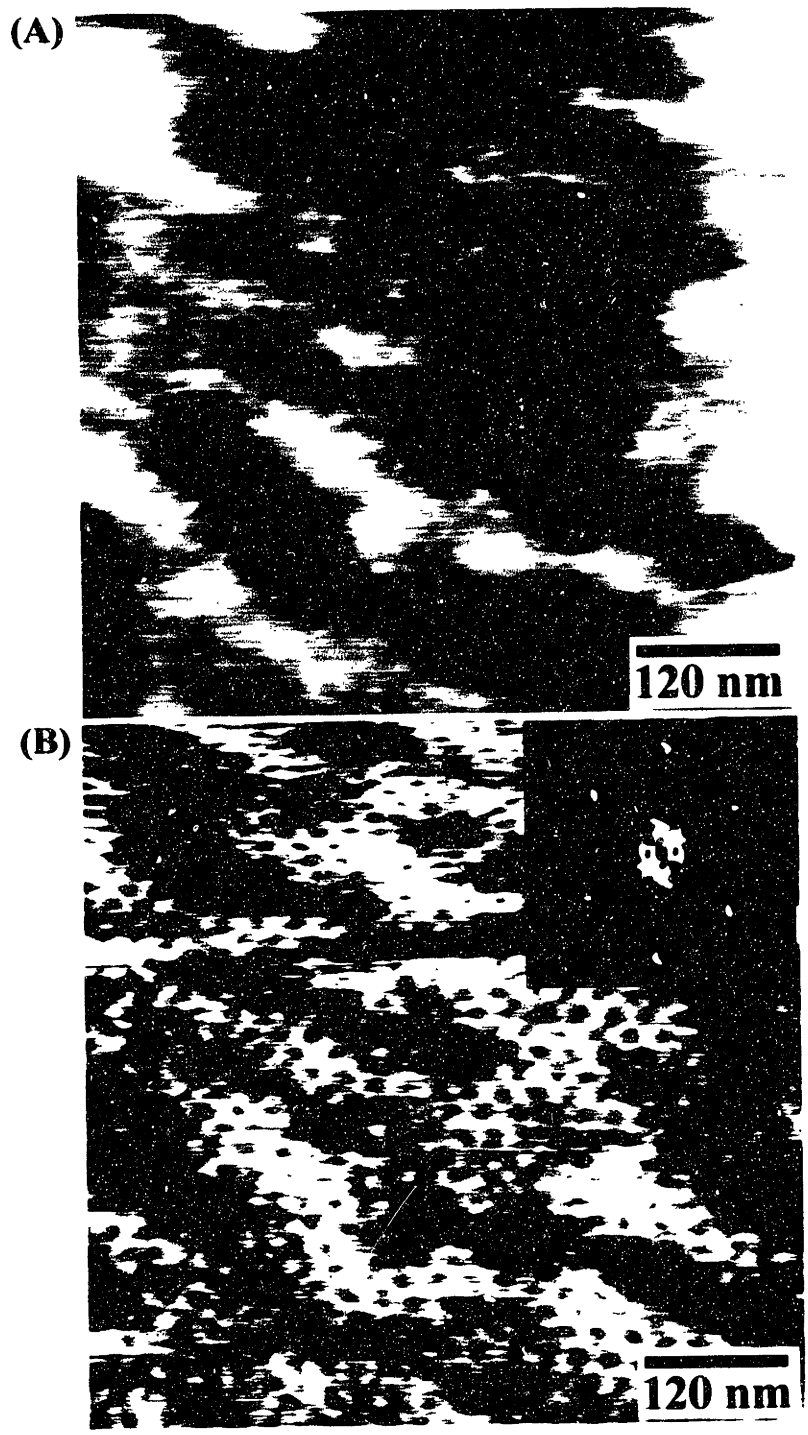

Figure A6.2 **(A) Height image of the unannealed P(S–B–S) roll–cast film viewed down the cylinder axis. Faint PS cylinders are visible along with large height variations. (B) Elasticity image for the same area. The 2D packing of the PS cylinders is clearly visible. The inset is a digital FFT of a smaller area which confirms the hexagonal packing of the cylinders.**

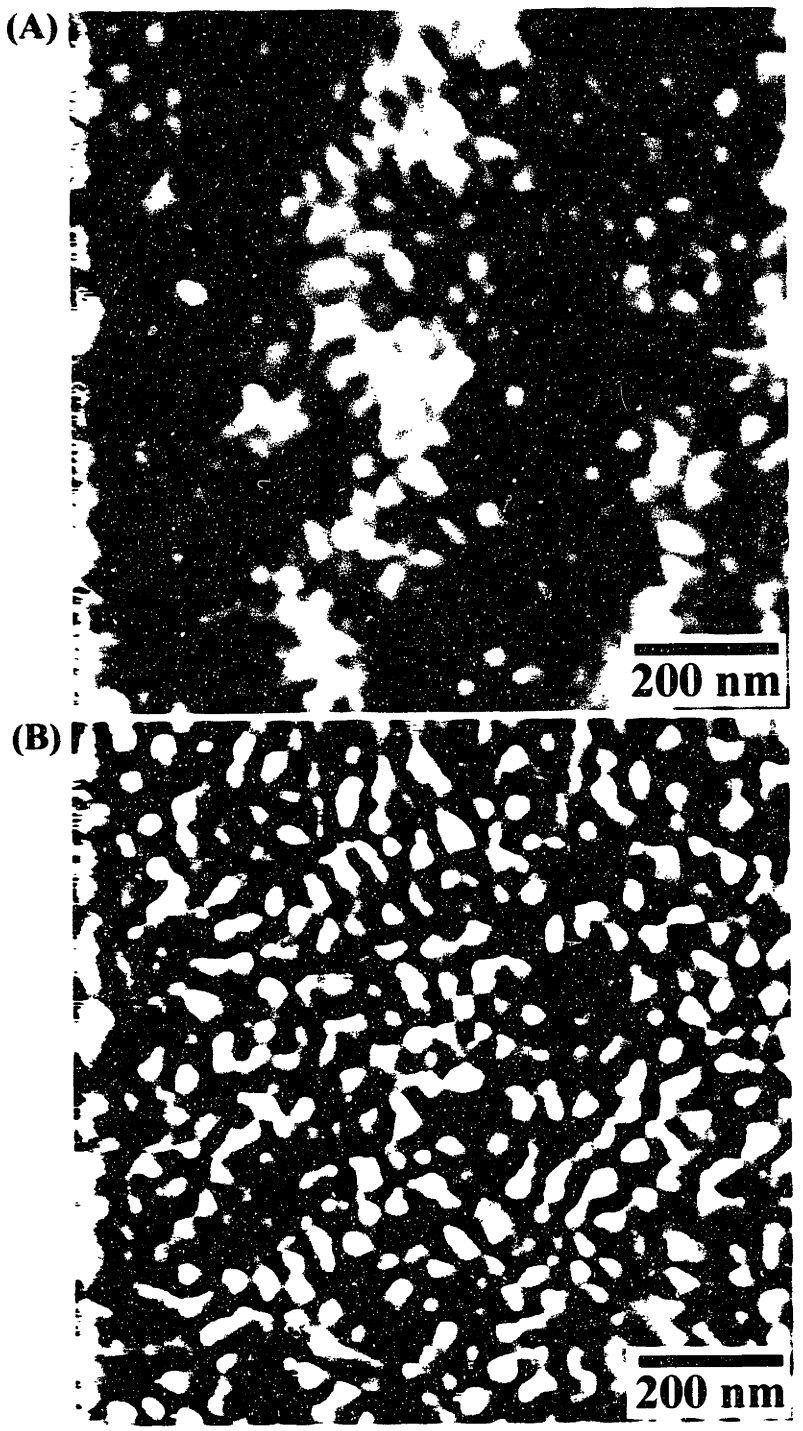

Figure A6.3 **(A) Height image of the unannealed spin coated P(S–b–MMA) thin film which shows both surface roughness and height variations due to the microphase separated morphology. (B) Elasticity image of the same area. The contrast arises solely from the differences in stiffness between PS an PMMA.**

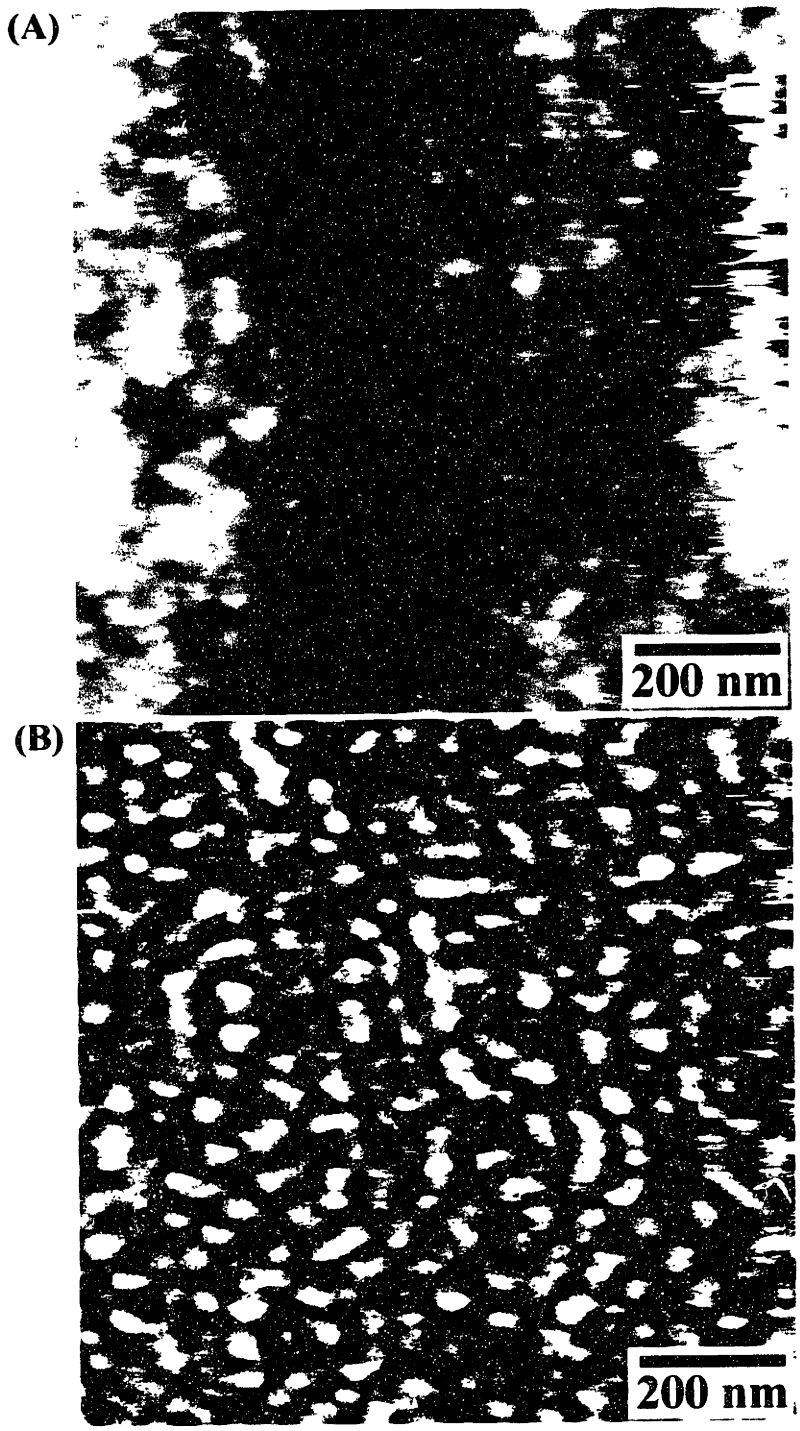

Figure A6.4 **(A) Height image of the annealed spin coated P(S–b–MMA) thin film which shows no apparent structure. Surface roughness and PS migration have obscured the block copolymer morphology. (B) Elasticity image of the same area. Even though the elasticity contrast is 1/3 that of the unannealed sample, the short–range lamellae are still visible.**

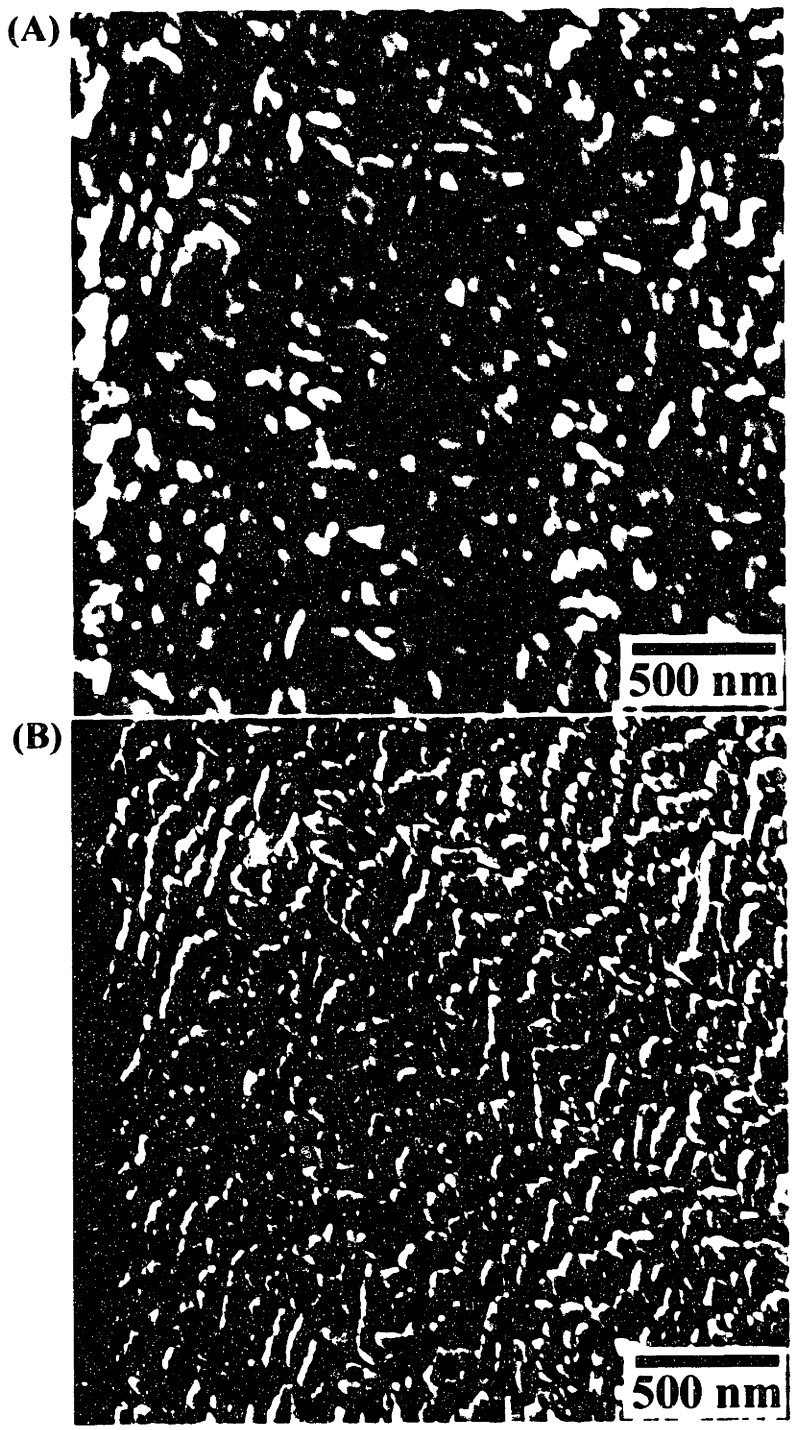

Figure A6.5 **(A) Height image of the unannealed P(HIC–b–S) ultrathin film which shows the zig–zag lamellar morphology. Numerous packing defects are present in the PHIC domains. (B) Elasticity image of the same area. The PS domains in the elasticity image are significantly narrower than the corresponding regions in the height image.**

Appendix 7: Determination of the Crystal Structure, Helical Conformation, and Orientation of the PHIC Block in the Zig-zag Morphology

The crystal structure, conformation, and orientation of the PHIC block in the zig-zag morphology were obtained from an analysis of SAED patterns of HS58/7. The inset to Figure 3.7b shows representative SAED pattern obtained from the PHIC rod domains in the zig-zag morphology. The electron diffraction pattern, which exhibits apparent fiber symmetry, shows that, in addition to being orientationally ordered on the molecular scale, the PHIC domains are crystalline. The large number (21) of reflections (a schematic diffraction pattern is shown in Figure A7.1) indicates that the degree of crystallinity is high. To the best of our knowledge, a full crystal structure determination of PHIC has never been performed. As mentioned earlier, however, WAXS of unoriented and drawn samples of PHIC was done by Clough [106]. From his data, he concluded that the PHIC chains adopted a 12_5 helix with a two monomer repeat unit of 3.1 Å. In addition, he found that crystallization from toluene and THF resulted in two different sets of d-spacings indicating polymorphism although no unit cells were proposed. As a result, an analysis of the SAED patterns had to be undertaken. The presence of meridional reflections indicates that in the unit cell the c axis is perpendicular to the a and b axes. By measuring the vertical spacing of the layer lines in the SAED pattern, the c axis repeat distance is calculated to be c = 15.6 Å. An analysis of the two equatorial reflections and the other layer line reflections revealed that the SAED pattern can be successfully indexed entirely with (0kl)-type reflections. As a result, only information in two directions of reciprocal space is present in the SAED patterns. Consequently, aside from c, only $b\sin\gamma$ = 13.08 Å can be determined. The presence of only (0kl) reflections is strongly indicative of a lack of fiber symmetry caused by preferred crystal growth of the

PHIC domains on the carbon substrate. Additional evidence for preferred crystal growth was provided by SAED experiments which showed additional equatorial reflections when the sample was tilted about the c axis.

WAXS of P(HIC-b-S) drawn fibers and X-ray powder diffraction of a bulk sample cast from toluene were performed to determine the remaining unit cell parameters and conclusively show whether the thin film samples exhibit a preferred crystal orientation. While the degree of orientation was moderate, the WAXS pattern of the fiber sample did exhibit fiber symmetry and showed a total of five equatorial reflections. The additional equatorial reflections confirmed that the PHIC domains in the thin film samples is oriented with the (010) planes normal to the substrate. Excluding the first reflection, dividing the remaining equatorial Bragg spacings by the 2nd Bragg spacing resulted in the $1:\sqrt{3}:\sqrt{4}:\sqrt{7}$ ratios expected for hexagonal packing of the rods, which disagrees with the d-spacings reported by Clough. The first reflection, which has a d-spacing of ~15.8 Å and whose intensity is minor relative to the second reflection, may be attributable to another crystal structure. Using the WAXS data, the remaining unit cell parameters are calculated to be $a = b = 15.1$ Å, and $\gamma = 120°$. The corresponding crystal density of PHIC is found to be 1.10 g/cm^3 for a unit cell containing two molecules, which agrees well with the experimentally measured [104] value of 1.00 g/cm^3. Although the WAXS data suggest hexagonal packing of the rods, the X-ray powder diffraction profile obtained from the bulk film cast from toluene showed several reflections which could not be indexed according to a hexagonal unit cell. These results further support Clough's findings of polymorphism in PHIC.

In addition to crystal structure information, valuable information on the molecular conformation of the PHIC rods was obtained by analyzing the intensity of the Bragg reflections corresponding to each layer line of the SAED pattern. From helical diffraction theory, the equation,

$$l = tn + um, \qquad \text{(A7.1)}$$

for a u_t helix (t turns for u units) can be derived where n and m are integers and l is the layer line index. Solutions of Equation A7.1 give the orders, n, of the Bessel functions which contribute to the helix structure factor on the lth layer line. Layer lines with low order Bessel functions, such as n = 0, 1, or 2, typically have strong intensity reflections. According to Clough, high intensity reflections for PHIC were observed on the l = 0, 2, 5, 7, and 12 layer lines, which agrees with the intensity distribution expected for a 12_5 helix. This intensity distribution, however, is not at all consistent with the layer line intensities observed from the P(HIC-b-S) SAED patterns. As a result, the intensity distributions for other helices were calculated and compared to the ED patterns. Table A7.1 shows the list of Bessel functions which contribute to each layer line for an 8_3 helix generated using Equation A7.1.

Table A7.1 List of the Bessel functions which contribute to each layer line for an 8_3 helix generated using Equation A7.1.

l	n	m	n	m	n	m
0	**0**	**0**	8	-3	-8	3
1	3	-1	-5	2		
2	-2	1	6	-2	-10	4
3	**1**	**0**	-7	3	9	-3
4	4	-1	-4	2		
5	**-1**	**1**	7	-2	-9	4
6	2	0	-6	3	10	-3
7	-3	2	5	-1		
8	**0**	**1**	8	-2	-8	4
9	3	0	-5	3		
10	-2	2	6	-1	-10	5
11	1	1	-7	4	9	-2
12	4	0	-4	3		
13	-1	2	7	-1	-9	5
14	2	1	-6	4	10	-2
15	-3	3	5	0		
16	0	2	8	-1	-8	5

The intensities resulting from an 8_5 helix are identical to those of an 8_3 helix because the helices differ only in their respective handedness. Inspection of Table A7.1 shows that out of the first eight layer lines, the l = 0, 3, 5, and 8 layer lines (bolded) will have the strongest reflections. Figure A7.1 shows strong reflections on the l = 3 and 5 layer lines which are characteristic of first order Bessel functions in agreement with Table A7.1. In addition, meridional reflections are only allowed on the layer lines that are integer multiples of eight because of the zero order Bessel functions, which is confirmed by the presence of the (008) and the (0016) reflections. The 1.95 Å d-spacing obtained

from the (008) reflection is equivalent to the projection of the intermonomer distance onto the major axis of the helix and is in good agreement with previously published values of 1.8-2.0 Å [160, 161]. Therefore, the PHIC block can be assigned a conformation of either an 8_3 or 8_5 helix which have a translation of 1.95 Å and rotation of 135° per monomeric unit along the c axis. The 8_3 helical conformation was also observed previously by Shmueli et al. in oriented poly(N-butyl isocyanate) films using X-ray diffraction [162]. A qualitative fit of the predicted Bessel function structure factors for an 8_3 or 8_5 helix to the measured intensity distributions of each layer line using the PHIC helix radius as a fitting parameter yielded a radius of ~3.25 Å. The equatorial reflections indicate hexagonal packing of the chains which suggests a two chain monoclinic or triclinic (pseudohexagonal) unit cell for PHIC.

So far we have discussed how SAED was used to obtain the crystal structure and helical conformation of the PHIC block. SAED, however, was also useful in the determination of the orientation of the PHIC chain axis with respect to the microphase separated morphology (zig-zags). By taking a SAED pattern of the zig-zag morphology and then defocusing the main (000) beam using the intermediate lens current control during the exposure, one obtains an image of both the diffraction pattern and of the real space morphology (out of focus). Figure A7.2 shows a schematic diagram of the defocused (000) bright field image of the zig-zag morphology superimposed on its respective electron diffraction pattern. Since the defocused bright field image is not rotated relative to the diffraction pattern in this mode of operation, Figure A7.2 shows clearly that the chain axis of the PHIC rods (arrow) is oriented normal to the zig-zag axis and at an equal but opposite angle with respect to the alternating lamellar normals.

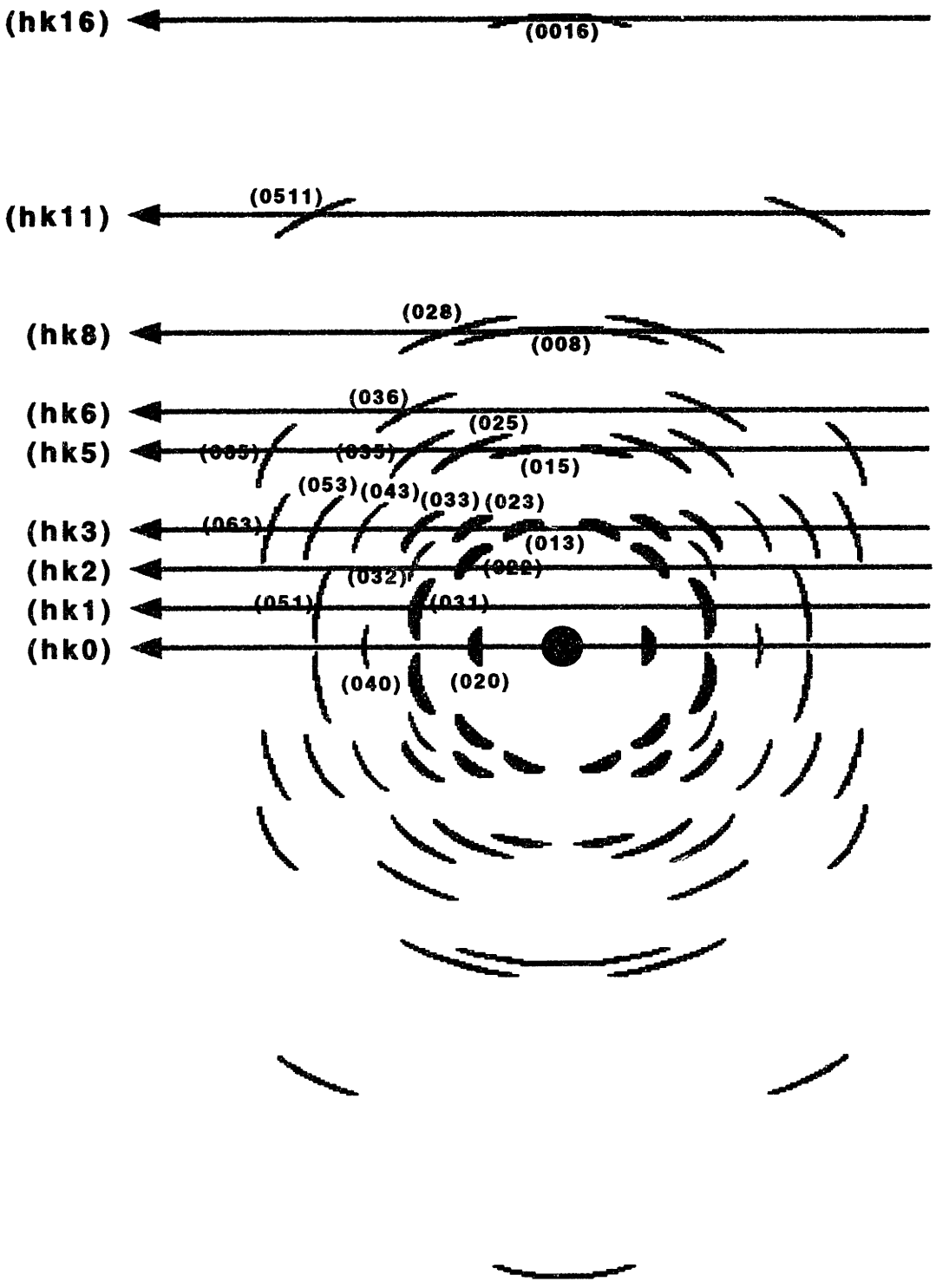

Figure A7.1 Indexed schematic diagram of the selected-area electron diffraction pattern obtained from HS58/7. All reflections are of the (0kl) type. The first meridional reflection is the (008).

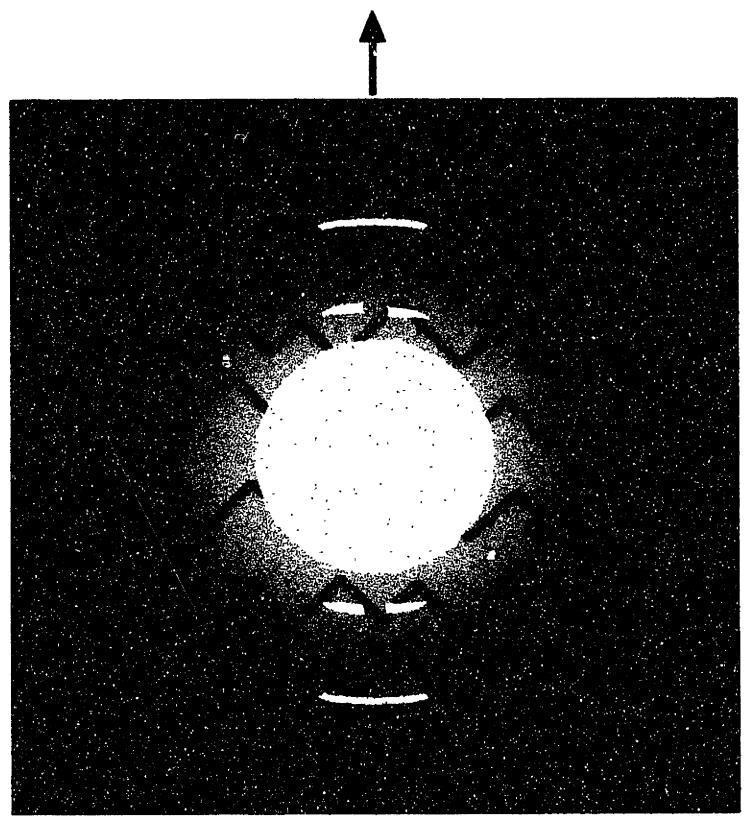

Figure A7.2 Schematic diagram of the electron diffraction pattern and superimposed defocused (000) bright field image of the zig-zag morphology. The pattern shows that the chain axis of the PHIC rods is normal to the zig-zag axis. The arrow indicates the direction of the PHIC chain axis.

Bibliography

1. Molau, G. E. In *Block Copolymers*; Aggarwal, S. L., Ed.; Plenum Press: New York, 1970.

2. Hashimoto, T.; Shibayama, M.; Kawai, H. "Domain-Boundary Structure of Styrene-Isoprene Block Copolymer Films Cast from Solution. 4. Molecular-Weight Dependence of Lamellar Microdomains", *Macromolecules* **1980**, *13*, 1237.

3. Hashimoto, T.; Fujimura, M.; Kawai, H. "Domain-Boundary Structure of Styrene-Isoprene Block Copolymer Films Cast from Solutions. 5. Molecular-Weight Dependence of Spherical Microdomains", *Macromolecules* **1980**, *13*, 1660.

4. Hashimoto, T.; Shibayama, M.; Kawai, H. "Ordered Structure in Block Polymer Solutions. 4. Scaling Rules on Size Fluctuations with Block Molecular Weight, Concentration, and Temperature in Segregation and Homogeneous Regimes", *Macromolecules* **1983**, *16*, 1093.

5. Bates, F. S.; Cohen, R. E.; Berney, C. V. "Small-Angle Neutron Scattering Determination of Macrolattice Structure in a Polystyrene-Polybutadiene Diblock Copolymer", *Macromolecules* **1982**, *15*, 589.

6. Thomas, E. L.; Kinning, D. J.; Alward, D. B.; Henkee, C. S. "Ordered Packing Arrangements of Spherical Micelles of Diblock Copolymers in Two and Three Dimensions', *Macromolecules* **1987**, *20*, 2934.

7. Thomas, E. L.; Alward, D. B.; Kinning, D. J.; Martin, D. C.; Handlin, D. L.; Fetters, L. J. "Ordered Bicontinuous Double Diamond Structure of Star Block Copolymers-- A New Equilibrium Microdomain Morphology", *Macromolecules* **1986**, *19*, 2197.

8. Hasegawa, H.; Tanaka, K.; Yamasaki, K.; Hashimoto, T. "Bicontinuous Microdomain Morphology of Block Copolymers. 1. Tetrapod-Network Structure of Polystyrene-Polyisoprene Diblock Copolymers", *Macromolecules* **1987**, *20*, 1651.

9. Schwark, D. W. "Influence of Interfacial Constraints on the Microdomain Morphology of Block Copolymers", Ph.D. Thesis; University of Massachusetts: Amherst, 1992.

10. Anderson, D. M.; Thomas, E. L. "Microdomain Morphology of Star Copolymers in the Strong-Segregation Limit", *Macromolecules* **1988**, *21*, 3221.

11. Hajduk, D. A.; Harper, P. E.; Gruner, S. M.; Honeker, C. C.; Thomas, E. L.; Fetters, L. J. "A Reevaluation of Bicontinuous Cubic Phases in Starblock Copolymers", *Macromolecules* **1995**, *28*, 2570.

12. Almdal, K.; Koppi, K. A.; Bates, F. S.; Mortensen, K. "Multiple Ordered Phases in a Block Copolymer Melt", *Macromolecules* **1992**, *25*, 1743.

13. Sakurai, S.; Kawada, H.; Hashimoto, T.; Fetters, L. J. "Thermoreversible Morphology Transition Between Spherical and Cylindrical Microdomains of Block Copolymers", *Macromolecules* **1993**, *26*, 5796.

14. Hamley, I. W.; Koppi, K. A.; Rosedale, J. H.; Bates, F. S. "Hexagonal Mesophases Between Lamellae and Cylinders in a Diblock Copolymer Melt", *Macromolecules* **1993**, *26*, 5959.

15. Winey, K. I.; Gobran, D. A.; Xu, Z.; Fetters, L. J.; Thomas, E. L. "Compositional Dependence of the Order-Disorder Transition in Diblock Copolymers", *Macromolecules* **1994**, *27*, 2392.

16. Hajduk, D. A.; Gruner, S. M.; Rangarajan, P.; Register, R. A.; Fetters, L. J.; Honeker, C. C.; Albalak, R. J.; Thomas, E. L. "Observation of a Thermotropic Order-Order Transition in a Diblock Copolymer", *Macromolecules* **1994**, *27*, 490.

17. Hajduk, D. A.; Harper, P. E.; Gruner, S. M.; Honeker, C. C.; Kim G.; Thomas, E. L.; Fetters, L. J. "The Gyroid: A New Equilibrium Morphology in Weakly Segregated Diblock Copolymers", *Macromolecules* **1994**, *27*, 4063.

18. Schulz, M. F.; Bates, F. S.; Almdal, K; Mortensen, K. "Epitaxial Relationship for Hexagonal-to-Cubic Phase Transition in a Block Copolymer Mixture", *Phys. Rev. Lett.* **1994**, *73*, 86.

19. Bates, F. S.; Schulz, M. F.; Khandpur, A. K.; Forster, S.; Rosedale, J. H.; Almdal, K.; Mortensen, K. "Fluctuations, Conformational Asymmetry and Block Copolymer Phase Behavior", *Faraday Discuss. Chem. Soc.* **1994**, *98*, 7.

20. Forster, S.; Khandpur, A. K.; Zhao, J.; Bates, F. S.; Hamley, I. W.; Ryan, A. J.; Bras, W. "Complex Phase Behavior of PI-PS Diblock Copolymers Near the Order-Disorder Transition", *Macromolecules* **1994**, *27*, 6922.

21. Khandpur, A. K.; Forster, S.; Bates, F. S.; Hamley, I. W.; Ryan, A. J.; Bras, W.; Almdal, K.; Mortensen, K. "The Polyisoprene-Polystyrene Diblock Copolymer Phase Diagram Near the Order-Disorder Transition", *Macromolecules* **1995**, *28*, 8796.

22. Thomas, E. L.; Anderson, D. M.; Henkee, C. S.; Hoffman, D. "Periodic area-minimizing surfaces in block copolymers", *Nature* **1988**, *334*, 598.

23. Meier, D. J. "Theory of Block Copolymers. I. Domain Formation in A-B Block Copolymers", *J. Polymer Sci.: Part C* **1969**, *49*, 361.

24. Helfand, E. "Block Copolymer Theory. III. Statistical Mechanics of the Microdomain Structure", *Macromolecules* **1975**, *8*, 552.

25. Helfand, E.; Wasserman, Z.R. "Block Copolymer Theory. 4. Narrow Interphase Approximation", *Macromolecules* **1976**, *9*, 879.

26. Helfand, E.; Wasserman, Z.R. "Block Copolymer Theory. 5. Spherical Domains", *Macromolecules* **1978**, *11*, 960.

27. Helfand, E.; Wasserman, Z.R. "Block Copolymer Theory. 6. Cylindrical Domains", *Macromolecules* **1980**, *13*, 994.

28. Ohta, T.; Kawasaki, K. "Equilibrium Morphology of Block Copolymer Melts", *Macromolecules* **1986**, *19*, 2621.

29. Leibler, L. "Theory of Microphase Separation in Block Copolymers", *Macromolecules* **1980**, *13*, 1602.

30. Matsen, M. W.; Schick, M. "Stable and Unstable Phases of a Diblock Copolymer Melt", *Phys. Rev. Lett.* **1994**, *72*, 2660.

31. Fredrickson, G. H.; Helfand, E. "Fluctuation Effects in the Theory of Microphase Separation in Block Copolymers", *J. Chem. Phys.* **1987**, *87*, 697.

32. Vavasour, J. D.; Whitmore, M. D. "Self-Consistent Mean Field Theory of the Microphases of Diblock Copolymers", *Macromolecules* **1992**, *25*, 5477.

33. Shull, K.R. "Mean-Field Theory of Block Copolymers: Bulk Melts, Surfaces, and Thin Films", *Macromolecules* **1992**, *25*, 2122.

34. Lescanec, R. L.; Muthukumar, M. "Density Functional Theory of Phase Transitions in Diblock Copolymer Systems", *Macromolecules* **1993**, *26*, 3908.

35. Matsen, M. W.; Bates, F. S. "Block Copolymer Microstructures in the Intermediate-Segregation Regime", *J. Chem. Phys.* (submitted).

36. Semenov, A. N. "Microphase Separation in Diblock-Copolymer Melts: Ordering of Micelles", *Macromolecules* **1989**, *22*, 2849.

37. Melenkevitz, J.; Muthukumar, M. "Density Functional Theory of Lamellar Ordering in Diblock Copolymers", *Macromolecules* **1991**, *24*, 4199.

38. Jackson, J. D. *Classical Electrodynamics*; John Wiley & Sons: New York, 1975.

39. Ditchburn, R. W. *Light*; Dover Publications, Inc.: New York, 1991.

40. Born, M.; Wolf, E. *Principles of Optics*; Pergamon Press: New York, 1959.

41. Nye, J. F. *Physical Properties of Crystals*; Oxford University Press: New York, 1995.

42. Fowles, G. R. *Introduction to Modern Optics*; Dover Publications, Inc.: New York, 1989.

43. Lord Rayleigh "On the Influence of Obstacles arranged in Rectangular Order upon the Properties of a Medium", *Phil. Mag.*, **1892**, *34*, 481.

44. Maxwell Garnett, J. C. "Colours in Metal Glasses and in Metallic Films.", *Phil. Trans. R. Soc. London* **1904**, *203*, 385.

45. Maxwell Garnett, J. C. "Colours in Metal Glasses, in Metallic Films, and in Metallic Solutions.-II.", *Phil. Trans. R. Soc. London* **1906**, *205*, 237.

46. Wiener, O. "Die Theorie Des Mischkörpers Für Das Feld Der Stationären Strömung Erste Abhandlung Die Mittelwertsätze Für Fraft, Polarisation Und Energie", *Abh. Sächs. Ges. Akad. Wiss., Math.-Phys. Kl.* **1912**, *32*, 575.

47. Bruggeman, D. A. G. "Berechnung verschiedener physikalischer Konstanten von heterogenen Substanzen 1. Dielektrizitätskonstanten und Leitfähigkeiten der Mischkörper aus isotropen Substanzen", *Ann. Phys.* **1935**, *24*, 636.

48. Folkes, M. J.; Keller, A. "Optical and Swelling Properties of Macroscopic "Single Crystals" of an S-B-S Copolymer. I. Samples Possessing a Lamellar Morphology", *J. Polym. Sci.* **1976**, *14*, 833.

49. Folkes, M. J.; Keller, A. "The birefringence and mechanical properties of a 'single crystal' from a three-block copolymer", *Polymer, Lond.* **1971**, *12*, 222.

50. Joannopoulos, J. D.; Meade, R. D.; Winn, J. N. *Photonic Crystals Molding the Flow of Light*; Princeton University Press: Princeton, 1995.

51. Yablonovitch, E.; Gmitter, T. J.; Leung, K. M. "Photonic Band Structure: The Face-Centered-Cubic Case Employing Nonspherical Atoms", *Phys. Rev. Lett.* **1991**, *67*, 2295.

52. Fink, Y.; Thomas, E. L. (personal communication, November 1996).

53. Tien, P. K.; Smolinsky, G.; Martin, R. J. "Thin Organosilicon Films for Integrated Optics", *Applied Optics* **1972**, *11*, 637.

54. Zernike, F. In *Integrated Optics*; Tamir, T., Ed.; Springer-Verlag: New York, 1975.

55. Chen, R. T.; Wang, M. R.; Sonek, G. J.; Jannson, T. "Optical interconnection using polymer microstructure waveguides", *Optical Engineering* **1991**, *30*, 622.

56. Tien, P. K. "Integrated optics and new wave phenomena in optical waveguides", *Reviews of Modern Physics* **1977**, *49(2)*, 361.

57. Tien, P. K.; Ulrich, R.; Martin, R. J. "Modes of Propagating Light Waves in Thin Deposited Semiconductor Films", *Appl. Phys. Lett.* **1969**, *14(9)*, 291.

58. Tien, P. K. "Light Waves in Thin Films and Integrated Optics", *Applied Optics* **1971**, *10(11)*, 2395.

59. Marcuse, D. *Theory of Dielectric Optical Waveguides*; Academic Press, Inc.: Boston, 1991.

60. Coulon, G.; Russell, T. P.; Deline, V. R.; Green, P. F. "Surface-Induced Orientation of Symmetric, Diblock Copolymers: A Secondary Ion Mass Spectrometry Study", *Macromolecules* **1989**, *22*, 2581.

61. Russell, T. P.; Coulon, G.; Deline, V. R.; Miller, D. C. "Characteristics of the Surface-Induced Orientation for Symmetric Diblock PS/PMMA Copolymers", *Macromolecules* **1989**, *22*, 4600.

62. Coulon, G.; Ausserre, D.; Russell, T. P. "Interference Microscopy on Thin Diblock Copolymer Films", *J. Phys. France* **1990**, *51*, 777.

63. Anastasiadis, S. H.; Russell, T. P.; Satija, S. K.; Majkrzak, C. F. "The Morphology of Symmetric Diblock Copolymers as Revealed by Neutron Reflectivity", *J. Chem. Phys.* **1990**, *92(9)*, 5677.

64. Green, P. F.; Christensen, T. M.; Russell, T. P. "Ordering at Diblock Copolymer Surfaces", *Macromolecules* **1991**, *24*, 252.

65. Russell, T. P.; Menelle, A.; Anastasiadis, S. H.; Satija, S. K.; Majkrzak, C. F. "Unconventional Morphologies of Symmetric, Diblock Copolymers Due to Film Thickness Constraints", *Macromolecules* **1991**, *24*, 6263.

66. Miayata, S.; Ogasawara, H.; Edel, V.; Watanabe T. "Second-harmonic generation in a five-layer waveguide-Large dimension tolerance for phase-matching", *Polymer Preprints* **1994**, *35(2)*, 211.

67. Kupfer, M.; Florsheimer, M.; Bosshard, C.; Gunter, P. "$\chi^{(2)}$-Inverted Langmuir-Blodgett Films for Guided-Wave Nonlinear Optics", *Polymer Preprints* **1994**, *35(2)*, 281.

68. Normandin, R.; Dai, H.; Janz, S.; Delage, A.; Brown, J.; Chatenoud, F. "Multilayer, nonlinear antiresonant waveguides for surface emitted optical mixing", *Appl. Phys. Lett.* **1993**, *62(2)*, 118.

69. Shakir, S. A.; Turner, A. F. "Method of Poles for Multilayer Thin-Film Waveguides", *Appl. Phys. A* **1982**, *29*, 151.

70. Chilwell, J.; Hodgkinson, I. "Thin-films field-transfer matrix theory of planar multilayer waveguides and reflection from prism-loaded waveguides", *J. Opt. Soc. Am. A* **1984**, *1(7)*, 742.

71. Polky, J. N.; Mitchell, G. L. "Metal-clad planar dielectric waveguide for integrated optics", *J. Opt. Soc. Am.* **1974**, *64(3)*, 274.

72. Tien, P. K.; Riva-Sanseverino, S.; Martin, R. J.; Ballman, A. A.; Brown, H. "Optical waveguide modes in single-crystalline $LiNbO_3$-$LiTa\ O_3$ solid-solution films", *Appl. Phys. Lett.* **1974**, *24(10)*, 503.

73. Conwell, E. M. "Modes in optical waveguides formed by diffusion", *Appl. Phys. Lett.* **1973**, *23(6)*, 328.

74. Lodge, T. P.; Fredrickson, G. H. "Optical Anisotropy of Tethered Chains", *Macromolecules* **1992**, *25*, 5643.

75. Swalen, J. D.; Tacke, M.; Santo, R.; Fischer, J. "Determination of Optical Constants of Polymeric Thin Films by Integrated Optical Techniques", *Optics Communications* **1976**, *18(3)*, 387.

76. Swalen, J. D.; Santo, R.; Tacke, M.; Fischer, J. "Properties of Polymeric Thin Films by Integrated Optical Techniques", *IBM J. Res. Develop.* **1977**, 168.

77. Kim, J.; Chin, I.; Smith, B. A.; Russell, T. P.; Mays, J. W. "On the Birefringence of Multilayered Symmetric Diblock Copolymer Films", *Macromolecules* **1993**, *26*, 5436.

78. Ptaszynski, B.; Terrisse, J.; Skoulios, A. "Solubilisation de polystyrene dans la phase lamellaire d'un copolymere bisequence polystyrene/polyisoprene", *Makromol. Chem.* **1975**, *176*, 3483.

79. Winey, K. I.; Thomas, E. L.; Fetters, L. J. "Swelling a Lamellar Diblock Copolymer by Homopolymer: Influences of Homopolymer Concentration and Molecular Weight", *Macromolecules* **1991**, *24*, 6182.

80. Tselikas, Y.; Hadjichristidis, N.; Lescanec, R. L.; Honeker, C. C.; Wohlgemuth, M.; Thomas, E. L. "Architecturally-Induced Tricontinuous Cubic Morphology in Compositionally Symmetric Miktoarm Starblock Copolymers", *Macromolecules* **1996**, *29*, 3390.

81. Boudenne, N.; Anastasiadis, S. H.; Fytas, G.; Xenidou, M.; Hadjichristidis, N.; Semenov, A. N.; Fleischer, G. "Thermodynamic Effects on Internal Relaxation in Diblock Copolymers", *Phys. Rev. Lett.* (submitted).

82. Henkee, C. S.; Thomas, E. L.; Fetters, L. J. "The Effect of Surface Constraints on the Ordering of Block Copolymer Domains", *J. Mat. Sci.* **1988**, *23*, 1685.

83. Mayes, A. M.; Russell, T. P.; Deline, V. R.; Satija, S. K.; Majkrzak, C. F. "Block Copolymer Mixtures As Revealed by Neutron Reflectivity", *Macromolecules* **1994**, *27*, 7447.

84. Gobran, D. A. "Phase Separation and Morphology of Diblock and Segmented Block Copolymers", Ph.D. Thesis; University of Massachusetts: Amherst, 1990.

85. Wu, S. *Polymer Interface and Adhesion*; Marcel Dekker: New York, 1982.

86. Flory, P. J. "Phase equilibria in solutions of rod-like particles", *Proc. R. Soc. London, (A)* **1956**, *243*, 73.

87. Perly, B.; Douy, A.; Gallot, B. "Block Copolymers Polybutadiene/Poly(benzyl-L-glutamate) and Polybutadiene/Poly(N^5-hydroxypropylglutamine) Preparation and Structural Study by X-ray and Electron Microscopy", *Makromol. Chem.* **1976**, *177*, 2569.

88. Douy, A.; Gallot, B. "Structure of AB copolymers with a polypeptide block: effect of the chain", *Polym. Eng. Sci.* **1977**, *17*, 523.

89. Nakajima, A.; Hayashi, T.; Kugo, K.; Shinoda, K. "Synthesis and Structural Study of the A-B-A Type Block Copolymer Consisting of Poly(γ-benzyl L-glutamate) as the A Component and Polybutadiene as the B Component", *Macromolecules* **1979**, *12*, 840.

90. Barenberg, S.; Anderson, J. M.; Geil, P. H. "Structure and properties of two plastic peptide triblock, ABA, copolymers of poly(γ-benzyl L-glutamate), A, and poly(butadiene/acrylonitrile), B", *Int. J. Biol. Macromol.* **1981**, *3*, 82.

91. Douy, A.; Gallot, B. "Amphipathic block copolymers with two polypeptide blocks: Synthesis and structural study of poly(N^{ε}-trifluoroacetyl-L-lysine)-polysarcosine copolymers", *Polymer* **1987**, *28*, 147.

92. Radzilowski, L. H.; Wu, J. L.; Stupp, S. I. "Monodisperse "Rodcoil" Copolymers", *Macromolecules* **1993**, *26*, 879.

93. Radzilowski, L. H.; Stupp, S. I. "Nanophase Separation in Monodisperse Rodcoil Diblock Polymers", *Macromolecules* **1994**, *27*, 7747.

94. Semenov, A. N.; Vasilenko, S. V. "Theory of the nematic-smectic-A transition in a melt of macromolecules consisting of a rigid and a flexible block", *Sov. Phys.-JETP (Engl. Transl.)* **1986**, *63(1)*, 70.

95. Halperin, A. "Smectic A-Smectic C Transition in Lamellae Formed by Rod-Coil Copolymers", *Europhys. Lett.* **1989**, *10(6)*, 549.

96. Halperin, A. "Rod-Coil Copolymers: Their Aggregation Behavior", *Macromolecules* **1990**, *23*, 2724.

97. Williams, D. R. M.; Frederickson, G. H. "Cylindrical Micelles in Rigid-Flexible Diblock Copolymers", *Macromolecules* **1992**, *25*, 3561.

98. Raphael, E.; de Gennes, P. G. "Plates, fences and needles: an example of the Skoulios effect", *Physica A* **1991**, *177*, 294.

99. Raphael, E.; de Gennes, P. G. "Aggregation of Flexible-Rigid-Flexible Triblock Copolymers", *Makromol. Chem., Macromol. Symp.* **1992**, *62*, 1.

100. Gurovich, E. "On Liquid Crystalline Copolymers", *Macromolecules* (in press).

101. Berger, M. N. "Addition Polymers of Monofunctional Isocyanates", *J. Macromol. Sci.-Revs. Macromol. Chem.* **1973**, *C9(2)*, 269.

102. Bur, A. J.; Fetters, L. J. "The Chain Structure, Polymerization, and Conformation of Polyisocyanates", *Chem. Revs.* **1976**, *76(6)*, 727.

103. Aharoni, S. M. "Rigid Backbone Polymers. 2. Polyisocyanates and Their Liquid-Crystal Behavior", *Macromolecules* **1979**, *12*, 94.

104. Aharoni, S. M.; Walsh, E. K. "Rigid Backbone Polymers. 4. Solution Properties of Two Lyotropic Mesomorphic Poly(isocyanates)", *Macromolecules* **1979**, *12*, 271.

105. Aharoni, S. M. "Rigid Backbone Polymers. 11. Solution Phase-Viscosity Relationship", *J. Polym. Sci.: Polym. Phys. Ed.* **1980**, *18*, 1439.

106. Clough, S. B. In *Characterization of Materials in Research Ceramics and Polymers*; Burke, J. J., Weiss, V., Eds.; Syracuse University Press: Syracuse, New York, 1975; pp 417-436.

107. *Digital Instruments, Inc. Nanoscope III Command Reference Manual, Version 3.0* (December 21, 1993; p. 35).

108. Levelut, A. M.; Germain, C.; Keller, P.; Liebert, L. "Two new mesophases in a chiral compound", *J. Phys. Fr.* **1983**, *44*, 623.

109. Chandani, A. D. L.; Gorecka, E.; Ouchi, Y.; Takezoe, H.; Fukuda, A. "Antiferroelectric Chiral Smectic Phases Responsible for the Tristable Switching in MHPOBC", *Jpn. J. Appl. Phys.* **1989**, 28(7), 1265.

110. Galerne, Y.; Liebert, L. "Smectic-O Films", *Phys. Rev. Lett.* **1990**, *64(8)*, 906.

111. Galerne, Y.; Liebert, L. "Antiferroelectric Chiral Smectic-O* Liquid Crystal", *Phys. Rev. Lett.* **1991**, *66(22)*, 2891.

112. P. Hamelin, Levelut, A. M.; Martinot-Lagarde, P.; Germain, C.; Liebert, L. "Structural and electro-optical studies of the smectic polymorphism of a homologous series of chiral molecules", *J. Phys. II Fr.* **1993**, *3*, 681.

113. Adams, J.; Gronski, W. "LC side chain AB-block copolymers with an amorphous A-block and a liquid-crystalline B-block", *Makromol. Chem. Rapid Comm.* **1989**, *10*, 553.

114. Zaschke, B.; Frank, W.; Fischer, H.; Schmutzler, K.; Arnold, M. "Synthesis and characterization of LC side chain AB blockcopolymers", *Polym. Bull.* **1991**, *27*, 1.

115. Kodaira, T.; Kazumi, M. "Block copolymers of narrow molecular-weight distribution with a side-chain liquid-crystalline polymeric block as one component", *Makromol. Chem.* **1992**, *193*, 1331.

116. Bohnert, R.; Finkelmann, H. "Liquid crystalline side-chain AB block copolymers by direct anionic polymerization of mesogenic methacrylate", *Macromol. Chem. Phys.* **1994**, *195*, 689.

117. Arnold, M.; Poser, S.; Fischer, H.; Frank, W.; Utschick, H. "Liquid-crystalline side chain block copolymers-synthesis, morphology and LC behaviour", *Macromol. Rapid Commun.* **1994**, *15*, 487.

118. Fischer, H.; Poser, S.; Arnold, M.; Frank, W. "On the Influence of the Morphological Structure on the Liquid Crystalline Side Chain Block Copolymers", *Macromolecules* **1994**, *27*, 7133.

119. Fischer, H.; Poser, S.; Arnold, M. "On the interaction of the morphological structure and the LC behaviour of LC side group block copolymers", *Liquid Crystals* **1995**, *18*, 503.

120. Fischer, H.; Poser, S.; Arnold, M. "Liquid Crystalline Side Group Block Copolymers with n-Butyl Methacrylate as an Amorphous A-Block: Synthesis and Characterization", *Macromolecules* **1995**, *28*, 6957.

121. Yamada, M.; Iguchi, T.; Hirao, A.; Nakahama, S.; Watanabe, J. "Synthesis of Side-Chain Liquid Crystalline Homopolymers and Block Copolymers with Well-Defined Structures by Living Anionic Polymerization and Their Thermotropic Phase Behavior", *Macromolecules* **1995**, *28*, 50.

122. Ringsdorf, H.; Schmidt, H. W. "Electro-optical effects of azo dye containing liquid crystalline copolymers", *Makrom. Chem.* **1984**, *185*, 1327.

123. *Side Chain Liquid Crystal Polymers*; McArdle, C. B., Ed.; Chapman and Hall: New York, 1989.

124. Friedel, G. "Les Etats Mesomorphes de la Matiere", *Ann. Phys.* **1922**, *18(9)*, 273.

125. Pansu, B.; Dubois-Violette, E. "Blue Phases: Experimental Survey and Geometrical Approach", *Colloque de Physique (Supplement au J. Physique, 23)*, **1990**, *51*, 281.

126. Chaikin, P. M.; Lubensky, T. C. *Principles of Condensed Matter Physics*; Cambridge University Press: New York, 1995.

127. Bornside, D. E.; Macosko, C. W.; Scriven, L. E. "On the Modeling of Spin Coating", *J. Imag. Tech.* **1987**, *13*, 122.

128. Bornside, D. E.; Macosko, C. W.; Scriven, L. E. "Spin Coating: One-Dimensional Model", *J. Appl. Phys.* **1989**, *66(11)*, 5185.

129. Weill, A.; Dechenauz, E. "The Spin-Coating Process Mechanism Related to Polymer Solution Properties", *Polym. Eng. Sci.* **1988**, *28*, 945.

130. Spangler, L. L.; Torkelson, J. M.; Royal, J. S. "Influence of Solvent and Molecular Weight on Thickness and Surface Topography of Spin-Coated Polymer Films", *Polym. Eng. Sci.* **1990**, *30*, 644.

131. Azzam, R. M. A.; Bashara, N. M. *Ellipsometry and Polarized Light*; North-Holland: New York, 1987.

132. Ulrich, R.; Torge, R. "Measurement of Thin Film Parameters with a Prism Coupler", *Appl. Opt.* **1973**, *12(12)*, 2901.

133. Kersten, R. T. "Numerical Solution of the Mode-Equation of Planar Dielectric Waveguides to Determine Their Refractive Index and Thickness by Means of a Prism-Film Coupler", *Opt. Commun.* **1973**, *9*, 427.

134. Young, R. J.; Lovell, P. A. *Introduction to Polymers*; Chapman and Hall: New York, 1991.

135. Fetters, L. J. (personal communication).

136. Thomas, E. L. In *The Encyclopedia of Polymer Science and Engineering*; Kroschwitz, J. I., Ed.; John Wiley: New York, 1986; Vol. 5, p. 644.

137. Vezie, D. L.; Thomas, E. L.; Adams, W. W. "Low Voltage, High Resolution SEM: A New Characterization Technique for Polymer Morphology", *Polymer* **1995**, *36(9)*, 1761.

138. Schwark, D. W.; Vezie, D. L.; Reffner, J. R.; Thomas, E. L.; Annis, B. K. "Characterization of the Surface Morpholopgy of Diblock Copolymers via Low-Voltage, High Resolution Scanning Electron Microscopy and Atomic Force Microscopy", *J. Mat. Sci. Let.* **1992**, *11*, 352.

139. Annis, B. K.; Schwark, D. W.; Reffner, J. R.; Thomas, E. L.; Wunderlich, B. "Determination of Surface Morphology of Diblock Copolymers of Styrene and Butadiene by Atomic Force Microscopy", *Makromol. Chem.* **1992**, *193*, 2589.

140. Collin, B.; Chatenay, D.; Coulon, G.; Ausserre, D.; Gallot, Y. "Ordering of Copolymer Thin Films As Revealed by Atomic Force Microscopy", *Macromolecules* **1992**, *25*, 1621.

141. Frommer, J. "Scanning Tunneling Microscopy and Atomic Force Microscopy in Organic Chemistry", *Angew. Chem. Int. Ed. Engl.* **1992**, *31*, 1298.

142. Maivald, P.; Butt, H. J.; Gould, S. A. C.; Prater, C. B.; Drake, B.; Gurley, J. A.; Elings, V. B.; Hansma, P. K. "Using force modulation to image surface elasticities with the atomic force microscope", *Nanotechnology* **1991**, *2*, 103.

143. Radmacher, M.; Tillmann, R. W.; Fritz, M.; Gaub, H. E. "From Molecules to Cells: Imaging Soft Samples with the Atomic Force Microscope", *Science* **1992**, *257*, 1900.

144. Radmacher, M.; Tillmann, R. W.; Gaub, H. E. "Imaging viscoelasticity by force modulation with the atomic force microscope", *Biophys. J.* **1993**, *64*, 735.

145. Florin, E. -L.; Radmacher, M.; Fleck, B.; Gaub, H. E. "Atomic force microscope with magnetic force modulation", *Rev. Sci. Instrum.* **1994**, *65(3)*, 639.

146. Overney, R. M.; Bonner, T.; Meyer, E.; Ruetschi, M.; Luthi, R.; Howald, L.; Frommer, J.; Guntherodt, H. -J.; Fujihara, M.; Takano, H. "Elasticity, wear, and friction properties of thin organic films observed with atomic force microscopy", *J. Vac. Sci. Technol. B* **1994**, *12(3)*, 1973.

147. Kajiyama, T.; Tanaka, K.; Ohki, I.; Ge, S. -R.; Yoon, J. -S.; Takahara, A. "Imaging of Dynamic Viscoelastic Properties of a Phase-Separated Polymer Surface by Force Oscillation Atomic Force Microscopy", *Macromolecules* **1994**, *27*, 7932.

148. Overney, R. M.; Meyer, E.; Frommer, J.; Guntherodt, H. -J.; Fujihara, M.; Takano, H.; Gotoh, Y. "Force Microscopy Study of Friction and Elastic Compliance of Phase-Separated Organic Thin Films", *Langmuir* **1994**, *10*, 1281.

149. Binnig, G.; Quate, C. F.; Gerber, C. "Atomic Force Microscope", *Phys. Rev. Lett.* **1986**, *56*, 930.

150. Pethica, J. B.; Oliver, W. C. "Tip Surface Interactions in STM and AFM", *Physica Scripta* **1987**, *T19*, 61.

151. Albalak, R. J.; Thomas, E. L. "Microphase Separation of Block Copolymer Solutions in a Flow Field", *J. Polym. Sci., Polym. Phys. Edn.* **1993**, *31*, 37.

152. Albalak, R. J.; Thomas, E. L. "Roll Casting of Block Copolymers and of Block Copolymer-Homopolymer Blends", *J. Polym. Sci., Polym. Phys. Edn.* **1994**, *32*, 341.

153. Albalak, R. J. (personal communication).

154. Albalak, R. J. "The Anisotropic Thermal Expansion of 'Single-Crystal' Triblock Copolymer Films", *Polymer* **1994**, *35(19)*, 4115.

155. Maxwell, B. "An Investigation of the Dynamic Mechanical Properties of Polymethyl Methacrylate", *J. Polym. Sci.* **1956**, *20*, 551.

156. Lethersich, W. "The rheological properties of dielectric polymers", *Brit. J. Appl. Phys.* **1950**, *1*, 294.

157. Wright, H.; Faraday, C. S. N.; White, E. F. T.; Treloar, L. R. G. "The elastic constants of oriented glassy polymers", *J. Phys. D: Appl. Phys.* **1971**, *4*, 2002.

158. Creton, C.; Kramer, E. J.; Hui, C. -Y.; Brown, H. R. "Failure Mechanisms of Polymer Interfaces Reinforced by Block Copolymers", *Macromolecules* **1992**, *25*, 3075.

159. Russell, T. P.; Mayes, A. M.; Kunz, M. S. *In Ordering in Macromolecular Systems*; Teramoto, A.; Kobayashi, M.; Norisuje, T., Eds.; Springer-Verlag: Berlin, 1994; p. 217.

160. Fetters, L. J.; Yu, H. "Equilibrium Conformation and "Worm-Like Coil" Configuration of Poly(n-alkyl isocyanates)", *Macromolecules* **1971**, *4*, 385.

161. Berger, M. N.; Tidswell, B. M. "Dilute Solution Viscosity and Conformation of Poly-N-Hexyl Isocyanate", *J. Polym. Sci., (IUPAC Intl. Symp. on Macromolecules, Helsinki, 1972)*, **1973**, *42*, 1063.

162. Shmueli, U.; Traub, W.; Rosenheck, K. "Structure of Poly(N-butyl Isocyanate)", *J. Polym. Sci. A* **1969**, *7*, 515.

Biographical Note

Education

Massachusetts Institute of Technology
Fall 1991 to Spring 1997. Graduated with a Ph.D. degree in Materials Science and Engineering with an emphasis on Polymers and minor in Physics, June 1997. GPA: 4.7/5.0. Thesis work involved research on the influence of a liquid crystalline block on the microstructure and optical properties of block copolymers.

Massachusetts Institute of Technology
Fall 1987 to Summer 1991. Graduated with a B.S. degree in Physics, June 1991. GPA: 4.6/5.0. Thesis involved performing time-of-flight powder neutron diffraction experiments on two bismuth-manganese compounds and analyzing the diffraction patterns using the Rietveld least-squares refinement method.

Experience

Massachusetts Institute of Technology
Summer 1991 to Spring 1997. Research Assistant in the Department of Materials Science and Engineering in the laboratory of Professor Edwin Thomas. Gained expertise in the following structural and optical characterization techniques: optical microscopy, optical diffraction, cross-sectional transmission electron microscopy, electron diffraction, atomic force microscopy (contact, tapping, and force modulation modes), small angle and wide angle X-ray diffraction, ellipsometry, and prism coupling. Helped develop a N-layer waveguide program to predict the optical waveguide modes of model structures. Authored numerous papers in leading scientific journals and presented work at several national conferences.

Fall 1994. Teaching Assistant in the Department of Materials Science and Engineering for the course *Structure of Materials*.

Argonne Summer Research Participation Program
Summer 1990. Participated as a researcher at Argonne National Laboratory under the supervision of Dr. Kent Crawford of the Intense Pulsed Neutron Source Division. Performed computer modeling and simulation to improve the linearity of a two-dimensional position sensitive neutron detector used in a small-angle neutron spectrometer.

MIT Undergraduate Research Opportunities Program
Summer 1988 through Summer 1989. Worked as a researcher under the supervision of Professor Sow-Hsin Chen, Department of Nuclear Engineering. Performed experiments studying the critical phenomena of phase separation and micellar formation in mixed micellar solutions using the light scattering technique of photon correlation spectroscopy. Constructed an accurate and versatile waterbath for the determination of numerous phase diagrams.

Publications

1. J. T. Chen, E. L. Thomas, C. K. Ober and G. Mao. Self-Assembled Smectic Phases in Rod-Coil Block Copolymers. *Science*, **273** (1996) 343.

2. G. Mao, J. Wang, S. R. Clingman, C. K. Ober, J. T. Chen and E. L. Thomas. Molecular Design, Synthesis, and Characterization of Liquid Crystal-Coil Diblock Copolymers with Azobenzene Side Groups. *Macromolecules*, (accepted).

3. E. L. Thomas, J. T. Chen, M. J. O'Rourke, C. K. Ober and G. Mao. Influence of a Liquid Crystalline Block on Microdomain Structure. *Macromolecular Symposia*, (in press).

4. C. K. Ober, J. Wang, G. Mao, E. J. Kramer, J. T. Chen and E. L. Thomas. Multiple Length Scale Self-Organization in Liquid Crystalline Block Copolymers. *Macromolecular Symposia*, (in press).

5. J. T. Chen and E. L. Thomas. The Use of Force Modulation Microscopy to Investigate Block Copolymer Morphology. *Journal of Materials Science* , **31** (1996) 2531.

6. J. T. Chen, E. L. Thomas, C. G. Zimba and J. F. Rabolt. Theoretical Prediction of the Optical Waveguiding Properties of Self-assembled Block Copolymer Films. *Macromolecules*, **28** (1995) 5811.

7. J. T. Chen, E. L. Thomas, C. K. Ober and S. S. Hwang. Zig-Zag Morphology of a Poly(styrene-b-hexyl isocyanate) Rod-Coil Block Copolymer. *Macromolecules*, **28** (1995) 1688.

Meeting Presentations and Abstracts

1. E. L. Thomas, M. J. O'Rourke, J. T. Chen, G. Mao, C. K. Ober, A. Avgeropoulos and N. Hadjichristidis. Influence of Block Type and Architecture on Microdomain Structure in Block Copolymers. Presented December 1996: Annual Meeting of the Materials Research Society in Boston, MA.

2. J. T. Chen, E. L. Thomas, C. K. Ober and G.-P. Mao. Phase Behavior of Rod-Coil Block Copolymers. Presented July 1996: Enrico Fermi International School on Physics: Complex Systems in Varenna, Italy.

3. E. L. Thomas, J. T. Chen, M. J. O'Rourke, C. K. Ober and G. Mao. Influence of a Liquid Crystalline Block on Microdomain Structure. Presented May 1996: NATO Advanced Research Workshop in Il Ciocco, Italy.

4. C. K. Ober, J. Wang, G. Mao, E. J. Kramer, J. T. Chen and E. L. Thomas. Simultaneous Organization on Different Length Scales; Liquid Crystalline Block Copolymers. Presented May 1996: NATO Advanced Research Workshop in Il Ciocco, Italy.

5. J. T. Chen, E. L. Thomas, C. K. Ober and G.-P. Mao. The Morphology Diagram of a Poly(styrene-b-hexyl isocyanate) Rod-Coil Block Copolymer. Presented April 1996: Annual Meeting of the Materials Research Society in San Fransisco, CA.

6. J. T. Chen, E. L. Thomas, C. K. Ober and G.-P. Mao. Phase Behavior of Rod-Coil Block Copolymers. Presented March 1996: Annual Meeting of the American Physical Society in St. Louis, CA.

7. J. T. Chen, E. L. Thomas, C. G. Zimba and J. F. Rabolt. Optical Waveguiding Properties of Block Copolymer and Multilayer Polymer Thin Films. Presented March 1995: Annual Meeting of the American Physical Society in San Jose, CA.

8. J. T. Chen, E. L. Thomas, C. K. Ober, S. S. Hwang and G.-P. Mao. The Influence of Solvent on the Competition Between Microphase Separation and the Liquid Crystalline Transition in Rod-Coil Block Copolymers. Presented March 1994: Annual Meeting of the American Physical Society in Pittsburgh, PA.

9. J. T. Chen, C. G. Zimba, E. L. Thomas and J. F. Rabolt. Theoretical Prediction of the Optical Waveguiding Properties of Block Copolymer Thin Films. Presented March 1994: Annual Meeting of the American Physical Society in Pittsburgh, PA.

10. B. L. Carvalho, J. T. Chen and E. L. Thomas. Morphology of Terraced Block Copolymer Films. Presented March 1994: Annual Meeting of the American Physical Society in Pittsburgh, PA.

11. R. K. Crawford, P. Thiyagarajan and J. T. Chen. Linearity and Calibration of Charge-Division and Rise-Time Encoded Gas PSDs. Presented May 1993: 12th Meeting of the International Collaboration on Advanced Neutron Sources (ICANS XII), United Kingdom.

12. J. T. Chen, E. L. Thomas, C. G. Zimba and J. F. Rabolt. Studies of Waveguiding Characteristics in PMMA/PS Diblock Copolymers Using Raman Spectroscopy and Integrated Optical Techniques. Presented April 1993: Annual Meeting of the Materials Research Society in San Fransisco, CA.

13. C. G. Zimba, J. T. Chen and E. L. Thomas. Raman Spectroscopy of Polymer Laminates: Modeling of Optical Field Distributions in Multilayer Waveguides. Presented January 1993: Annual Meeting of the Western Spectroscopy Association in Asilomar, CA.

14. C. G. Zimba and J. T. Chen. Waveguide Raman Spectroscopy of Polymer Laminates. Presented October 1992: Annual Meeting of the Fed. of Analytical Chemistry and Spectroscopy Societies in Cleveland, OH.

15. B. Carvalho, J. T. Chen and S. H. Chen. Phase Separation and Critical Phenomenon in Mixed diC7-diC8 phosphatidylcholine/Water Micellar Solutions. Presented November 1989: Annual AIChE Meeting in San Francisco, CA.

Awards

1. Winner of the MRS Graduate Student Award at the 1996 Materials Research Society Spring Meeting.

2. Finalist in the Frank J. Padden Jr. Graduate Research Award at the March 1995 Annual Meeting of the American Physical Society, Division of High Polymer Physics.

3. Won third prize in the M.I.T. Hoechst-Celanese Poster Competition, February 1995

4. Sigma Pi Sigma (Physics Honor Society)

5. Outstanding College Students of America

6. Massachusetts Commonwealth Scholarship Award, 1987

THESIS PROCESSING SLIP

FIXED FIELD: ill _____ name _____

index _____ biblio _____

▶ COPIES: (Archives) Aero Dewey Eng Hum

Lindgren Music Rotch (Science)

TITLE VARIES: ▶☑ in degree book, "Crystalline" is replaced by the word "Crystal"

NAME VARIES: ▶☐ _____

IMPRINT: (COPYRIGHT) _____

▶ COLLATION: 290 l

▶ ADD. DEGREE: _____ ▶ DEPT.: _____

SUPERVISORS: _____

NOTES:

cat'r: date:

page: J164

▶ DEPT: MatSci&E

▶ YEAR: 1997 ▶ DEGREE: Ph.D.

▶ NAME: CHEN, John Tsen-Tao